18th Conference of Czech and Slovak Physicists

with participation of Hungarian and Polish Physical Societies

Olomouc, Czech Republic, September 16–19, 2014

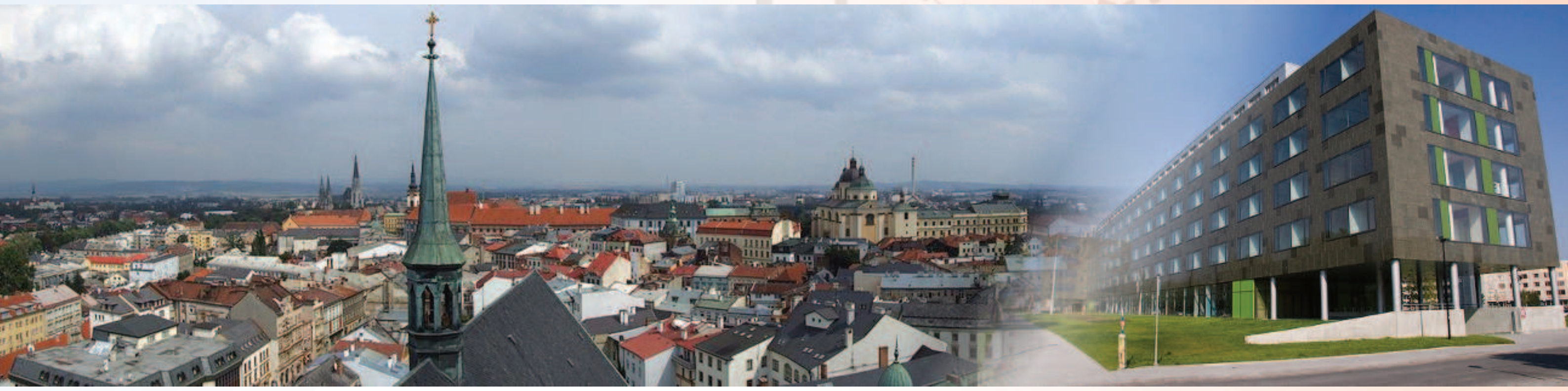

Conference Proceedings

18th Conference of Czech and Slovak Physicists with participation of Hungarian and Polish Physical Societies was organised by the Czech Physical Society (http://www-ucjf.troja.mff.cuni.cz/cfs/) and Slovak Physical Society (http://kf.elf.stuba.sk/~slovenska_fyzikalna_spolocnost/) in cooperation with the European Physical Society (http://www.eps.org), Roland Eötvös Physical Society (http://www.elft.hu) and the Polish Physical Society (http://ptf.net.pl). Financial support from the European Physical Society is gratefully acknowledged.

Programme committee

Organising committee

No English-language editing and proofreading was done either by the publisher or by the editors, so the quality of language of papers is under the authors' responsibility.

Editors: Libor Machala a Lukáš Richterek
Executive Editor: Prof. RNDr. Zdeněk Dvořák, DrSc.
Responsible Editor: Mgr. Jana Kreiselová

1. edition

Palacký University, Olomouc, Czech Republic 2015

ISBN 978-80-244-4725-4 (CD)
ISBN 978-80-244-4726-1 (on-line)

Contents

Foreword

The 18th conference of Czech and Slovak physicists was organized with the participation of Hungarian and Polish physical societies for the first time. Thus the conference became international and the conference language was English. Palacký University in Olomouc welcomed more than 110 participants who presented 12 plenary lectures, 50 oral lectures and 27 posters. The participants could enjoy the visit of the general secretary of European Physical Society *Mr. David Lee* and the chair of European Physical Society *Prof. John Dudley.* The main purpose of the conference was the meeting of physicists from central European regions and opportunity for young scientists to present their results. The opening ceremony was held in a representative Archbishop palace. After introductory speeches of *Prof. Mašláň*, *Assoc. Prof. Jan Mlynář*, *Mr. David Lee* and *Assoc. Prof. Libor Machala*, the prizes of Milan Odehnal were awarded to young scientist. Just after the ceremony, they had opportunity to present their main results. In addition to conventional contributions, there was a series of lectures associated with huge international corporations such as ATLAS, STAR, COMPASS, FAIR, HADES, ALICE, and HiLASE. Besides scientific program, the participants could enjoy excursion to the rooms in the Archbishop palace, where Franz Joseph I. temporarily lived, further a joint dinner in small brewery. The ceremonial dinner was organized directly at the faculty terrace with living music. In summary, the conference was pleasant and we believe in a follow up of these traditional conferences in future.

Libor Machala
Roman Kubínek
Lukáš Richterek

The Phase Diagram of Quantum Chromodynamics: lattice results

Sándor D. Katz[1]

[1]katz@bodri.elte.hu, Institute for Theoretical Physics, Eötvös University,
MTA-ELTE Lendület Lattice Gauge Theory Research Group, Budapest, Pazmany P. setany 1/A, H-1117

Abstract. The QCD phase diagram is studied using non-perturbative lattice calculations. Results for the order of the transition, the transition temperature and the equation of state are presented. At non-vanishing chemical potential, direct lattice calculations are impossible due to the sign problem. Several methods are available for moderately small chemical potentials. Results for the phase diagram and equation of state are shown.

1 Introduction

During the evolution of the universe there was a transition at $T \approx 200$ MeV. It is related to the spontaneous breaking of the chiral symmetry of QCD. The nature of the QCD transition affects our understanding of the universe's evolution. Extensive experimental work is currently being done with heavy ion collisions to study the QCD transition. Both for the cosmological transition and for high energy collisions, the net baryon densities are quite small, thus the baryonic chemical potentials (μ) are much less than the typical hadron masses. A calculation at μ=0 is directly applicable for the cosmological transition and most probably also determines the nature and absolute temperature of the transition at high energy heavy ion collisions (most recently at LHC). The $\mu > 0$ regime of the QCD phase diagram is relevant for lower energy collisions (e.g. at FAIR at GSI). A particularly interesting possibility is the existence of a critical point at finite temperature and finite μ which can be searched for by experiments. Neutron stars are described by the large μ part of the phase diagram.

Though advanced perturbative techniques can provide results down to several times the transition temperature, the most interesting regimes of the phase diagram (i.e. around the transition line) can only be accessed using non-perturbative techniques. Among these techniques, lattice QCD is the most systematic one; a short introduction will be given in the next section.

In this review the recent results of the Wuppertal-Budapest group are discussed. The order and the absolute scale of the transition. as well as the equation of state are determined using physical quark masses and a continuum extrapolation. For moderate chemical potentials, results are presented for the transition line and the equation of state. The findings are compared to those of the 'HotQCD' collaboration.

2 Lattice formulation

Thermodynamical quantities can be obtained from the partition function which can be given by a Euclidean path-integral:

$$Z = \int \mathcal{D}U\mathcal{D}\bar{\Psi}\mathcal{D}\Psi e^{-S_E(U,\bar{\Psi},\Psi)}, \qquad (1)$$

where U and $\bar{\Psi}, \Psi$ are the gauge and fermionic fields and S_E is the Euclidean action. The lattice regularization of this action is not unique. There are several possibilities to use improved actions which have the same continuum limit as the straightforward unimproved ones. The advantage of improved actions is that the discretization errors are reduced and therefore a reliable continuum extrapolation is possible already from larger lattice spacings. On the other hand, calculations with improved actions are usually more expensive than with the unimproved one.

Usually S_E can be split up as $S_E = S_g + S_f$ where S_g is the gauge action containing only the self interactions of the gauge fields and S_f is the fermionic part. The gauge action has one parameter, the β gauge coupling, while the parameters of S_f are the m_q quark masses and the μ_q chemical potentials. Usually the masses of the light u,d quarks are taken equal so there are two mass parameters, m_{ud} and m_s. For the fermionic action the two most widely used discretization types are the Wilson and staggered fermions. Our choice is to use a tree level Symanzik improved gauge action for S_g and a stout improved staggered fermion action for S_f [1]. This choice is motivated by at least two reasons. It is computationally relatively cheap (comparable to the unimproved actions) and the discretization effects coming from $T = 0$ and $T > 0$ simulations are balanced.

For the actual calculations finite lattice sizes of $N_s^3 N_t$ are used. The physical volume and the temperature are related to the lattice extensions as:

$$V = (N_s a)^3, \qquad T = \frac{1}{N_t a}. \qquad (2)$$

Therefore lattices with $N_t \gg N_s$ are referred to as zero temperature lattices while the ones with $N_t < N_s$ are finite temperature lattices.

In order to carry out $T > 0$ simulations we have to fix the parameters of the action, the gauge coupling and the quark masses. This is usually done at zero temperature, where the results of lattice computations can be compared to experiments. In order to fix three parameters, three quantities are needed. We chose to use the pion and kaon masses (m_π, m_K) and the leptonic decay constant of the kaon (f_K). These can all be determined from $T = 0$ lattice simulations. Lattice calculations can only yield dimensionless quanti-

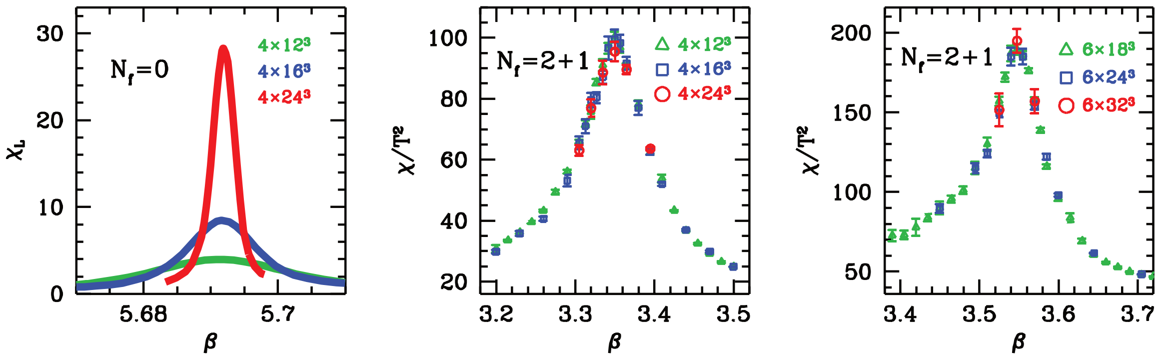

Figure 1. The volume dependence of the susceptibility peaks for pure SU(3) gauge theory (Polyakov-loop susceptibility, left panel) and for full QCD (chiral susceptibility on N_t=4 and 6 lattices, middle and right panels, respectively).

ties, i.e. am_π, am_K and af_K, where a is the lattice spacing. For any value of the coupling, the mass parameters can be tuned to obtain the correct ratios for m_π/f_K and m_K/f_K. These $m_{ud}(\beta)$ and $m_s(\beta)$ functions are called the line of constant physics (LCP). All finite T simulations have to be carried out along the LCP. Different points of the LCP describe the same physics at different lattice spacings. The lattice spacing can be obtained by comparing e.g. the determined af_K value to the physical f_K.

A very important step of any lattice analysis is the continuum extrapolation. Several simulations have to be carried out at different lattice spacings and the results have to be extrapolated to the continuum. Since $T = 1/(N_t a)$, if we are interested in a given temperature range (around the transition) then a decreasing lattice spacing corresponds to increasing N_t. In this paper, several different lattice resolutions are used which are characterized by $N_t = 4, 6, 8, 10, 12$ and 16. The corresponding lattice spacings are approximately 0.3 – 0.075 fm.

3 The order of the transition

In this section the nature of the QCD transition is discussed. The details of the calculations can be found in [2]. In order to determine the nature of the transition one should apply finite size scaling techniques for the chiral susceptibility $\chi = (T/V)\cdot(\partial^2 \log Z/\partial m_{ud}^2)$. This quantity shows a pronounced peak as a function of the temperature. For a first order phase transition, such as in the pure gauge theory, the peak of the analogous Polyakov susceptibility gets more and more singular as we increase the volume (V). The width scales with 1/V the height scales with volume (see left panel of Figure 1). A second order transition shows a similar singular behavior with critical indices. For an analytic transition (what we call a crossover) the peak width and height saturates to a constant value. That

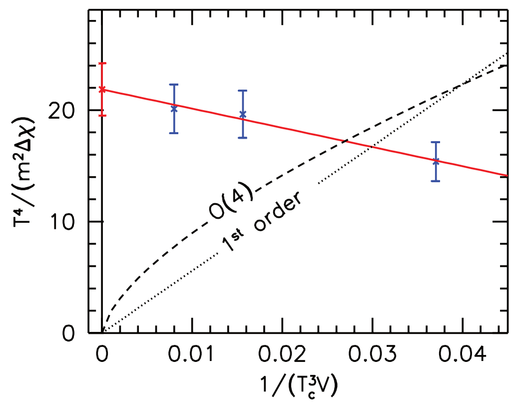

Figure 2. Continuum extrapolated susceptibilities $T^4/(m^2\Delta\chi)$ as a function of $1/(T_c^3 V)$. For true phase transitions the infinite volume extrapolation should be consistent with zero, whereas for an analytic crossover the infinite volume extrapolation gives a non-vanishing value. The continuum-extrapolated susceptibilities show no phase-transition-like volume dependence, though the volume changes by a factor of five. The V→∞ extrapolated value is 22(2) which is 11σ away from zero. For illustration, we fit the expected asymptotic behaviour for first-order and O(4) (second order) phase transitions shown by dotted and dashed lines, which results in chance probabilities of 10^{-19} (7×10^{-13}), respectively.

is what we observe in full QCD on N_t=4 and 6 lattices (middle and right panels of Figure 1). We see an order of magnitude difference between the volumes, but a volume independent scaling. It is a clear indication for a crossover. These results were obtained with physical quark masses for two sets of lattice spacings. Note, however, that for a final conclusion the important question remains: do we get the same volume independent scaling in the continuum?

We carried out a finite size scaling analysis with the continuum extrapolated height of the renormalized susceptibility. The renormalization of the chiral susceptibility can be done by taking the second derivative of the free energy density (f) with respect to the renormalized mass (m_r). The logarithm of the partition function contains quartic divergences. These can be removed by subtracting the free energy at $T = 0$: $f/T^4 = -N_t^4 \cdot [\log Z(N_s, N_t)/(N_t N_s^3) - \log Z(N_{s0}, N_{t0})/(N_{t0} N_{s0}^3)]$. This quantity has a correct continuum limit. The subtraction term is obtained at T=0, for which simulations are carried out on lattices with N_{s0}, N_{t0} spatial and temporal extensions (otherwise at the same parameters of the action). The bare light quark mass (m_{ud}) is related to m_r by the mass renormalization constant m_r=$Z_m \cdot m_{ud}$. Note that Z_m falls out of the combination $m_r^2 \partial^2/\partial m_r^2 = m_{ud}^2 \partial^2/\partial m_{ud}^2$. Thus, $m_{ud}^2 [\chi(N_s, N_t) - \chi(N_{s0}, N_{t0})]$ also has a continuum limit (for its maximum values for different N_t, and in the continuum limit we use the shorthand notation $m^2 \Delta\chi$).

In order to carry out the finite volume scaling in the continuum limit we took three different physical volumes. For these volumes we calculated the dimensionless combination $T^4/m^2\Delta\chi$ at 4 different lattice spacings: 0.3 fm was always off, otherwise the continuum extrapolations could be carried out. The volume dependence of the continuum extrapolated inverse susceptibilites is shown on Figure 2.

Our result is consistent with an approximately constant behaviour, despite the fact that we had a factor of 5 difference in the volume. The chance probabilities, that statistical fluctuations changed the dominant behaviour of the volume dependence are negligible. As a conclusion we can say that the staggered QCD transition at $\mu = 0$ is a crossover.

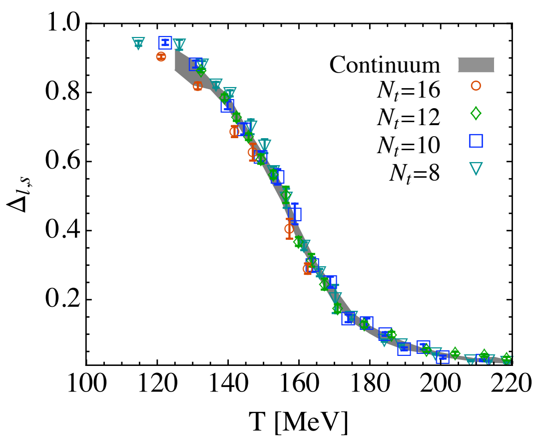

Figure 3. Renormalized chiral condensate as a function of the temperature.

4 The transition temperature

An analytic crossover, like the QCD transition has no unique T_c, different observables and/or definitions may lead to different temperatures.

In ref. [3] we considered three quantities to locate the transition point: the chiral susceptibility, the strange quark number susceptibility and the Polyakov-loop. The obtained temperatures were 151(3)(3) MeV, 175(2)(4) MeV and 176(3)(4) MeV, respectively. The first errors come from the finite temperature analysis, the second ones from the $T = 0$ scale setting. We used physical quark masses and four lattice spacings corresponding to $N_t = 4, 6, 8$ and 10. These results, especially the one coming from the chiral susceptibilty, are in contradiction with those of ref. [4]. They obtain $T_c = 192(7)(4)$ MeV from both the chiral susceptibility and Polyakov loop susceptibility. They used $N_t = 4$ and 6 lattices with a p4 improved action.

Due to this discrepancy both collaborations improved on their data. We have used physical quark masses also for the $T = 0$ simulations and took even finer lattice spacings ($N_t = 12$) at finite temperature [5] and later also even finer lattices ($N_t = 16$) [6]. The results changed only within their uncertainties. The HotQCD collaboration uses two lattice actions (asqtad and p4) and they extended their simulations to $N_t = 8$ lattices [7]. Later they employed a new discretization (HISQ) and went up to $N_t = 12$ lattices [8]. In the following we compare the latest results of the two groups to each other.

The light quark chiral condensate ($\langle\bar\psi\psi\rangle$) is minus one times the first derivative of the free energy density with respect to the light quark mass. It is ultraviolet divergent, a possible way of removing divergences was proposed in [9]. *If one assumes* that the additive divergences of the free energy density depend on the quark masses only through the combination $m_{ud}^2 + m_s^2$, then one can get rid of the additive divergences in $\langle\bar\psi\psi\rangle$ by using the strange quark condensate ($\langle\bar s s\rangle$):

$$\Delta_{l,s} = \langle\bar\psi\psi\rangle - \frac{2m_{ud}}{m_s}\langle\bar s s\rangle. \tag{3}$$

The remaining multiplicative divergences can be removed by dividing with the same quantity at zero temperature:

$$\Delta_{l,s} \to \frac{\Delta_{l,s}(T)}{\Delta_{l,s}(T=0)}. \tag{4}$$

In Figure 3 we plot this quantity as a function of the temperature. If one defines the transition temperature as the inflection point of this curve, in the continuum limit we get $T_c = 157(3)(3)$ MeV where the first error is coming again from $T > 0$ and the second from the scale setting. A slightly different renormalization of the condensate results in a compatible result: $T_c = 155(3)(3)$ (see Ref. [6]). The latest result of the HotQCD collaboration for the same quantity is $T_c = 154(9)$ MeV: the original discrepancy of 2006 has been resolved.

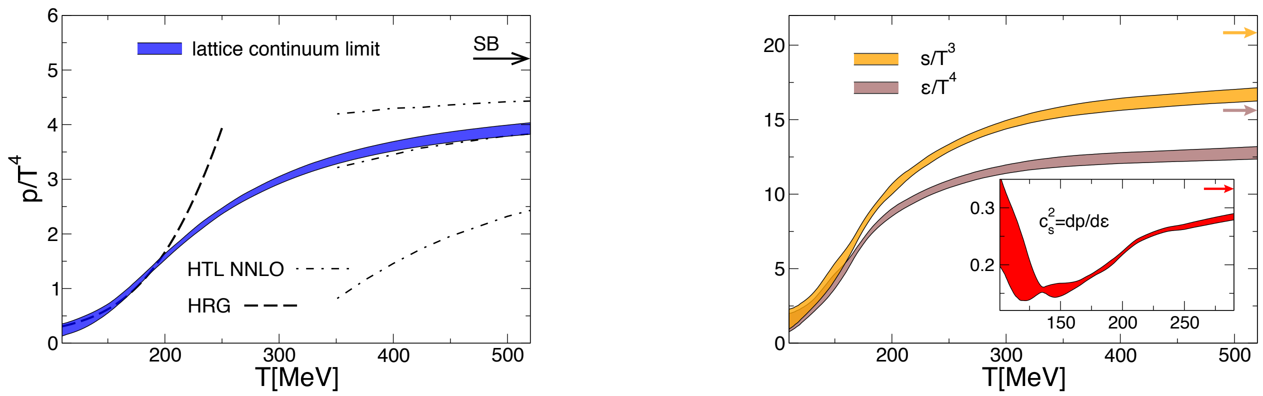

Figure 4. Left: the pressure as a function of temperature. The HRG prediction is indicated by the black dashed line at low temperatures, at high temperature we show a comparison to the NNLO HTL result of ref. [12] using three different renormalization scales ($\mu = \pi T$, $2\pi T$ or $4\pi T$). Right: entropy density (s) and energy density (ϵ) as functions of temperature. The insert shows the speed of sound squared.

5 Equation of state

Besides finding the transition temperature one can also give the equation of state (EoS) of hadronic/gluonic matter well below or above the transition T (or also for $\mu > 0$). All thermodynamical quantities can be obtained from the grand canonical partition function, e.g. for the energy density and the pressure:

$$\epsilon(T) = \frac{T^2}{V}\frac{\partial(\log Z)}{\partial T} \quad p(T) = T\frac{\partial(\log Z)}{\partial V}. \tag{5}$$

For large homogeneous systems, the $\log Z$ is proportional to the volume and thus the pressure is equal to the free energy density. Unfortunately the partition function is not directly calculable on the lattice. The usual method to compute the pressure is the integral method: derivatives of $\log Z$ with respect of the action parameters (β, m_q, μ_q) are determined and the free energy is reconstructed as an integral in this space:

$$p = \frac{T}{V}\log Z = \tag{6}$$
$$\frac{T}{V}\int d(\beta, m_q, \mu_q)\left(\frac{\partial \log Z}{\partial \beta}, \frac{\partial \log Z}{\partial m_q}, \frac{\partial \log Z}{\partial \mu_q}\right).$$

The partial derivatives are simple observables: the gauge action, the chiral condensate and the density.

At low temperatures, below the transition, one expects that QCD is well approximated by a non-interacting gas of hadrons. All thermodynamic quantities can be calculated from the corresponding hadron resonance gas model (HRG) and can be compared to lattice results at low temperatures. In all cases we find a good agreement up to ≈ 130 MeV.

The first result for the equation of state from the Wuppertal-Budapest collaboration was presented in [1] where $N_t = 4$ and $N_t = 6$ lattices were used and no continuum extrapolation was attempted. In Ref. [10] lattices up to $N_t = 10$ (and $N_t = 12$ for one temperature) were used and even though no continuum extrapolation was performed, results with different lattice spacings were very close to each other. The full, continuum extrapolated result using lattice spacings up to $N_t = 16$ was published in Ref. [11]. Figure 4 shows the pressure (left), the energy density (right), the entropy density (right) as well as the speed of sound (right, insert) taken from this publication. The lattice results are compared to the HRG predictions at low temperature. The pressure is also compared to Hard Thermal Loop (HTL) perturbation theory at high temperatures.

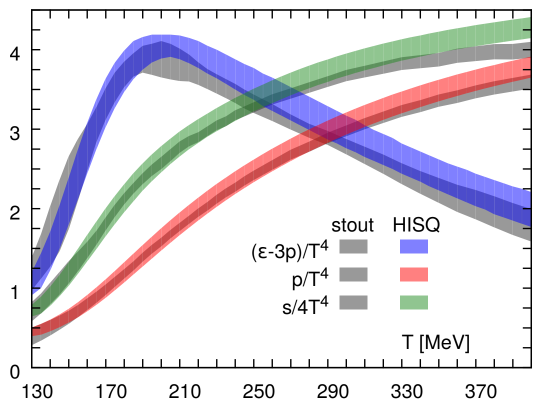

Figure 5. Comparison of the equation of state with that of the HotQCD collaboration [13].

A well suited quantity to compare results with other collaborations is the interaction measure, $(\epsilon - 3p)/T^4$ which can be calculated directly from the partition function without any integration. This quantity around T_c showed a discrepancy with the recent results of the HotQCD collaboration [7] where they used asqtad and p4 actions up to $N_t = 8$. Similarly to the transition temperature this discrepancy has been resolved recently. The latest result of the HotQCD collaboration uses HISQ fermions up to $N_t = 12$. Figure 5 shows the comparison and the nice agreement between the two collaborations.

6 Non-vanishing chemical potential

Since fermionic fields are represented by Grassmann variables, one has to integrate them out before any

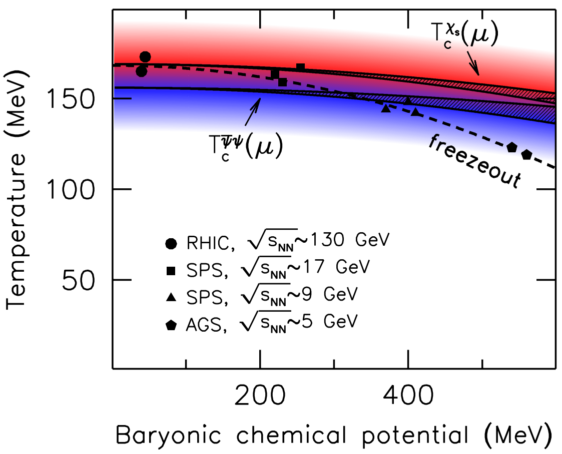

Figure 6. The phase diagram at non-vanishing chemical potentials. The upper curve is determined from the quark number susceptibility, the lower one from the chiral condensate. The points show freezeout temperatures extracted from various experiments.

Monte-Carlo techniques can be applied. Fortunately the fermionic action ($S_f = \sum_{x,y} \bar\Psi_x M_{xy} \Psi_y$) is bilinear in the fields (M is the fermion matrix, containing the discretization of the continuum Dirac operator and the quark mass), so Equation (1) leads to:

$$Z = \int \mathcal{D}U \det M[U] e^{-S_g[U]} \tag{7}$$

At $\mu = 0$ the determinant of M can be shown to be positive and real, so the above path integral can be evaluated using Monte-Carlo techniques. Unfortunately at $\mu > 0$ this no longer holds, the determinant can take complex values and a direct evaluation is not possible anymore. This is called the complex action or sign problem.

A simple, but powerful way to get around the sign problem is the overlap improving multiparameter reweighting [14]. The partition function at finite μ can be rewritten as:

$$\begin{aligned} Z = \int \mathcal{D}U e^{-S_g(\beta,U)} \det M(m,\mu,U) = \\ \int \mathcal{D}U e^{-S_g(\beta_0,U)} \det M(m_0,\mu=0,U) \\ \left\{ e^{-S_g(\beta,U)+S_g(\beta_0,U)} \frac{\det M(m,\mu,U)}{\det M(m_0,\mu=0,U)} \right\}, \end{aligned} \tag{8}$$

where the second line contains a positive definite action which can be used to generate the configurations and the terms in the curly bracket in the last line are taken into account as an observable. The expectation value of any observable can be then written in the form:

$$< O >_{\beta,m,\mu} = \frac{\sum O(\beta,m,\mu) w(\beta,m,\mu)}{\sum w(\beta,m,\mu)} \tag{9}$$

with $w(\beta,m,\mu)$ being the weights of the configurations defined by the curly bracket of Equation (8).

This reweighting technique made it possible to determine the phase diagram on the $\mu - T$ plane up to $\mu \approx 1.5T$ in $N_f = 4$ [14] and $N_f = 2+1$ [15, 16] staggered QCD on $N_t = 4$ lattices. The transition points were located in these cases by finding the Lee-Yang zeroes of the partition function.

The use of Equation (8) requires the exact calculation of determinants on each gauge configuration which is computationally very expensive. Instead of using the exact formula, one can make a Taylor expansion for the determinant ratio in the weights [17] (for simplicity assuming no reweighting in the mass):

$$\begin{aligned} \ln\left(\frac{\det M(\mu)}{\det M(0)}\right) &= \sum_{n=1}^{\infty} \frac{\mu^n}{n!} \frac{\partial^n \ln \det M(0)}{\partial \mu^n} \\ &\equiv \sum_{n=1}^{\infty} R_n \mu^n. \end{aligned} \tag{10}$$

Taking only the first few terms of the expansion one gets an approximate reweighting formula. The advantage of this approximation is that the coefficients are derivatives of the fermion determinant at $\mu = 0$, which can be well approximated stochastically. However, due to the termination of the series and the errors introduced by the stochastic evaluation of the coefficients we do not expect this method to work for as large μ values as the full technique.

This expansion made it possible to determine the phase diagram on $N_t = 6, 8$ and 10 lattices and perform a continuum extrapolation. Since at $\mu = 0$ the transition is a crossover, we studied two observables which give different transition temperatures: the chiral condensate and the strange quark number susceptibility. Would the transition become stronger for increasing μ the two transition temperatures should converge towards each other. The result is shown in Figure 6. There is no evidence for the strengthening of the transition. Note, however, that this is a leading order calculation in μ, a full reweighting might produce a non-monotonic behavior which can result in a critical point similarly to the $N_t = 4$ case [15, 16].

Besides the transition line, one can also determine the equation of state for non-vanishing chemical potential. Results using full reweighting on $N_t = 4$ lattices can be found in Refs [18, 19]. Again, by using Taylor expansion, one can go to larger lattices [20, 21]. In Ref. [22] our collaboration presented a continuum extrapolated result for the equation of state using a leading order expansion in μ. One can use various setups for the chemical potential, our choice was to set $\mu_u = \mu_d = \mu_L/3$ and μ_s such that the total strangeness is zero. The results are shown in Figure 7.

7 Conclusions

Lattice QCD has reached an era where continuum extrapolated, precision calculation of thermodynamics observables is possible. We presented results for the order of the transition, the transition temperature and the equation of state for $\mu = 0$ and for the

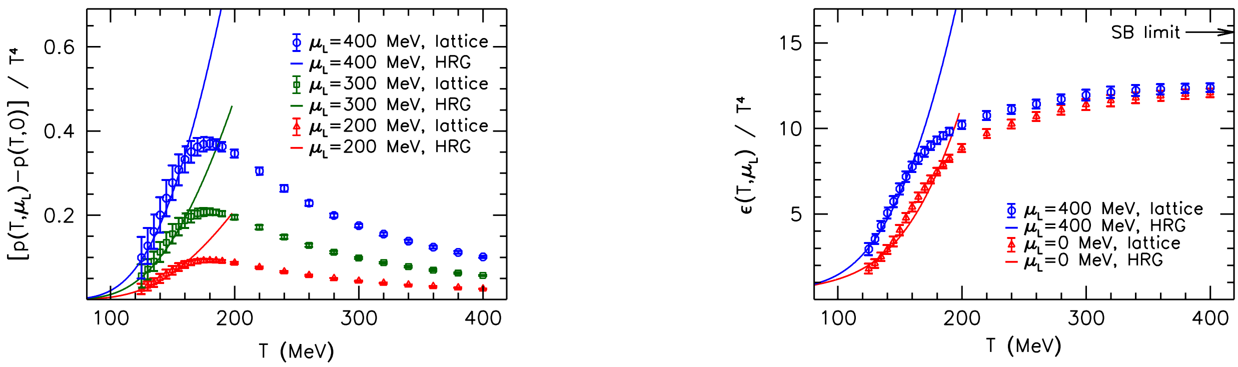

Figure 7. Left: The finite μ contribution to the pressure for various light chemical potentials. The HRG results are shown for comparison at low temperature. Right: the energy density for two chemical potentials. The HRG results are shown by the continuous lines.

phase diagram and the equation of state at $\mu > 0$. Once the continuum extrapolation has been carried out, the results are not allowed to depend on the used discretization. Therefore, results of different collaboration should agree with each other. It has been shown that after years of discrepancies, different collaborations now have a consensus on the transition temperature and the equation of state.

References

[1] Y. Aoki, Z. Fodor, S. D. Katz and K. K. Szabo, JHEP **0601**, 089 (2006), [arXiv:0510084 [hep-lat]].

[2] Y. Aoki, G. Endrodi, Z. Fodor, S. D. Katz and K. K. Szabo, Nature **443**, 675 (2006), [arXiv:0611014 [hep-lat]].

[3] Y. Aoki, Z. Fodor, S. D. Katz and K. K. Szabo, Phys. Lett. B **643**, 46 (2006), [arXiv:0609068 [hep-lat]].

[4] M. Cheng, N. H. Christ, S. Datta, J. van der Heide, C. Jung, F. Karsch, O. Kaczmarek and E. Laermann *et al.*, Phys. Rev. D **74**, 054507 (2006), [arXiv:0608013 [hep-lat]].

[5] Y. Aoki, S. Borsanyi, S. Durr, Z. Fodor, S. D. Katz, S. Krieg and K. K. Szabo, JHEP **0906**, 088 (2009), [arXiv:0903.4155 [hep-lat]].

[6] S. Borsanyi *et al.* [Wuppertal-Budapest Collaboration], JHEP **1009**, 073 (2010), [arXiv:1005.3508 [hep-lat]].

[7] A. Bazavov, T. Bhattacharya, M. Cheng, N. H. Christ, C. DeTar, S. Ejiri, S. Gottlieb and R. Gupta *et al.*, Phys. Rev. D **80**, 014504 (2009), [arXiv:0903.4379 [hep-lat]].

[8] A. Bazavov, T. Bhattacharya, M. Cheng, C. DeTar, H. T. Ding, S. Gottlieb, R. Gupta and P. Hegde *et al.*, Phys. Rev. D **85**, 054503 (2012), [arXiv:1111.1710 [hep-lat]].

[9] M. Cheng, N. H. Christ, S. Datta, J. van der Heide, C. Jung, F. Karsch, O. Kaczmarek and E. Laermann *et al.*, Phys. Rev. D **77**, 014511 (2008), [arXiv:0710.0354 [hep-lat]].

[10] S. Borsanyi, G. Endrodi, Z. Fodor, A. Jakovac, S. D. Katz, S. Krieg, C. Ratti and K. K. Szabo, JHEP **1011**, 077 (2010), [arXiv:1007.2580 [hep-lat]].

[11] S. Borsanyi, Z. Fodor, C. Hoelbling, S. D. Katz, S. Krieg and K. K. Szabo, Phys. Lett. B **730**, 99 (2014), [arXiv:1309.5258 [hep-lat]].

[12] J. O. Andersen, L. E. Leganger, M. Strickland and N. Su, JHEP **1108**, 053 (2011), [arXiv:1103.2528 [hep-ph]].

[13] A. Bazavov *et al.* [HotQCD Collaboration], Phys. Rev. D **90** 9, 094503 (2014), [arXiv:1407.6387 [hep-lat]].

[14] Z. Fodor and S. D. Katz, Phys. Lett. B **534**, 87 (2002), [arXiv:0104001 [hep-lat]].

[15] Z. Fodor and S. D. Katz, JHEP **0203**, 014 (2002), [arXiv:0106002 [hep-lat]].

[16] Z. Fodor and S. D. Katz, JHEP **0404**, 050 (2004), [arXiv:0402006 [hep-lat]].

[17] C. R. Allton, S. Ejiri, S. J. Hands, O. Kaczmarek, F. Karsch, E. Laermann, C. Schmidt and L. Scorzato, Phys. Rev. D **66**, 074507 (2002), [arXiv:0204010 [hep-lat]].

[18] Z. Fodor, S. D. Katz and K. K. Szabo, Phys. Lett. B **568**, 73 (2003), [arXiv:0208078 [hep-lat]].

[19] F. Csikor, G. I. Egri, Z. Fodor, S. D. Katz, K. K. Szabo and A. I. Toth, JHEP **0405**, 046 (2004) [hep-lat/0401016].

[20] C. R. Allton, S. Ejiri, S. J. Hands, O. Kaczmarek, F. Karsch, E. Laermann and C. Schmidt, Phys. Rev. D **68**, 014507 (2003) [hep-lat/0305007].

[21] C. R. Allton, M. Doring, S. Ejiri, S. J. Hands, O. Kaczmarek, F. Karsch, E. Laermann and K. Redlich, Phys. Rev. D **71**, 054508 (2005) [hep-lat/0501030].

[22] S. Borsanyi, G. Endrodi, Z. Fodor, S. D. Katz, S. Krieg, C. Ratti and K. K. Szabo, JHEP **1208**, 053 (2012) [arXiv:1204.6710 [hep-lat]].

Study of CP Violation and Physics Beyond the Standard Model at the Belle experiment

Daniel Červenkov[1]

[1]cervenkov@ipnp.troja.mff.cuni.cz, Institute of Particle and Nuclear Physics, Faculty of Mathematics and Physics, Charles University in Prague, V Holešovičkách 2, 180 00 Prague 8, Czech Republic

Abstract. Charge-parity (CP) violation is a firmly established feature of weak interactions of the Standard Model. However, there are still many crucial open questions. E.g., the strength of CP violation incorporated into the SM is insufficient to explain the observed cosmological matter anti-mater asymmetry by many orders of magnitude. We present a short explanation of where the Standard Model quark sector CP violation comes from and why it requires the existence of 3 quark generations. We derive unitarity triangles and angles that are the actual CP violation parameters that are usually measured. We go on to introduce the Belle experiment and some of the motivation for the upgrade it's currently undergoing — the lack of New Physics observation at the energy frontier as well as several 'anomalous' measurements from Belle itself.

1 Introduction

Although symmetries are inseparable part of Nature, much of the texture of this world is due to symmetry breaking. The particular case we will be discussing, CP violation, is the reason we live in a matter dominated universe. Without it, the world would look quite different today — there wouldn't be much of anything except radiation, as most of the matter and antimatter would have annihilated shortly after the Big Bang.

An important fact that is well worth mentioning is that the CP violation present in the Standard Model is not sufficient to explain the amount of matter observed in the universe - it can explain only about one galactic mass. Therefore, a number of physicists are looking for new sources of CP violation. However we will discuss only the one that is firmly established within the Standard Model — the quark sector CP violation.

2 Charged Current

To get a handle on CP violation we can look at the charged current structure. Considering only two quark generations, the structure of the charged current Lagrangian describing an up-type quark transition to a down-type quark and vice versa can be seen in Equation 1 [1]. In the rightmost part, we have consolidated the two terms from the left hand side into a single term using matrix notation. This approach is quite useful, as examining the matrix's properties can give us valuable insight.

$$\begin{aligned}\mathcal{L}_{CC} \propto\, &\bar{u}\gamma^\mu \frac{1-\gamma^5}{2}(V_{ud}d + V_{us}s)W_\mu^+ \\ &+ \bar{c}\gamma^\mu \frac{1-\gamma^5}{2}(V_{cd}d + V_{cs}s)W_\mu^+ + c.c. = \\ &= (\bar{u}\,\bar{c})\gamma^\mu \frac{1-\gamma^5}{2}\begin{pmatrix}V_{ud} & V_{us}\\ V_{cd} & V_{cs}\end{pmatrix}\begin{pmatrix}d\\ s\end{pmatrix} W_\mu^+ + c.c.\end{aligned} \tag{1}$$

Let us start by counting the number of the, so called, mixing matrix's parameters. In general, there are 4 complex parameters, which is equivalent to 8 real ones. However, the matrix has to be unitary — this is a very reasonable assumption as it guarantees probability conservation. The unitarity condition can be expressed as $VV^\dagger = I$. For a 2×2 matrix, this translates to 4 constraints.

Moreover, an arbitrary complex phase can be absorbed into each of the quark fields $\bar{u}$, $\bar{c}$, d and s, as we have freedom in defining them. However, an overall phase is unobservable, therefore we have only 3 additional constraints.

Combining all of the above, we see that the matrix has just $8-4-3=1$ parameter and we can choose the relative phases freely. A standard choice is:

$$\begin{pmatrix}\cos\theta_C & \sin\theta_C\\ -\sin\theta_C & \cos\theta_C\end{pmatrix} \tag{2}$$

and it is called 'Cabibbo matrix'.

When exchanging quarks for anti-quarks in an arbitrary interaction vertex, we have to look at a charge conjugated (c.c.) part of the Lagrangian (with respect to the part describing quarks). For example:

$$\begin{aligned}&(\bar{d}\,\bar{s})\gamma^\mu \frac{1-\gamma^5}{2}\begin{pmatrix}\cos\theta_C & \sin\theta_C\\ -\sin\theta_C & \cos\theta_C\end{pmatrix}^\dagger \begin{pmatrix}u\\ c\end{pmatrix} W_\mu^- = \\ =&(\bar{d}\,\bar{s})\gamma^\mu \frac{1-\gamma^5}{2}\begin{pmatrix}\cos\theta_C & -\sin\theta_C\\ \sin\theta_C & \cos\theta_C\end{pmatrix}^* \begin{pmatrix}u\\ c\end{pmatrix} W_\mu^-\end{aligned} \tag{3}$$

The term that is relevant for, e.g., the u quark is:

$$(\cos\theta_C\bar{d} + \sin\theta_C\bar{s})\gamma^\mu\frac{1-\gamma^5}{2}uW_\mu^- \tag{4}$$

Comparing that to the non-charge conjugated analogue:

$$\bar{u}\gamma^\mu\frac{1-\gamma^5}{2}(\cos\theta_C d + \sin\theta_C s)W_\mu^+ \tag{5}$$

we see that the amplitudes for both vertices are exactly the same — there is no CP violation. This is because the complex conjugation of the mixing matrix in Equation 3 is trivial as the matrix is real.

3 Cabibbo-Kobayashi-Maskawa Matrix

Two Japanese physicists, Kobayashi and Maskawa, argued, that while no CP violation is possible within the standard charged current with just two quark generations, it arises naturally with three generations [2].

Let us repeat the previous counting exercise with the Cabibbo-Kobayashi-Maskawa (CKM) matrix:

$$V_{CKM} = \begin{pmatrix} V_{ud} & V_{us} & V_{ub} \\ V_{cd} & V_{cs} & V_{cb} \\ V_{td} & V_{ts} & V_{tb} \end{pmatrix} \tag{6}$$

In this case, there are 9 complex parameters, or 18 real ones. The unitarity condition still holds, however for a 3×3 matrix it is equivalent to 9 constraints. And after repeating the same trick with absorbing phases into the quark fields, we are left with $18 - 9 - 5 = 4$ parameters.

We may now ask ourselves, whether we can again take V_{CKM} real. It follows from definitions, that a real unitary matrix is actually an orthogonal matrix. In this case a member of $O(3)$. However, it is easy to show that an $O(3)$ matrix has only 3 free parameters [3]. Therefore, we can conclude that V_{CKM} invariably has to be complex.

The complex conjugation of the mixing matrix mentioned in the previous section is no longer trivial — CP violation arises and Nature treats matter and anti-matter differently!

4 Unitarity Triangle

The CP violation parameters that are actually usually measured are 'unitarity triangle angles'. As was already mentioned in the previous sections, the CKM matrix is unitary and thus subject to certain constraints. Namely elements of a unitary matrix V satisfy

$$(V^\dagger V)_{ij} = (VV^\dagger)_{ij} = \delta_{ij}. \tag{7}$$

For a 3x3 unitary matrix such as the CKM matrix, this translates into nine conditions. The six relations with $i \neq j$ define a triangle in the complex plane — a sum of any three complex numbers that is equal to zero does (although the triangle can be degenerate). By convention the triangle defined by

$$V_{ud}V_{ub}^* + V_{cd}V_{cb}^* + V_{td}V_{tb}^* = 0 \tag{8}$$

is used for the definition of three unitarity angles used in B physics; see Figure 1. Such a choice has the benefit that the angles are of equal order, hence they can be measured independently with reasonable relative errors.

5 Belle Experiment

The Belle experiment uses the KEKB asymmetric e^+e^- collider. The energy asymmetry is essential for the so-called time dependent measurements, which are used to extract many CP violation parameters from experimental data.

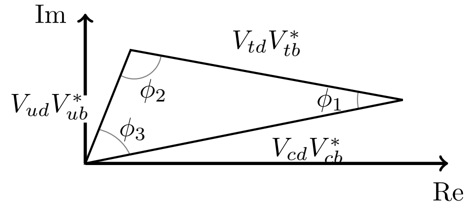

Figure 1. Unitarity triangle in the complex plane.

KEKB/Belle is currently undergoing an upgrade. The resulting machine will be called SuperKEKB/Belle II. There are several facts and ideas that motivated this upgrade. E.g., so far none of the LHC experiments have observed any New Physics (NP). There is a possibility that NP scale is higher than ∼10 TeV; out of LHC's reach.

However, B-factories such as Belle search for new particles in a different way. The potential new particles would contribute to the studied processes via loops in Feynman diagrams. Because they would be virtual, they could be off the mass-shell and their presence could be observed even if the collider's energy was not sufficient to create the actual particles.

It should be noted, that the effect of NP in indirect searches is expected to be tiny and has not been observed so far. However, there have been several 'anomalous' measurements:

- Asymmetry $A_{CP}(B^0 \to K^+\pi^-) \neq A_{CP}(B^+ \to K^+\pi^0)$ (5.6σ discrepancy)
- Unexpectedly large $D^0 - \bar{D}^0$ mixing (although SM has large uncertainties)
- Branching ratio $\mathcal{B}(B \to D^{(*)}\tau\nu)$(∼5$\sigma$ discrepancy)

It is clear, that many of these measurements would benefit greatly from increased statistics, to either reveal them as statistical fluctuations, or as genuine signs of NP.

This is where Belle II comes in. It will have 40× higher luminosity than Belle [4] (which is, to this date, the highest luminosity machine ever built). It's commissioning is planned for 2015 and first physics runs for 2016.

At the present time the Belle II collaboration has 560 members from 97 institutions spread across 23 countries. Among them are also 7 Czech members — 4 faculty and 3 students from the Charles University in Prague. They are working mostly on the pixel detector and tracking as well as on a few physics analyses using the Belle data sample.

References

[1] J. Hořejší, *Fundamentals Of Electroweak Theory* (Karolinum Press, 2003).

[2] M. Kobayashi, T. Maskawa, Progr. Theoret. Phys. **49**, 652 (1973).

[3] G. Costa, G. Fogli, *Symmetries and group theory in particle physics.* (Springer, 2012).

[4] T. Abe *et al.*, [arXiv:1011.0352] (2010).

Secondary pion beam for HADES experiment at GSI

Lukáš Chlad[1,2], Jerzy Pietraszko[3], and Wolfgang Koenig[3]

[1] *chlad@ujf.cas.cz, Faculty of Mathematics and Physics, Charles University in Prague, Ke Karlovu 3, 121 16 Praha 2, Czech Republic*
[2] *Nuclear Physics Institute of the ASCR, v.v.i., Řež 130, 250 68 Řež, Czech Republic*
[3] *GSI Helmholtzzentrum für Schwerionenforschung GmbH, Planckstrasse 1, 642 91 Darmstadt, Germany*

Abstract. During summer 2014, the HADES collaboration had the opportunity to measure pion collisions with different nuclei. These measurements were done with two objectives. The first being the investigations of hadrons with strange quarks and their behaviour at normal nuclear density. The analysis of this will concentrate specifically on ϕ meson and Λ baryon production. The focus on properties of baryonic resonances in the region of $N(1520)$ and $N(1535)$ formed the second objective. Special emphasis is put on beamline detectors which use different particle detection techniques. In particular, the scintillator based Hodoscope and diamond based Start detector will be discussed. Advantages and disadvantages of using diamond detectors will be mentioned as well as their usage in future FAIR projects.

1 HADES experiment

The **H**igh **A**cceptance **Di**-**E**lectron **S**pectrometer (HADES), installed at SIS18 at the GSI Helmholtzzentrum für Schwerionenforschung, aims to study changes of hadron properties in nuclear matter (both normal and high nuclear density) [1]. This can be done thanks to the electromagnetic decay of studied hadrons since the electrons created by this decay do not interact via strong interaction with nuclear matter and therefore, provide undisturbed information. The layout of the HADES spectrometer is shown in Figure 1.

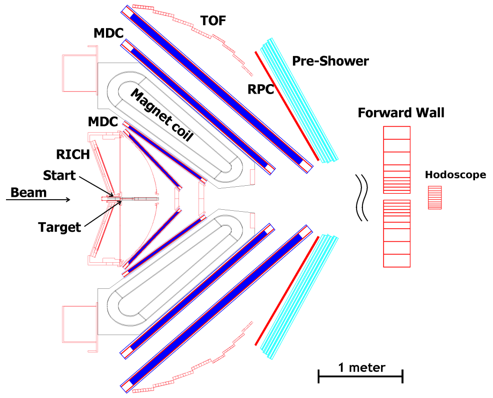

Figure 1. HADES experiment cross-section during π^- beamtime.

2 START detector

In order to achieve the goals of the HADES pion beam experiment [2], the Start detector must adhere to several requirements. First of all the detector must be thin in the sense of multiple scattering, i.e. keep the thickness of detector as low as possible and construct it using materials with low proton number Z. Secondly, it must have a time resolution better than 100 ps and in addition, the rate capability should be higher than 1 MHz. It should also provide position resolution around 2 mm and must be operational in a vacuum. All of these requirements are satisfied in the design of the scCVD diamond detector.

The final technical solution of the Start detector can be seen in Figure 2. The detector is made from 9 mono-crystalline diamonds of size $4.6 \times 4.6\,\mathrm{mm}^2$ and thickness $300\,\mu$m. With the aim of achieving desirable position resolution, each diamond is divided into 4 channels by segmented metallization. Each of these separate channels has its own readout electronic chain. The first stage of this chain consists of preamplifiers implemented directly on the PCB board (Printed Circuit Board) with diamond, as is seen in the schematic diagrams in Figure 2. The signal is then led outside of the vacuum chamber and into the booster and shaper. Lastly the signal passes through a NINO discriminator board, which is connected to a TRB3 board that provides time measurement (via TDC) and communication with the Data Acquisition system of the HADES [3].

3 Time resolution

To find the time resolution of START detector we made two independent analysis.

3.1 Non-interacting pions

The first of the two methods made use of pions that did not interact with the target and continued flying straight, uninfluenced by the magnetic field of the HADES magnet. The Hodoscope was placed at a distance of 5.5 m from the Start detector to detect non-interacting pions (the interaction probability is only 5%). The problem that must be addressed is that the DAQ trigger was defined by the overlap coincidence of the signal from the Start detector and that from TOF or RPC. This condition only separates events in which some pions from the beam interact with nuclei in the target. Fortunately, there is a $2\,\mu$s time window set around the trigger signal, when the signals from detectors are also stored in output data files.

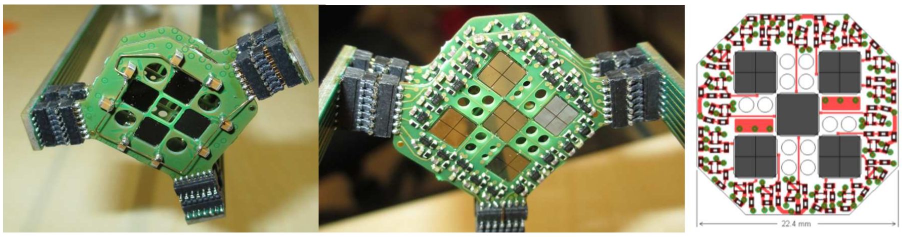

Figure 2. Scheme and photo of the Start detector.

By subtracting measured time t_0 at Start and time t_1 at the Hodoscope for each pion the distribution that is shown in Figure 3 is obtained. It is clear that from the σ of this gauss-like distribution, only the combined resolution of the detectors ($\sigma^2 = \sigma^2_{\mathrm{Start}} + \sigma^2_{\mathrm{Hodo}}$) can be deduced. Since neither σ_{Start} nor σ_{Hodo} is known separately, the assumption $\sigma_{\mathrm{Start}} = \sigma_{\mathrm{Hodo}} = \frac{\sigma}{\sqrt{2}}$. After the cut on the middle of the scintillator rods of hodoscope and so called time-walk correction for START detector we get a result $\sigma_{\mathrm{Start}} = 170\,\mathrm{ps}$.

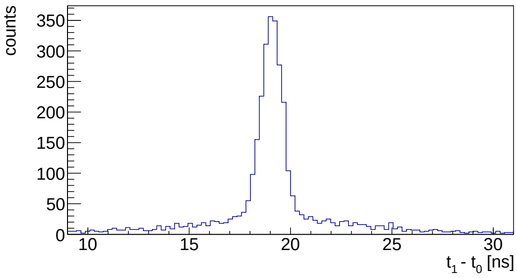

Figure 3. Distribution of time of flight for pions from the Start detector to the Hodoscope.

3.2 Produced dielectrons

This section will provide details of the second method that was implemented in order to obtain the pure Start time resolution. This method is based on the measurement of the time of flight of electron-positron pairs (t_{e^-} resp. t_{e^+}) by one of the TOF or RPC detectors and the Start detector (t_0 of the pion that interacted with the target). Identification of both leptons is done by the RICH detector. The goal lies in finding the total time resolution $\sigma_{\mathrm{Start+ToF}}$ from the distribution of $t_{\mathrm{e}^\pm}$ and also the time resolution of TOF/RPC detector[1] from the distribution of $t_{\mathrm{e}^+} - t_{\mathrm{e}^-}$. It should be noted that from this distribution $\sigma = \sqrt{2} \cdot \sigma_{\mathrm{ToF}}$ is obtained since two particles are detected. It is then simple to get the pure time resolution of the Start detector from $\sigma_{\mathrm{Start}} = \sqrt{\sigma^2_{\mathrm{Start+ToF}} - \sigma^2_{\mathrm{ToF}}}$. In all following pictures the symbol *blue cross* for TOF data and *red plus* for RPC data are used. The distribution of σ_{ToF} (time resolution) of the TOF/RPC detector depending on the Start channel number through which the pion that interacted with the target flew and (giving the electron/positron pair) is shown in Figure 4. As can be seen the distribution is independent of the Start channel number as can be expected. The final time resolution for each START channel one can see in Figure 5 where the time-walk correction was applied and ToF time resolution subtracted. From this picture one can also see that both methods are giving comparable results.

[1]Because $t_{\mathrm{e}^\pm} = t_\pm - t_0$ (where $t_\pm$ is the measured time by the TOF/RPC detector of the positron/electron), $t_{\mathrm{e}^+} - t_{\mathrm{e}^-} = t_+ - t_-$ and it can be seen that this difference is not influenced by the measurement of the Start detector.

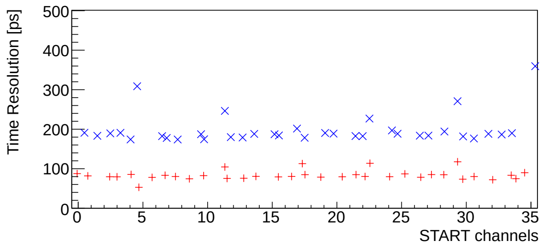

Figure 4. Time resolution of the TOF/RPC detector.

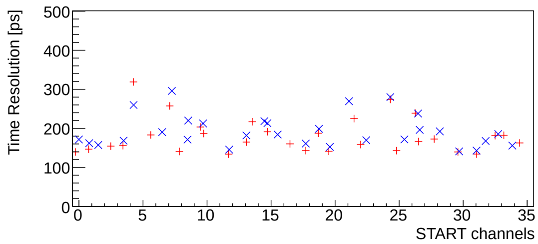

Figure 5. Time resolution of the Start detector.

References

[1] P. Salabura for HADES collaboration, Eur. Phys. J. A **41**, 243-277 (2009)

[2] The HADES collaboration, *TDR - A secondary pion beam for HADES experiment* (Internal HADES document,2013)

[3] J. Michel *et al.*, IEEE Transactions on Nuclear Science **58** 4, 1745 - 1750 (2011)

Reentrance in an exactly soluble mixed-spin Ising model on TIT lattices

Jana Čisárová[1] and Jozef Strečka[1]

[1]jana.cisarova@upjs.sk, Institute of Physics, Faculty of Science, P. J. Šafárik University, Park Angelinum 9, 040 01 Košice

Abstract. The mixed spin-(1/2, 1) Ising model on two geometrically frustrated lattices with "triangles-in-triangles" (TIT) structure is exactly solved using the generalized star-triangle transformation, which establishes a rigorous mapping correspondence with the equivalent spin-1/2 Ising model on a triangular lattice. Finite-temperature phase diagrams reflect critical behaviour including reentrant phase transitions with either two or three successive critical points for both TIT lattices.

1 Introduction

Frustrated spin systems have received much attention since they may exhibit a variety of interesting phenomena such as unusual ground states with a non-zero residual entropy, enhanced magneto-caloric effect, order-from-disorder effect or reentrant phase transitions [1]. The first exactly solved model displaying reentrant phase transitions was a two-dimensional Ising model on a centered square lattice with nearest- and next-nearest-neighbour interactions [2]. In the present paper, we will rigorously study a mixed spin-$\frac{1}{2}$ and spin-1 Ising model on two topologically different but geometrically related TIT lattices with a uniaxial single-ion anisotropy, which also shows a reentrant phenomenon.

2 Model and method

Let us introduce a mixed spin-$\frac{1}{2}$ and spin-1 Ising model on two geometrically related TIT lattices, which are schematically depicted in Figure 1. As one can see from this figure, both considered TIT lattices can be derived from a simple triangular lattice by placing an additional triangle of decorating sites either into each up-pointing triangle (TIT1 lattice displayed in the upper part of Figure1) or into each triangle (TIT2 lattice shown in the lower part of Figure1) of the underlying triangular lattice. Suppose furthermore that the nodal sites of the original lattice are occupied by the Ising spins $\sigma = \pm 1/2$, while the decorating lattice sites are occupied by the Ising spins $S = \pm 1, 0$. The total Hamiltonian of this mixed spin-($\frac{1}{2}$, 1) Ising model defined on both TIT lattices can then be written as a sum over the Hamiltonians of the six-spin clusters $\mathcal{H} = \sum_{k=1}^{\gamma N} \mathcal{H}_k$, one of which is schematically illustrated in the central part of Figure 1 (N denotes the total number of the nodal lattice sites and γN labels the total number of the decorating triangles, i.e. $\gamma = 1$ for the TIT1 lattice and $\gamma = 2$ for the TIT2 lattice). The cluster Hamiltonian $\mathcal{H}_k$ is given as follows

$$\mathcal{H}_k = -J \sum_{i=1}^{3} S_{k,i} S_{k,i+1} - J_1 \sum_{i=1}^{3} S_{k,i}(\sigma_{k,i} + \sigma_{k,i+1}) - D \sum_{i=1}^{3} S_{k,i}^2, \quad (1)$$

with the convention $\sigma_{k,4} \equiv \sigma_{k,1}$ and $S_{k,4} \equiv S_{k,1}$ for the Ising spin variables $\sigma_l = \pm\frac{1}{2}$ and $S_i = \pm 1, 0$ placed at the nodal and decorating lattice sites, respectively. The parameter J describes the pair interaction between the nearest-neighbour decorating spins, the parameter J_1 stands for the pair interaction between the nearest-neighbour nodal and decorating spins, respectively, and the parameter D marks the single-ion anisotropy acting on the decorating spins only.

A crucial step in finding the exact solution for the mixed-spin (1/2,1) Ising model on both investigated TIT lattices lies in the calculation of its partition function, which can be found with the help of the generalized star-triangle transformation [3] that is schematically illustrated in the central part of Figure 1 (for more details on the calculation procedure see Ref. [4]). With the use of this method one can obtain an exact mapping relationship between the partition function $\mathcal{Z}$ of the mixed spin-($\frac{1}{2}$, 1) Ising model on the TIT lattice and the partition function $\mathcal{Z}_{\rm IM}$ of the corresponding spin-$\frac{1}{2}$ Ising model on a simple triangular lattice with effective nearest-neighbour interaction

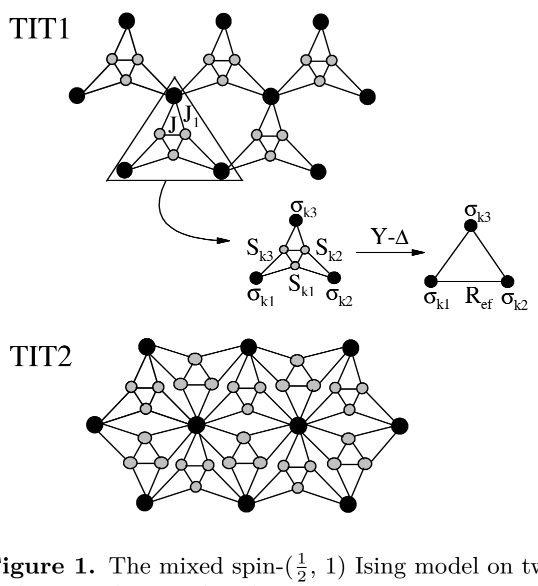

Figure 1. The mixed spin-($\frac{1}{2}$, 1) Ising model on two TIT lattices along with a diagrammatic representation of the star-triangle transformation used for an elementary six-spin star cluster. Large black circles denote lattice positions of the nodal Ising spins $\sigma = \frac{1}{2}$ and small grey ones lattice positions of the decorating Ising spins $S = 1$.

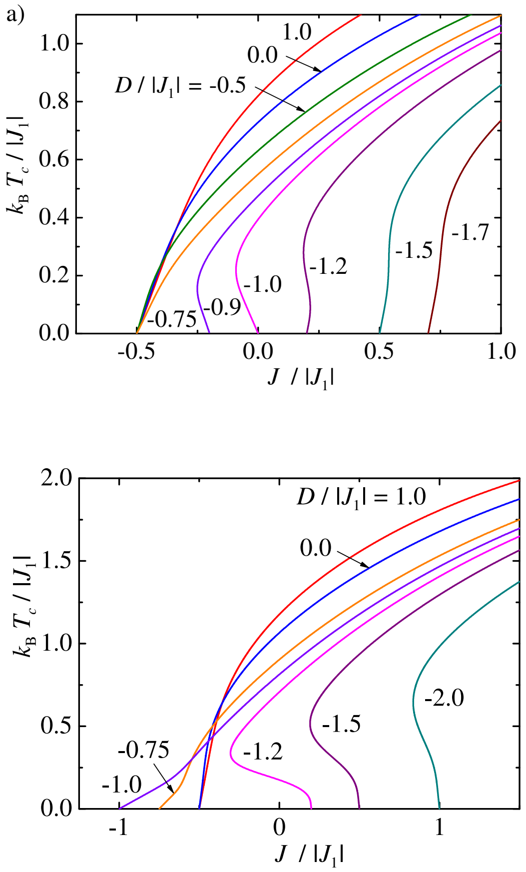

Figure 2. Critical temperature of the mixed spin-($\frac{1}{2}$, 1) Ising model as a function of the interaction ratio $\frac{J}{J_1}$ for several values of the single-ion anisotropy $\frac{D}{J_1}$ on: (a) TIT1 lattice; (b) TIT2 lattice.

$\gamma J_{\rm eff}$

$$\mathcal{Z}(\beta, J, J_1, D) = A^{\gamma N} \mathcal{Z}_{\rm IM}(\beta, \gamma J_{\rm eff}) \tag{2}$$

involving the standard notation for the inverse temperature $\beta = 1/(k_{\rm B}T)$. Note that the effective interaction is twice as large for the TIT2 lattice than for the TIT1 lattice. Using the established mapping equivalence (2) between the partition functions, the critical points of the mixed-spin Ising model on the TIT lattices can be simply located by equating the effective nearest-neighbour coupling $\beta\gamma J_{\rm eff}$ with its critical value $\ln 3$ (for more details see Ref. [4]).

3 Results

Now, let us proceed to a discussion of the most interesting results obtained for the critical behaviour of the mixed spin-($\frac{1}{2}$, 1) Ising model on the two considered TIT lattices. The critical temperature does not depend on a sign of the interaction constant J_1 and hence, the strength of this interaction $|J_1|$ will henceforth serve as the energy unit. First, let us mention that the ground state of both investigated TIT lattices constitute two spontaneously long-range ordered phases OP1 and OP2, three disordered phases DP1, DP2 and DP3 and one unusual phase ODP, which is critical for the lattice TIT1 but is partially ordered and partially disordered for the TIT2 lattice (the detailed ground-state analysis and description of individual ground states is presented in Ref. [4]). Figure 2 displays the critical temperature of the mixed spin-($\frac{1}{2}$, 1) Ising model on both TIT lattices as a function of the interaction ratio $\frac{J}{|J_1|}$ for several values of the relative strength of the single-ion anisotropy $\frac{D}{|J_1|}$. As one can see, the most crucial difference in the critical behaviour of two considered TIT lattices can be viewed in a greater resistance of the TIT2 lattice with respect to the spin frustration. As a matter of fact, the mixed spin-($\frac{1}{2}$, 1) Ising model on the TIT2 lattice becomes firmly disordered merely for the stronger antiferromagnetic interaction between the decorating spins $\frac{J}{J_1} < -1$ than the analogous model on the TIT1 lattice being disordered for any $\frac{J}{J_1} < -\frac{1}{2}$. Apart from this difference, the critical lines of the mixed spin-($\frac{1}{2}$, 1) Ising model on the TIT2 lattice exhibit more pronounced reentrant phase transitions with two consecutive critical points (compare for instance both dependences for $\frac{D}{J_1} = -1.2$), whereas the same model on the TIT1 lattice exhibits less pronounced reentrant phase transitions that might have however up to three successive critical points (see the dependence for $\frac{D}{J_1} = -1.2$).

4 Conclusion

The present article deals with the mixed spin-($\frac{1}{2}$, 1) Ising model on two geometrically frustrated TIT lattices, which has been exactly solved with the use of generalized star-triangle transformation establishing a rigorous mapping equivalence with the corresponding spin-$\frac{1}{2}$ Ising model on a simple triangular lattice. It has been shown that a mutual interplay between the spin frustration and single-ion anisotropy is responsible for an emergence of reentrant phase transitions with either two or three successive critical points, which are more pronounced for the mixed-spin Ising model on the TIT2 lattice than for the analogous model on the TIT1 lattice.

Acknowledgement

This work was financially supported by the grant VVGS-PF-2014-434 and the ERDFEU (European Union European regional development fund) grant No. ITMS26220120005 (activity 3.2.).

References

[1] H. T. Diep, *Frustrated Spin Systems (World Scientific*, Singapore, 2004).

[2] V. G. Vaks, A. I. Larkin and N. Ovchinnikov, Sov. Phys.-JETP **22**, 820 (1966).

[3] J. Strečka, On the Theory of Generalized Algebraic Transformations, (LAP LAMBERT Academic Publishing, Saarbrucken, 2010).

[4] J. Strečka, J. Čisárová, Physica A **392**, 5633 (2013) 5633.

Influence of resonance decays on triangular flow in heavy-ion collisions

Jana Crkovská[1], Larissa Bravina[2], and Evgeny Zabrodin[2,3]

[1]Faculty of Nuclear Sciences and Physical Engineering, Czech Technical University in Prague, Břehová 7, Prague 110 00, Czech Republic, crkovjan@fjfi.cvut.cz
[2]Department of Physics, University of Oslo, P. O. Box 1048 Blindern, N-0316, Oslo, Norway
[3]Skobeltsyn Institute of Nuclear Physics, Lomonosov Moscow State University, Leninskie Gory, GSP-1, Moscow 119991, Russian Federation

Abstract. Anisotropic flow in relativistic collisions of heavy-ions yields important information about the state of the hot and dense matter created in the reactions. Study of triangular flow in Pb+Pb interactions at LHC was performed within Monte Carlo HYDJET++ model. HYDJET++ combines both parametrized hydrodynamics for soft p_T particle spectra and microscopic jet quenching generator for hard p_T spectra, giving a realistic prediction for vast number of hadron species. The model also enables study of influence of final-state interactions on flow of created hadrons. Triangular flow patterns of pions, kaons and protons were studied at different centralities. Scaling of triangular flow with number of constituent quarks is discussed.

1 Introduction

Collective flow of particles can yield valuable information about the hot and dense medium created in relativistic nucleus-nucleus collisions, known as quark-gluon plasma (QGP). The initial anisotropy of the overlap region and the subsequent expansion of the fireball after the collision due to the pressure gradients inside give rise to momentum anisotropy of outcoming particles. The azimuthal distribution of detected particles with respect to reaction plane Ψ_R can be expanded into a Fourier series

$$\frac{\mathrm{d}N}{\mathrm{d}\varphi} = \frac{N}{2\pi}\left[1 + 2\sum v_n \cos\left(n(\varphi - \Psi_R)\right)\right], \quad (1)$$

with the Fourier coefficients describing high flow harmonics

$$v_n = \langle \cos\left(n(\varphi - \Psi_R)\right)\rangle \quad (2)$$

and bear the name of directed, elliptic and triangular flow for v_1, v_2 and v_3 respectively. Measuring the magnitude of the flow coefficients can yield information about the state of the medium produced immediately after the initial scattering. Elliptic flow presented the dominant contribution to anisotropic flow in semi-peripheral and peripheral interactions. However with energies such as at LHC, the higher coefficients grow significantly and become dominant at small impact parameters. Results from LHC suggest that in central collisions the main part of the anisotropic flow originates from the triangular flow [1].

A prominent feature of elliptic flow is the number-of-constituent-quarks scaling (NCQ), first observed at RHIC [2]. The elliptic flow for identified particles scales as $v_2/n_q(kE_T/n_q)$. Such behaviour implies formation of flow on partonic level, when the QGP is still present, and favours coalescence formation scenario. Preliminary results from STAR experiment suggest that v_3 scales as $v_3/n_q^{3/2}(kE_T/n_q)$ [3].

2 HYDJET++

HYDJET++ [4] stands for HYDrodynamics with JETs and is a Monte Carlo heavy-ion event generator. It is a superposition of hydrodynamical part and jet part. These are treated independently. Among the advantages of this model is the possibility to study separately hydrodynamical behaviour and influence of jet quenching, its efficiency, its ability to reproduce realistic shapes of distributions and that it includes a vast table of resonances.

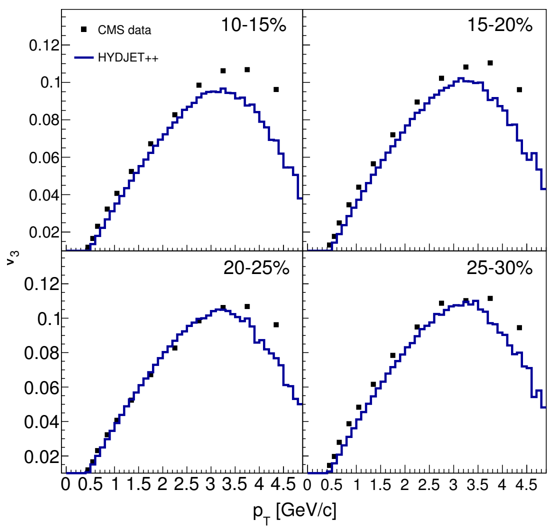

Figure 1. Triangular flow of charged particles in Pb+Pb at $\sqrt{s_{NN}} = 2.76$ TeV. Histograms are HYDJET++ calculations, squares are CMS data [6].

3 Triangular flow at LHC

Hereby we studied the influence of decays of the resonances on triangular flow at LHC energies. HYDJET++ was tuned to give realistic shapes of v_2 and v_3 distributions [5]. In Figure 1 the v_3-distributions over transverse momentum p_T for charged particles (protons, pions and kaons) in Pb+Pb collisions at $\sqrt{s_{NN}} = 2.76$ TeV obtained with HYDJET++ (histogram) are compared with CMS data [6]. The model provides a particulary good description of data in soft p_T region. The overall shape of the distribution corresponds to the trend observed in experiment as advertised.

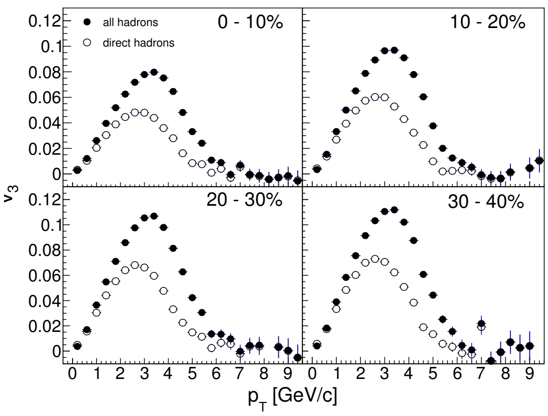

Figure 2. Triangular flow distribution $v_3(p_T)$ for all charged particles (full circles) and direct charged particles (open circles) in Pb+Pb at $\sqrt{s_{NN}} = 2.76$ TeV.

Figure 2 shows the triangular flow $v_3(p_T)$ of all charged particles (full circles) and of only directly produced particles (open circles) in Pb+Pb at $\sqrt{s_{NN}} = 2.76$ TeV in four centrality bins. The effect of resonance decays is significant both in magnitude and in position of the maximum of distributions. The maximum of the distribution is shifted to higher p_T of about 10% while the amplitude difference is about 40% in all centrality bins.

NCQ scaling of triangular flow at LHC was also studied. We considered the v_3 to scale as $v_3/n_q^{3/2}$. Results for protons, kaons and pions are shown in Figure 3 (a, b) for all hadrons and directly produced hadrons respectively. Plots (c, d) show the distributions (a, b) respectively divided by the corresponding distribution for proton. Proton and pion distributions seem to follow the scaling for low p_T, however the kaon distribution deviates by more than 50%. For directly produced kaons the deviation from scaling is more significant, while protons and pions are still well scaled. The conclusion remains the same as for elliptic flow[7]: NCQ scaling is violated at LHC, but resonance decays drive the corresponding ratios v_2/n_q and $v_3/n_q^{2/3}$ towards the scaling fulfilment. The role of jet quenching in the violation of the NCQ scaling still needs to be clarified.

4 Conclusion

We performed a study of the effect of resonance decays on the triangular flow in Pb+Pb collisions within the HYDJET++ framework. The model provides a fair description of v_3 with centrality. It was found that resonances influence significantly the shape of flow distributions: for v_3 we observed in maximum a shift of about 10% to higher p_T and growth of about 40% in amplitude. It is vital to further study the flow of mother and daughter particles as well as influence of jets to better understand the dynamics of the system.

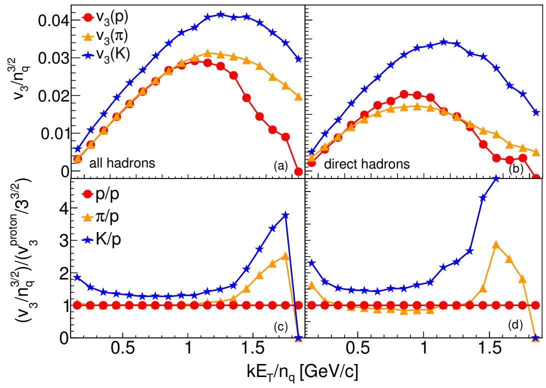

Figure 3. Number-of-constituent-quarks scaling for triangular flow in Pb+Pb at $\sqrt{s_{NN}} = 2.76$ TeV. Distributions for all protons (circles), pions (triangles) and kaons (stars) are shown in (a), for direct particles in (b). The distributions of all particles divided by the proton distribution are depicted in (c), (d) shows the same for direct particles.

Acknowledgement

This work was supported by the grant of the Grant Agency of Czech Republic n.13-20841S and by the Grant Agency of the Czech Technical University in Prague, grant No. SGS13/215/OHK4/3T/14.

References

[1] K. Aamodt *et al.* (ALICE Collaboration), Phys. Rev. Lett. **107**, 032301 (2011).
[2] A. Adare *et al.* (PHENIX Collaboration), Phys. Rev. Lett. **98**, 162301 (2007).
[3] X. Sun (for STAR Collaboration), J. Phys.: Conf. Ser. **535**, 012005 (2014).
[4] I. P. Lokhtin *et al.*, Comp. Phys. Comm. **180**, 779–799 (2009).
[5] L. V. Bravina *et al.*, Eur. Phys. J. C **74**, 2807 (2014).
[6] S. Chatrchyan *et al.* (CMS Collaboration), Phys. Rev. C **87**, 014902 (2013).
[7] G. Eyyubova *et al.* Phys. Rev. C **80**, 064907 (2009).

Higher flow harmonics and ridge effect in PbPb collisions in HYDJET++ model

G. Eyyubova[1], V. L. Korotkikh[2], I. P. Lokhtin[2], S. V. Petrushanko[2], A. M. Snigirev[2], L. V. Bravina[3], and E. E. Zabrodin[3]

[1]eyyubgyu@fjfi.cvut.cz, Czech Technical University in Prague, Faculty of Nuclear Sciences and Physical Engineering
[2]Skobeltsyn Institute of Nuclear Physics, Lomonosov Moscow State University, Moscow, Russia
[3]University of Oslo, Department of Physics, Norway

Abstract. The hybrid model HYDJET++, which includes soft and hard physics, is employed for the analysis of dihadron angular correlations measured in PbPb collisions at $\sqrt{s_{NN}} = 2.76$ TeV. The possible triangular shape fluctuation of the initial overlap density of the colliding nuclei was implemented in HYDJET++ by the modulation of the final freeze-out hypersurface with the appropriate triangular coefficient, which results in triangular flow v_3. Along with elliptic flow v_2, it generates a specific structure of dihadron angular correlations on relative azimuthal angle in a broad range of relative pseudoraidities ($\Delta\eta\Delta\varphi$). The comparison of model results with the LHC data on long-range angular correlations is presented for different collisions centralities.

1 Introduction

The measurement of azimuthal anisotropy and angular correlations of particle is an important tool for exploring properties of matter produced in nuclear-nucleus collisions. The two-particle angular correlation function, $C(\Delta\eta, \Delta\varphi)$, in relative pseudorapidity $\Delta\eta = \eta^{\rm tr} - \eta^{\rm a}$ and azimuth $\Delta\varphi = \varphi^{\rm tr} - \varphi^{\rm a}$ is sensitive to collective flow of particles as well as to any other particle correlations in azimuthal angle and pseudorapidity. In the collective flow dominated regime the pair distribution can be presented as a Fourier decomposition:

$$\frac{dN^{pairs}}{d\Delta\varphi} \propto 1 + 2\sum_{n=1}^{\infty} V_n(p_T^{\rm tr}, p_T^{\rm a}) \cos n(\Delta\varphi), \qquad (1)$$

where indexes refer to two particles in a pair, usually called "trigger" and "associated" ones. The study of dihadron angular correlations in heavy ion collisions has revealed the new phenomena in collision dynamics, the so called ridge and double-hump structure [1–3], which are currently associated with the existence of triangular collective flow, v_3 [4]. Triangular flow, as well as higher flow harmonics, may arise due to initial state fluctuations in a collision geometry. In heavy ion collisions the long range (at large $|\Delta\eta| > 2$) features of the angular dihadron correlations at low and intermediate momenta $p_{\rm T}$ in central and mid-central collisions were shown to be described with the sum of the Fourier harmonics $v_2 - v_6$, found from independent flow analysis methods [3].

In this work we present the description of dihadron correlation function $C(\Delta\eta, \Delta\varphi)$ in PbPb at $\sqrt{s_{\rm NN}} = 2.76$ TeV with HYDJET++ model, which includes only two independent collective flow harmonics, v_2 and v_3. We study the appearance of higher order harmonics V_n, $n > 3$, in correlation function and compare it with the experimental data.

2 HYDJET++ model

The basic principals of HYDJET++ model are described in a manual [5]. The model combines two components which correspond to soft and hard physics. The hard part of the model is based on PYTHIA [6] and PYQUEN [7] generators, which simulate parton-parton collisions, parton energy loss and hadronisation. The soft part of the model do not have hadronisation and evolution from initial state, but represents a thermal hadron production already at the freeze-out hypersurface in accordance with hydrodynamical calculations (adapted from FAST MC generator [8]).

The elliptic modulation of the final freeze-out hypersurface at each impact parameter b and a modulation of flow velocity profile are implemented in HYDJET++, which result in elliptic flow v_2. Additional triangular modulation of freeze-out hypersurface:

$$R(\varphi, b) \propto \frac{\sqrt{1-\epsilon(b)}}{\sqrt{1+\epsilon(b)\cos 2(\varphi - \Psi_2)}}[1+\epsilon_3(b)\cos 3(\varphi+\Psi_3)], \qquad (2)$$

produces triangular flow v_3. The reaction planes Ψ_2 and Ψ_3 are uncorrelated, $\epsilon(b)$, ϵ_3 and $\delta(b)$ are the parameters. v_2 and v_3 anisotropies are tuned to reasonably describe data at low p_T. The interference between v_2 and v_3 in the final state leads to appearance of higher order flow harmonics [9].

2.1 Results

The two-particle correlation function is defined as the ratio of pair distribution in the same event to the combinatorial pair distribution, where pairs are not correlated:

$$C(\Delta\eta, \Delta\varphi) \equiv \frac{d^2N^{\rm pair}}{d\Delta\eta d\Delta\varphi} = \frac{N^{\rm mixed}}{N^{\rm same}} \times \frac{d^2N^{\rm same}/d\Delta\eta d\Delta\varphi}{d^2N^{\rm mixed}/d\Delta\eta d\Delta\varphi}, \qquad (3)$$

where $N^{\rm mixed}$, $N^{\rm same}$ are the number of pairs in the same and mixed events. Here we construct the back-

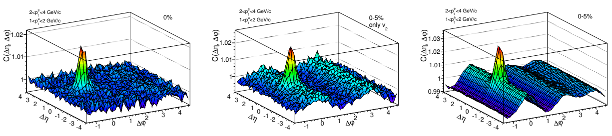

(a) (b) (c)

Figure 1. 2D correlation function in HYDJET++ for $2 < p_{\mathrm{T}}^{\mathrm{tr}} < 4$ GeV/c and $1 < p_{\mathrm{T}}^{\mathrm{a}} < 2$ for (a) central collisions with impact parameter $b = 0$, (b) centrality 0-5% with only v_2, and (c) centrality 0-5% with both v_2 and v_3 present.

ground from two single particle spectra:

$$\frac{d^2N^{\mathrm{mixed}}}{d\Delta\eta d\Delta\varphi} = \int \frac{d^2N^{\mathrm{tr}}}{d\eta^{\mathrm{tr}}d\varphi^{\mathrm{tr}}}\frac{d^2N^{\mathrm{a}}}{d\eta^{\mathrm{a}}d\varphi^{\mathrm{a}}}\delta_{\mathrm{a}}^{\mathrm{tr}}d\eta^{\mathrm{a}}d\eta^{\mathrm{tr}}d\varphi^{\mathrm{a}}d\varphi^{\mathrm{tr}}, \tag{4}$$

where $\delta_{\mathrm{a}}^{\mathrm{tr}} = \delta(\eta^{\mathrm{tr}} - \eta^{\mathrm{a}})\delta(\varphi^{\mathrm{tr}} - \varphi^{\mathrm{a}})$. Fourier harmonics V_n from Eq. (1) are defined directly from $C(\Delta\varphi)$:

$$V_n = \langle cos(\Delta\varphi)\rangle = \frac{\sum_i C_i(\Delta\varphi_i)\cdot\cos(n\Delta\varphi_i)}{\sum_i C_i(\Delta\varphi_i)}. \tag{5}$$

Angular dihadron correlations contains all possible types of two particle correlations. The most of sources for two- or many-particle correlations is presented in the model, i.e femtoscopic correlations, resonance decays, jets, collective flow. The long range correlations over η appear in the model only due to collective flow. The correlation function $C(\Delta\eta, \Delta\varphi)$ calculated in HYDJET++ in PbPb collision at $\sqrt{s_{\mathrm{NN}}} = 2.76$ TeV for $2 < p_{\mathrm{T}}^{\mathrm{tr}} < 4$ GeV/c and $1 < p_{\mathrm{T}}^{\mathrm{a}} < 2$ is presented in Figure 1 for the cases of (a) no collective flow (zero impact parameter), (b) only elliptic flow v_2 is turned on and (c) both elliptic and triangular flow are present. The jet peak is highly suppressed at away-side ($\Delta\varphi \approx \pi$) due to jet quenching, though remnants of it can be seen over broad $\Delta\eta$ range at away-side. Figure 1 (a) shows that no long-range azimuthal correlations are present at the near-side and they appear in presence of elliptic flow with the characteristic $\cos(2\Delta\varphi)$ pattern, Figure 1 (b). They are flat in relative pseudorapidity up to $\Delta\eta \approx 4$, which corresponds to flat pseudorapidity shape of collective flow in the model. The triangular flow enhances these near-side correlations, often referred as ridge, and also modifies away-side structure, producing double-hump (see Figure 1 (c)). The 1D correlation function $C(\Delta\varphi)$ was calculated for long-range azimuthal correlations for $1 < p_{\mathrm{T}}^{\mathrm{a}} < 1.5$ GeV/c, $3 < p_{\mathrm{T}}^{\mathrm{tr}} < 3.5$ GeV/c for different centralities. Figure 2 shows the Fourier coefficients V_n, calculated from $C(\Delta\varphi)$ in comparison with CMS data [10]. At central collisions all the coefficients V_n are lower than in data. At mid-central collision V_n describe data rather well. At peripheral collisions V_2 in the model is much higher than in data, which corresponds to the fact that the model does not describe data well on single-particle v_2 in the region $3 < p_T < 3.5$ GeV/c [9]. We note, that there is no v_1 in the model. Nevertheless, the V_1 component appears due to momentum conservation violation. As can be seen from Figure 2, higher order coefficients V_n, $n > 3$ appear in the model in $C(\Delta\varphi)$ decomposition, though they decrease rapidly with n. These coefficients at low p_T can only originate from collective flow v_2 and v_3.

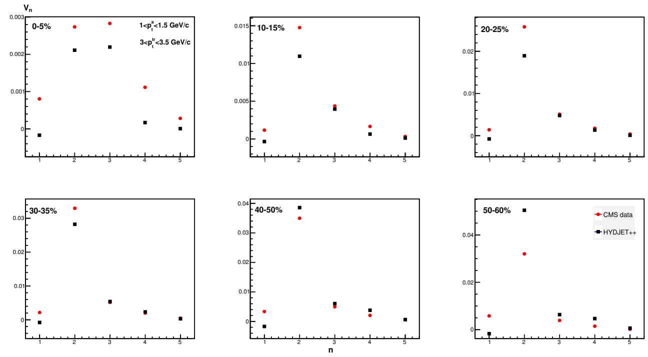

Figure 2. Fourier coefficients V_n for $3 < p_{\mathrm{T}}^{\mathrm{tr}} < 3.5$ GeV/c and $1 < p_{\mathrm{T}}^{\mathrm{a}} < 1.5$ for different centralities in HYDJET++ and in data [10].

3 Conclusions

In HYDJET++ model the collective flow for non-central collisions is introduced via elliptic and triangular modulation of the freeze-out volume and rotation of velocities of emitted particles. Such a simple mechanism allows us to describe dihadron correlations at mid-central collisions, where collective flow dominates over fluctuations.

This publication was supported by the European social fund within the framework of realizing the project „Support of inter-sectoral mobility and quality enhancement of research teams at Czech Technical University in Prague“, CZ.1.07/2.3.00/30.0034.

References

[1] A. Adare *et al.* [PHENIX Collaboration], Phys. Rev. **C 78**, 014901 (2008).

[2] M. M. Aggarwal *et al.* [STAR Collaboration], Phys. Rev. **C 82**, 024912 (2010).

[3] K. Aamodt *et al.* [ALICE Collaboration], Phys. Rev. Lett. **107**, 032301 (2011).

[4] B. Alver and G. Roland, Phys. Rev. **C 81**, 054905 (2010) [Erratum-ibid. **C 82**, 039903 (2010)].

[5] I. P. Lokhtin, L. V Malinina, S. V. Petrushanko, A. M. Snigirev, I. Arsene, K. Tywoniuk, Comput. Phys. Commun. **180**, 779 (2009).

[6] T. Sjostrand, S. Mrenna, P. Skands, JHEP **0605**, 026 (2006).

[7] I. P. Lokhtin, A.M. Snigirev, Eur. Phys. J. C **45**, 211 (2006).

[8] N.S. Amelin *et al.*, Phys. Rev. **C 77**, 014903 (2008).

[9] L. V. Bravina, B. H. Brusheim Johansson, G. K. Eyyubova, V. L. Korotkikh, I. P. Lokhtin, L. V. Malinina, S. V. Petrushanko and A. M. Snigirev *et al.*, Eur. Phys. J. C **74**, 2807 (2014).

[10] S. Chatrchyan *et al.* [CMS Collaboration], Eur. Phys. J. C **72**, 2012 (2012).

Ideal hydrodynamic modeling of quark-gluon plasma

Zuzana Fecková[1,2] and Boris Tomášik[2,3]

[1] zuzana.feckova1@student.upjs.sk, University of Pavol Jozef Šafárik, Šrobárova 2, 04001 Košice, Slovakia
[2] Matej Bel University, Tajovského 40, 97401 Banská Bystrica, Slovakia
[3] FNSPE, Czech Technical University in Prague, Břehová 7, 11519 Prague 1, Czech Republic

Abstract. We present a new algorithm for solving ideal relativistic hydrodynamics based on Godunov method with exact solution of Riemann problem with an arbitrary equation of state. Standard numerical tests are executed, such as sound wave propagation and shock tube problem. Low numerical viscosity and high precision are attained with proper discretization.

1 Introduction

Quark gluon plasma is nowadays experimentally studied in ultrarelativistic heavy ion collisions. After the nuclei collide the dense and hot matter soon thermalizes and expands. This expansion has been successfully described by relativistic hydrodynamics. Its hydrodynamic modeling requires sophisticated numerical methods, which can cope with complicated initial conditions, possibly leading to shock waves. A class of high-resolution shock-capturing methods particularly suited to solve this problem are Godunov methods. We present a new numerical scheme for ideal relativistic hydrodynamics using the exact solution of Riemann problem for an arbitrary equation of state (EoS).

2 Hydrodynamical modeling

Relativistic hydrodynamic equations have the following form:

$$\begin{aligned} \partial_\mu n^\mu &= 0, \\ \partial_\mu T^{\mu\nu}_{(0)} &= 0, \end{aligned} \tag{1}$$

where n^μ is the flow of a conserved charge. In nuclear collision the relevant charge is baryon number, thus $n^\mu = n_B u^\mu$, where $u^\mu = \gamma(1, \vec{v})$ is the flow velocity, γ being the Lorentz factor. Our model covers the nuclear collisions at highest energies, where the net baryon density is practically zero. Therefore the first equation loses its meaning and we are left with only the second equation that expresses the conservation of energy and momentum. The energy and momentum tensor in ideal case, which we are considering, is:

$$T^{\mu\nu}_{(0)} = (\epsilon + p)u^\mu u^\nu - p g^{\mu\nu}, \tag{2}$$

where ϵ is energy density, p is pressure and $g^{\mu\nu} = \mathrm{diag}(1, -1, -1, -1)$ is the Minkowski metric. The second equation can be rewritten in a different form, useful for numerical implementation:

$$\partial_t U + \partial_x F(U) = 0. \tag{3}$$

where

$$\begin{aligned} U = \big((\epsilon + p)\gamma^2 - p, (\epsilon + p)\gamma^2 v^1, \\ (\epsilon + p)\gamma^2 v^2, (\epsilon + p)\gamma^2 v^3\big)^T, \end{aligned} \tag{4}$$

$$\begin{aligned} F^i = \big((\epsilon + p)\gamma^2 v^i, (\epsilon + p)\gamma^2 v^i v^1 + \delta^{i1} p, \\ (\epsilon + p)\gamma^2 v^i v^2 + \delta^{i2} p, (\epsilon + p)\gamma^2 v^i v^3 + \delta^{i3} p\big)^T. \end{aligned} \tag{5}$$

The presented equations are solved numerically in the latter form using Godunov method. In this method we consider a piecewise constant distribution of variables inside the cells of a numerical grid. The interface of two neighbouring cells presents a discontinuity, where the Riemann problem is solved. Its solution allows us to compute fluxes of conserved variables U at the interface [1, 2]. Computing the fluxes on the left and right boundary of the cell, we obtain the values of variables U at the next time-step:

$$U_i^{t+\Delta t} = U_i^t + \frac{\Delta x}{\Delta t}(F_{i+1/2} - F_{i-1/2}), \tag{6}$$

where U_i^t is the value of a variable in the i^{th} cell at time t and $F_{i-1/2}(F_{i+1/2})$ is the flux at its left (right) boundary.

3 Numerical tests

The sound wave propagation test consists of simulating a sound wave in the numerical grid. We impose the following initial conditions:

$$\begin{aligned} p_{\mathrm{init}}(x) &= p_0 + \delta p \sin\frac{2\pi x}{\lambda}, \\ v_{\mathrm{init}}(x) &= \frac{\delta p}{c_s(\epsilon_0 + p_0)} \sin\frac{2\pi x}{\lambda}, \end{aligned} \tag{7}$$

with parameters $p_0 = 10^3$ fm^{-4}, $\delta p = 10^{-1}$ fm^{-4}. Since the variation of pressure is sufficiently small $\delta p \ll p_0$, we can consider the linearized analytic solution and compare this solution to the values obtained by numerical computation to evaluate the precision of our numerical scheme. The precision and its dependance on the number of cells in the numerical grid is studied with $L1$ norm evaluated after one time-step over one wavelength [3]:

$$L(p(N_{\mathrm{cell}}), p_s) = \sum_{i=1}^{N_{\mathrm{cell}}} |p(x_i; N_{\mathrm{cell}}) - p_s(x_i)| \frac{\lambda}{N_{\mathrm{cell}}}, \tag{8}$$

The dependance of $L1$ norm on the number of cells is shown in Figure 1. The precision improves with finer discretization, as expected, and is very good for grids larger than $N_{\mathrm{cell}} \gtrsim 500$. We have also evaluated

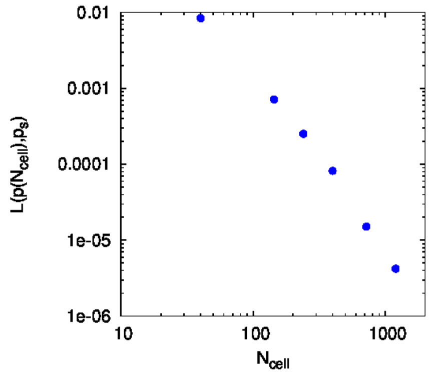

Figure 1. Dependance of $L1$ norm on number of cells in the numerical grid.

the numerical viscosity of the scheme η_{num}, using $L1$ norm:

$$\eta_{\mathrm{num}} = -\frac{3\lambda}{8\pi^2} c_s(\epsilon_0 + p_0) \ln \left[1 - \frac{\pi}{2\lambda\delta p} L(p(N_{\mathrm{cell}}), p_s) \right]. \tag{9}$$

Since quark gluon plasma is expected to have very low viscosity, the artificial dissipation of the numerical scheme must be kept very low too. In Figure 2 we present the dependance of numerical viscosity η_{num} on the number of cells in the grid. It decreases with number of cells and its values are adequately small.

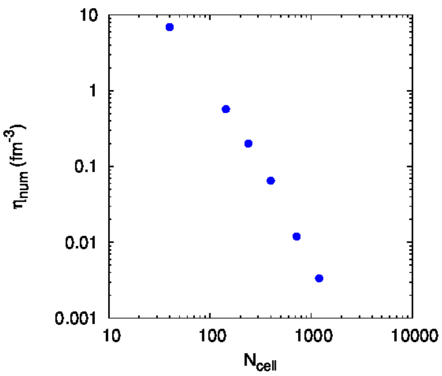

Figure 2. Dependance of numerical viscosity η_{num} on number of cells in the numerical grid.

We continue with the shock tube problem. It consists of imposing special initial conditions with a discontinuity in energy density between two constant states. With ideal gas EoS, the energy density corresponds to temperature in the left(right) half: $T_L = 400$ MeV ($T_R = 200$ MeV). The initial velocity is zero over the whole grid. With time, the discontinuity will disolve with a rarefaction wave propagating to the left, to the region of higher energy density, and a shock wave propagating to the right, where energy density is lower. In Figure 3 we show the profile of energy density in the grid after 100 time-steps. We see that

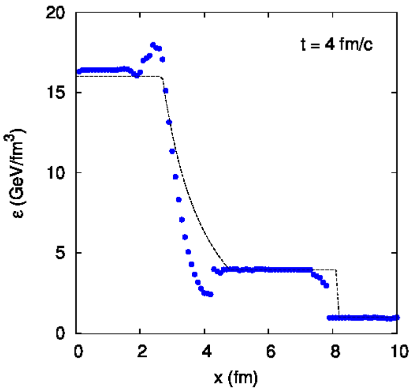

Figure 3. Profile of energy density ϵ in the numerical grid after 100 time-steps (our scheme in blue, analytic solution in black).

the numerical solution (blue) is comparable to the analytic solution (black). The scheme is able to handle the initial discontinuity, having only small problems at the head and the tail of the rarefaction wave. The profile of velocity after 100 time-steps, which we show in Figure 4, replicates the analytic solution similarly well.

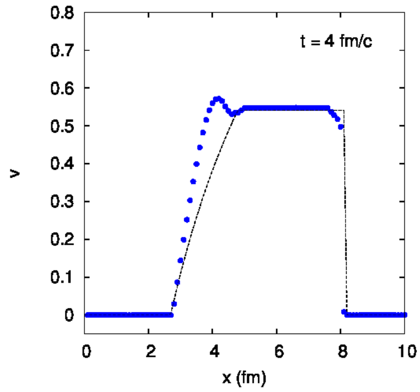

Figure 4. Profile of velocity v in the numerical grid after 100 time-steps (our scheme in blue, analytic solution in black).

Thus, we saw that we have built a new tool for ideal hydrodynamical modeling of quark gluon plasma, a Godunov-type numerical scheme with exact solution of Riemann problem for an arbitrary EoS. We have tested the scheme in 1D and have obtained promising results. The precision and numerical viscosity, resulting from sound wave propagation test, are satisfactory and will guide our choice of discretization when applying the scheme to other problems. The results of shock tube problem show that the scheme is able to handle discontinuities and large gradients in energy density well.

References

[1] S. K. Godunov, Mat. Sb. **47** 357 (1959).
[2] J. A. Pons, J. Fluid Mech. **422**, 152 (2000).
[3] Y. Akamatsu *et al.*, J. Comput. Phys. **256**, 34 (2014).

Open heavy flavor measurements at STAR

Pavol Federič[1] (for the STAR Collaboration)

[1]pavol.federic@gmail.com, Nuclear Physics Institute of the ASCR, v. v. i., Řež 130, 250 68 Řež, Czech Republic

Abstract. Measurements of open heavy flavor production at the Relativistic Heavy Ion Collider (RHIC) can play an important role in understanding the properties of hot and dense nuclear matter created in ultrarelativistic heavy-ion collisions. Properties of this new state of matter, strongly interacting Quark-Gluon Plasma (sQGP), have been a subject of extensive measurements at RHIC in the past decade. Due to their large masses, charm and bottom quarks are produced mainly in hard scatterings in the early stage of a collision and their number is virtually unaffected in later stages of the medium evolution. Heavy flavor quarks therefore provide a unique means of exploring the properties of the sQGP. In these proceedings we report recent STAR open heavy flavor results at various center-of-mass energies in p+p, Au+Au and U+U collisions.

1 Introduction

Heavy-flavor (c and b) quarks are predominantly produced in the initial hard scatterings in heavy-ion collisions at RHIC. Their interactions with the deconfined medium are sensitive to the medium dynamics. Thus heavy-flavor quarks are suggested as excellent probes to study the properties of the quark-gluon plasma, a hot and dense nuclear medium created at RHIC. In these proceedings, we present recent open heavy-flavor measurements by the STAR experiment in p+p, Au+Au, and U+U collisions.

2 Charm production in p+p collisions

Precise measurements of heavy-flavor production cross section in p+p collisions are essential to validate perturbative QCD (pQCD) and provide a baseline to interpret heavy-flavor measurements in heavy-ion collisions for the study of the sQGP. Open charm mesons can be fully reconstructed through hadronic decay channels, $D^0 \to K^-\pi^+$ and $D^{*+} \to D^0\pi^+ \to K^-\pi^+\pi^+$ (the charge conjugate is always implied if not otherwise stated). After subtracting the combinatorial background contribution (estimated using wrong charge-sign combinations or rotating the momentum direction of the decayed pions), the D^0 and D^+ production cross sections can be extracted taking into account D meson decay branching ratios, detector acceptance, and efficiency [1]. The D meson cross sections are converted to the $c\bar{c}$ production cross section using the charm quark fragmentation ratios.

STAR has measured $c\bar{c}$ production cross section in p+p collisions with data taken in 2009 and 2012 at $\sqrt{s}$ = 200 GeV. The first measurement was done with minimum bias (MB) events as a function of p_T for $0.6 < p_T < 6$ GeV/c [1]. The later measurement, using data taken in 2012, was done with both MB events and "high tower" (HT) events triggered on energy deposition in a Barrel ElectroMagnetic Calorimeter (BEMC) tower above certain thresholds. The HT results, after correcting for the trigger efficiency are consistent with the MB results in the overlapping p_T region. This analysis extends the p_T range down to 0 GeV/c due to the larger MB data sample size, and up to 10 GeV/c, thanks to the inclusion of the HT data sample. Both results are consistent with each other, and in agreement with fixed order, next-to-leading logarithm (FONLL) pQCD calculations [2]. A similar analysis has also been done using data taken in p+p collisions at $\sqrt{s}$ = 500 GeV, with both MB and HT events. The $c\bar{c}$ production cross section is measured as a function of p_T for $1 < p_T < 20$ GeV/c. The results are consistent with the latest FONLL calculations [3], as shown in Figure 1.

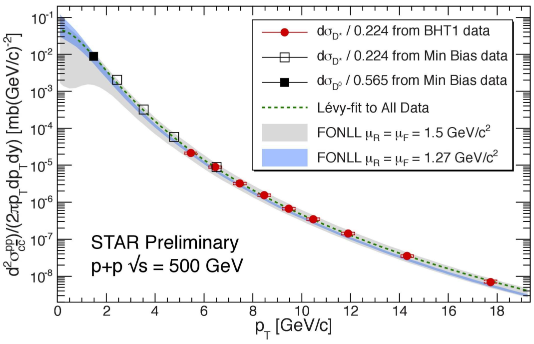

Figure 1. Preliminary $c\bar{c}$ production cross section in p+p collisions measured with the STAR experiment (points) and pQCD calculations (shaded bands) [3] at $\sqrt{s}$ = 500 GeV.

3 D^0 mesons in Au+Au collisions

Differences in the kinematic distributions of particles between heavy-ion collisions and p+p collisions can be quantified by the nuclear modification factor, $R_{AA} = \frac{1}{\langle N_{bin}\rangle}\frac{N_{AA}}{N_{pp}}$, where N_{AA} (N_{pp}) is the invariant yield in heavy-ion (p+p) collisions, and $\langle N_{bin}\rangle$ the number of binary nucleon collisions averaged over the considered centrality interval. STAR has measured D^0 meson invariant yields as a function of p_T for different centrality intervals in Au+Au collisions at $\sqrt{s_{NN}}$ = 200 GeV, and in U+U collisions at $\sqrt{s_{NN}}$ = 193 GeV, where the average Bjorken energy density is predicted to be about 20% higher than that of Au+Au collisions in the same centrality interval [4].

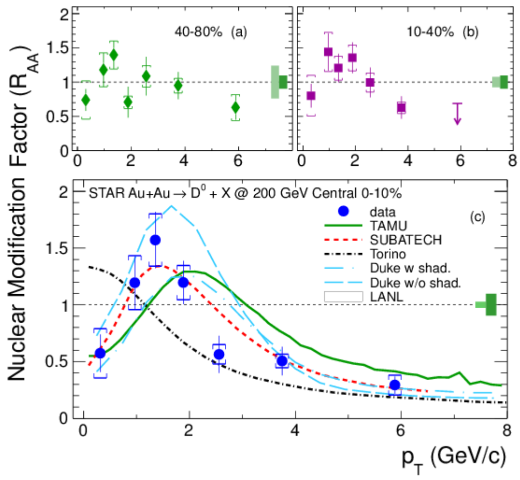

Figure 2. D^0 R_{AA} as a function of p_T for Au+Au collisions at $\sqrt{s_{NN}}$ = 200 GeV at mid-rapidity with different model calculations [5].

The measured R_{AA} in Au+Au collisions are shown in Figure 2 [5]. In the 0-10% centrality interval we observe a strong suppression at high p_T and an enhancement at intermediate p_T around 1.3 GeV/c. The R_{AA} in the 40-80% centrality interval is consistent with unity. The suppression of D^0 meson production at large p_T in Au+Au and U+U collisions follows a global trend as a function of the number of participant nucleons in the collisions [6]. Such a suppression is consistent with that measured for $\pi^{\pm}$. The measured R_{AA} of D^0 mesons in the most central Au+Au collisions are compared to various model calculations. We find that model calculations including a substantial amount of charm-medium interaction and hadronization through both fragmentation and coalescence can describe the data. The charm-medium interaction can explain the suppression at large p_T, while coalescence could be important for the enhancement at p_T around 1.3 GeV/c.

4 Non-photonic electrons

Non-photonic electron (NPE) measurements are a complementary way to study open heavy flavor hadrons through their semi-leptonic decays. Data reported in these proceedings were collected in Au+Au collisions at $\sqrt{s_{NN}}$ = 39, 62.4 and 200 GeV.

At $\sqrt{s_{NN}}$ = 200 GeV, NPE production in central and mid-central collisions is suppressed compared to FONLL, similar to D^0. However, the suppression is not observed at $\sqrt{s_{NN}}$ = 62.4 GeV. The measurement of eliptic flow v_2 at $\sqrt{s_{NN}}$ = 200 GeV is done using 2-particle ($v_2\{2\}$) and 4-particle ($v_2\{4\}$) correlations [7]. Figure 3 shows the measured $v_2\{2\}$ of NPE in Au+Au collisions. Finite $v_2\{2\}$ at low p_T indicates strong charm-medium interaction. At high p_T ($p_T >$ 3 GeV/c) we observe increase of v_2 which can arise from non-flow effects such as jet-like correlations or from path length dependence of heavy quark energy

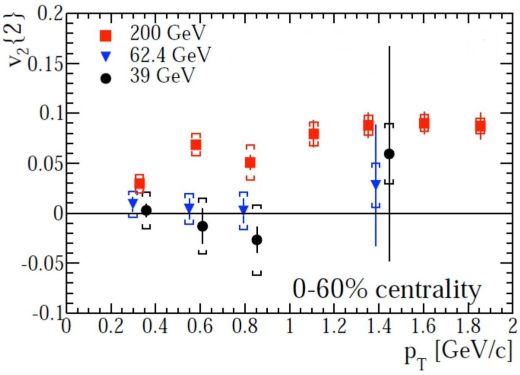

Figure 3. NPE elliptic flow v_2 in Au+Au collisions at $\sqrt{s_{NN}}$ = 39, 62.4 and 200 GeV [7].

loss. The v_2 result of NPE at $\sqrt{s_{NN}}$ = 39 and 62.4 GeV are consistent with no flow at $p_T < 1$ GeV/c. The results are compared with theoretical models. None of them give satisfactory descriptions for both R_{AA} and v_2 simultaneously.

5 Summary

In summary, STAR observed strong NPE and D^0 suppression at high p_T in Au+Au collisions at $\sqrt{s_{NN}}$ = 200 GeV, but no NPE suppression is seen at $\sqrt{s_{NN}}$ = 62.4 GeV at $p_T <$ 5.5 GeV/c compare with pQCD calculations. Also, similar sizes of D^0 nuclear modification factors are seen in Au+Au and U+U collisions [6]. D^0 R_{AA} at $\sqrt{s_{NN}}$ = 200 GeV can be described by calculations that include strong charm-medium interactions and coalescence hadronization. Large NPE v_2 is observed at $\sqrt{s_{NN}}$ = 200 GeV. At lower energies, v_2 at $p_T <$ 1 GeV/c is consistent with zero.

6 Acknowledgements

The publication has been supported by the MEYS grant CZ.1.07/2.3.00/20.0207 of the European Social Fund (ESF) in the Czech Republic: "Education for Competitiveness Operational Programme" (ECOP).

References

[1] L. Adamczyk *et al.* (STAR collaboration), Phys. Rev. D **86** (2012) 072013.

[2] M. Cacciari, P. Nason, and R. Vogt, Phys. Rev. Lett. **95** (2005) 122001.

[3] R. E. Nelson, R. Vogt, and A. D. Frawley, Phys. Rev. C **87** (2013) 014908.

[4] D. Kikola, G. Odyniec, and R. Vogt, Phys. Rev. C **84** (2011) 054907.

[5] L. Adamczyk *et al.* (STAR Collaboration) Phys. Rev. Lett. **113**, (2014) 142301.

[6] Z. Ye (for the STAR collaboration), Nucl. Phys. A (2014), DOI:10.1016/j.nuclphysa.2014.08.106.

[7] L. Adamczyk *et al.* (STAR Collaboration) 2014 (Preprint arXiv:1405.6348).

Study of charge of the top quark in the ATLAS experiment

Pavol Federič[1]

[1]pavol.federic@gmail.com, Nuclear Physics Institute of the ASCR, v. v. i., Řež 130, 250 68 Řež, Czech Republic

Abstract. A measurement of the top quark electric charge was carried out in the ATLAS experiment at the Large Hadron Collider (LHC) using $2.05 fb^{-1}$ of data at a centre-of-mass energy of 7 TeV. In units of the elementary electric charge, the measured top quark charge is 0.64 ± 0.02 (stat.) ± 0.08 (syst.). This result strongly favours SM and excludes models with an exotic quark with charge $-4/3$ instead of the top quark by more than 8σ.

1 Introduction

It is generally accepted that the particle discovered at Fermilab in 1995 [1, 2] is the Standard Model (SM) top quark. However, a few years after the discovery a theoretical model appeared proposing an "exotic" quark of charge –4/3 and mass ≈ 170 GeV/c^2 as an alternative to the SM top quark at this mass value [3].

A measurement of the top quark charge at LHC with $2.05 fb^{-1}$ of proton-proton collision data collected by the ATLAS experiment at $\sqrt{s} = 7$ TeV is presented [4]. The top quark charge measurement is based on reconstructing the charges of the top quark decay products. The dominant decay channel of the top quark, $t \to W^+b$ ($\bar{t} \to W^-\bar{b}$), has a W boson and a b-quark in the final state. While the charge of the W boson can be determined through its leptonic decay, the b-quark charge is not directly measurable, as the b-quark hadronisation process results in a jet of hadronic particles (b-jet). It is possible however to establish a correlation between the charge of the b-quark and a weighted sum of the electric charges of the particles belonging to the b-jet.

2 Top quark charge determination

In the SM, the top quark is expected to decay according to

$$t^{(2/3)} \to b^{(-1/3)} + W^{(+1)}, \tag{1}$$

while the exotic quark (t_{X}) with charge –4/3 is assumed to decay according to

$$t_{\mathrm{X}}^{(-4/3)} \to b^{(-1/3)} + W^{(-1)}, \tag{2}$$

where the electric charges of the particles are indicated in parentheses.

To determine the b-jet charge a weighting technique was employed in which the b-jet charge is defined as a weighted sum of the b-jet track charges:

$$Q_{b-\mathrm{jet}} = \frac{\sum_i Q_i |\vec{j} \cdot \vec{p}_i|^\kappa}{\sum_i |\vec{j} \cdot \vec{p}_i|^\kappa}, \tag{3}$$

where Q_i and $\vec{p}_i$ are the charge and momentum of the i-th track, $\vec{j}$ defines the b-jet axis direction, and κ is a parameter which was set to be 0.5.

The reconstructed events are selected using criteria designed to identify the lepton(electron or muon) + jets final states, i.e. $t\bar{t}$ events in which one of the W bosons decays leptonically and the other hadronically.

The variable that is used to distinguish between the SM and exotic model scenarios is the combined lepton–b-jet charge (hereafter referred to as the combined charge) which is defined as

$$Q_{\mathrm{comb}} = Q_{b-\mathrm{jet}} \cdot Q_\ell, \tag{4}$$

where $Q_{b-\mathrm{jet}}$ is the charge of the b-jet calculated with Equation (3) and Q_ℓ the charge of the lepton, the two being associated via the ℓb-pairing described below.

The ℓb-pairing is based on the invariant mass distribution of the lepton and the b-jet, $m(\ell, b\text{-jet})$. If the assignment is correct, assuming an ideal invariant mass resolution, $m(\ell, b\text{-jet})$ should not exceed the top quark mass provided that the decaying particle is the SM top quark. Otherwise, if the lepton and b-jet are not from the same decaying particle, there is no such restriction. The ℓb-pairing requires events with two b-tags and only the events with b-jets that satisfy the conditions:

$$\begin{aligned} m(\ell, b\text{-jet}_1) < m_{\mathrm{cut}} \quad &\text{and} \quad m(\ell, b\text{-jet}_2) > m_{\mathrm{cut}} \\ &\text{or} \\ m(\ell, b\text{-jet}_2) < m_{\mathrm{cut}} \quad &\text{and} \quad m(\ell, b\text{-jet}_1) > m_{\mathrm{cut}} \end{aligned} \tag{5}$$

are accepted. Here b-jet$_1$ and b-jet$_2$ denote the two b-tagged jets ordered in descending order of transverse momentum.

3 Results

The results for the combined charge are summarized in Table 1. This table contains the mean combined charge for the different channels. The combined charge for the exotic model was obtained by inverting the signal $t\bar{t}$ and single-top-quark combined charges while the non-top-quark background charge was not changed. The inversion of the b-jet charge (or lepton charge) in a lepton–b-jet pair, provided that the lepton and b-jet come from a top quark decay, corresponds to a change of the decaying quark charge from 2/3 to –4/3. The data agree with the SM top quark hypothesis within the uncertainties.

A total systematic uncertainties for the reconstruction of the combined charge in the electron and muon channels combined is 13.2%..

Lepton channel	$\langle Q_{\text{comb}} \rangle$ SM expected	XM expected	Data
e	-0.075 ± 0.006	0.073 ± 0.006	-0.079 ± 0.008
μ	-0.074 ± 0.006	0.065 ± 0.006	-0.075 ± 0.007
$e + \mu$	-0.075 ± 0.004	0.069 ± 0.004	-0.077 ± 0.005

Table 1. Reconstructed mean combined charge, $\langle Q_{\text{comb}} \rangle$, for the data in the different lepton + jets channels compared to those expected in the SM and the exotic model (XM). The uncertainties include the statistical uncertainties scaled to 2.05 fb^{-1} and the uncertainties in the cross sections and integrated luminosity.

3.1 Statistical comparison of the SM and exotic model

The compatibility of the data with the SM hypothesis of the top quark charge of 2/3 – was evaluated using a statistical model based on the Cousins–Highland approach [5]. The test statistic used for this purpose is the mean value of the combined charge. Due to finite detector resolution and finite sample size, the mean value of the combined charge observed in the experiment can be treated as one realization of a random variable, $\bar{Q}$, the distribution of which characterizes all possible outcomes of the experiment. This variable can be expressed as

$$\bar{Q} = (1 - r_{\text{b}} - r_{\text{t}}) \cdot Q_{\text{s}} + r_{\text{b}} \cdot Q_{\text{b}} + r_{\text{t}} \cdot Q_{\text{t}}, \qquad (6)$$

where Q_{s}, Q_{b} and Q_{t} are the combined charge mean values for the signal, background and single-top-quark processes, respectively, and r_{b} (r_{t}) is the fraction of the background (single-top-quark) events in the total sample of the candidate events. In Figure 1 the distributions from the pseudo-experiments of the observed mean combined charge ($\bar{Q}$) are shown for both hypotheses, the SM (solid blue line) and the exotic model (dashed red line). The magenta line in this plot corresponds to the experimentally observed value Q_{obs}. The figure shows the results for the combined electron and muon channels.

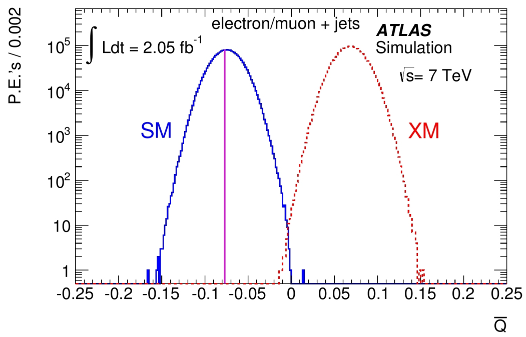

Figure 1. The expected distribution of the mean value of the combined charge, $\bar{Q}$, for the electron and muon channels resulting from pseudo-experiments for the SM (solid blue line) and the exotic (dashed red line) hypothesis for an integrated luminosity of 2.05 fb^{-1}. The magenta vertical line represents the value measured in the data.

The two hypotheses are compared by calculating the p-value, the probability of obtaining a test statistic at least as extreme as the one that was actually observed provided that the null hypothesis is true. The p-values for the SM scenario are high (the two-sided p-value is more than 80%) while those for the exotic hypothesis are very small (less than 10^{-7}). Converting the p-value into the number of standard deviations for the exotic-scenario mean combined charge distribution, an exclusion at the level higher than 8σ is obtained for the combination of the electron and muon channels.

3.2 Electric charge of the top quark

The top quark charge can be directly inferred from the background-subtracted Q_{comb} data distribution using a Q_{comb} to b-jet charge calibration coefficient obtained from Monte Carlo (MC). From the SM value of the b-quark charge ($Q_b = -1/3$) and the mean reconstructed value of the combined charge ($\langle Q_{\text{comb}} \rangle$) for signal events, the b-jet charge calibration coefficient $C_{\text{b}} = Q_{\text{b}} / \langle Q_{\text{comb}} \rangle$ is found to be 4.23 ± 0.03 (stat.) $\pm$ 0.07 (syst.) when evaluated using the full $t\bar{t}$ MC sample. The top quark charge then can be calculated as

$$Q_{\text{top}} = 1 + Q_{\text{comb}}^{(\text{data})} \times C_b \ , \qquad (7)$$

where $Q_{\text{comb}}^{(\text{data})}$ is the reconstructed b-jet charge obtained from the data after the subtraction of the expected background. The mean value of the top quark charge for lepton + jets channel is 0.64 ± 0.02 (stat.) $\pm$ 0.08 (syst.). This result is obtained from the mean of the combined histogram of Q_{comb} for the two channels. The quoted systematic uncertainty includes uncertainties on the calibration constant and all the uncertainties on the mean combined charge as described below.

4 Conclusion

The top quark charge has been studied using 2.05 fb^{-1} of data accumulated by the ATLAS experiment at a centre-of-mass energy of 7 TeV. The measured top quark charge is 0.64 ± 0.02 (stat.) $\pm$ 0.08 (syst.). This result strongly favours the SM and excludes models with an exotic quark with charge –4/3 instead of the top quark by more than 8σ.

References

[1] CDF collaboration, Phys. Rev. Lett. **74**, 2626 (1995).

[2] D0 collaboration, Phys. Rev. Lett. **74**, 2632 (1995).

[3] D. Chang, W.-F. Chang and E. Ma, Phys. Rev. D **59**, 091503 (1999).

[4] ATLAS Collaboration, JHEP **11**, 031 (2013).

[5] R. D. Cousins and V. L. Highland, Nucl. Instrum. Meth. A **320**, 331 (1992).

Unfolding of energies of fusion products measured by the activation probe at JET

O. Ficker[1,3], J. Mlynar[1], G. Bonheure[2], A. Murari[4], S. Popovichev[5], and JET EFDA contributors

[1]*Institute of Plasma Physics AS CR, Za Slovankou 3, 18200 Praha 8, Czech Republic*
[2]*European Commission, Fusion Energy Unit, Directorate for Research & Innovation, Brussels, Belgium*
[3]*oficker@gmail.com, FNSPE, Czech Technical University in Prague, Brehova 7, Praha 1, Czech Republic*
[4]*Consorzio RFX, Corso Stati Uniti 4, I-35127, Padova, Italy*
[5]*Culham Centre for Fusion Energy , Abindgon, Oxon, OX14 3DB, UK*

Abstract. Providing a detection method for diagnostic of charged fusion products in tokamaks presents a major challenge, while its absolute calibration with a sufficient accuracy and its capability to withstand harsh fusion reactor environment will be required. A novel type of detector that meets most of these requirements, based on an activation probe, was tested in JET and other European facilities. This probe proved to be extremely robust due to its simple construction. It is equipped with samples of well defined isotopic abundance. The materials of the samples are selected with respect to the undergoing nuclear reactions during the exposition to the flux of fusion products. The amounts of activated nuclei due to the reactions in these materials could be measured via ultra-low-level gamma spectroscopy [1]. The feasibility of the proton spectrum reconstruction from measured activities is examined in this contribution with the help of the algorithm based on the Tikhonov regularisation constrained by minimum Fisher information. The reliability of the method was previously illustrated using synthetic proton data [4]. The reconstruction of the proton spectrum is difficult as it depends on several geometrical factors, therefore a basic analysis of stability is introduced to support the encouraging results.

1 Activation probe

The activation probes were used in Textor, ASDEX-U and JET tokamaks. The JET probe was equipped with the highest number of samples sensitive to fusion protons and neutrons. The activation samples (made of pure metals, alloys or ceramic materials) were attached to the holder and put inside the vacuum chamber.

The activation probe is quite different to other diagnostics methods of fusion products. Due to its construction, the probe is highly resistant to the fusion reactor environment: mechanical shocks, high heat loads, temperature and pressure cycling, etc. The nuclear reactions of the sample nuclei allow the determination of the primary particle type and energy. On the other hand, this detector does not allow for immediate data processing and the post-mortem analysis in low-level spectrometric laboratories is expensive and time consuming.

2 Unfolding of spectra

The unfolding of spectra is a typical inverse problem. The process of activation by the fusion protons could be expressed by the system of linear equations

$$A_i = \sum_j^N R_{ij} S_j + \xi_i, \tag{1}$$

where A_i are measured activities, S_j is the discretized proton energy spectrum, R_{ij} is the response matrix that reflects the cross-sections of reactions and the geometry of the probe, $i = 1, ..., M$ are the indices of the samples and ξ_i the unavoidable errors of the measuring process. The evaluation of the proton spectrum from measured activities is an ill-posed problem and the direct inversion of (1) is not possible.

The inverse problem must be regularised by suitable restrictions on the solution. One of the most successful regularisation methods is the Minimum Fisher Regularisation. This method transforms the solving of the linear equation (1) into the search for the minimum of the following functional

$$\Lambda_{MF} = \frac{1}{2}\chi^2 + \alpha_R I_F. \tag{2}$$

χ^2 is the goodness-of-fit parameter, in this case

$$\chi^2 = \frac{1}{M} \sum_i^M \left(\frac{A_i - \sum_j^N R_{ij} S_j}{\sigma_i} \right)^2, \tag{3}$$

where σ_i are data errorbars; α_R is the regularisation parameter and I_F is the Fisher information measure of the resulting spectrum defined by

$$I_F = \int \frac{1}{S(E)} \left(\frac{\mathrm{d}S(E)}{\mathrm{d}E} \right)^2. \tag{4}$$

The minimisation of the functional (2) determines the most suitable smooth solution of the problem.

3 Results

The hexagonal probe presented in Figure 1 was exposed to the flux of fusion products inside the vacuum chamber of JET during pulses #72622 - #72635. The D-^{3}He fuel mixture was used. For the unfolding, the data from 23 proton-induced channels (different in nuclear reaction and position of the sample) were used, including the stacked samples that

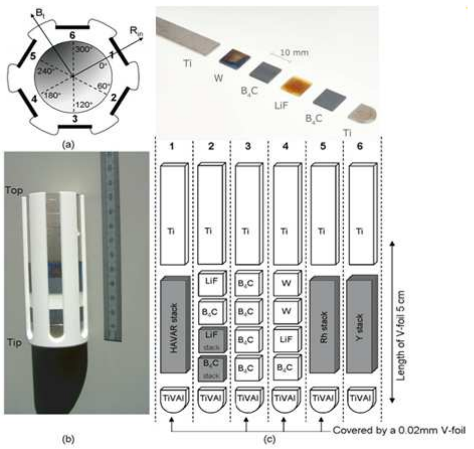

Figure 1. Activation probe used at JET, position of samples on the holder.

improved the energy resolution. The activities were analysed in three underground ultra-low-level gamma ray laboratories.[1]

Only errorbars of the measurement of activity were considered. The differences in the flux of fusion products on the different samples were partially compensated, yet could affect the unfolding. The values of given activity errorbars are not sufficient for the equation (2) and had to be aligned by additive or multiplicative constant to get realistic estimation.

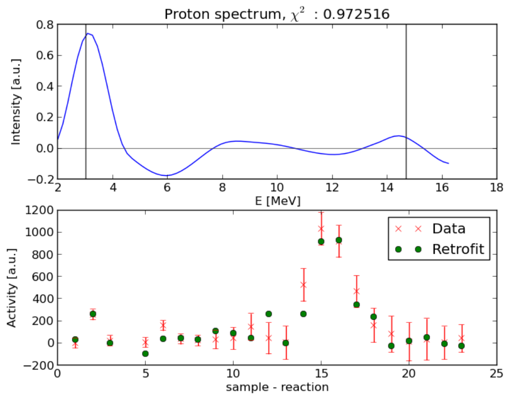

Figure 2. Reconstructed proton spectrum (top) and measured activation data compared to the retrofit of the reconstruction (bottom).

In the reconstructed proton spectrum, the peaks of both DD and D^3He protons were identified at energies 3 MeV and 14.7 MeV, respectively. However, the nature of the MFR introduces negative values to the reconstructed spectrum (Figure 2).

To avoid this behaviour, the values of the retrofit corresponding to the negative part of the reconstructed spectrum may be added to the measured activities to secure the non-negativity of the spectrum in the next iteration of the MFR loop.

The result of this modification is in the Figure 3, where the different attitudes to the error estimation are compared. It is obvious that the restriction on negative values has increased the presence of the additional peak that has no physical explanation. On the other hand, the corrections of errorbars cause only minor changes to the shape of the spectrum. The method is also resistant to minor manipulations of the response matrix.

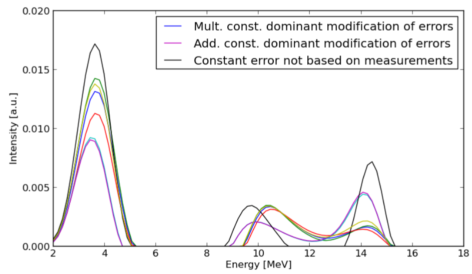

Figure 3. Reconstructed spectrum with restriction on negative values, comparison of different attitudes to the modification of errorbars.

4 Summary

The spectrum of fusion protons produced in the tokamak reactor may be derived from the activation data. Further tests and improvements of the response matrix are necessary to establish the activation probe as a useful detector.

Acknowledgements

This work, supported by grant of the Czech Science Foundation GA P205/10/2055 and by EURATOM, was carried out within the framework of the European Fusion Development Agreement.

References

[1] G. Bonheure *et al.*, Nuclear Fusion **52**, 083004 (2012).

[2] J. Mlynar, J. M. Adams, L. Bertalot, S. Conroy, Fusion Eng. Des. **74(1–4)**, 781–786 (2005).

[3] R. A. Forrest, FISPACT-2007 Technical Report UKAEA FUS 534, (2007) (available online).

[4] J. Mlynar, G. Bonheure, O. Ficker, K. Bauer, S. Popovichev, A. Murari, 55th Ann. Meet. APS Plasma Physics Division, UP8.00003 (2013).

Υ production at the STAR experiment

Jana Fodorová[1] (for the STAR Collaboration)

[1]fodorjan@fjfi.cvut.cz, Faculty of Nuclear Sciences and Physical Engineering, Czech Technical University in Prague, Břehová 7, 115 19 Praha 1, Czech Republic

Abstract. We present recent STAR results on Υ production in p+p, d+Au, Au+Au collisions at $\sqrt{s_{NN}}$ =200 GeV and U+U collisions at $\sqrt{s_{NN}}$ =193 GeV. These results are compared to theoretical calculations and to results from other experiments.

1 Quarkonia in heavy-ion collisions

Quark-gluon plasma (QGP), a novel state of deconfined nuclear matter, can be created in high-energy heavy-ion collisions. Properties of the QGP have been studied by the STAR experiment at the Relativistic Heavy Ion Collider (RHIC) in Brookhaven National Laboratory.

Measurements of quarkonium production are an important tool in the study of properties of the matter produced in heavy-ion collisions. Heavy quarkonia, i.e. the bound states of heavy quarks and their antiquarks ($c\bar{c}$ – charmonia and $b\bar{b}$ – bottomonia), have been predicted to dissociate inside the QGP due to Debye color screening of quark and antiquark potential [2]. Since different quarkonium states have different binding energies and the Debye screening length depends on the temperature attained by the QGP medium, each state is expected to break up at a different medium temperature [3]. Therefore, the suppression pattern of various quarkonium states can serve as an effective "thermometer" of the QGP. However, there are also other effects which can influence quarkonium production, such as cold nuclear matter (CNM) effects including shadowing/anti-shadowing of parton distribution functions and final state nuclear absorption, and statistical coalescence of quark-antiquark pairs in the QGP. Bottomonia are expected to be less affected by these effects than charmonia and, therefore, are considered to be a cleaner probe of the QGP.

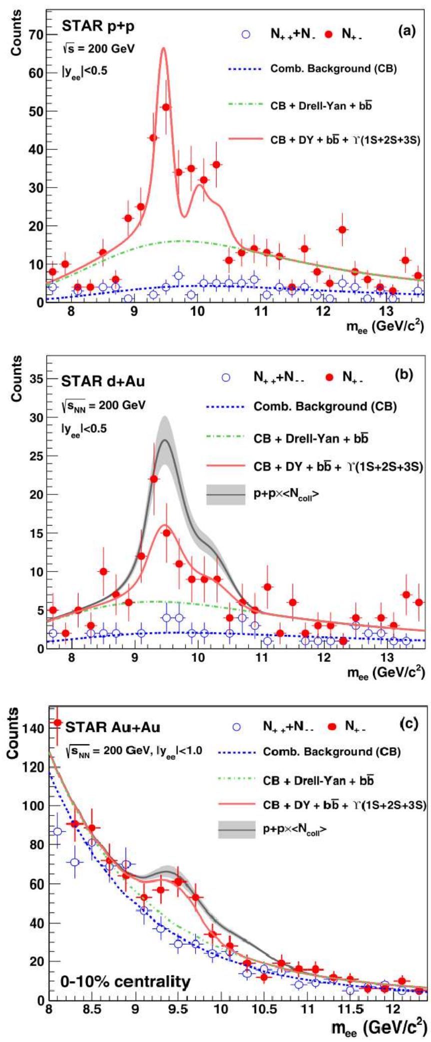

Figure 1. Invariant mass distributions of unlike-sign (full circles) and like-sign (open circles) electron pairs at mid-rapidity in p+p (a), d+Au (b), and Au+Au (c) collisions at $\sqrt{s_{NN}}$ =200 GeV [4].

2 The STAR detector

The STAR detector [1] was designed to investigate the strongly interacting matter by detecting and identifying charged particles at mid-rapidity ($|\eta| < 1$) with full azimuthal coverage. Its main subdetectors used for particle identification are the Time Projection Chamber (TPC), Time of Flight (TOF) detector, and Barrel Electromagnetic Calorimeter (BEMC).

The TPC is the main tracking device of the STAR detector and provides particle identification by measuring ionization energy loss (dE/dx). The TOF measures the time of flight of particles and improves particle identification capabilities at low p_T, while the BEMC is used to measure energies of and identify high p_T electrons.

3 Data analysis and results

At STAR, Υ production has been measured via the dielectron decay channel $\Upsilon \to e^+e^-$ (B.R.∼ 2.4%) in p+p, d+Au, Au+Au collisions at $\sqrt{s_{NN}}$ =200 GeV and in U+U collisions at $\sqrt{s_{NN}}$ =193 GeV. Figure 1 shows the invariant mass distributions of e^+e^- pairs in p+p (a) and d+Au (b) collisions in the rapidity region $|y_{ee}| < 0.5$ and in Au+Au (c) collisions in the region $|y_{ee}| < 1.0$. Gray bands in Figure 1b and 1c correspond to the Υ yield from the p+p data scaled by the averaged number of binary collisions $< N_{coll} >$ in d+Au and Au+Au data, respectively.

Modification of the quarkonium production in collisions of nuclei A+B compared to p+p collisions can be expressed by the nuclear modification factor R_{AB} given as a ratio of quarkonium yields in heavy-ion collisions and yields in p+p collisions scaled by $< N_{coll} >$:

$$R_{AB}(p_T, y) = \frac{1}{< N_{coll} >} \frac{\mathrm{d}^2 N_{AB}/\mathrm{d}p_T\mathrm{d}y}{\mathrm{d}^2 N_{pp}/\mathrm{d}p_T\mathrm{d}y}. \quad (1)$$

$R_{AB} > 1$ ($R_{AB} < 1$) corresponds to enhancement (suppression) of the production.

For a correct interpretation of results from heavy-ion collisions we must understand the CNM effects. STAR has measured Υ(1S+2S+3S) production at $\sqrt{s_{NN}}$ =200 GeV in d+Au collisions [4] where QGP formation is not expected. The rapidity dependence of the measured R_{dAu} is shown in Figure 2. The results are compared to PHENIX data and theoretical calculations which include shadowing and/or initial state parton energy loss [5, 6]. The models are in agreement with the data except in the $y \sim 0$ region where the considered CNM effects alone may not be enough to explain the observed suppression.

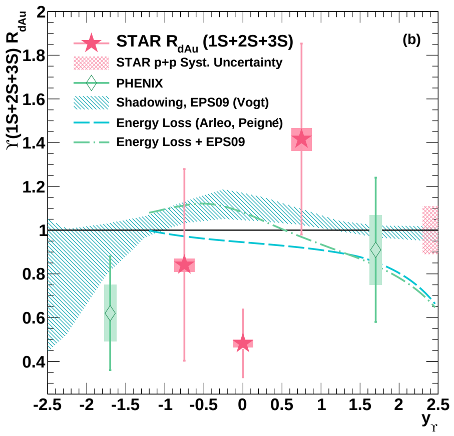

Figure 2. STAR R_{dAu} of Υ meson [4] as a function of rapidity compared to model calculations [5, 6].

Nuclear modification factors of Υ(1S+2S+3S) production in d+Au, Au+Au, and U+U collisions are presented in Figure 3 as a function of centrality (represented by the number of participant nucleons N_{part}).

The STAR Au+Au and U+U results show a similar trend of the suppression increasing with centrality. A significant suppression is observed in the most central collisions and is consistent, within uncertainties, with results obtained at LHC [7].

The R_{AA} is also compared to model calculations by Strickland and Bazow [8] incorporating thermal dissociation of Υ in expanding partonic medium. The STAR results favor a model version in which the heavy quark potential is based on internal energy over the free energy based one. However, it should be noted that this model does not include CNM effects. The strong binding scenario in a model proposed by Rapp *et al.* [9], which includes CNM effects in addition, is also consistent with STAR results.

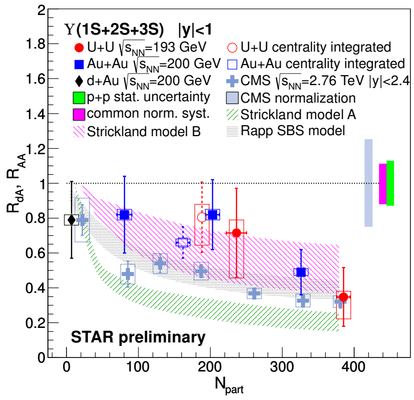

Figure 3. Υ R_{AA} as a function of N_{part} at $|y| < 1$. STAR results in U+U, d+Au, Au+Au collisions are compared to CMS data [7] and model calculations [8, 9].

4 Summary

Υ production was studied in $\sqrt{s_{NN}}$ =200 GeV p+p, d+Au, Au+Au and $\sqrt{s_{NN}}$ =193 GeV U+U collisions. Suppression seen in Au+Au collisions indicates the presence of deconfined nuclear matter in heavy-ion collisions. To make stronger conclusions from Au+Au results further study of CNM effects is needed. This will be provided in the future p+Au collisions at RHIC.

Acknowledgements

This work was supported by the grant of the Grant Agency of Czech Republic n.13-20841S and by the Grant Agency of the Czech Technical University in Prague, grant No. SGS13/215OHK4/3T/1 4.

References

[1] K. H. Ackermann *et al.* [STAR Collaboration], Nucl. Instrum. Meth. A **499**, 624 (2003).

[2] T. Matsui, H. Satz, Phys. Lett. B **178**, 416 (1986).

[3] Á. Mócsy, P. Petreczky, Phys. Rev. D **77**, 014501 (2008).

[4] L. Adamczyk *et al.* [STAR Collaboration], Phys. Lett. B **735**, 127 (2014).

[5] R. Vogt, R. E. Nelson, A. D. Frawley, ConfinementX, 203 (2012).

[6] F. Arleo, S. Peigne, JHEP **1303**, 122 (2013).

[7] S. Chtrchyan *et al.* [CMS Collaboration], Phys. Rev. Lett. **109**, 222301 (2012).

[8] M. Strickland, D. Bazow, Nucl. Phys. A **879**, 25 (2012).

[9] A. Emerick, X. Zhao and R. Rapp, Eur. Phys. J. A **48**, 72 (2012).

Addressing nanoscale soft-matter problems by computational physics and physical computation – an example of facilitated lubrication in a two-surface system with hydrodynamic interlayer

Adam Gadomski[1], Wiesław Urbaniak[2], and Roland G. Winkler[3]

[1]agad@utp.edu.pl, Department of Physics, University of Technology & Life Sciences, 85796 Bydgoszcz, Poland
[2]wurban@ukw.edu.pl, Faculty of Mathematics, Physics and Technical Sciences, Kazimierz Wielki University, 85-867 Bydgoszcz, Poland
[3]r.winkler@fz-juelich.de, Theoretical Soft Matter & Biophysics, FZ Jülich GmbH, 52428 Jülich, Germany

Abstract. Soft-matter physics viewed as an emerging discipline of physics, is as yet devoid of its own well established methods, as taken them mainly from condensed matter theory and statistical, as well as computational, classical and quantum physics. There appears a number of hot problems in this emerging area of (bio)physically motivated research that needs both computational-physics and physical-computation methods to apply. In particular, the problems of utmost concern are: (1) biomatter (dis)ordered aggregation; (2) formation of (nonlinear) viscoelastic assemblies; (3) nanoscale-oriented and amphiphile-structure involving friction, and lubrication (hydro)dynamic effects on functioning of natural surfaces-involving systems. In this concise address, a need of dedicated computational methods for the latter problem will be put forward, and an expression of deriving its range of detailed exploration will be specified through a computational challenge.

1 Introduction and problem statement

If two rubbing corrugated (bio)surfaces, opposed to one another upon dynamic friction conditions, would relax by active participation of a complex-fluid and multi-component hydrodynamic interlayer [1], one might address at least two legitimate questions: (a) how would the viscoelastic and hydrodynamic interlayer structurally rearrange upon either normal or slightly sheared lateral friction conditions? (b) which are relevant levels of such a rearrangement in terms of the natural scale characteristics' conditions, such as object sizes, magnitudes of the forces and values of the energies?

Let us assume that the principal mesoscopic unit in the friction-lubrication process in articulating joints is a multilayered amphiphilic aggregate, one might build an overall picture of its decisive role played by the micelle [1] as a roller bearing, and, addressing the nanoscale, an overall channeling superstructure, able to transmit ions through its intra- and interspaces, Figure 1. A reversed micelle is indicated to be a structural device responsible for the transmission [2]. It is comprised of amphiphilic molecules each of which is made up of one hydrophilic/polar head and two hydrophobic legs, Figure 1. The heads are always exposed toward water pools, whereas the micellar core is going to represent a channel for hydrogen ions, expressing their motions – a structural cooperative, inherently (nano)hydrodynamic effect [3, 4] of importance in facilitated lubrication of the cartilage [1, 2].

2 Passage between meso- and nanoscales

The limits of the above drawn scenario concern first comprehensive experimental evidences confirming it in full—the picture should be taken fairly hypothetical as yet [1, 2]. Yet, at the micelles' formation mesoscopic level, the Avrami-Kolmogorov/A-K (albeit dispersive) phase-change kinetic picture can first be proposed. The near-surface amphiphiles, assembled there as multilayer phases are to be transformed to reversed micelles (Figure 1). The dispersive/fractal kinetics take for granted that a tribomicellization kernel $K(t)$ would be, in the most sensitive case, dependent inverse-powerly on time t, like $K(t) \sim t^{-\nu}$ (ν, a tribomicellization characteristic exponent), which also provides some Random Walk characteristics, coming from an association between the viscosity-expressing $K(t)$ term, and its corresponding diffusional counterpart [4], designated by $\langle r_H^2{}^+(t)\rangle$ (average $\langle\ldots\rangle$ taken over a nano-channel subspace), which is the *MSD* of the hydrogen (H^+) ions [1, 5, 6]. Based on it, the nanoscale effects due to $H-$bonds extensive afterload breakages, and resulting creations of hydrodynamic waves of H^+ ions [4], able to penetrate the inter-micellar and/or intra-micellar cavities, manifest readily; see [1], and analogous star-polymer (hydrodynamic) frictional effect [3]. Albeit, another relevant question (Table 1) applies: what about other ions that are also of system's reach [2]? Could one rely on changing the complex-fluid viscosity picture [4, 6] based on either ions? If it is so indeed, to which degree it is plausible to occur for H^+?

2.1 Some mention on mesoscale formulation

The coupling between the mesoscale dynamical-system dependent SAPL concentration variables [1, 2], via the tribomicellization kernel *K(t)*, is capable of recovering the dynamics' average subtleties of the cartilage. It has been demonstrated that a certain promising merger between meso- and nanoscale, Table 1, has been offered in terms of a spectral parameter h, obeying a resulting structure–property cartilage's mechanical paradigm [1, 2].

One then may rephrase after Richard Feynman: "There is plenty of room at the bottom", which means here: it is worth exploring and experimentally checking out the nanoscale friction contribution even more

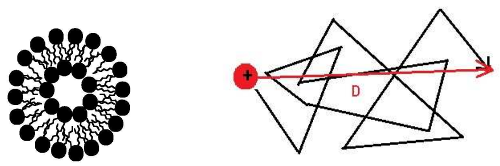

Figure 1. Unified view of the reverse micelle (left), a small colloidal aggregate comprised of lipidic molecules, drawn as heads (polar residues) with two legs (hydrophobic residues) [2]. A hydrogen ion H^+ [4] (right) is virtually able to travel, as in a wire, an end-to-end (red) distance D within the micellar milieu.

in-depth, rendering the overall problem as worthy experimental validation. Also, there can be another conceptual link to be introduced. In short, it is due to accepting a complete analogy between the dynamic friction coefficient α, and the (non)directional H^+ diffusion coefficient (denoted by D, and related via time account with the *MSD* [1, 4]), Figure 1, which both quantities appear to be fairly related to each other, $\alpha \sim D$.

3 Computational challenges discussed

As to proceed one could examine, in terms of molecular dynamics (MD) type simulation, the interacting behavior in such complex hydrodynamic, explicit-water containing, milieus [3–6], in a way comparative to multiparticle-collision dynamics (MPC) in low *Re*-number systems. An impressive realization with star polymers [3], being to some extent reminiscent of micelles' interactions [1, 2], can be worth exploiting. After performing MPC check-out, one may also look more deeply into bulk vs. structured water behavior [5, 6], associated with the changes within the examined interaction map, attempting then on entailing them with appearances of the H^+ (Figure 1) hydrodynamic waves [4], undergoing the Grotthuss type H^+ conduction and pH-milieu dependent quantum mechanism to be transformed to the corresponding Random Walk characteristics of the friction system in nanoscale cavities/wires [1, 2, 5, 6].

Mesoscale	Nanoscale
Micelles' creation-annihilation	Hydrophilicity of oppositely acting surfaces
Buiding up a biopolymer micellar network	Constitution of the dynamic ionic passages within the net
Rearrangement of amphiphilic micelles into a set of ion channels	Enhanced, normal and decelerated Random Walk of hydrogen or other ions
Micelles' blowing-up in favor of multilayers restitution	Ion-action altered viscosity as seen in dynamic-friction terms

Table 1. Qualitative comparison of decisive factors coming from meso- and nanoscale (hydro)dynamic phenomena

3.1 Remarks on toward-nanoscale further steps

So-envisioned hybrid type, thus MPC technique, working in vital cooperation with certain kind Brownian dynamics (BD; memory-involving Langevin [1], and assisted due to the A-K schedule, by a kinetic, $t-$scale including (kinetic) MC technique, is proposed to pave the way ahead. A highlight of such computer experiment at the nanoscale would be to link sensitively the Grotthuss type H^+ conduction mechanism [4, 6] with viable structural changes within the micellar membraneous, interfacial assemblages [7], and the H^+ wires within them [1, 5]. The latter are primarily transferable to poor or good capability of sustaining even severe friction conditions, also the ones under hydrodynamic shear effect at the nanoscale.

As a consequence of the above, a formal relationship is to be disclosed as a simple example of the small-scale structure–property relationship, experienced virtually by an articular cartilage under normal or lateral loads, in most effective (Debyean) material relaxation conditions [1]. Otherwise, one would expect non-Debye departures from the low-dissipation type of relaxation habit, showing up its response in such hydrodynamically expressing systems.

4 General remark and perspective

The undisputable complexity of this soft-matter system [7] considered here in brief, Table 1, can be successfully coped with as a formidable problem dissolved into potent logic of hybrid computational models consisting of clear analytical and numerical attempts first [1], but examined then in depth by simulation methods (MPC, MD, BD). Such statement is positively verified if the methods [3] are applied to thoroughly performed experiments [4–7].

The most attractive perspective on (bio)tribological [1–3] studies, can rest on high-standard level of professional discussions of the main principal investigators: theorists, computer simulators, and finally, experimenters [2, 7], working upon resting on quite-in-parallel interrelation within the complex task sketched, and toward its relevance for human health care [8].

References

[1] A. Gadomski *et al.*, Math. Biosci. **244**, 188 (2013).
[2] Z. Pawlak, A. Oloyede, Biosystems **94**, 193 (2008).
[3] S. P. Singh, R. G. Winkler, G. Gompper, Phys. Rev. Lett., **107**, 158301 (2011).
[4] J. D. Bernal, H. A. Fowler, J. Chem. Phys. **1**, 515 (1933).
[5] J. F. Nagle, H. J. Morowitz, PNAS **75**, 298 (1978).
[6] S. Cukierman, BBA-Bioenergetics **1757**, 876 (2006).
[7] D.A. Bradley *et al.*, Nucl. Instr. Methods Phys. Res. A **619**, 330 (2010).
[8] A partial support by BS39/14 is acknowledged by AG.

.

Recognizing an applied-physics and physicochemical succession of Jan Czochralski, an outstanding European crystal grower and personality

Adam Gadomski[1] and Jan Kłos[2]

[1]agad@utp.edu.pl, University of Technology & Life Sciences, Department of Physics, 85796 Bydgoszcz, Poland
[2]klosjan@kul.lublin.pl, John Paul II Catholic University of Lublin, Faculty of Philosophy, 20950 Lublin, Poland

Abstract. A question will be asked, and then partly answered, as to what degree Jan Czochralski, a great Polish chemist, crystallographer and metallurgist, or even material (metal) scientist, and applied physicist, should in terms of his research achievements belong to (physicochemical) metallurgy or had to be recognized rather as a chemist, working with metals and their "derivatives"; not mentioning that some part of his research would equally well be placed within applied physics' reach. The bare ground for answering the question addresses the fact that he did his integrated research within physicochemical and even mechanochemical (as a specific important subject) metallurgy of fairly complex as well as very practical systems that he was able to resolve thoroughly by his investigations. Moreover, his personal turnovers, and the overall historical and political context, influenced his impressive research accomplishments to a really great extent.

1 Commencing with an early, very fruitful period of Czochralski's activity

Jan Czochralski (1885–1953) was born in Kcynia close to Bydgoszcz in Poland, approximately halfway between Warsaw and Berlin. His most recognized work on single metallic crystals and their growth rates was published in *Zeitschrift für physikalische Chemie*, received for publication in August 1916, but not published until two years later [1]. This article was an example – not often seen these days – of being precise and specific in presenting research achievements. In just three pages the researcher reported on his new findings – that a new method of pulling metallic single crystals had been discovered in terms of their growth rates (and nucleation-ionic promoters), and that it had been applied for testing crystal growth of three metals: *Sn*, *Pb*, and *Zn*. This raised then great admiration both in Poland and abroad [2].

As a consequence of this work, he is still recognized as one of the founders of today's crystal-growth technology and research, although originally his method was rather elaborated for the three metals invoked above. It should be realized that Jan Czochralski invented the famous method during his stay and work in Berlin for the AEG (Allgemeine Elektrizitats-Gesellschaft) company, also using the AEG laboratory facilities. He also benefitted from collaboration with a German researcher W. von Mollendorff and developed much of his knowledge on the crystallography of metals, as dealt with by means of X-ray diffraction, during this time span of the first few years of the second decade of twentieth century [3].

2 Keeping on performing research and inventing

In order to increase his activity in metal science and technology he moved from Berlin to Frankfurt on Main, where he progressed with his work on metallurgical methods to obtain new alloys, as well as on metal based composites, leading to the production of bearings (so called metal B), and on AI-based wires and contacts in electrical circuits. He also became interested in the ductility of materials, and mechanical properties of polycrystals. Yet, with his German coworkers, his main concern was on the principles of the metallurgical processes, such as: the role of defects, and specifically of dislocations, in efficiently yielding (im)pure metals and alloys; stress-strain and recrystallization characteristics; phase equilibria and transitions associated with their manifestations, and the likes. It is also to be noted that during his activity in Frankfurt on Main for *Metallbank und Metallgesellschaft* he was able to propose in one of his papers "Radiotechnics in Service of Metal Science" in 1925 a sort of radiomicroscope, thus some prototype of modern scanning microscopes, serving for detection of non-metallic inclusions in the surface of a metallic sample [4]. (Notice that at present such tasks belong to standard practical problems of surface science and applied physics.)

Years of (in)activity	Count of published papers
1919	0
1933 − 34	0
1936 − 37	16 + 16
1939	0

Table 1. Publication scores of Jan Czochralski: best and worst counts in the number of papers published

2.1 Apparently practical problem taken

It turned out that Czochralski was to a great extent an individual, satisfying criteria of – no doubt- open-mindedness quite far exceeding his specialised professionalism. Two instances may support this point of view. There exists a paper printed in Poland (Sosnowiec) witnessing to a special deal his activity as a geochemist. While a well-known chemistry professor

Where / When vs. What	Best accomplishment in research	Professional position's characteristic	Important private event
Berlin period 1905–1919	1918: CZ method of pulling single crystals	Laboratory staff and special-purpose investigator	Marriage and family creation with Margerita Haase
Frankfurt on Main period 1920–1928	1925: radiomicro-scope (surface forces apparatus)	Independent researcher; secretary and president of metallurgical society	Patenting metal B – bearing's material for railways; presidency of the society; benefitting from own inventions
Warsaw period 1929–1945	1936–37: best score, see Table 1	Institute's director; technical- university professor	Creating a milieu of high-level physical metallurgy specialists; helping people during the war; mecenate for artists

Table 2. Key facts from Czochralski's life and research

in the capital of Poland he was directly asked by the local authorities of his birth town Kcynia to resolve a "hot" problem of whether are there any underground reservoirs of natural oil in Kcynia, and in its vicinity (Pałuki), or is there something else staying behind it? Researcher's answer after thorough enough examination of the so stated problem was that there are no underground oil resources on the spot, and the fluid that wets constantly the nearby grounds originates from some quite forgotten and long-existing storage pools for fuel, tar, industrial lubricants and other, mostly liquid, wastes, where the containers keeping them stored, neither truly tight nor really free of corrosional influence, have steadily polluted and concaminated all the nearby spots by creating over many their activity years certain sewage areas of pretty high ecological devastation.

2.2 Seemingly ecology oriented activity

In fact, there also remains available some information that points to Czochralski's broadly spread out activity in the area of ecology. In particular, it became anticipated because in a renowned McGraw-Hill dictionary there appeared a notion that the so-called Czochralski's process was roughly equivalent to the term 'antropopression', well known in ecology [1]. Albeit, until now, it has not been proved in sufficient detail that he really coined that sound term.

3 Culmination of his research activity and its unexpected freezing out

In the turn of the years 1928/1929 Czochralski quite unexpectedly accepted the invitation of the Polish State President I. Mościcki, himself quite an eminent chemist, and as a consequence of it, he moved to Warsaw, where a Warsaw University of Technology professorship in chemistry had been presented to him with its positive reception. Since it was likely that Jan Czochralski had no matriculation exam passed, this was only formally possible after the university presented to him the prestigious title of honorary doctorate. In Warsaw he also refreshed effectively his interest in X-ray diffraction methods as applied to metal structure research. For his achievements while performing research in Warsaw, see Table 1 and Table 2.

4 Summary

Czochralski contributed extraordinarily, especially because of inventing the so fruitful method of crystallizing metals, turned in the 1950s by US researchers to growing germanium, and slightly thereafter, silicon crystals, to many aspects of, what we now call, applied physics and modern chemical technology as well as of materials science. To be specific, his theory of recrystallization, though being particularly (and first) proposed for *Sn*, still deserves great recognition. One may have in mind his recrystallization three-dimensional diagrams, wherein on the axes of the coordinate system invented by Czochralski one can find: mechanical characteristic displacement, average grain linear size, and finally, system's temperature [1–4].

In last word, it is to say that Czochralski's political attitude during World War II remained at as high as possible level, as it was also the case of his scientific practical accomplishments, Table 2. It has also been verified by thorough research over archival materials that his attitude was always remained as the most ethical and moral – other examples are just at hand [5].

References

[1] P. Tomaszewski, *Jan Czochralski. Restored.* (Oficyna Wydawnicza Atut, Wrocław, 2013).
[2] A. Gadomski, Europhys. News **35**, 20 (2004).
[3] A. Gadomski, Annals Philos. **61**, 137 (2013).
[4] J. Czochralski, *Moderne Metallkunde in Theorie und Praxis.* (Springer-Verlag, Berlin, 1924).
[5] J. Klos, J. Market Moral. **6**, 161 (2003).

Thermodynamic Properties of Two-Dimensional System of Small Magnets

Michal Géci[1], Martin Liščinský[2], and Mária Šviková[3]

[1]michal.geci@atlas.sk, Faculty of Electrical Engineering and Informatics, Technical University of Košice, Letná 9, 042 00 Košice, Slovakia

[2]martin.liscinsky@gmail.com, Faculty of Electrical Engineering and Informatics, Technical University of Košice, Letná 9, 042 00 Košice, Slovakia

[3]svikova@gmail.com, High school of st. Thomas Aquinas, Zbrojničná 3, 040 01 Košice, Slovakia

Abstract. In granular system (collection of macroscopic particles) the dissipative nature of grains means that any dynamical study requires energy injection, typically involving vibration or shear. An important feature of this class of systems is that the driving and dissipation mechanisms can be made to balance such that a steady state is achieved. Recent investigation of such non-equilibrium steady states has shown that connections with equilibrium statistical mechanics may provide a useful analogy. In our experiment we study system of 6 mm sized disc magnets moving on an air layer. Uniform steady – state motion is excited by air, blown into air table. Magnetic moments of the magnets in our experiment are oriented perpendicularly to the layer so that magnets repel each other by dipolar magnetic interaction. By changing the velocity of the air current blown to the air table we influenced effective temperature calculated through particle velocities. The movement of particles was recorded with a webcam and we created scripts in Matlab to analyze videos and to determine effective temperature, particle trajectories and velocity distribution.

1 Introduction

The formation of big arrays of ordered organic and inorganic building blocks is one of the most exciting fields in materials science and technology. The study of self-organization of particles is important for both fundamental research as in applications for example in the fabrication of nano-structured particle systems and in soft-matter physics which include colloids, liquid crystals, foams, granular materials and even biological tissues. In granular system (collection of macroscopic particles) the dissipative nature of grains means that any dynamical study requires energy injection, typically involving vibration or shear. An important feature of this class of systems is that the driving and dissipation mechanisms can be made to balance such that a steady state is achieved. Recent investigation of such non-equilibrium steady states has shown that connections with equilibrium statistical mechanics may provide a useful analogy. For example, one sphere on a turbulent air flow has been shown to exhibit equilibrium like dynamics with single effective temperature that holds at all timescales [1]. The mechanically driven granular systems composed of stainless steel spheres interacting through hard core [2] and Coulomb force [3] were developed for the study of 2D melting. Our experimental system belongs to the same class of the systems.

2 Experiment

We place 64 disc magnets (weight: 0.67 g, 6 mm in diameter and 1 mm high, NdFeB, N45) on plexiglas pad of an air table. Magnetic moments of the magnets are oriented perpendicularly to the layer. Magnets repel each other by dipolar magnetic interaction. Square magnetic edge with side of 22.3 cm magnetically repulses the discs. Magnets are moving freely on an air layer. We can influence their velocities by changing the flow rate of air blown to the air table (Figure 1).

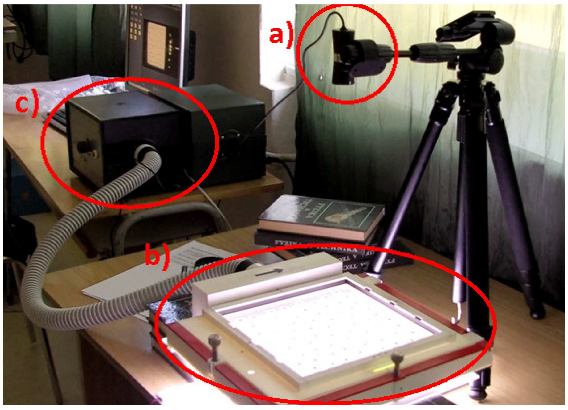

Figure 1. View of an experimental setup a) webcam b) air table with magnetic particles c) air blower.

We record the system with a webcam, with frame rate 30 fps. We trace trajectories of each magnet (particle) by analyzing video with our own program for particle tracking written in Matlab. This program compares each frame of a video with a background that is a screenshot of the system with erased particles. It load's parts of video and makes binary images of particles by computing differences between pixels in a video frame and the background. That means the image looks like a black rectangle with white areas, that are recognized as particles. Then the image is processed by filters to get rid of falsely recognized particles. The coordinates are then sorted and assigned to each particle. From these results we get two kinds of information: The first one is a position of every particle in the system. Using this information we can draw Delaunay triangulation, Voronoi diagram, trajectories of particles and pair correlation function. The second kind of information is the distance that particle travels between two frames. We can use this information to compute properties like velocity, mean square displacement and Maxwellian distribution.

3 Statistical analysis

The temperature T is directly related to the kinetic energy K by the well-known equipartition formula, assigning an average kinetic energy $k_B T/2$ per degree of freedom. For two dimensional system we have

$$K = N k_B T. \tag{1}$$

N is a number of particles, k_B is Boltzmann constant, m is mass of one particle, and v_i is the velocity of i^{th}-particle. We define effective temperature by equation:

$$\tau = \frac{2k_B}{m} T = \frac{\sum_{i=1}^{N} v_i^2}{N} \tag{2}$$

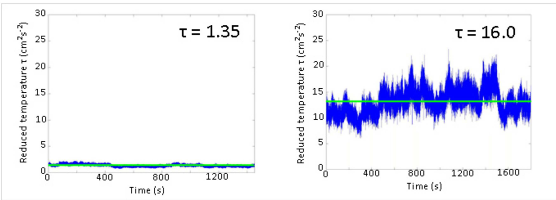

Figure 2. Fluctuations of temperature (y-axis) with time (x-axis) during constant air flow. The green line shows the mean value. Values of effective temperature τ are in $\mathrm{cm^2 s^{-2}}$.

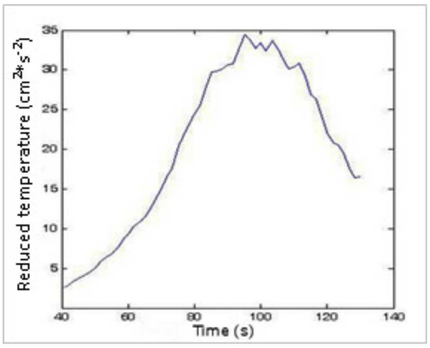

Figure 2. Dependence of reduced temperature with time during continuous increasing of velocity of air blowing.

We can influence effective temperature by changing the intensity of air current blown to the air table. In Figure 3 we can see the change of reduced temperature during continuous increasing of velocity of air blowing. The increase of reduced temperature with increasing air velocity is in agreement with [4] however in their work maximum was not observed.

Probability of particle having velocity v at given temperature is given by Maxwell-Boltzmann distribution [5]. For 2D system it is:

$$f = \frac{\mathrm{d}N}{N} \cdot \frac{1}{\mathrm{d}v} = \frac{m}{k_B T} \cdot e^{-\frac{mv^2}{2k_B T}} \cdot v \tag{3}$$

In Figure 3, on the histograms of velocity distribution we can see typical shift of the maximum to higher velocities with rising temperature. Histograms represent experimental results and red line is a theoretical curve computed using equation (3). Values of reduced temperature τ are in units $\mathbf{cm^2 s^{-2}}$. Nice agreement between experimental and theoretical values support the usefulness of the concept of effective temperature in our experimental system.

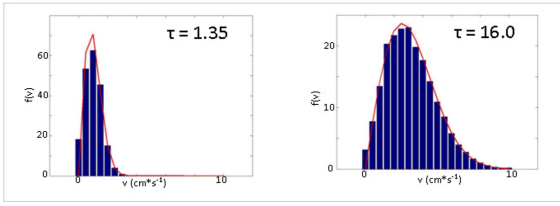

Figure 3. Maxwell-Boltzmann distribution.

4 Conclusion

In our experiment we study system of 6 mm sized disc magnets moving on an air layer. Uniform steady – state motion is excited by air, blown into air table. Magnetic moments of the magnets in our experiment are oriented perpendicularly to the layer so that magnets repel each other by dipolar magnetic interaction. By changing the velocity of the air current blown to the air table we influenced effective temperature calculated through particle velocities. The movement of particles was recorded with a webcam and we created scripts in Matlab to analyze videos and to determine effective temperature, particle trajectories and velocity distribution. Air driven granular systems were studied previously in several works[1, 4] with accent on the problem when and why driven systems exhibit equilibrium - like behavior. However neither air driven system with magnetic dipolar interactions nor melting behavior in air driven system were studied yet.

References

[1] R. P. Ojha, P. A. Lemieux, P. K. Dixon, A. J. Liu, D. J. Durian, Nature **427**, 521 (2004).
[2] P. M. Reis, R. A. Ingale, M.D. Shattuck, Phys. Rev. Lett. **96**, 258001 (2006).
[3] X. H. Zheng and R. Grieve, Phys. Rev. B. **73**, 064205 (2006).
[4] R. P. Ojha, A.R. Abate, D.J. Durian, Cond-mat **2**, 0406742 (2004).
[5] L. Landau, E. Lifshitz: *Statistical Physics*. 3. ed. (Pergamon Press, Oxford, 1980). ISBN 978-0-7506-3372-7.

The top-BESS vector resonance triplet confronted with the LHC measurements

Mikuláš Gintner[1,3] and Josef Juráň[2,3]

[1]gintner@fyzika.uniza.sk, Physics Dept., U. of Žilina, Žilina, Slovakia
[2]josef.juran@utef.cvut.cz, Physics Institute, Silesian U. in Opava, Opava, Czech Republic
[3]Institute of Experimental and Applied Physics, CTU in Prague, Prague, Czech Republic

Abstract. Recently we have formulated an effective Lagrangian desribing phenomenology of a hypothetical $SU(2)_{L+R}$ triplet of vector resonances originating from strongly-interacting scenarios of physics beyond the Standard model. We present the confrontation of the Lagrangian predictions with the findings of the LHC detectors obtained in the LHC run-1.

1 Introduction

In the light of the up-to-date LHC findings the models of strongly interacting electroweak (EW) symmetry breaking remain viable alternative for physics beyond the Standard model (SM). Composite degrees of freedom accompanying such strong scenarios can be effectively decribed by the formalism of the effective Lagrangians.

Recently we have formulated such an effective Lagrangian (nicknamed "the top-BESS model"[1]) describing a hypothetical $SU(2)_{L+R}$ triplet of vector resonances with specific direct couplings to the third quark generation [1]. Here, we present the experimental limits imposed on the Lagrangian's free parameters by the electroweak precision data and confront the top-BESS model predictions with the findings of the LHC detectors obtained in the LHC run-1.

2 Theory facing experiment

2.1 The top-BESS model sketch

The top-BESS model is an $SU(2)_L \times SU(2)_R \to SU(2)_{L+R}$ non-linear sigma model based effective Lagrangian aspiring to describe phenomenology of strongly broken electroweak symmetry. Beside the $SU(2)_L \times U(1)_Y$ gauge bosons and the three generations of fermions the model is augmented with the $SU(2)_{L+R}$ singlet scalar resonance standing for the newly discovered 125-GeV higgs-like boson.

The $SU(2)_{L+R}$ triplet of hypothetical vector resonances has been introduced in the model. The vector triplet has been brought in as gauge fields via the hidden local symmetry approach [2]. Thus far we have followed the BESS model formulated in 1980's by Casalbuoni *et al* [3]. Phenomenology of these resonances is what stays in the center of our investigation.

In the top-BESS model the vector resonance couples directly to the third quark generation only. The direct interactions are proportional to b_L (left fermions) and b_R (right fermions). The free parameter p can disentangle the right bottom coupling from the right top coupling. While $p = 1$ leaves both interactions equal, the $p = 0$ turns off the right bottom quark interaction completely and maximally breaks the $SU(2)_R$ part of the Lagrangian symmetry down to $U(1)_{R3}$. The symmetry of the Lagrangian admits non-SM interaction of the fermions with the EW gauge bosons that we include under the assumption that they apply to the third quark generation only. These interactions are proportional to the free parameters λ_L and λ_R.

In the unitary (physical) gauge the new physics part of the (t, b) Lagrangian assumes the form

$$\begin{aligned}\mathcal{L}^{\rm NP}_{(t,b)} &= ib_L\bar{\psi}_L(\not{V} - \not{W})\psi_L \\ &\quad +ib_R\bar{\psi}_R P(\not{V} - \not{B}^{R3})P\psi_R \\ &\quad +i\lambda_L\bar{\psi}_L(\not{W} - \not{B}^{R3})\psi_L \\ &\quad +i\lambda_R\bar{\psi}_R P(\not{W} - \not{B}^{R3})P\psi_R \qquad (1)\end{aligned}$$

where $\not{W}_\mu = ig\not{W}^a_\mu\tau^a$, $\not{B}^{R3} = ig'\not{B}\tau^3$, $\not{V}_\mu = i\frac{g''}{2}\not{V}^a_\mu\tau^a$, and $P = \mathrm{diag}(1, p)$, considering $0 \le p \le 1$.

The deviation of the Higgs to EW gauge bosons couplings from their SM values has been parameterized by the prefactor a. The same prefactor parameterizes the coupling of the Higgs boson to the vector triplet. In addition, the anomalousness of the Higgs-to-fermion couplings is parameterized by the prefactors c_i where i runs through the SM fermions doublets.

2.2 The present status of relevant observables

The direct LHC bottom limits on the vector resonance masses are strongly model dependent. The third quark generation partial compositeness admits the limits to be as low as 300 GeV. The most restrictive bottom limit of slightly below 1 TeV is obtained when no compositeness of the SM fermions is assumed [4].

The combination of the LHC data and the electroweak precision data from SLC, LEP-1, LEP-2, and the Tevatron restricts a to be within 10% of the SM value at 95%CL [5]. The combined ATLAS+CMS+TEVATRON data restrict the anomalous Higgs-to-top coupling prefactor to $0.82 \le c_t \le 1.22$ at 95%CL [6]. At a given value of a the experimental limits for other top-BESS free parameters g'', p, $\Delta L = b_L - 2\lambda_L$, and $\Delta R = b_R + 2\lambda_R$ can be derived

[1] It should be called "effective Lagrangian" rather than "model". It is to play a similar role with respect to some strong fundamental theory beyond the SM as the Chiral Perturbative Theory plays with respect to the QCD.

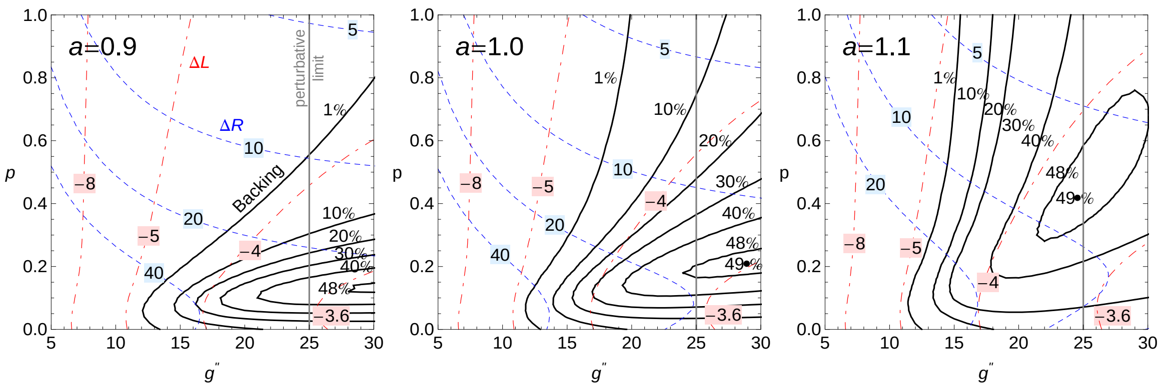

Figure 1. The best-fit values of ΔL (dot-dashed) and ΔR (dashed) and the iso-backing contours (solid) for the preselected values of g'', p, and a. Sensitivity to the Higgs-to-fermion couplings is negligible. The low-energy Lagrangian cut-off scale is $M_\rho \approx \Lambda = 1$ TeV. The naive perturbative upper limit in g'' is indicated by the vertical solid line.

by fitting the low-energy (pseudo)observables ϵ_1, ϵ_2, ϵ_3 [7], $\Gamma_b(Z \to b\bar{b})$ [8], and $\mathrm{BR}(B \to X_s\gamma)$ [9].

The decay $H \to \gamma\gamma$ is the loop level process in the SM. The dominant SM contributions to the process come from the $W^\pm$ and top quark loops and they tend to cancel each other. The cancellation strengthen the sensitivity of the decay to hypothetical BSM particles in the loop. The best-fit signal strength relative to the standard model prediction $\mu(H \to \gamma\gamma)$ is $1.14^{+0.26}_{-0.23}$ (CMS) [10] and 1.17 ± 0.27 (ATLAS) [11].

2.3 Results and conclusions

The best fits of the top-BESS model parameters based on fitting ϵ_1, ϵ_2, ϵ_3, $\Gamma_b(Z \to b\bar{b})$, and $\mathrm{BR}(B \to X_s\gamma)$ for three various values of a are depicted in Figure 1. The best-fit value of p found in our analysis seems to support the assumption of some models of partial fermion compositeness that the new strong physics resonances couple stronger to the right top quark than to the right bottom quark.

Assuming negligible effect of the top-BESS on the Higgs production cross sections and on the total Higgs widths the relative $\gamma\gamma$ signal strength can be expressed in terms of the $H \to \gamma\gamma$ decay widths

$$\mu(H \to \gamma\gamma)_{\mathrm{tBESS}} \approx \Gamma/\Gamma_{\mathrm{SM}}(h \to \gamma\gamma)$$
$$\approx \left[1 - \frac{2}{7}(c_t - 1) + \frac{9}{7}(a-1) + \frac{9}{8}a\right]^2, \qquad (2)$$

where the first and second terms after unit represent contributions from the anomalous couplings of the Higgs to the top quark and to the EW gauge bosons, respectively ($c_t^{\mathrm{SM}} = a^{\mathrm{SM}} = 1$). The last term is the contribution from the interaction of the Higgs with the vector resonance triplet assuming the same coupling prefactor a as for the EW gauge bosons.

The most recent LHC data on $\mu(H \to \gamma\gamma)$ disfavors the top-BESS model in its presented setup; e.g., if $c_t = a = 1$ then $\mu(H \to \gamma\gamma)_{\mathrm{tBESS}} = 4.52$. Nevertheless, this setup could be viewed as simplistic. For example, the interactions of the Higgs boson to the electroweak gauge bosons could be disentangled from its interaction to the vector resonance. It would modify (2) so that the current experimental limit could be satisfied. In more complex/realistic scenarios, resonances of different kinds and more general coupling patterns can be introduced. This is the subject of our further investigation.

References

[1] M. Gintner and J. Juran, Eur. Phys. J. C **73**, 2577 (2013); M. Gintner, J. Juran and I. Melo, Phys. Rev. D **84**, 035013 (2011).

[2] M. Bando, T. Kugo and K. Yamawaki, Phys. Rept. **164**, 217 (1988).

[3] R. Casalbuoni, S. De Curtis, D. Dominici and R. Gatto, Phys. Lett. B **155**, 95 (1985); Nucl. Phys. B **282**, 235 (1987).

[4] B. Bellazzini, C. Csaki, J. Hubisz, J. Serra and J. Terning, JHEP **1211**, 003 (2012).

[5] A. Falkowski, F. Riva and A. Urbano, JHEP **1311**, 111 (2013); K. Cheung, J. S. Lee and P. Y. Tseng, arXiv:1407.8236 [hep-ph].

[6] J. Bernon, B. Dumont, S. Kraml, arXiv:1409.1588 [hep-ph].

[7] S. Schael *et al.*, Phys. Rept. **427**, 257 (2006).

[8] K. Nakamura *et al.* (Particle Data Group Collaboration), J. Phys. G **37**, 075021 (2010).

[9] Y. Amhis *et al.* (Heavy Flavor Averaging Group Collaboration), arXiv:1207.1158 [hep-ex].

[10] V. Khachatryan *et al.* (CMS Collaboration), arXiv:1407.0558 [hep-ex].

[11] G. Aad *et al.* (ATLAS Collaboration), arXiv:1408.7084 [hep-ex].

Barriers of using models and modelling in medical biophysics education

Viera Haverlíková[1] and Ivan Haverlík[2]

[1]viera.haverlikova@fmed.uniba.sk, Faculty of medicine, Comenius University, Sasinkova 2, 813 72 Bratislava, Slovak Republic

[2]haverlik@fmph.uniba.sk, Faculty of mathematics, physics and informatics, Comenius University, Mlynská dolina, 842 48 Bratislava, Slovak Republic

Abstract. Using models and modelling in medical biophysics education play increasingly important role. The paper presents results of two pilot research studies realised in the frame of project KEGA 020UK-4/2014 "Innovation in the content, forms and methods of practical exercises of Biophysics and Medical Biophysics to the study of Medicine and Biomedical Physics". The research realised with first-year medical students was focused on students' conceptions about models and using electric circuit to model blood circulation. Results show that most students think of models as physical copies of reality, not as conceptual representations. This makes using of educational models ineffective, if there is none or low visual similarity with investigated phenomena. Understanding the theory of modelling was examined in survey realised with first-year-master-degree students of biomedical physics. One-third of respondents demonstrated serious misunderstanding of modelling principles and misunderstanding of relationship between original and model in science.

1 Introduction

The role of models and simulation in medical education extremely increased in recent two decades. Three-dimensional models, screen-based simulations, interactive patient simulators and high-fidelity mannequins are even more frequently used in training of clinical skills and team communication, due their safety for patients, repetitive utilisation, and financial effectiveness. These models and simulations can help students to develop the ability to recognise their own limitations and knowledge gaps.

Furthermore Evidence-Based Medicine assumes that students understand the process of scientific research and the process of building the knowledge. And these processes are inseparably connected with models and modelling.

The necessity to develop understanding of models and modelling among medical students and students of biomedical physics inspired our research.

2 Goal

The general goal of realised research was to innovate the content, forms and methods of practical exercises of Biophysics and Medical Biophysics to the study of Medicine and Biomedical Physics. Specific goal of presented research was to identify student's most common barriers of using models and modelling and develop educational activities that can overcome such barriers.

3 Background – student's common misconception about modelling

Upper secondary students typically understand models as physical copies of reality, not as conceptual representations. They do not have idea that the usefulness of a model can be tested by comparing its implications to actual observations of real phenomena/system.

Many students do not accept the explanatory role of models, if the model shares only its abstract form with the phenomenon. They accept this role more willingly, if many of the material features are the same for the model and the real phenomenon [1].

Some upper secondary students think that everything they learn in science classes is factual. They are not able to distinguish observation of real phenomena and model.

4 Research among medical students

4.1 Sample

The research was realised among 1st year medical students studied general medicine at the Faculty of medicine, Comenius University in Bratislava in academic year 2013/2014. In all phases of research 29 students were involved (23 Female, 6 Male). All of them graduated at general upper secondary schools, none of them graduated in physics.

4.2 Methods

The research had four phases:

- Short introductory discussion.
- Anonymous written questionnaire with closed questions, where students had to choose one of 3 alternative answers. This questionnaire was administered at the very beginning of practical training in biophysics.
- Short interview and observation of students' activity in the 5th week of semester, when students realised the task: Blood redistribution model [2].
- Analysis of student's measurement protocols.

4.3 Results

In introductory discussion all students stated that they understand the concept of model and modelling (as well as concepts physical theory and experiment).

The questionnaire showed that more than 70% misunderstood the term model (Table 1):

Statement	Number of students
model is smaller size copy of reality	1
model must be visually similar to reality	20
model means simplification of reality, visual similarity is not necessary	8

Table 1. Students' conceptions about model

Students interviewed at the beginning of practical training focused on blood redistribution model [2] manifested their ongoing misunderstanding. Only two students were able to explain principles of the blood redistribution model, the analogy between hydrodynamic blood circulation system and the electric circuit. Observation of students' activity showed that 3 more students were able to follow step-by-step instruction to measure the task. All the others students (24) didn't understand the task at all and looked for a copy of reality, e.g.: "But, where does the blood flow?" They do not understand model as conceptual representation.

Subsequent analysis of measurement protocols showed, that students are not used to think about particular conditions of measurement. Barrier of unsufficient knowledge in mathematics and limited experience with graphs influenced students' ability to evaluate and interpret data as well as formulate a conclusion.

5 Research among biomedical-physics-students

Biomedical physicists have to be able not only to use different types of models and simulation and understand them, but also create new models at different level of complexity in order to create new knowledge.

5.1 Sample

Students in 1st year master degree study of biomedical physics at the Faculty of mathematics, physics and informatics, Comenius University in Bratislava in academic years 2007/08 – 2009/10 took part in the research. Totally 26 students were involved.

5.2 Methods

Written test used for examination in compulsory subject Mathematical modelling of biosystems was used as a as a research tool. In the test students had to decide whether the given statement is true or false.

Totally 60 tests collected in regular examination, 1st and 2nd re-examination were quantitatively analysed.

5.3 Results

In four variants of question focused on understanding black boxes method, students scored 20%. In four variants of question focused on modelling of conditioned and unconditioned reflex students scored 70%.

Students obviously do not understand modelling methodology, but they are able to consider models of concrete phenomena.

6 Conclusions and suggestions

Research results showed that most of medical students do not understand the value of modelling in learning and role of modelling in creating a new knowledge. Most of medical-biophysics students reached the level of concrete operational stage in cognitive development with regard of modelling methodology.

understanding of models and modelling we suggest the systematic using of models in biophysics education from the very beginning. It seems to be extremely important to us wide variety of models (concrete, visual, verbal, mathematical, mental/qualitative, quantitative/static, dynamic) and develop new forms of education focused on modelling and its role in science (e.g. activity "Black boxes investigation" focused on the process of building a scientific knowledge [3]).

Acknowledgement

This work was supported by KEGA 020UK-4/2014 "Innovation in the content, forms and methods of practical exercises of Biophysics and Medical Biophysics to the study of Medicine and Biomedical Physics".

References

[1] PROJECT 2061 - Benchmarks, [online], American Association for the Advancement of Science [quoted 2014-08-13], `http://www.project2061.org/publications/bsl/online/index.php`.

[2] K. Kozlíková, J. Martinka, *Theory and Tasks for Practicals on Medical Biophysics* (Tribun EU, Brno, 2010), pp 115-116, 197-199.

[3] V. Haverlíková, I. Haverlík, Student's argumentation in black boxes' investigations, In: 19th Conference of Slovak Physicists Proceedings. Košice: Slovak Physical Society, 2013. pp. 73-74

Development of children's modelling skills through non-formal activities

Viera Haverlíková[1,2]

[1] haverlikova@scholaludus.sk, SCHOLA LUDUS, FMFI UK, Mlynská dolina, 842 48 Bratislava, Slovak Republic
[2] viera.haverlikova@fmed.uniba.sk, Faculty of medicine, Comenius University, Sasinkova 2, 813 72 Bratislava, Slovak Republic

Abstract. Modelling is recognised as one of basic scientific skills. Its development is declared as a part of education already at primary schools. Nevertheless pedagogical researches showed serious misunderstanding of modelling among pupils and students of all ages. New forms and methods enhancing modelling skills were developed during more than twenty years of non-formal educational project SCHOLA LUDUS. The paper presents briefly educational game and creative-discovery workshop – new forms of activities developed and proved within the frame of summer camps SCHOLA LUDUS: Experimentáreň that is designed to children aged 9 to 15.

1 Introduction

Models are essential in production, dissemination and acceptance of scientific knowledge. In education, models help to build a bridge between the scientific theory and experience. State curriculum declares modelling skills as one of specific competencies developed not only in physics, but in science education since primary level.

Nevertheless pedagogical researches showed serious misunderstanding of modelling among pupils and students of all ages. Children often cannot recognize, when they work with model and when they work with physical reality, in what condition is the model valid, what are limits of models' application [1, 2]. Development of modelling skills through traditional formal education seems to be quite limited. May be the non-formal education helpful in this context?

2 Non-formal education and the SCHOLA LUDUS Project

Non-formal education has no rigorous definition. In general it means education, which primary goal is not getting a certificate, diploma, or higher qualification. Its goal is gratification by knowing and achievement of internal demands. Non-formal education is based on voluntariness and self-confidence. Originally it was developed out of school. In recent years non-formal education becomes an integral part of life-long education and a complement of formal (school-) education. It is open, flexible and creative. Moreover non-formal education seems to be an important source of innovations in formal education.

The SCHOLA LUDUS project develops since 1992 various forms of non-formal education:
– exhibitions,
– creative-discovery workshops,
– educational games,
– science theatres,
– competitions,
– summer camps, etc.

Since 1992 SCHOLA LLUDUS develops annually physics summer camp for 9 – 15 years old children. The program of the summer camp is focused on different topics year after year (e.g. sound, energy, balloons, paper, food, human body), but the main goals persist: to inspire children, motivate and stimulate their interest in science, encourage inquiry and develop cognitive skills, creativity, and communication skills of participants. Modelling is considered as an essential part of achieving these goals.

3 Modelling in SCHOLA LUDUS

Modelling in SCHOLA LUDUS summer camps is initiated by observing daily life, natural phenomena and / or real objects that provide the key case. Parallel method is used to draw attention to various aspects of investigated phenomena and to look for similarities and differences.

Educational game is an example of developed innovative educational methods that support understanding the role of modelling. For example in the game "The driver", participants observe and investigate offered models (prepared by educator) and use them in order to find answers to given questions [3]. Context familiar to the pupil's experience and interests, challenging tasks and alert on player's misconceptions and discrepancies encourage cognitive progress of participants. But using models in educational games is mainly unconscious without educator's intervention.

To support children's intentional modelling, an original interactive science theatre „Einstein's dream and jumping cows" was created [4]. Approach used in the theatre was later developed into the SCHOLA LUDUS pro-science theory of teaching and learning [5].

The SCHOLA LUDUS pro-science theory of teaching and learning is based on authentic pedagogy, thinking-based learning and cognitive constructivism. Its unit is a teaching and learning cycle consisting of 7 stages:

1. Action – first experience,
2. Describing – description of observed process / system,
3. Mapping – finding different aspects, classification of features,

4. Modelling – building up functional models,
5. Abstracting – definition of general concepts, laws,
6. Embedding – definition of the acquired conceptual change and novelty,
7. Valuation - using knowledge in new context, acquire awareness of its utility.

Above mentioned teaching and learning cycle is applied in Creative-discovery workshops (CDW) - an innovative teaching method developed initially for non-formal education, but already proved also in school education.

Besides several creative-discovery workshops developed in SCHOLA LUDUS Summer camps, where modelling is an integral part of the workshop (e.g. workshop "Water suction" in Paper physics or "Measurement of atmospheric pressure" in Meteorology), also some particular workshops focused directly on development of modelling skills were developed (e.g. "Modelling the sound propagation" [6] or "Modelling joints in human body").

3.1 Creative-discovery workshop "Modelling joints in human body"

The workshop was originally developed for the summer camp SCHOLA LUDUS: Experimentáreň 2014 focused on physics in human body.

Action – first experience is provided by a game "Human body alphabet", where children use their own bodies to write different words. Afterwards children utilise this experience in describing of possible movements of different parts of human skeleton. In next step children create a list (map) of different characteristics of bones connections with help of human body pictures and schemas. The core of the creative-discovery workshop is focused on modelling – creating 3D models of the chosen joint. In the stage abstracting children try to formulate knowledge - basic types of joints in human body. Embedding and Appreciation is realised by creating an „artificial hand" (each group can manufacture one part of the hand – fingers, elbow, shoulder – Figures 1 and 2).

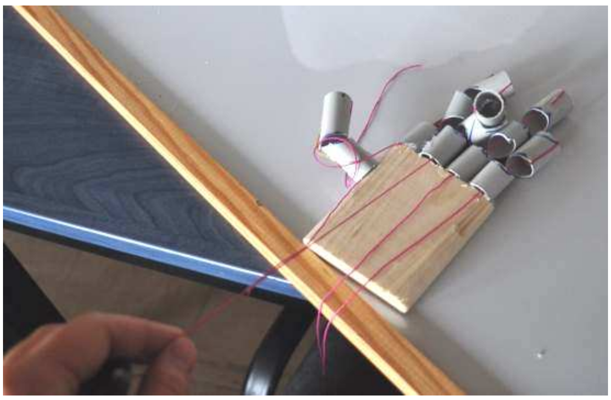

Figure 1. Model of fingers made by 14-years old children.

Figure 2. Model of shoulder joint made by 13-years old boys.

4 Conclusion

We consider developing of modelling skills as extremely important in science education. Realisation of above mentioned non-formal activities showed that children are interested in modelling. They like to create their own models, but they have only very limited experience with modelling from their daily lives. This limited experience creates a significant barrier in learning modelling and using models in learning process.

References

[1] PROJECT 2061 – Benchmarks, [online], American Association for the Advancement of Science [quoted 2014-08-13], http://www.project2061.org/publications/bsl/online/index.php.

[2] V. Haverlíková, I. Haverlík, Barriers of using models and modelling in medical biophysics education. In: *18th Conference of Czech and Slovak Physicists* (Olomouc, September 16–19, 2014), p. 41.

[3] V. Biznárová. Educational games in physics. In: *Informal Learning and Public Understanding of Physics* (Ljubljana: University of Ljubljana, 2006), pp. 108–114.

[4] I. Bazovský Observer's, Dilemma – examples from kinematics (*14th Conference of Slovak Physicists*, 2004).

[5] K. Teplanová, SCHOLA LUDUS theory of teaching and learning. In: *17th Conference of Slovak Physicists* (Bratislava: Slovak Physical Society, 2009, ISBN 978-80-969124-7-6), pp. 93–94.

[6] V. Haverlíková, M. Hodosyová, SCHOLA LUDUS creative-discovery workshop in formal and non-formal education. In: *17th Conference of Slovak Physicists* (Bratislava: Slovak Physical Society, 2009, ISBN 978-80-969124-7-6), pp. 99–100.

The frequency dependence of the impedance caused by a single domain wall displacement in cylindrical magnetic wire

M. Kladivová[1], J. Ziman[2], and V. Šuhajová[3]

[1] Maria.Kladivova@tuke.sk, Department of Physics, Technical University of Košice, Letná 9, 042 00 Košice, Slovakia
[2] Jan.Ziman@tuke.sk
[3] Viktoria.Suhajova@tuke.sk

Abstract. A study of a single magnetic domain wall contribution to impedance due to its motion for intermediate frequency region (100 kHz – a few MHz) is presented for a domain wall between circular domains. A simple theoretical model of the wall trapped in a quadratic potential well, for which possible influence of skin effect is tested using the model with scalar permeability, is proposed. It follows from this model that the frequency dependence of a domain wall contribution to the impedance exhibits a single maximum for the frequency of an AC current equal to the natural frequency of the domain wall moving in a quadratic potential well.

1 Introduction

Giant magneto-impedance (GMI) effect in Co-based amorphous cylindrical wires has been subject of many studies and it has already found place in many technical applications [1]. In present work, results of the study of magnetic domain walls contribution to the impedance due to its motion for intermediate frequency region (100 kHz – few MHz) are presented for a single domain wall (DW) between circular domains. Characteristic frequency dependence of domain wall contribution to the impedance with a single maximum has been observed experimentally in amorphous $Co_{68.2}Fe_{4.3}Si_{12.5}B_{15}$ wire with nominal diameter of 125 µm for two cases [2]. New experimental evidence and a simple theoretical model for interpretation of the observed characteristic frequency dependence is presented in this paper.

2 Experimental

Amorphous low-magnetostrictive ferromagnetic $Co_{68.2}Fe_{4.3}Si_{12.5}B_{15}$ wire with nominal diameter of 125 µm, prepared using the in-rotating-water-quenching technique, was used for the measurements.

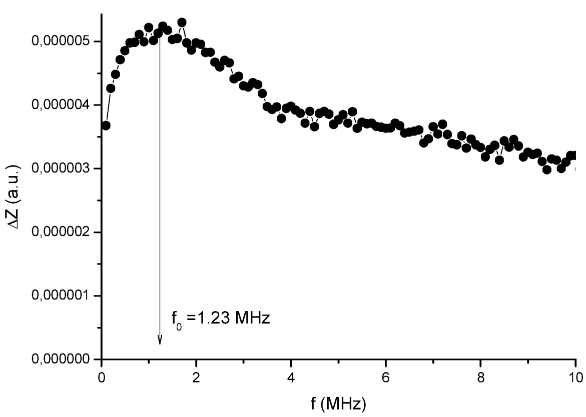

Figure 1. Experimental dependence of impedance due to the wall motion vs. frequency of ac current.

The measurements were carried out on a sample which was current (0.7 A for 3 minutes) annealed with simultaneous application of tensile stress (367 MPa). Influence of torsion stress during treatment was minimized. In this way a well-defined circular anisotropy was induced. A single domain wall could be created and manipulated in a similar way as in [3]. The difference ΔZ between impedance of a part of the wire when DW was present and impedance after DW displacement from this part of the wire for different frequencies is shown in Figure 1. As can be seen a single maximum is observed at frequency of 1.23 MHz.

3 Theoretical model

We consider a cylindrical ferromagnetic wire with circular anisotropy and domain structure consisting of two domains separated by a single DW (see Figure 2). AC current I with angular frequency Ω

$$I = I_0 \mathrm{e}^{-\mathrm{i}\Omega t} \tag{1}$$

is flowing through the wire.

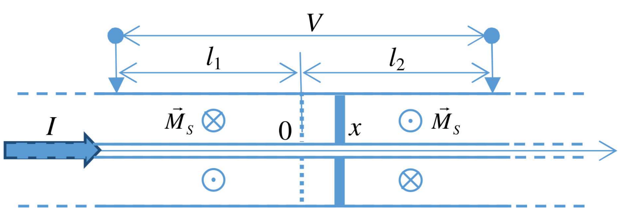

Figure 2. Model of domain structure with a single domain wall between circular domains in a cylindrical magnetic wire. Wall displacement x caused by current I is indicated. The wall is located close to the centre of the region along which voltage V is measured.

Domain wall is located approximately in the middle of the part of the wire $l_1 \approx l_2$ along which voltage V is measured. Equation of motion of the wall can be expressed as follows

$$m\frac{\mathrm{d}^2x}{\mathrm{d}t^2} + \beta\frac{\mathrm{d}x}{\mathrm{d}t} + kx = 2\mu_0 M_S \frac{R}{3} I \,\mathrm{P}\,(R,\delta) \tag{2}$$

where β is damping coefficient, k restoring force coefficient, m is inertial mass of the wall, R is radius of the wire, M_S is saturation magnetization and $\mathrm{P}(R,\delta)$ is a parameter which modifies net force acting on the wall due to skin effect characterized by skin depth δ.

The solution of this equation is well known. The wall oscillates with angular frequency Ω

$$x = A\mathrm{e}^{-\mathrm{i}(\Omega t+\alpha)} \tag{3}$$

and amplitude A of oscillations is given by formula

$$A = h\frac{f(\Omega)}{\Omega}, \qquad f(\Omega) = \frac{\Omega}{\sqrt{(\omega_0^2-\Omega^2)+4b^2\Omega^2}} \tag{4}$$

and

$$2b = \frac{\beta}{m},\ \omega_0^2 = \frac{k}{m},\ h = \frac{2\mu_0 M_S R\mathrm{P}(R,\delta)}{3m} I_0. \tag{5}$$

The voltage induced due to wall oscillations can be calculated using Faraday's law

$$V = -\frac{\mathrm{d}\Phi_\varphi}{\mathrm{d}t}, \tag{6}$$

where Φ_φ is circular magnetic flux. For situation in Figure 2 and for uniform circular component of magnetization $\Phi_\varphi = M_S$ circular magnetic flux is given by formula

$$\Phi_\varphi = \frac{2\mu_0 M_S}{3}R\,x + \frac{\mu_0 M_S}{3}R\ (l_1 - l_2)\,. \tag{7}$$

Voltage induced due to wall oscillations can be now expressed as

$$V = V_0\mathrm{i}\mathrm{e}^{-\mathrm{i}(\Omega t+\alpha)}, \qquad V_0 = A\Omega\frac{2\mu_0 M_S}{3}R \tag{8}$$

Combining Eqs. (4), (5), (6) and (10) the wire impedance can be expressed as

$$Z = \frac{V_0}{I_0} = \frac{4(\mu_0 M_S)^2 R^2}{9m}\mathrm{P}(R,\delta)\,f(\Omega) \tag{9}$$

The function $f(\Omega)$ has a maximum for $\Omega = \omega_0$.

Possible influence of skin effect (represented by parameter $\mathrm{P}(R,\ \delta)$) can be tested using simplest approach with scalar permeability μ. In the framework of this approach parameter P can be expressed as

$$\mathrm{P}(R,\delta) = \frac{3}{R^2 J_1(\kappa R)}\int_0^R r J_1(\kappa r)\,\mathrm{d}r \tag{10}$$

where J_1 is Bessel function of first order, parameter

$$\kappa = \left(\frac{1+i}{\delta}\right), \qquad \delta = \sqrt{\frac{2\rho}{\Omega\mu}}$$

and ρ is resistivity, for our sample it is $1.28\times10^{-6}\ \Omega$m. Frequency dependences of magnitude of parameter P calculated using (10) with relative circular permeability $\mu_{\varphi r}$ as a parameter are shown in Figure 3. It can be seen that for relative permeability up to 10 the magnitude of P is close to 1 and even for relative permeability of 100, the skin effect only slightly influences net force acting on the wall for frequencies lower than 3 MHz. It can be expected that relative circular permeability is very low for our sample with well-defined circular anisotropy. Finally we can conclude that experimental dependence of the domain wall contribution to the impedance ΔZ with a single maximum in Figure 1 can be explained by presented model. Moreover parameter ω_0 can be determined from this dependence.

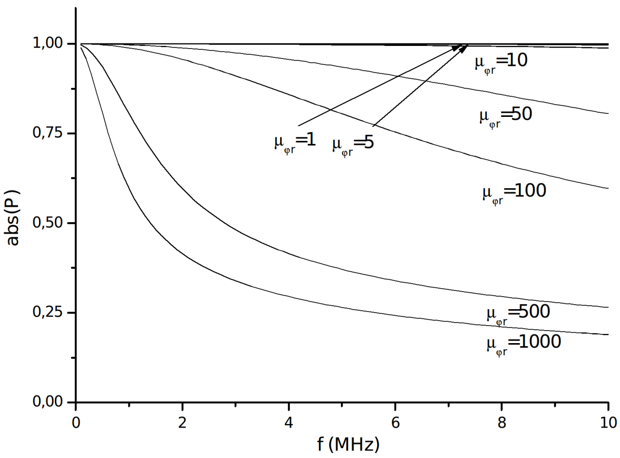

Figure 3. Magnitude of P as a function of current frequency with relative circular permeability $\mu_{\varphi r}$ as a parameter.

4 Acknowledgment

This research was supported by the Slovak Research and Development Agency under contract No. APVV-0027-11 and also by VEGA grant No. 1/0778/12 of the Scientific grant agency of the Ministry of Education of the Slovak Republic.

References

[1] M. Knobel, M. Vázquez, L. Kraus, Handbook of Magnetic Materials **15**, 497 (2003).

[2] J. Ziman, V. Šuhajová, M. Kladivová, sent for publication.

[3] J. Ziman, M. Kladivová, B. Zagyi, J. Magn. Magn. Mater. **234**, 529 (2001).

Influence of Heat Treatment on Magnetic Properties of Amorphous Ferromagnetic $Fe_{40}Ni_{38}Mo_4B_{18}$ Microwires

Eva Komová[1], Filip Šidík[2], and Rastislav Varga[3]

[1]eva.komova@tuke.sk, Department of Aerodynamics and Simulations, Faculty of Aeronautics, Technical University Košice, Rampova 7, 041 54 Košice, Slovakia
[2]filip.sidik@gmail.com, Department of Aerodynamics and Simulations, Faculty of Aeronautics, Technical University Košice, Rampova 7, 041 54 Košice, Slovakia
[3]rastislav.varga@upjs.sk, Institute of Physics, Faculty of Sciences, P. J. Safarik University, Park Angelinum 9, 041 54 Košice, Slovakia

Abstract. The evolution of the structure of the annealed amorphous ferromagnetic $Fe_{40}Ni_{38}Mo_4B_{16}$microwires and its interplay with magnetism has been studied. Nanocrystalline $Fe_{40}Ni_{38}Mo_4B_{16}$microwires were obtained from amorphous precursors after heat treatment at 700 K. Their structure consists of γ-(Fe, Ni) nanocrystals, having diameter of about 10 nm, embedded in residual amorphous matrix. It has been shown that nanocrystalline microwires exhibit much higher stability and very good soft magnetic properties. This can be used in many applications like magnetic sensors of temperature, mechanical stresses, magnetic field, etc.

1 Introduction

Amorphous glass-coated microwires with about 10 μm in diameter represent a novel technological family of metallic materials. Great variety of the chemical composition, sizes and geometric rations (radius of the metallic nucleus relative to the glass coating thickness) provides a wide range of interesting magnetic properties useful in the number of industrial and engineering applications. However, the crucial parameter for their application is the time and temperature stability. The solution can be found in nanocrystalline microwires prepared by the heat treatment from amorphous precursors which exhibit much higher stability and very good soft magnetic properties.

One possible option is the nanocrystalline $Fe_{40}Ni_{38}Mo_4B_{18}$ alloy, which is a new nanocrystalline soft magnetic material and exhibits positive magnetostriction. The nanostructured $Fe_{40}Ni_{38}Mo_4B_{18}$ specimens, obtained by annealing of the amorphous alloy in the temperature range from 650 K to 1060 K have a microstructure of a γ-(Fe, Ni) crystallites with average grain size 10 nm embedded in a residual amorphous matrix [1]. Such alloy in ribbon shape is an object for GMI study, too [2]. In this article we investigate the influence of Joule-heating and crystallization on the GMI effect in $Fe_{40}Ni_{38}Mo_4B_{18}$ wires.

2 Experiment and discussion

Object of our study were microwires of nominal composition $Fe_{40}Ni_{38}Mo_4B_{16}$ (total diameter of 12 µm) with positive magnetostriction, obtained by Taylor-Ulitovsky technique. Amorphous structure is thermodynamically metastable. Thermal annealing of amorphous materials is a suitable method for their transformation to new nanocrystalline state with the remarkable structural and magnetic properties.

The nanocrystalline structure consists of grains, size of several nanometers, embedded in a residual amorphous matrix. Microstructure of the annealed microwires of given composition was studied by high-energy x-ray diffraction. It has been confirmed that originally amorphous alloy partially crystallizes at $T_a > 620\,K$, where γ-(Fe, Ni) grains of size up to 10 nm are created [1].

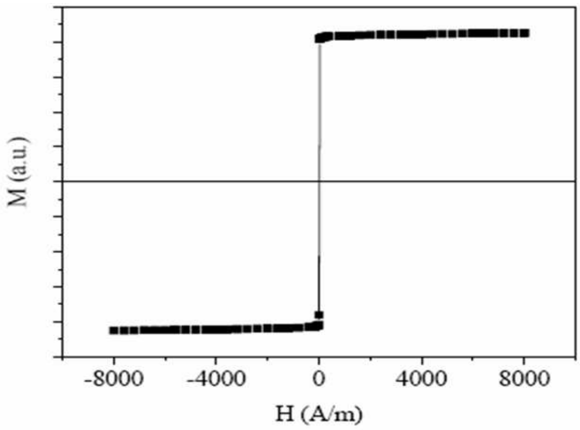

Figure 1. Hysteresis loop of the nanocrystalline $Fe_{40}Ni_{38}Mo_4B_{18}$ microwire annealed at 700 K.

Microwires with positive magnetostriction exhibit bistable magnetic behaviour which is characterized by a single giant Barkhausen jump at a remagnetizing switching field H_{sw} [3]. It gives rise to square hysteresis loop. Figure 1 shows the perfect rectangular hysteresis loop measured after nanocrystallization of $Fe_{40}Ni_{38}Mo_4B_{16}$ microwire at the room temperature. Bistability is kept in the nanocrystalline state.

We have studied the influence of the thermal treatment on the stress dependence of the switching field during the devitrification of amorphous $Fe_{40}Ni_{38}Mo_4B_{16}$ microwires. The stress dependence can be explained considering the magnetoelastic contribution to the switching mechanism which is modified applying the tensile stresses and changing the magnetostriction constant through thermal treatments [4]. We show that by adequate treatment of the sample, it is possible to vary the stress sensitivity of the sample. As-cast sample shows strong dependence of the switching field on the applied stress σ (Figure 2). During the annealing of the microwires at low temperatures, the stresses created in their production are released, what results in the decrease of the switching field and its stress dependence. On the other hand, the nanocrystalline microwire, annealed at the temperatures from 650 K to 700 K, shows no stress dependence of the switching field, what is probably caused by very low magnetostriction.

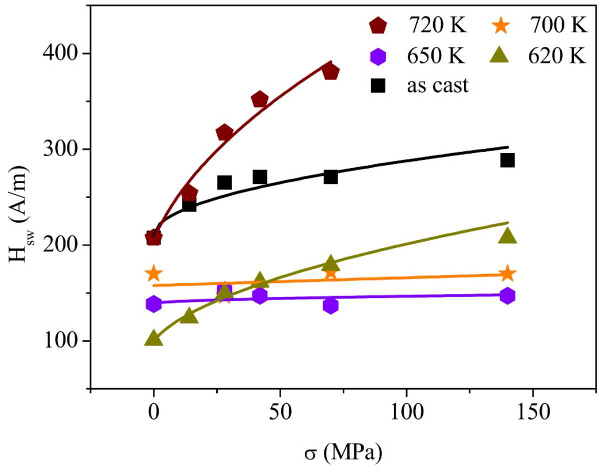

Figure 2. Stress dependence of the switching field H_{sw} after different thermal treatments.

The microwires with vanishing negative magnetostriction, together with its circumferential domain structure, are ideal for sensor applications based on the GMI effect [5].

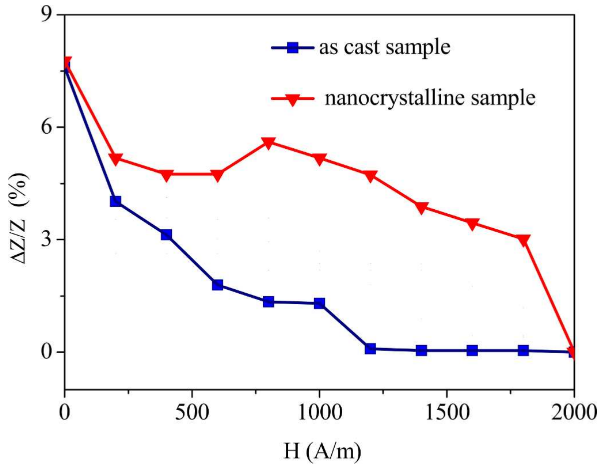

Figure 3. Relative impedance $\Delta Z/Z$(H) of the as cast and nanocrystalline $Fe_{40}Ni_{38}Mo_4B_{16}$ microwire.

A recent investigation has shown that, by lightly annealing the amorphous wires with positive magnetostriction, the radial domain structure weakens, and gives way to a circumferential domain structure; this is due to surface crystallization. This leads to an increase in the GMI effect [6]. These results motivated us to explore the GMI in annealed $Fe_{40}Ni_{38}Mo_4B_{18}$ microwires (Figure 3). The relative impedance $\Delta Z/Z$ for the as cast wire is small and decreases quickly achieving maximum of about 7.60 %. In order to achieve the nanocrystalline state, the wires were submitted to heat treatment by using a current annealing technique (over 18 mA for 10 min). The variation of GMI value indicates the structural transformation and change of magnetic behaviour in $Fe_{40}Ni_{38}Mo_4B_{18}$ alloy after thermal treatment. The nanocrystallization after Joule-heating at the DC current of 19.5 mA has resulted in a small increase of relative impedance but its value of 7.77 % is comparable to that of the as-cast sample. This effect is probably related to the magnetostriction decrease during the first stage of the crystallization.

3 Conclusion

The $Fe_{40}Ni_{38}Mo_4B_{16}$microwires exhibit bistability even in the nanocrystalline state.

At low annealing temperatures, the strong switching field dependence on the stress can be obtained, which is useful for stress sensing elements. Close to the optimal annealing temperature (700 K), no stress dependence of the switching field was detected. Such behavior is useful for the different sensing elements (temperature, current), which must not be stress sensitive.

GMI magnetic field dependence can be modified by the heat treatment only slightly.

4 Acknowledgement

This work was supported by Slovak VEGA grants No.1/0060/12, APVV-0027-11 and APVV-0266-10.

References

[1] E. Komová, M. Varga, R. Varga, P. Vojtaník, J. Bednarčík, J. Kováč, M. Provencio, M. Vázquez, *Appl. Phys. Lett.* **93**, 062502 (2008).

[2] P. Jantaratana, S. Pasuksan, *Kasetsart Journal* (Nat. Sci.) **43**, 205-209 (2009).

[3] P. Manh-Huong, P. Hua Xin, *Progress in Materials Science* **53,** 323-420 (2008).

[4] E. Komová, M. Varga, R. Varga, P. Vojtaník, J. Torrejon, M. Provencio, M. Vázquez, *Acta Physica Polonica A* **113**, 135 (2008).

[5] A. Zhukov, M. Ipatov, A. Talaat, V. Zhukova, C. Garcia, *Journal of the Korean Physical Society* **62**, 1382-1387 (2013).

[6] N. A. Usov, A. S. Antonov, A. N. Lagarkov, *JMMM* **185**, 159-173 (1998).

Study of azimuthal anisotropy of hadron production via Monte Carlo simulation

Renata Kopečná[1] and Boris Tomášik[1,2]

[1]kopecren@fjfi.cvut.cz, FNSPE, Czech Technical University in Prague, Břehová 7, 115 19 Praha 1, Czech Republic
[2]boris.tomasik@umb.sk, Univerzita Mateja Bela, Tajovského 40, 974 01 Banská Bystrica, Slovakia

Abstract. The quark-gluon plasma (QGP) is very hot and dense form of matter, where quarks and gluons are deconfined. It can be produced in high-energy nuclear collisions, studied at facilities such as Relativistic Heavy Ion-Collider (RHIC) or Large Hadron Collider (LHC). Important means in the studies of QGP properties are anisotropies of the transverse collective flow of hot fireball. They show up via anisotropies of hadron momentum distributions. We present simple Monte Carlo toy model which generates hadron distributions with azimuthal anisotropy. It is used in designing and testing analysis tools for the anisotropy coefficients.

1 Introduction

Initial conditions in heavy-ion collisions fluctuate from event to event. It turns out that anisotropies in the collective flow are reflected in the particle momentum distribution with respect to the reaction plane. They give us information about the initial conditions and about the early evolution of the system, since they are developed mainly in the first moments during the collision. However, the collisions are not ideally symmetric, there are quantum fluctuations, the initial nuclear geometry varies from event to event, the initial energy density distribution is anisotropic. All these effects cause flow anisotropies. Those anisotropies are most significant for non-central collisions. Studying them can provide an insight into QGP properties. More details can be found in [1].

Our goal here is to implement Monte Carlo toy model with given profile of the azimuthal angle distribution of pion transverse momenta. Next step is to extract the nth differential flows using correlations and histograms.

2 Angle distribution

We study collective flow anisotropies via azumithal distribution of particles. Common way of study is expanding the distributions to Fourier series:

$$\frac{\mathrm{d}N}{\mathrm{d}^2 p_T} = \frac{\mathrm{d}N}{2\pi p_T \mathrm{d}p_T}\left[1+\sum_{n=1}^{\infty} 2v_n \cos(n(\Phi-\Psi_n))\right] . \tag{1}$$

In our toy model generator we used coefficients up to pentagonal flow: $v_1 = 0.1$, $v_2 = 0.05$, $v_3 = 0.03$, $v_4 = 0.01$ and $v_5 = 0.005$; $\mathit{\Psi}_n$ is generated randomly for every event.

3 Transverse momentum distribution

The p_T distribution is expressed as

$$\frac{\mathrm{d}N}{\mathrm{d}p_T} = C p_T e^{-\frac{p_T}{T}} , \tag{2}$$

where T is a parameter and C denotes normalization constant. We choose $T = 400\,\mathrm{MeV}$.

We cannot use the transformation method since the cummulative distribution function is not invertible. From Equation (2) the uniform random deviate x (i.e. dimensionless $x \in \langle 0,1))$ is related to p_T as:

$$x = C\int \mathrm{d}p_T\, p_T\, e^{-\frac{p_T}{T}} = -CT(T+p_T)e^{\frac{-p_T}{T}} , \tag{3}$$

where C is normalisation factor. In our case, $C = -1/T^2$. The required inverse function can be expressed in terms of *Lambert function* W:

$$p_T(x) = -T\left(1+W\left(\frac{x}{e}\right)\right) . \tag{4}$$

One way of approximating $W(x)$ uses the recurrent relation

$$W(x) = \ln\left(\frac{x}{\ln\left(\frac{x}{\ln\left(\frac{x}{\ln(\ldots)}\right)}\right)}\right) . \tag{5}$$

This approach is simple, for small number of iterations it is even fast. We chose initial $W_0(x)$ and then iterate according to $W_{n+1}(x) = \ln(x/\ln(W_n(x)))$. The reliability of this method strongly depends on the number of iterations. An example is shown in Figure 1 (top and middle). On the top is the histogram for 5 iterations, the black line illustrates the desired shape of the distribution (2) with $T = 400\,\mathrm{MeV}$. It is obvious that 5 iterations are not precise enough. The big discontinuity around $p_t = 2T = 800$ MeV is caused by a problem because of the limit of Equation (5). The other histograms are fitted with the function $p_T\, exp\left(p_0 + \frac{p_T}{p_1}\right)$, where p_0 is scale parameter, thus p_1 should be equal to T.

Another interesting topic is the dependence on $W_0(x)$. For higher number of iteration, choosing some small number (0.1 is sufficient) is an approximation good enough. It does not significantly affect the resulting distribution, choosing better first-guess slows down the computation and for 10 iteration the difference is negligible. However, for 5 iterations, using the *Branch-point* expansion suggested in [2] only up to the first coefficient leads to much better results; cf. top and bottom panels of Figure 1.

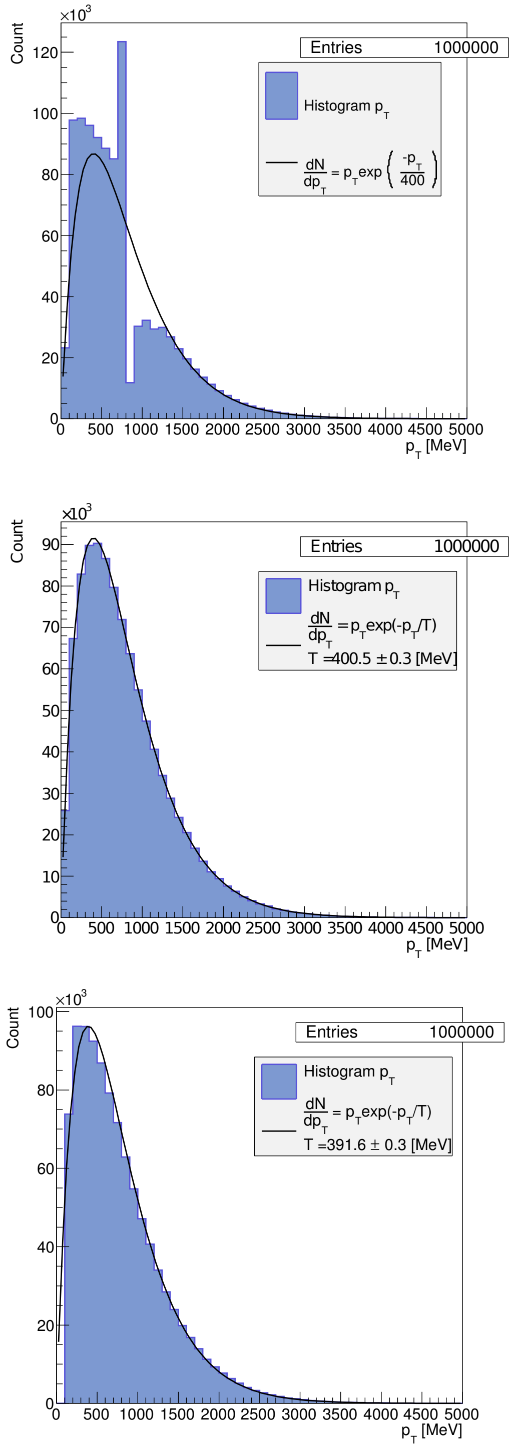

Figure 1. Histograms of p_T generated via Equations (4) and (5). Top: 5 iterations with $W_0 = 0.1$; middle: 10 iterations with $W_0 = 0.1$; bottom: 5 iterations with $W_0(x) = 1 - \sqrt{2(1 + xe)}$. Histograms in the middle and at the bottom are fitted with with the analytic distribution function, the fitted value of T is indicated.

4 Analysis

We produced 5000 events, each consisting of 5000 pions, using the methods described above. For generating p_T, we chose the Lambert function evaluated with 10 iterations with initial $W_0\,(x) = 1 - \sqrt{2(1 + xe)}$. We analyzed the data using cumulant method and the results agree with initial input parameters. Cumulant method is a good aproximation assuming small p_T dependence, negligible nonflow and constant flow fluctuations [1]. Our program meets all of these requirements. For p_T-integrated elliptic flow, there were no negative v_2^2. After root extracting, we obtained $v_2 = 0.0496 \pm 0.0001$ and $v_3 = 0.0299 \pm 0.0002$. The results are displayed in the Figure 2.

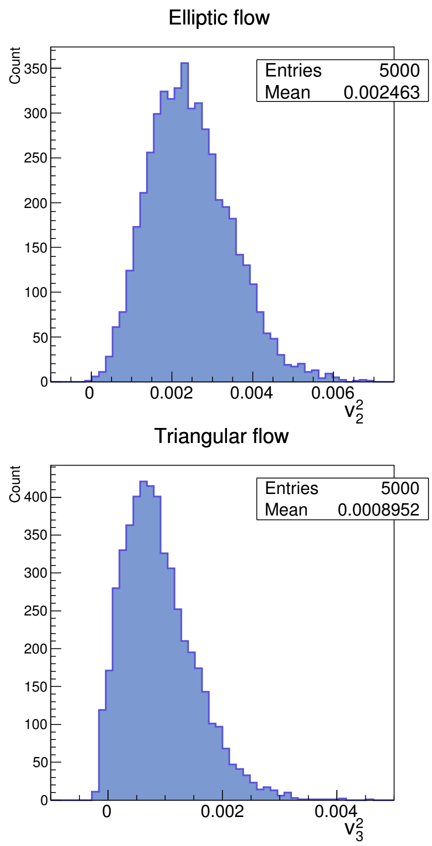

Figure 2. Histograms of v_2^2 and v_3^2 obtained with the cumulant method for pions from 5000 toy model events.

5 Conclusions

We described a simple Monte Carlo toy model for hadron p_T generation. To this end we developed a method of generating random numbers from the given distribution, and successfully tested its use. Our analysis of the generated data agrees with the initial parameters.

Acknowledgment RK thanks the Physics Department of FNSPE, CTU for supporting the attendance of this conference.

References

[1] S. A. Voloshin, A. M. Poskanzer, R. Snelling, arXiv:0809.2949 [nucl-ex] (2008).

[2] D. Veberic, Having Fun with Lambert W(x) Function, arXiv:1003.1628 (2010).

Models of GMI effect in ferromagnetic microwire

Jozef Kravčák[1]

[1]jozef.kravcak@tuke.sk, Department of Physics, FEI, Technical University of Košice, Park Komenského 2, 042 00 Košice, Slovak Republic

Abstract. Presented contribution brings a brief overview of recent theoretical models dealing with giant magneto-impedance (GMI) effect in a ferromagnetic microwire. Irreversible magnetization processes on the wire surface: magnetization rotation, formation of a domain structure around local surface defects and domain wall displacement are analysed in the model.

1 Introduction

As cast glass-covered ferromagnetic amorphous thin $Co_{70.5}Fe_{4.5}Si_{15}B_{10}$ wire (microwire) of a diameter of 17.8 μm (Figure 1) with small negative magnetostriction has been prepared by Taylor-Ulitovski technique. The relatively small negative magnetostriction results in the creation of a wide almost circularly magnetized shell domain structure and a narrow axially magnetized core [1]. The preferential orientation of the spontaneous magnetization (magnetic anisotropy) in the microwire is given by magnetostriction and shape anisotropy. Different mechanical properties of the ferromagnetic metallic central part and of the glass cover of the microwire are responsible for deviation of spontaneous magnetization from circumferential (circular) direction in the shell of the microwire (helical magnetic anisotropy). Additional removing of the glass cover gives the possibility to decrease the helical anisotropy. Considering giant magneto−impedance (GMI) effect which is mainly a surface effect, is very sensitive to the rotation of magnetization in the shell of a microwire, GMI measurements are often used to determine surface magnetic properties of cobalt based microwires [2]. The scanning electron microscopy (SEM) image (Figure 2) of the mechanically removed glass cover reveals its random bonding with the metallic central part of the microwire. Nevertheless the local isolated glass fragments remain strongly fixed on metallic surface (Figure 2). It is possible to deduce a complex inhomogeneous distribution of radial, axial and torsional mechanical stresses in the metallic part of the microwire induced during its preparation procedure.

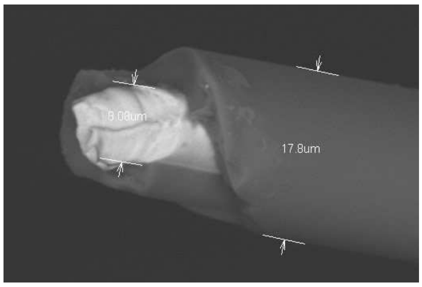

Figure 1. SEM image of glass covered ferromagnetic amorphous $Co_{70.5}Fe_{4.5}Si_{15}B_{10}$ microwire of a diameter d=17.8 μm.

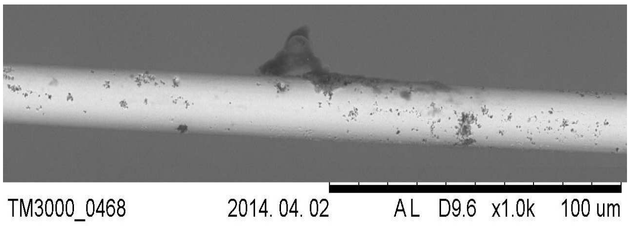

Figure 2. SEM image of ferromagnetic amorphous $Co_{70.5}Fe_{4.5}Si_{15}B_{10}$ microwire without glass cover of a diameter d=8.1 μm.

2 Models of hysteresis in GMI effect

2.1 Irreversible magnetization rotation

In case of a circular wire it is convenient to use cylindrical coordinates. Helical magnetic anisotropy is given by a preferential orientation (easy axis) of the spontaneous magnetization $\boldsymbol{M_0}$ of the microwire at zero external magnetic field what can be expressed as $\boldsymbol{M_0} = (0, M_\phi , M_z) = (0, M_s \cos\alpha, M_s \sin\alpha)$, where M_s is the saturation magnetization, α is the angle of deviation of the easy axis of magnetization from the circumferential direction of the microwire (spiral angle, $0 < \alpha < 90°$).

The angle α determines the shape of the hysteresis loop of the microwire (Figure 3) during its magnetization along z-axis with irreversible magnetization rotation at the critical field [3]. The magnetization curve for $\alpha = 90°$ is without hysteresis (reversible magnetization rotation) and in this case the longitudinal wire z-axis represents a hard axis of magnetization.

2.2 Model of surface domain structure

Details of the metallic surface of the microwire, studied by means of SEM (Figure 2), revealed surface defects (pits), where the glass cover is bonded to metal. The measured GMI dependences of as-cast $Co_{70.5}Fe_{4.5}Si_{15}B_{10}$ microwire with glass cover and after glass cover removing in Figure 4 displays the double-peak behaviour. The theoretical explanation is that for very low amplitudes of circular field strength H_ϕ any reversible domain wall motion at higher frequencies (≥1 MHz) is negligible due to strong damping process and magnetization rotation takes place only

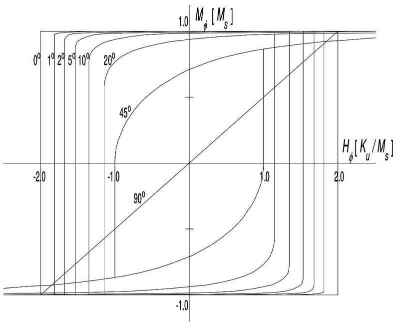

Figure 3. Calculated reduced magnetization curves M_ϕ (H_ϕ) in case of irreversible magnetization rotation and helical magnetic anisotropy for various value of α (in degrees).

in the shell of the microwire. The positions of the couple of sharp peaks ($H = \pm H_{\mathrm{m}}$) are always symmetrical with respect to zero external magnetic fields strength $H = 0$ and correspond to the critical field of irreversible magnetization rotation. The dispersion of the critical field altogether with local variation of the easy axis of magnetization affects the peaks shape.

The formation of a secondary small GMI peaks (inset in Figure 4) has been observed after glass cover removing. The theoretical explanation is that the blade-shaped domains [4], displayed in Figure 5, are formed on both sides of surface defects (pits) to minimize magnetostatic energy. The blade-shaped domains are also responsible for hysteresis observed in GMI dependence.

3 Conclusion

A quasistatic model based on the minimization of the free energy of domain structure [5] was developed to explain the existence of peaks in the GMI dependence in Figure 4, if only a circular anisotropy is present.

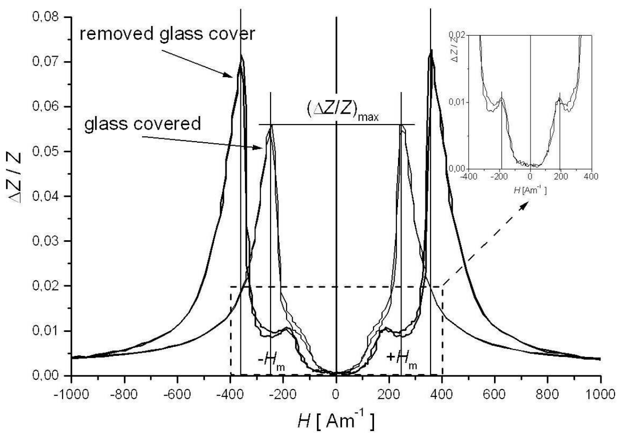

Figure 4. GMI dependence measured at the frequency of 1 MHz and at the amplitude $i_{\mathrm{ac}} = 1\,\mathrm{mA}$ in as-cast $Co_{70.5}Fe_{4.5}Si_{15}B_{10}$ microwire of a diameter $d = 8.1\,\mu\mathrm{m}$ with glass cover and after glass cover removing.

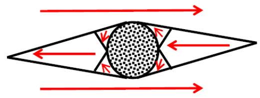

Figure 5. Scheme of the blade-shaped domains [4] on the surface of the wire closing the defect (pit).

The following extensions have to be added in models reflecting:

1. The helical anisotropy and the irreversible magnetization rotation on the microwire surface manifesting itself in hysteresis.
2. The residual domain structure formed around local surface defects (pits) on the microwire surface manifesting itself in hysteresis and formation of the secondary small GMI peaks (inset in Figure 4).

Acknowledgement

The presentation of this paper was financially supported by grants of Slovak Research and Development Agency No. APVV-0027-11 and Scientific Grant Agency of the Ministry of Education of Slovak Republic No. VEGA-1/0778/12.

References

[1] L. V. Panina, K. Mohri, T. Uchiyama, M. Noda, K. Bushida, IEEE Trans. Magn. **31**, 1249 (1995).

[2] M. Knobel, M. Vázquez, L. Kraus, *Handbook of Magnetic Materials 15, Ed. by K. H. J. Buschow* (Elsevier Science B.V., 2003), 497.

[3] S. Chikazumi, *Physics of Magnetism* (John Wiley &Sons, Inc., New York, 1964), 281.

[4] R. S. Tebble, D. J. Craik, *Magnetic Materials* (John Wiley&Sons, Inc., London, New York, 1969), 391.

[5] A F. L. A. Machado, S. M. Rezende, Journal of Applied Physics **79**, 6558 (1996).

Production of photons and hadrons on nuclear targets

Michal Křelina[1] and Ján Nemčík[1,2]

[1]*michal.krelina@fjfi.cvut.cz, Czech Technical University in Prague, FNSPE, Brehova 7, 11519 Prague, Czech Republic*
[2]*nemcik@saske.sk, Institute of Experimental Physics SAS, Watsonova 47, 04001 Kosice, Slovakia*

Abstract. We investigate nuclear effects in production of large-p_T hadrons and direct photons in pA and AA collisions corresponding to energies at RHIC and LHC. Calculations of nuclear invariant cross sections include additionally the nuclear broadening and the nuclear modification of parton distribution functions. We demonstrate that at large p_T and forward rapidities the complementary effect of initial state interactions (ISI) causes a significant nuclear suppression. Numerical results for nuclear modification factors R_A and R_{AA} are compared with available data at RHIC and LHC. We perform also predictions at forward rapidities which are expected to be measured by the future experiments.

1 Introduction

Recent experimental measurements of hadron and direct photon production [1–3] allow to investigate nuclear effects at medium and large transverse momenta p_T. This should help us to understand properties of a dense medium created in heavy ion collisions (HICs). Manifestations of nuclear effects are usually studied through the nucleus-to-nucleon ratio, the so called nuclear modification factor, $R_A(p_T) = \sigma_{pA\to h(\gamma)+X}(p_T)/A\,\sigma_{pp\to h(\gamma)+X}(p_T)$ for pA collisions and $R_{AB}(p_T) = \sigma_{AB\to h(\gamma)+X}(p_T)/AB\,\sigma_{pp\to h(\gamma)+X}(p_T)$ for minimum bias (MB) AB collisions.

In this paper we focused on suppression at large p_T, $R_A(p_T) < 1$ ($R_{AA} < 1$) indicated at midrapidity, $y = 0$, by the PHENIX data [1] on π^0 production in central dAu collisions and on direct photon production in central $AuAu$ collisions [2]. Such a suppression can not be interpreted by the onset of coherence effects (gluon shadowing, color glass condensate) due to large values of Bjorken x. The same mechanism of nuclear attenuation should be arisen especially at forward rapidities where we expect much stronger onset of nuclear suppression as is demonstrated by the BRAHMS and STAR data [3]. Here the target Bjorken x is $\exp(y)$-times smaller than at $y = 0$ allowing so a manifestation of coherence effects. However, assuming their dominance at RHIC forward rapidities then the same effects causing a strong suppression should be expected also at LHC at $y = 0$, what is in contradiction with ALICE data [4].

We interpret alternatively the main source of this suppression as multiple initial state interactions (ISI) of the projectile hadron and its debris during propagation through the nucleus. This leads to a dissipation of energy resulting in a suppressed production rate of particles as was stressed in [5, 6]. The corresponding suppression factor reads [5],

$$S(\xi) \approx 1 - \xi, \qquad (1)$$

where $\xi = \sqrt{x_F^2 + x_T^2}$, and $x_F = 2p_L/\sqrt{s}$; $x_T = 2p_T/\sqrt{s}$. This factor leads to a suppression at large-p_T ($x_T \to 1$) and also at forward rapidities ($x_F \to 1$).

2 Results

Calculations of pp, pA and AA cross sections were performed employing the parton model, which corresponds to collinear factorization expression modified by intrinsic transverse momentum dependence [7].

In the RHIC energy range at $y = 0$ besides Cronin enhancement at medium-high p_T and small isotopic corrections at large p_T one should not expect any nuclear effects since no coherence effects are possible. However, the PHENIX data [1, 2] indicate large-p_T suppression, which is more evident for hadron and direct photon production in central dAu and $AuAu$ collisions, respectively, as is demonstrated in Figure 1 (lower box) and in Figure 2 (middle box). Such a suppression is caused by ISI effects, Equation (1), and is depicted by the solid lines, while the dotted lines without ISI effects overestimate the PHENIX data at large p_T.

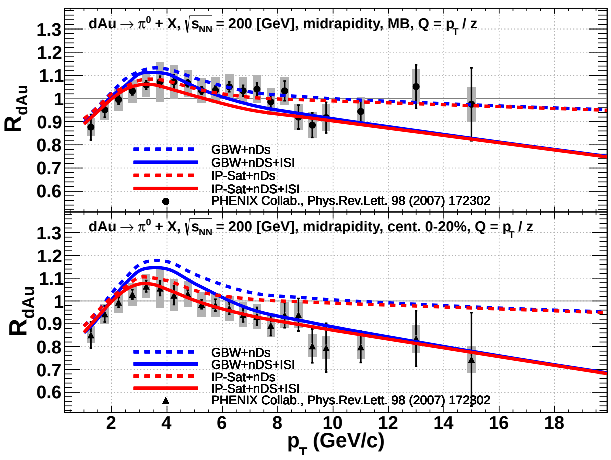

Figure 1. Nuclear modification factor $R_{dAu}(p_T)$ for π^0 production at $\sqrt{s} = 200$ GeV for MB - upper box and for the centrality interval $0 - 20\,\%$ - lower box.

In the LHC energy range at $y = 0$, we do not expect any ISI effects, Equation (1), and the ALICE data [4] on hadron production in pPb collisions allow so to test only model predictions for the Cronin enhancement at medium-high p_T. The corresponding comparison demonstrates a good agreement as is shown in Figure 3 by the solid and dotted lines manifesting so a weak effect of nuclear shadowing. How-

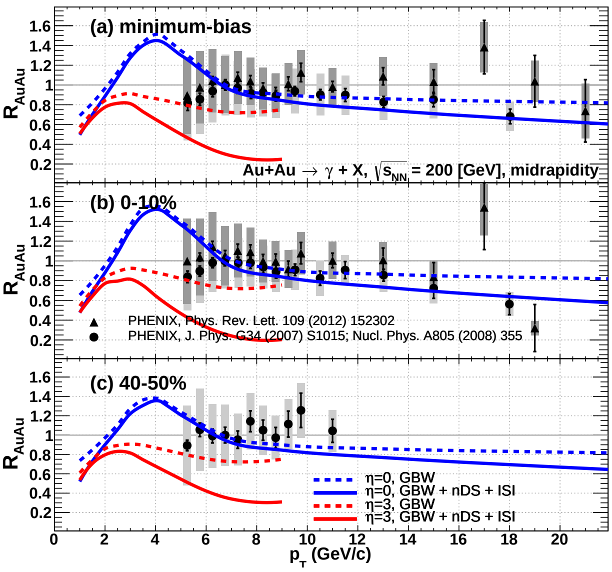

Figure 2. Nuclear modification factor $R_{AuAu}(p_T)$ for direct photon production at $\sqrt{s} = 200$ GeV for different centrality intervals at $y = 0$ and $y = 3$.

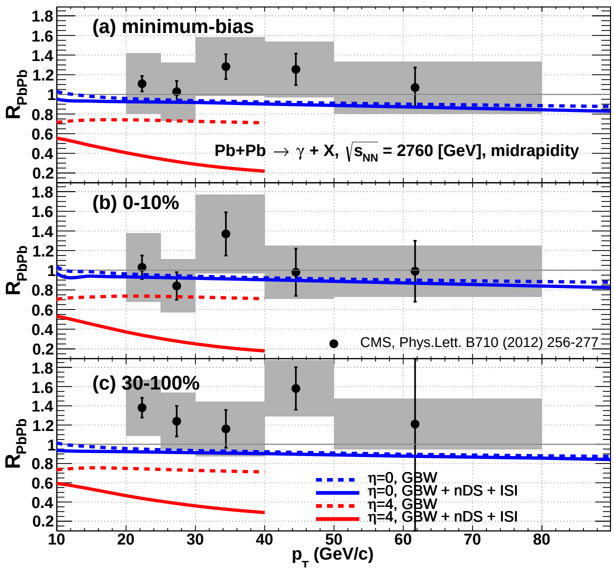

Figure 4. Nuclear modification factor $R_{PbPb}(p_T)$ for direct photon production at $\sqrt{s} = 2760$ GeV for different centrality intervals at $y = 0$ and $y = 4$.

ever, ISI effects causing a significant large-p_T suppression can be arisen at forward rapidities as is depicted in Figure 3 by the dashed and dot-dashed lines calculated at $y = 2$ and $y = 4$.

Direct photons produced in a hard reaction are not accompanied with any final state interaction, either energy loss or absorption and represent so a cleaner probe for a dense medium created in HICs. The CMS data [8] on direct photon production in $PbPb$ collisions at $y = 0$ presented in Figure 4 show only a manifestation of isotopic corrections at large-p_T due to a weak onset of ISI effects. Similarly as for hadron production, ISI effects cause a significant large-p_T suppression at forward rapidities as is shown in Figure 4 by the solid lines calculated at $y = 4$.

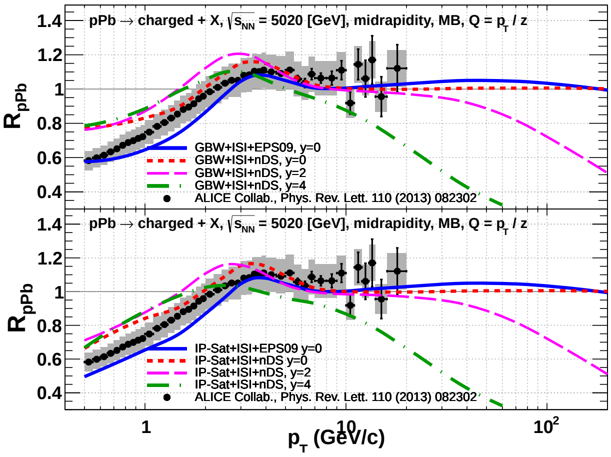

Figure 3. Nuclear modification factor $R_{pPb}(p_T)$ for charge hadron production at $\sqrt{s} = 5020$ GeV and at several rapidities, $y = 0, 2$ and 4.

3 Conclusions

Employing the parton model, corresponding to collinear factorization expression modified by intrinsic transverse momentum dependence, we predict large-p_T suppression of hadrons and direct photons produced on nuclear targets. The main source for suppression comes from ISI effects, which are dominant at large x_F and/or x_T. ISI effects at LHC are irrelevant at $y = 0$ but we predict a strong suppression at forward rapidities that can be verified by the future measurements.

Acknowledgements

This work has been supported in part by the grant 13-20841S of the Czech Science Foundation (GAČR), by the Grant MŠMT LG13031, by the Slovak Research and Development Agency APVV-0050-11 and by the Slovak Funding Agency, Grant 2/0020/14.

References

[1] S. S. Adler *et al.* [PHENIX Collab.], Phys. Rev. Lett. **98**, 172302 (2007); Phys. Rev. Lett. **109**, 152302 (2012).

[2] S. Afanasiev *et al.* [PHENIX Collab.], Phys. Rev. Lett. **109**, 152302 (2012); T. Sakaguchi Nucl. Phys. A **805**, 355 (2008).

[3] I. Arsene *et al.* [BRAHMS Collab.], Phys. Rev. Lett. **93**, 242303 (2004); J. Adams *et al.* [STAR Collab.], Phys. Rev. Lett. **97**, 152302 (2006).

[4] B. Abelev *et al.* [ALICE Collab.], Phys. Rev. Lett. **110**, 082302 (2013).

[5] B. Z. Kopeliovich *et al.*, Nucl. Phys. B **146**, 171 (2005).

[6] B. Z. Kopeliovich *et al.*, Phys. Rev. C**72**, 054606 (2005); B.Z. Kopeliovich and J. Nemchik, J. Phys. G **38**, 043101 (2011).

[7] M. Krelina and J. Nemchik, Nucl. Phys. B (Proc. Suppl.)**245**, 239 (2013).

[8] S. Chatrchyan *et al.* [CMS Collab.], Phys. Lett. B **710**, 256 (2012).

Study of high-p_T hadron-jet correlations in ALICE

Filip Křížek[1] for the ALICE Collaboration

[1]krizek@ujf.cas.cz, Nuclear Physics Institute AS CR, Hlavní 130, 25068 Řež u Prahy, Czech Republic

Abstract. Jets provide unique probes of the medium created in ultrarelativistic heavy-ion collisions. Here, the observed jet quenching phenomena in central collisions prove that jets are sensitive to interesting properties of strongly-coupled matter. In addition, jet production in elementary processes, such as pp collisions, is well understood within the framework of perturbative QCD, providing a rigorous theoretical basis for jet quenching calculations. We report the measurement of semi-inclusive p_T spectra of charged particle jets that recoil from a high-p_T hadron trigger in Pb–Pb and pp collisions at $\sqrt{s_\mathrm{NN}} = 2.76$ TeV and $\sqrt{s} = 7$ TeV, respectively. In this analysis, the copious yield of uncorrelated trigger hadron-jet matchings in central Pb–Pb collisions is removed by calculating the difference between two spectra corresponding to disjoint trigger hadron p_T ranges. This procedure does not impose any fragmentation bias on the recoil jet population, which is thus collinear and infrared safe.

1 Introduction

Hadrons with a high transverse momentum p_T as well as jets that are produced in ultrarelativistic heavy-ion collisions originate from initial hard parton-parton interactions. Hard scattering processes are recognized to be convenient probes of the medium created during the interaction of two nuclei. High multiplicity environment of a heavy-ion collision makes, nevertheless, a jet analysis difficult since the rare products of hard scattering are embedded into a densely populated background. Therefore when a jet reconstruction algorithm is used, it also clusters together soft particles from the background. One possibility to suppress the contribution of these artificial jets is to require that the jet has a high-p_T track constituent. This condition, however, imposes a bias on the jet fragmentation and can possibly affect the results especially in the case when one intends to study quenched jets that do not differ much from the background. As was shown in [1] hadron-jet coincidence measurements allow to avoid such fragmentation bias. Following this idea we report on the analysis of trigger hadron associated p_T spectra of jets in Pb–Pb collisions at a center-of-mass energy per nucleon-nucleon pair $\sqrt{s_\mathrm{NN}} = 2.76$ TeV.

2 Data analysis

Presented data were measured with the ALICE detector [2]. The analysis is based on a sample of 9 M events (0-10% centrality) and 3 M events (0-20% centrality) of Pb–Pb collisions at $\sqrt{s_\mathrm{NN}} = 2.76$ TeV form 2010 and 2011, respectively. For the jet reconstruction we used charged tracks with pseudorapidity coverage $|\eta| < 0.9$ and $p_\mathrm{T} > 150$ MeV/c. Jets were defined by means of the anti-k$_\mathrm{t}$ algorithm [3] using three resolution parameters $R = 0.2$, 0.4 and 0.5. Analyzed jets were fully contained within the ALICE acceptance, i.e. $|\eta_\mathrm{jet}| < 0.9 - R$. The background energy density ρ was estimated with the area based method [4]. The p_T of a jet was then event by event corrected for the underlying event activity by subtracting the product of the estimated background density and jet area from the reconstructed jet p_T.

The raw p_T spectra of jets need to be corrected for the momentum smearing induced by background fluctuations and for detector response. The corresponding response matrix that relates the p_T of matched reconstructed jets on the particle and detector level is assumed to factorize into a product of matrices that describe both effects. To correct the measured spectra the response matrix was inverted using the SVD [5] and Bayesian [6] approach.

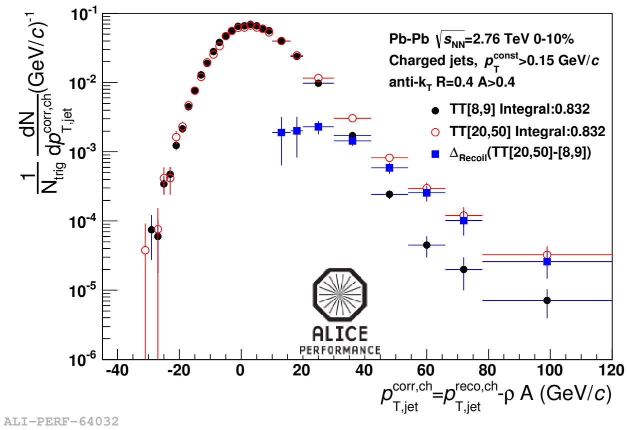

Figure 1. Raw p_T spectra of recoil jets associated with two disjoint trigger hadron p_T intervals, [8,9] GeV/c and [20,50] GeV/c. The corresponding Δ_recoil distribution was calculated based on Equation (2). See text for more details.

We studied jets that are nearly back-to-back in azimuth w.r.t. a high-p_T trigger hadron, namely $|\varphi_\mathrm{trig} - \varphi_\mathrm{jet} - \pi| < 0.6$ rad. By this choice the high-p_T trigger hadron originates more likely from a parton that is closer to the surface of the collision zone [7]. Therefore, the recoiling jet is biased towards larger path length in the medium. Figure 1 shows background corrected, per trigger normalized raw p_T spectra of recoil jets corresponding to two disjoint trigger hadron p_T ranges, $[8, 9]$ GeV/c and $[20, 50]$ GeV/c. On average the trigger hadrons in the higher p_T bin result from hard scattering processes with larger Q^2, hence the associated recoil jets have also a harder p_T spectrum as can be seen from the positive part of the distribution. On the other hand, jet yield per trigger in the negative part of the spectrum does not depend on trigger p_T. This part of the distribution is dominated by the cases where the trigger hadron was associated with a background jet. Assuming that the number of background jets is independent of trigger p_T we introduce the following observable

$$\Delta_{\mathrm{recoil}} = \frac{1}{N_{\mathrm{trig}}}\frac{\mathrm{d}N_{\mathrm{jet}}}{\mathrm{d}p_\mathrm{T}}\bigg|_{\mathrm{TT}[20,50]} - \frac{1}{N_{\mathrm{trig}}}\frac{\mathrm{d}N_{\mathrm{jet}}}{\mathrm{d}p_\mathrm{T}}\bigg|_{\mathrm{TT}[8,9]} \quad (1)$$

where N_{trig} is the number of trigger hadrons in the given bin. The subtraction removes the contribution of the background jets in the Δ_{recoil} distribution. Another advantage of this observable is that it does not impose any bias on the jet fragmentation.

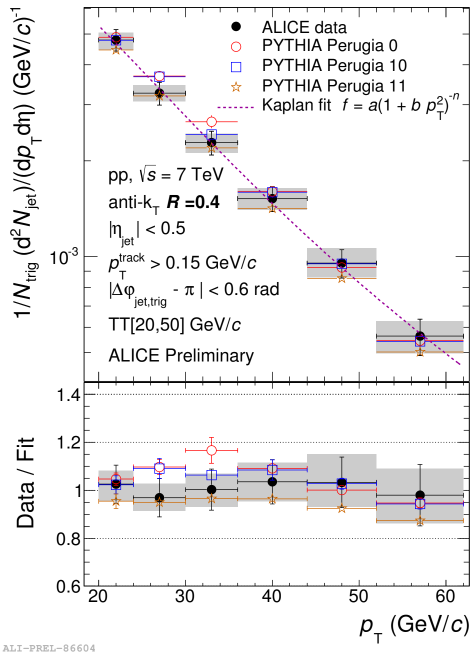

Figure 2. Top: Per trigger normalized p_T spectrum of anti-$\mathrm{k_t}$ $R = 0.4$ recoil charged jets associated with a [20,50] GeV/c trigger hadron in pp at $\sqrt{s} = 7$ TeV. Systematic uncertainties on the measured data are marked by the gray boxes. ALICE data are compared to PYTHIA Perugia tunes. Bottom: Ratio of the data sets w.r.t. to the Kaplan function fit of the measured data.

The medium-induced modification of jet fragmentation is studied by the ratio $\Delta I_{AA} = \Delta^{\text{Pb-Pb}}_{\mathrm{recoil}}/\Delta^{\mathrm{pp}}_{\mathrm{recoil}}$ where the reference $\Delta^{\mathrm{pp}}_{\mathrm{recoil}}$ spectrum is measured in pp collisions at the same center-of-mass energy. Owing to the limited statistics of the pp data at $\sqrt{s} = 2.76$ TeV the reference spectrum was determined by means of the PYTHIA event generator using Perugia 10 tune [8]. To test the reliability of PYTHIA as a reference its predictions were compared with the data measured in pp at $\sqrt{s} = 7$ TeV (168 M minimum bias events from 2010). The analysis of recoil jet spectra in pp at $\sqrt{s} = 7$ TeV closely followed the Pb–Pb data analysis. Underlying event activity was estimated in a $R = 0.4$ cone rotated by 90 deg in azimuth w.r.t. the leading jet in event. The corrected spectra are compared with spectra generated by the PYTHIA Perugia tunes, see Figure 2. Our studies suggest that the Perugia 10 tune provides the best description of the data.

Figure 3 presents ΔI_{AA} evaluated using pp reference from PYTHIA Perugia 10. The ΔI_{AA} ratio exhibits a suppression of the recoil jet yield in Pb–Pb relative to pp which reflects the jet quenching phenomenon. Within the statistical and systematic uncertainties no p_T dependence is observed.

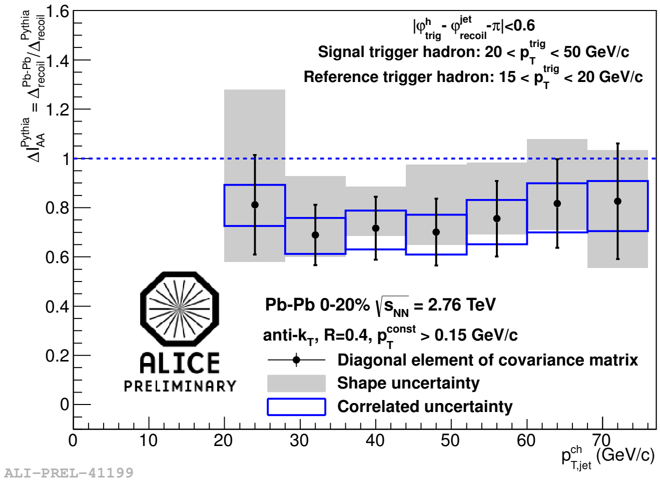

Figure 3. ΔI_{AA} corresponding to anti-$\mathrm{k_t}$ $R = 0.4$ jets in Pb–Pb at $\sqrt{s_{\mathrm{NN}}} = 2.76$ TeV. The pp reference was estimated by PYTHIA Perugia 10 tune.

To conclude, hadron-jet correlation observables represent a promising way to study modification of jet fragmentation in medium. Their main advantage is that they do not impose a fragmentation bias on the recoil jet and in addition, they allow to study low p_T jets with large radii and with a minimum infrared cutoff.

The work has been supported by the MEYS grant CZ.1.07/2.3.00/20.0207 of the European Social Fund (ESF) in the Czech Republic: “Education for Competitiveness Operational Programme” (ECOP) and by the grant LG 13031 of the Ministry of Education of the Czech Republic.

References

[1] G. O. V. de Barros *et al.*, [arXiv:1208.1518 [hep-ex]] (2012).
[2] ALICE collaboration, J. Instrum. **3**, S08002 (2008).
[3] M. Cacciari *et al.*, Eur. Phys. J. C **72**, 1896 (2012).
[4] M. Cacciari *et al.*, Phys. Lett. B **659**, 119 (2008).
[5] A. Höcker, Nucl.Instrum.Meth. A **372**, 469 (1996).
[6] G. D’Agostini, Nucl.Instrum.Meth. A **362**, 487 (1995).
[7] T. Renk, Phys. Rev. C **87**, 2 (2013).
[8] P. Skands, Phys. Rev. D **82**, 074018 (2010).

Structure changes in transformer oil based magnetic fluids in magnetic field

J. Kúdelčík[1], P. Bury[1], Š. Hardoň[1], P. Kopčanský[2], and M. Timko[2]

[1]kudelcik@fyzika.uniza.sk, Department of physics, University of Žilina, Univerzitná 1, 010 01 Žilina, Slovak Republic
[2]Department of Magnetism, IEP SAS, Watsonova 47, 040 01 Košice, Slovak Republic

Abstract. Magnetic fluid in the presence of external magnetic field can consist of individual magnetic nanoparticles, dimers and higher oligomers, chains, clusters and their various combinations. These structures can be studied by acoustic spectroscopy, because they interaction with acoustic wave causes its additional absorption. The changes in the acoustic attenuation observed in the magnetic fluid transformer oil based subjected to a jumped magnetic field were significant. The time development of acoustic attenuation allows characterizing the processes during the measurement. After the magnetic field removal, the decrease of attenuation depends on the lifetime of nanoparticle structures. However, the temperature of magnetic fluids had also very important influence on the structural changes because of the mechanism of thermal motion that acts against the cluster creation.

1 Introduction

Nanotechnology is very progressive research area and their results can be found in many parts of our daily life. Nanoparticles are used in technology, biology, chemistry and other areas to improve the properties of various materials. Magnetic fluids containing magnetic nanoparticles have also interesting physical properties that have found wide application in technology and medicine. The transformer oil-based magnetic fluids can have better thermal and insulating properties and their dielectric breakdown strength is changed [1, 2].

One of the useful methods of studying changes in the ferrofluid structure is based on the measurements of changes in the acoustic wave attenuation $\Delta\alpha$ under the influence of an external magnetic field. The interaction between the acoustic waves and the magnetic nanoparticles or their combination leads to additional attenuation of acoustic wave compared to that in the carried liquid, so we can indicate characteristic properties and structure of magnetic liquid.

Acoustic wave propagation in magnetic fluid was studied by several authors both theoretically and experimentally [3–5]. Under the effect of an external magnetic field the nanoparticles of magnetic fluid become arranged into agglomeration, forming chains stiffening the liquid structure. From computer simulations results that chainlike clusters are formed along magnetic field direction, but clusters can have various shapes.

In the present contribution the measurements of the acoustic wave attenuation for the frequency 12.65 MHz as a function of magnetic field at different temperature were performed in the experimental arrangement already described [6].

2 Experimental results

The magnetic fluid (MF) used in experiments consisted of magnetite nanoparticles (FeO.Fe2O3) with the mean diameter $d = 9.8\,\mathrm{nm}$ ($\sigma = 0.28\,\mathrm{nm}$) and various concentration (Table 1) coated with oleic acid as a surfactant that were dispersed in transformer oil MOGUL.

Volume fraction	0.5 %	1.0 %	2.0 %
Density [g/cm^3]	860	890	920
Magnetization [mT]	2.3	3.4	6.3

Table 1. The parameters of used magnetic fluid

The attenuation of acoustic wave in magnetic fluid depends on the applied magnetic field, the rate of its changes and the temperature as well as the concentration of nanoparticles. Figures 1(a–c) present the changes of acoustic attenuation for jump change of magnetic field from zero to the constant of value 300 mT during next 60 minutes. The change of acoustic attenuation at the jump change of magnetic field was practically immediate. For the 0,5% and 1.0% MF attenuation increases with similar course for all temperatures during the first 50 minutes until it reaches constant values, the magnitude of which depends on used temperature. In the case of 2.0% MF for 22 °C and 30 °C the development of acoustic attenuation at first increases during tenth of minutes until it reaches maximal value that time position depends on temperature. After reaching its maximum the acoustic attenuation slowly decreases to the constant value corresponding to a new state of equilibrium. After the magnetic field is switched-off, the acoustic attenuation decreases to its initial value. From the longtime of decrease it follows that the lifetimes of the created structures are several tenth of minutes.

The changes of acoustic attenuation are the reflection of structural changes caused by rearrangement of magnetic nanoparticles inside magnetic fluids. These structural changes are the results of the interaction between the external magnetic field and the magnetic moment of the nanoparticle in magnetic fluids. There are various types of structures like: dimers, trimmers, higher oligomers, think or rough chains, clusters and their various combinations.

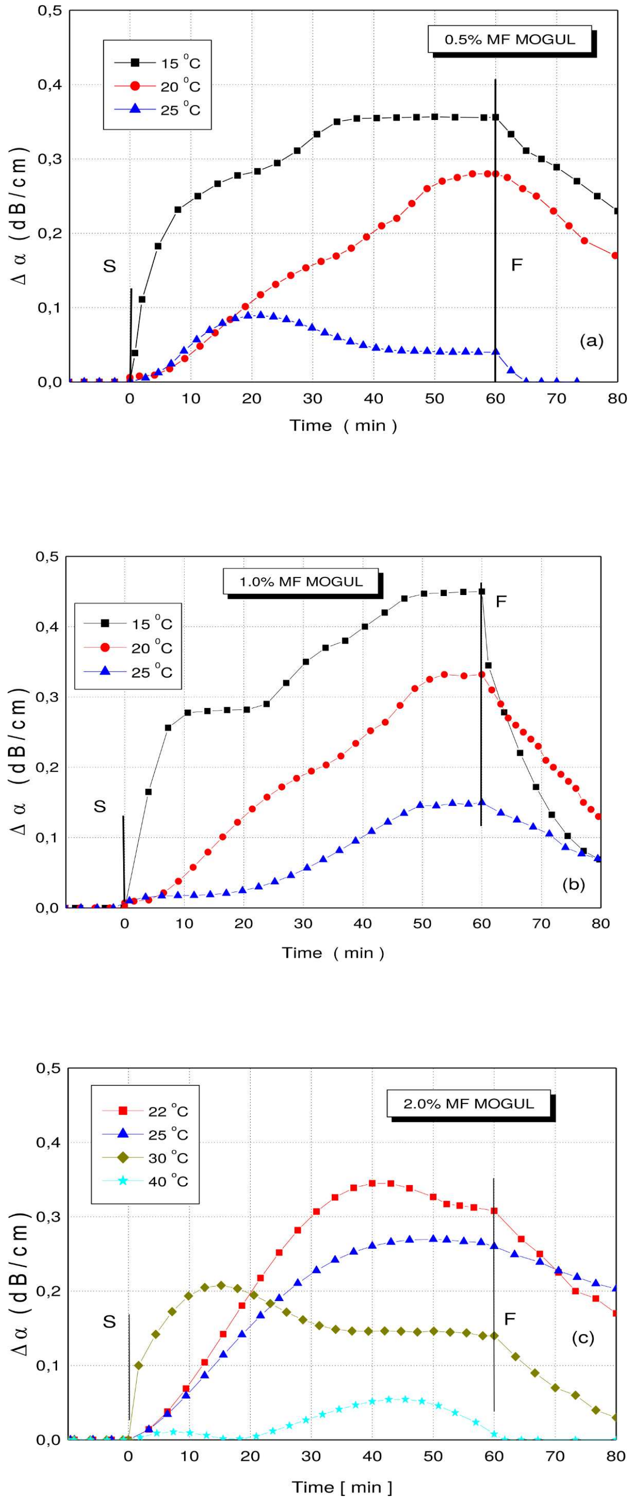

Figure 1. Experimental data of acoustic attenuation for jump change of the magnetic field to value 300 mT measured at various temperatures for 0.5% (a) 1.0% (b) and 2.0% (c) magnetic fluid based on MOGUL.

The application of the constant magnetic field clearly induces that processes leading to the creation of structures are time dependent and step-by-step. This means gradual increase of nanoparticles into structures. Firstly dimmers than trimers and higher oligomers are created. As in this case the magnetic field is relative strong so we can suppose the existence of long thin chains, clusters or rough chains. For 2.0% MF the structural changes are similar until to the maximum of the change of acoustic attenuation. The observed following decrease of the acoustic attenuation is caused by new process of mutual coupling of chains. As a result of coupling of thin chains are rough chains or clusters. Under rough chains we can assume the formation of several bulks consist of several (2–5) nanoparticles, where similar results give also numerical simulations. In the case of cluster in bulk there are more than 6 nanoparticles. The measurements were done also at various temperatures and for all cases we can see its strong influence on the change of acoustic attenuation. At lower temperature, the creation of nanoparticles structures is more effective because Brown thermal motion is not so effective to destroy these structures. The thermal motion increases with increasing temperature those results in decrease of both number and size of structures. The reduced size of clusters and shorter length of chains then induce the decrease of acoustic attenuation.

3 Conclusion

The influences of both magnetic field and temperature on the structures of investigated magnetic fluids based on the transformer oil MOGUL were observed using acoustic spectroscopy. The effect of external magnetic field on the creation of structures of nanoparticles in magnetic fluids was confirmed and their influence on the development of attenuation was described. At concentration under 2.0 % the stabilization effect after some time was observed. The measurements also confirmed that the lifetime of these structures or clusters is relative long.

Acknowledgements

This work was supported by VEGA projects 2/0045/13.

References

[1] J. Kúdelčík, P. Bury, P. Kopčanský, M. Timko, Physics Procedia **9**, 78 (2010).

[2] J. C. Lee, W. H. Lee, S. S. H. Lee, Materials Research Bulletin **47(10)**, 2984 (2012).

[3] A. Jozefczak, T. Hornowski, A Skumiel, Ferrofluid Int J Thermophys **32**, 795 (2011).

[4] S. R. Kruti, V. Upadhay, Pramana – Journal Physics **77(2)**, 345 (2011).

[5] J. Kúdelčík, P. Bury, P. Kopčanský, M. Timko, Comunication **16(1)**, 33 (2014).

[6] J. Kúdelčík, P. Bury, J. Drga, P. Kopčanský, V. Závišová, M. Timko, Journal of Magnetism and Magnetic Materials **326**, 75 (2013).

Improvement of stability of platinum catalyst for hydrogen fuel cells

Miroslava Lacková[1] and Vladimír Komanický[2]

[1]*miroslava.lackova@student.upjs.sk*
[2]*vladimir.komanicky@upjs.sk, Faculty of Science, Centre of Low Temperature Physics, Faculty of Science, P. J. Šafárik University, Park Angelinum 9, 041 54 Košice, Slovakia*

Abstract. Catalysts degradation due to substrate oxidation is one of the main problems in hydrogen fuel cells. We tested corrosion stability of platinum metal deposited on two substrates. We used SIGADUR® G glassy carbon and SIGADUR® G glassy carbon modified with titanium nitride. Both materials show high resistance toward oxidation which should increase also stability of platinum catalysts. We performed accelerated stability tests emulating fuel cell in operation. Platinum catalysts deposited on these substrates show improved stability when compared to traditional substrates based on VULCAN XC72.

1 Introduction

In the past decade the fuel cell technology has made significant progress towards commercialization. Polymer electrolyte membrane fuel cells (PEM FC) received broad attention because their portability makes them suitable for automotive applications. The cost and the durability of a PEM fuel cells system are the major problems hindering their commercialization [1, 2].

Currently, the carbon black supported platinum nanoparticles (Pt/C) remain the state-of-the-art electrocatalysts and Vulcan XC-72 carbon black is the most popular catalyst support. It has been shown [3, 4], that standard carbon support undergoes corrosion under the oxidizing conditions present in the fuel cell, which leads to degradation of catalyst and significant reduction of the PEM fuel cell life time.

In this regard, it is important to explore supports with high corrosion resistance. Titanium nitride is a promising support material because of good electrical conductivity and outstanding corrosion resistance. TiN can outperform standard carbon supports [5].

In this study we compare performance of this material with another promising substrate material, namely SIGRADUR® G glassy carbon, which is specifically formulated to be extremely stable at highly oxidizing conditions.

2 Experimental

Two types of substrates were used, namely: SIGRADUR® G glassy carbon (Sigradur GC) and 10 nm TiN layer to sputtered on Sigradur GC (TiN). On both types of substrates we sputtered 1, 5 and 10 monolayers (ML) of Pt.

These six samples were characterized by scanning electron microscopy (SEM) and atomic force microscopy (AFM). SEM images were taken with VEGA (TESCAN) electron microscope at 30 keV.

Electrocatalytic activity of platinum deposited on Sigradur GC and TiN was performed in standard three electrode set up with potentiostat (Autolab PGSTAT 302N). A silver / silverchloride electrode (3M KCl) is used as a reference electrode. All samples were cycled 1000 times between -0.125 V to 1.075 V with scan rate $50\,\mathrm{m\cdot s^{-1}}$ in 0.1 M $HClO_4$ electrolyte at room temperature. Electrochemical surface area (ECSA) in cm^2 was calculated from the area under the hydrogen desorption peaks of CV curves in the beginning and after 1000 cycles. Current density was calculated from the geometric area of the substrates.

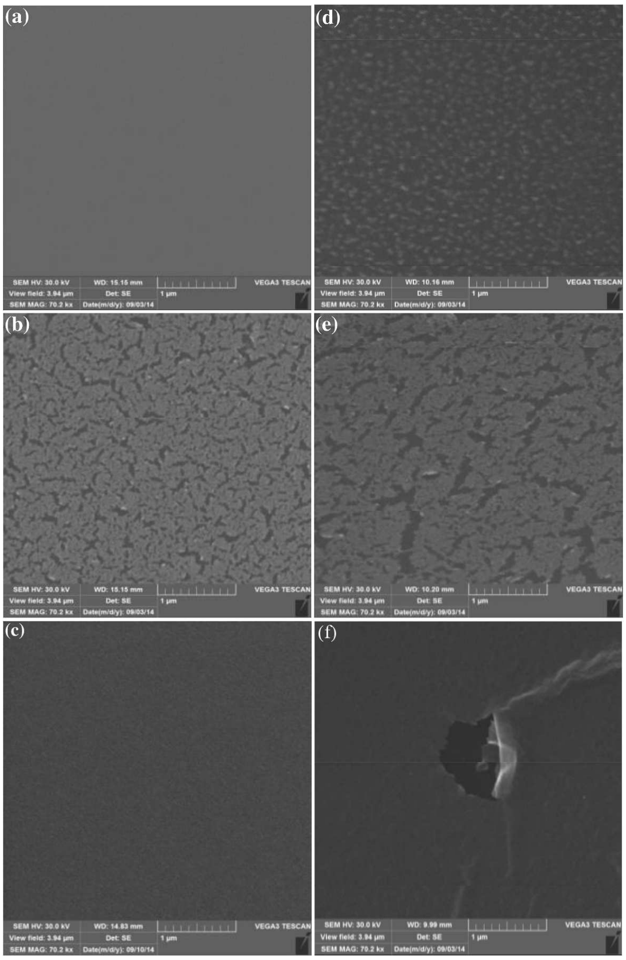

Figure 1. SEM images of (a)–(c): 1, 5, 10 ML Pt on Sigradur GC; (d)–(f): 1, 5, 10 ML Pt on TiN after 1000 cycles. Magnification 70 kx.

3 Results and discussion

3.1 Morphology characterisation

Surface of both type of substrates Sigradur GC and TiN before cycling was smooth and without defects.

Figure 1 (a–c) shows samples with 1, 5 and 10ML of Pt on Sigradur GC after 1000 cycles; (d-f) represents samples with 1, 5 and 10ML Pt on TiN after 1000 cycles. From these images it can be seen that all TiN samples changed morphology after potential cycling resulting in formation of cracks and even individual islands and particles. Most likely lower stability of Pt films on TiN is caused by lower adhesion between these two materials. Pt films on Sigradur GC are very stable, we observed only change of morphology with 5 ML Pt thin films.

3.2 Electrochemical characterisation

Figure 2 (a) and (b) shows characteristic CV curves of 1 ML Pt on Sigradur GC and TiN respectively in 0.1M $HClO_4$. The ECSA for the TiN samples shows significant decrease after 1000 cycles when compared to Sigradur GC. Table 1 shows calculated ESCA decrease in % for both types of substrates.

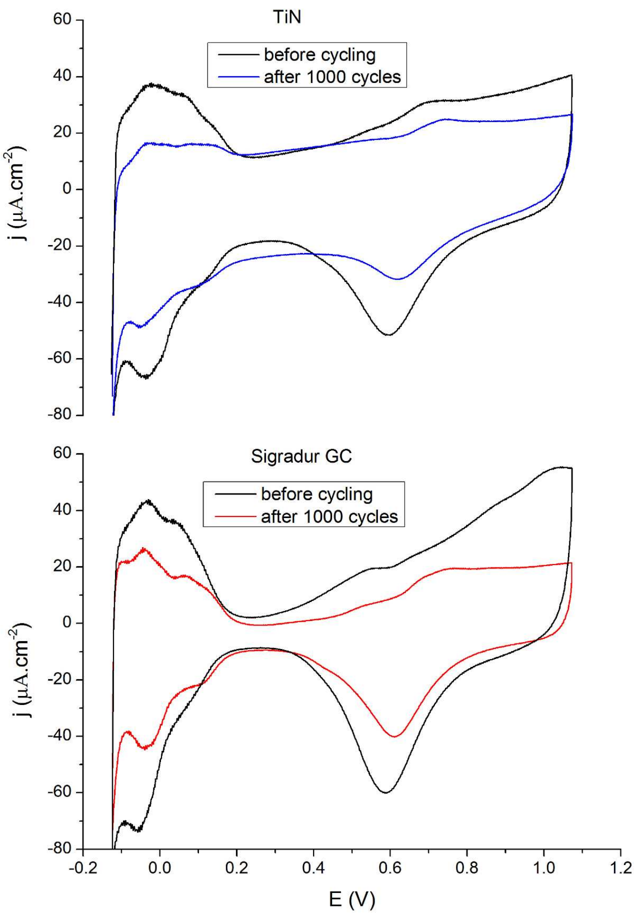

Figure 2. Cyclic voltammograms of (a) 1ML Pt on Sigradur GC, (b) 1ML Pt on TiN in 0.1M $HClO_4$ at 50 mVs^{-1}.

Loss of ECSA (%)	Sigradur GC	TiN
1 ML Pt	24	88
5 ML Pt	28	35
10 ML Pt	−7	16

Table 1. Loss of electrochemical surface area (ECSA) from cyclic voltammograms

4 Conclusions

* SEM measurements show that Pt films on Sigradur GC are very stable.
* From electrochemistry measurements it was concluded that ECSA of Pt on Sigradur GC after 1000 cycles is larger than the ECSA of Pt on TiN sputtered on Sigradur GC.
* Literature describes TiN as one of the most corrosion resistant substrates for PEM electrocatalysts. We find that Platinum thin films deposited on SIGRADUR® G glassy carbon are even more stable. Our results show that SIGRADUR® G is a very promising substrate for manufacturing highly stable catalysts.

Acknowledgement

This work has been supported by ERDF EU project No. ITMS26220120005.

References

[1] Borup *et al.* Chem. Rev. **107**, 3904-51 (2007).
[2] Satyapal. Hydrogen program overview [PDF doc.] (2009).
[3] Avasara *et al.* Electrochim Acta **55**, 4756-71 (2010).
[4] Shao *et al.* J Power Sources **171**, 558-66 (2007).
[5] Avasara *et al.* Electrochemica Acta **55**, 9024 (2010).

Scanning Charge-Transient Microscopy/Spectroscopy

Štefan Lányi[1] and Vojtech Nádaždy[2]

[1] *lanyi@savba.sk, Institute of Physics, Slovakian Academy of Sciences, Bratislava, Slovakia*
[2] *vojtech.nadazdy@savba.sk*

Abstract. The response of semiconductors and dielectrics to voltage pulses resulting in capacitance and/or current transients is a proven method of analysis of defect states in the gap of materials. Whereas the capacitance response reflecting the relaxation of depletion layer in *pn* or *Schottky* junctions requires sufficiently high conductivity, the current or charge transients also from low-conductivity semiconductor structures or insulators can be analyzed. In focus of this contribution is the second method. Recently the sensitivity of a setup was increased to make the method applicable locally [1]. For good reproducibility of data the positioning of the probe, i. e. reproducible probe-to-surface distance or force pressing the tip to the surface, is now ensured using a tuning-fork-based lateral force AFM. We call the instrument Scanning Charge-Transient Microscope (SQTM). We present results obtained on graphene oxide monolayer.

1 Introduction

Since its invention, the scanning probe microscopy has become the probably most frequently used imaging tool, offering up to atomic resolution. Though its ability to correctly image surface morphology developed to a high level, its analytical abilities lag behind microscopies utilizing electron or ion beams. The goal of the present contribution is to introduce the possibility to analyze electrically active defects in semiconductor and dielectric structures.

The defects of interest are e.g. deep levels in the gap of the material or relaxation of injected charge carriers in organic semiconductors. The method we consider in this respect useful is a modification of Deep Level Transient Spectroscopy. It has two main modifications. The original capacitance-transient spectroscopy [2] can be applied to semiconductors with high conductivity, in which it reflects the relaxation of the depletion layer boundary. More generally applicable is the current- or charge-transient modification [3], which can be applied also to less conducting systems.

The temperature scan used in DLTS is not applicable in microscopy, in which analysis of many points is the goal. Instead of it suitable isothermal scans are used.

The method applied macroscopically uses planar electrodes deposited to the surface of the sample and the problem is one-dimensional. If one of the electrodes is replaced by a sharp tip, the geometry becomes three-dimensional. Thus the effective electrode area will change depending on the tip/sample separation in contactless, or the surface deformation in contact mode. Thus precise positioning of the probe is prerequisite to achieve reproducible results.

2 The microscope

The scanner is built from bimorph piezoelements [4]. Its low height enables short connection of the probe to the input. This reduces the capacitance loading and the consequent decrease of sensitivity. The outer electrodes of the parallel bimorphs are grounded, thus forming an effective shield. Active is the central brass electrode. Double-S bending is achieved by inversely polarized ¼ long end sections of the plates.

The probe uses a quartz tuning fork perpendicular to the imaged surface, with a sharpened 80 µm tungsten wire, soldered to one of the electrodes. The tip oscillates parallel with the surface. Operation in AFM mode corresponds to lateral force sensing. The arrangement ensures smaller stray capacitance then would result with fork approximately parallel with the surface. Direct connection of the probe tip to the tuning fork enables two-wire connection, simplifies its construction and exchange of probes.

The preamplifier is a switched integrator. During the excitation pulse the integrating capacitor is shorted, which prevents overloading. The integration takes place on a 70 fF capacitor, in the feedback of FET-input operational amplifier. Integration of 437 electrons yields 1 mV output voltage. The theoretical, though yet not achieved resolution is 67 electrons.

2.1 Operation in AFM mode

Although the role of the tuning fork sensor connected to a phase-locked loop circuit is primarily to control the tip to surface distance, the instrument is at the same time also a lateral force AFM. With a driving voltage of 0,6 mV the tip oscillates with sub-nm amplitude.

A *dc* input current, either leakage through the saample or amplifier input current would sooner or later overload the integrator. Therefore it is periodically discharged shorting the integrator capacitor. At a maximum output voltage of 2 V and 1 pA charging current it has to happen every 140 ms. During the discharging the PLL circuit is blocked to prevent improper reaction.

2.2 Operation in IQTS mode

The charge-transient spectroscopy can operate either in contact- or non-contact mode. In the second case the transients are recorded through the series capacitance formed between the tip and the sample, what reduces the sensitivity. On the other hand, if a large *dc* current (in excess of a few pA) would flow through the sample, contact mode would require too frequent discharging and thus limit the applicable time span of recording the transients.

3 Results

Figure 1 shows an LF AFM image of graphene oxide film, deposited by LB technique to ITO on glass. Figures 2 and 3 show IQT spectra taken in contact- and non-contact mode.

The transients were converted to peaks using the scheme $\Delta Q(t) = C_{\text{int}}\,[U(t) - 3/2U(2t) + 1/2U(4t)]$, which yields the relaxation time $\tau = t_{\max}$. C_{int} is the integrator capacitance. To reduce the noise, 20 scans were averaged. The noise can be further reduced by off-line filtering [1].

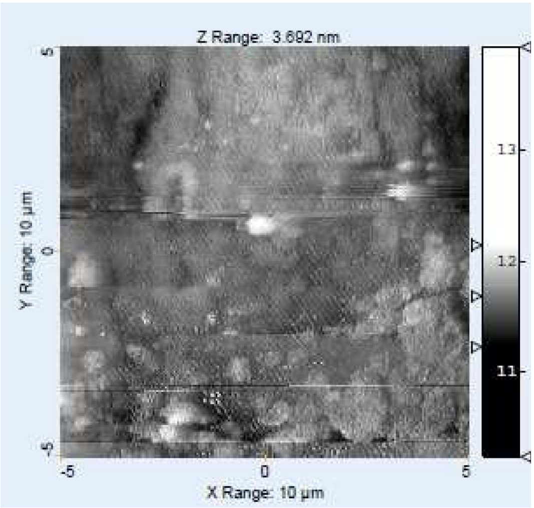

Figure 1. LF AFM image of graphene oxide on ITO/glass.

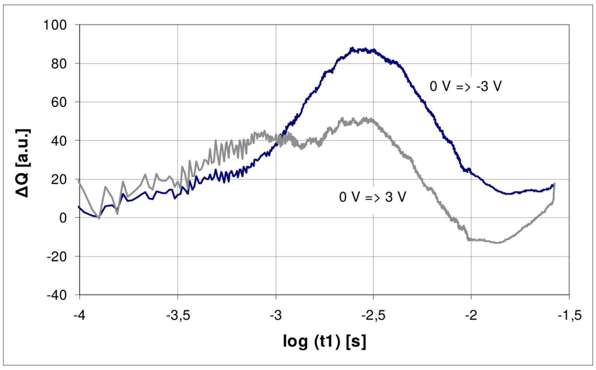

Figure 2. Spectra of graphene oxide in contact mode at zero bias and 3 V excitation pulses of both polarities.

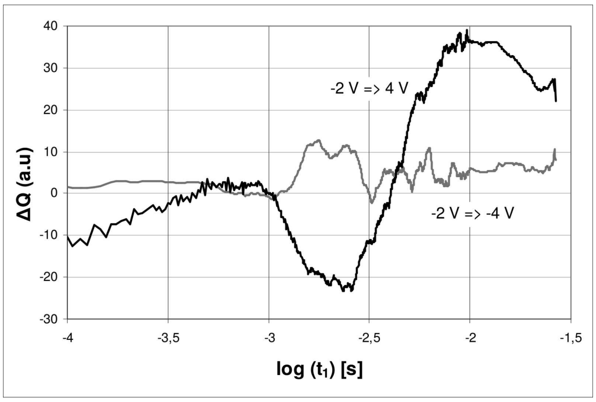

Figure 3. IQT spectra of graphene oxide in non-contact mode.

4 Conclusions

Though the role of probe position control is the reproducible tip/surface separation, the setup is successfully utilised also as a LF AFM. To cover a large range of relaxation times the time span of transients is at least up to approximately tentimes the time of peak maximum $t_{\max}$. In systems, in which the initial state is not affected by preceding excitation, noise reduction may benefit from averaging multiple scans. The slowness of the measurement suggests its application to selected points rather than to the entire sample surface.

Acknowledgement

Support from Research and Development Support Agency contract APVV-0096-11, VEGA Grants 2/0099/14 and 2/0041/11, SAS-TUBITAK JRP 2013/6, and Centre of Excellence SAS FUNMAT is acknowledged.

References

[1] Š. Lányi, V. Nádaždy, Ultramicroscopy **110**, 655 (2010).

[2] D. V. Lang, J. Appl. Phys. **45**, 3023 (1974).

[3] K. I. Kirov, K. B. Radev, Phys. Stat. Sol. (a) **63**, 711 (1981).

[4] Š. Lányi and M. Hruškovic, Rev. Sci. Instrum. **73**, 2923 (2002).

The Relativistic Mean-Field Calculations of the Properties of Light Atomic Nuclei

Jozef Leja[1,2] and Štefan Gmuca[2]

[1] jozef.leja@stuba.sk, Faculty of Mechanical Engineering, Slovak University of Technology, Bratislava, Slovakia
[2] stefan.gmuca@stuba.sk, Institute of Physics, Slovak Academy of Sciences, Bratislava, Slovakia

Abstract. The paper deals with the calculations of the properties of light atomic nuclei. The calculations have been performed in the framework of the relativistic mean-field theory with various model parameterizations. The results of the calculations have been compared with the experimental results.

1 Introduction

The relativistic mean-field theory is a relativistic quantum field theory describing atomic nucleus as a system of relativistic particles interacting through the meson exchange.

2 The Relativistic Mean-Field Theory

The model [1, 2] starts from a Lagrangian density (1) including nucleon field, isoscalar-scalar σ-meson field, isoscalar-vector ω-meson field, isovector-vector ρ-meson field and electromagnetic field.

$$\begin{aligned} L = {} & \overline{\psi}_1 \left(\mathrm{i}\gamma_\mu \partial^\mu - M\right) \psi_i + \\ & + \overline{\psi}_i \left[g_\sigma \sigma - g_\omega \gamma_\mu \omega^\mu - g_\rho \gamma_\mu \vec{\tau} \cdot \vec{\rho}^\mu - e\gamma_\mu \frac{1-\tau_3}{2} A^\mu \right] \psi_i + \\ & + \frac{1}{2}\partial_\mu \sigma \partial^\mu \sigma - \frac{1}{2} m_\sigma^2 \sigma^2 - \frac{1}{4} O_{\mu\nu} O^{\mu\nu} + \frac{1}{2} m_\omega^2 \omega_\mu \omega^\mu - \\ & - \frac{1}{4} \vec{R}_{\mu\nu} \vec{R}^{\mu\nu} + \frac{1}{2} m_\rho^2 \vec{\rho}_\mu \vec{\rho}^\mu - \frac{1}{4} F_{\mu\nu} F^{\mu\nu} - \\ & - \frac{1}{3} b_\sigma \sigma^3 - \frac{1}{4} c_\sigma \sigma^4 + \frac{1}{4} c_\omega \left(\omega_\mu \omega^\omega\right)^2 \end{aligned} \tag{1}$$

The masses M, m_σ, m_ω, m_ρ, the coupling constants g_σ, g_ω, g_ρ, and the selfinteraction constants b_σ, c_σ, c_ω, are the free parameters of the model. The field equations follow from the Euler-Lagrange equations in a standard way. Two approximations are necessary for their solution. The first one is the mean-field approximation introduced by replacing the field operators for mesons and electromagnetic fields by their expectation values. The second one is the no-sea approximation realized by exclusion of the filled Dirac sea of negative energy states.

The nucleon spinor can by written in standard form (2).

$$\psi_i(r,z,\varphi) = \frac{1}{\sqrt{2\pi}} \begin{pmatrix} f_i^+(r,z)\, e^{\mathrm{i}\left(\Omega_i - \frac{1}{2}\right)\varphi} \\ f_i^-(r,z)\, e^{\mathrm{i}\left(\Omega_i + \frac{1}{2}\right)\varphi} \\ \mathrm{i} g_i^+(r,z)\, e^{\mathrm{i}\left(\Omega_i - \frac{1}{2}\right)\varphi} \\ \mathrm{i} g_i^-(r,z)\, e^{\mathrm{i}\left(\Omega_i + \frac{1}{2}\right)\varphi} \end{pmatrix} \zeta_i \tag{2}$$

The ζ_i represents the isospinor and quantum number Ω_i is the eigenvalue of operator $\mathbf{J}_z$. The components of nucleon spinor obey the set of Dirac equations (3–6).

$$\left(M^* + S + V_0\right) f_i^+ + \partial_z g_i^+ + \left[\partial_r + \frac{\left(\Omega_i + \frac{1}{2}\right)}{r}\right] g_i^- = \varepsilon_i f_i^+ \tag{3}$$

$$\left(M + S + V_0\right) f_i^- - \partial_z g_i^- + \left[\partial_r - \frac{\left(\Omega_i - \frac{1}{2}\right)}{r}\right] g_i^+ = \varepsilon_i f_i^- \tag{4}$$

$$\left(M + S - V_0\right) g_i^+ + \partial_z f_i^+ + \left[\partial_r + \frac{\left(\Omega_i + \frac{1}{2}\right)}{r}\right] f_i^- = -\varepsilon_i g_i^+ \tag{5}$$

$$\left(M + S - V_0\right) g_i^- - \partial_z f_i^- + \left[\partial_r - \frac{\left(\Omega_i - \frac{1}{2}\right)}{r}\right] f_i^+ = -\varepsilon_i g_i^- \tag{6}$$

The S and V_0 denote scalar and vector potentials calculated from scalar and vector fields (7,8).

$$S = g_\sigma \sigma \tag{7}$$

$$V_0 = g_\omega \omega_0 + g_\rho \tau_3 \rho_0^{(3)} + e\frac{(1-\tau_3)}{2} A_0 \tag{8}$$

The meson fields and electromagnetic field obey the Klein-Gordon equations (9–12).

$$\left(-\frac{1}{r}\partial_r r \partial_r - \partial_z^2 + m_\sigma^2\right) \sigma = -g_\sigma \rho_S - b_\sigma \sigma^2 - c_\sigma \sigma^4 \tag{9}$$

$$\left(-\frac{1}{r}\partial_r r \partial_r - \partial_z^2 + m_\omega^2\right) \omega_0 = -g_\omega \rho_V + c_\omega \omega_0^3 \tag{10}$$

$$\left(-\frac{1}{r}\partial_r r \partial_r - \partial_z^2 + m_\rho^2\right) \rho_0^{(3)} = g_\rho \rho_I \tag{11}$$

$$\left(-\frac{1}{r}\partial_r r \partial_r - \partial_z^2\right) A_0 = e\rho_P \tag{12}$$

The source terms of Klein-Gordon equations are the scalar density (13), the vector density (14), the isovector density (15) and the proton density (16).

$$\rho_S = 2\sum_{i>0} \left[\left(|f_i^+|^2 + |f_i^-|^2\right) - \left(|g_i^+|^2 + |g_i^-|^2\right)\right] \tag{13}$$

$$\rho_V = 2\sum_{i>0} \left[\left(|f_i^+|^2 + |f_i^-|^2\right) + \left(|g_i^+|^2 + |g_i^-|^2\right)\right] \tag{14}$$

$$\rho_I = 2\sum_{i>0} \tau_3 \left[\left(|f_i^+|^2 + |f_i^-|^2\right) + \left(|g_i^+|^2 + |g_i^-|^2\right)\right] \tag{15}$$

$$\rho_P = 2\sum_{i>0} \frac{(1-\tau_3)}{2} \left[\left(|f_i^+|^2 + |f_i^-|^2\right) + \left(|g_i^+|^2 + |g_i^-|^2\right)\right] \tag{16}$$

The expression for the total energy (17) can be derived from Lagrangian density.

$$E = \sum_i \varepsilon_i - \\ - \frac{1}{2}\int \left(g_\sigma \sigma \rho_S + g_\omega \omega_0 \rho_V + g_\rho \rho_0^{(3)} \rho_I + e A_0 \rho_P\right) \mathrm{d}^3 x + \\ + \int \left(\frac{1}{3} b_\sigma \sigma^3 + \frac{1}{4} c_\sigma \sigma^4 - \frac{1}{4} c_\omega \omega_0^4\right) \mathrm{d}^3 x \quad (17)$$

The pairing correlations have been introduced using the BCS theory [3, 4] and the pairing energy and the centre of mass correction have been included into the total energy.

3 Results and discussion

We have performed calculations of the properties of light even-even nuclei from proton drip-line to neutron drip-line. The calculations have been performed with NL-BA [5], NL3* [6], TM1, TM2 [7] and TMA [8] parameterizations. The calculated binding energies have been compared with the experimental data taken from the latest atomic mass evaluation [9]. The differences between calculated and experimental values obtained for calcium isotopes are plotted in Figure 1.

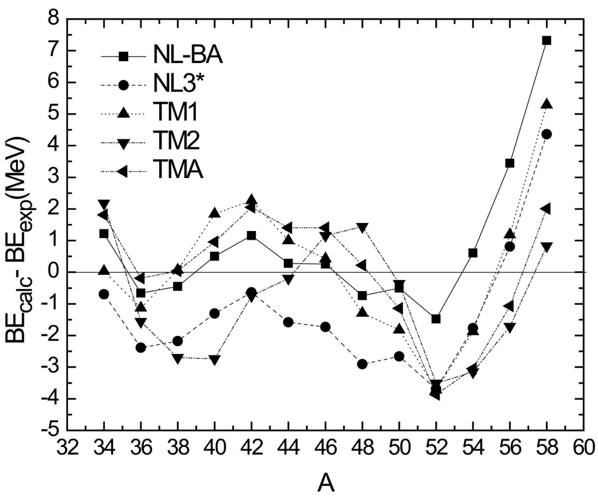

Figure 1. The binding energy differences for calcium isotopes.

We can see the good agreement with experimental data for all parameterizations from ^{34}Ca to ^{54}Ca. In this region NL-BA parameterization demonstrates the best agreement with experimental data. For extremely neutron-rich nuclei ^{56}Ca and ^{58}Ca NL-BA parameterization shows the worst results. For ^{56}Ca the best agreement was achieved with NL3* parameterization and for ^{58}Ca with TM2 parameterization. In proton rich region we can observe the perfect agreement for TM1 parameterization in the case of ^{34}Ca nucleus.

4 Conclusion

The predictions of the relativistic mean-field theory exhibit satisfactory agreement with experimental results in the region of light atomic nuclei from proton drip-line to neutron-drip line. The relativistic mean-field theory represents one of the most successful nuclear models in modern nuclear theory.

Acknowledgments

This work was supported by the Scientific Grant Agency of the Ministry of Education of the Slovak Republic and Slovak Academy of Sciences under the grant VEGA 2/0176/13 and the Slovak Research and Development Agency under the grant APVV-0177-11.

References

Here are some examples for an article and a book:

[1] J. D. Walecka, *Theoretical Nuclear and Subnuclear Physics* (World Scientific, Singapore, 2004).

[2] L. N. Savushkin, H. Toki, *The Atomic Nucleus as a Relativistic System* (Springer, Berlin, 2004).

[3] W. Greiner, J. A. Maruhn, *Nuclear Models* (Springer, Berlin, 1996).

[4] P. Ring, P. Shuck, *The Nuclear Many-Body Problem* (Springer, New York, 1980).

[5] Š. Gmuca, *Proc. 2nd Int. Conf. Fission and Properties of Neutron-Rich Nuclei* (World Scientific, Singapore, 2000), 75–78.

[6] G. A. Lalazissis *et al.* Phys. Lett. B **671**, 36–41 (2009).

[7] Y. Sugahara, H. Toki, Nucl. Phys. A **579**, 557–572 (1994).

[8] Y. Sugahara, *PhD. Thesis*, (Tokyo Metropolitan University, 1995).

[9] G. Audi *et al.*, Chinese Phys. C **36**, 1603–2014 (2012).

Melting Behavior of Two-Dimensional Air-Driven System of Small Magnets

Martin Liščinský[1], Michal Géci[2], and Mária Šviková[3]

[1]martin.liscinsky@gmail.com, Faculty of Electrical Engineering and Informatics, Technical University of Košice, Letná 9, 042 00 Košice, Slovakia
[2]michal.geci@atlas.sk, Faculty of Electrical Engineering and Informatics, Technical University of Košice, Letná 9, 042 00 Košice, Slovakia
[3]svikova@gmail.com, High school of st. Thomas Aquinas, Zbrojničná 3, 040 01 Košice, Slovakia

Abstract. In this work, we study configurational and melting properties of a system of finite number of small disc magnets moving on an air layer produced by an air table to imitate two-dimensional (2D) Wigner-like crystal. By changing the velocity of the air current blown to the air table we influence effective temperature calculated through particle velocities. Our results show, that a 2D hexagonal lattice forms at low temperature while with increasing temperature we can observe a change of the lattice symmetry from hexagonal to square. The dependence of averaged number density of defects on the temperature exhibits sudden increase indicating transition to the liquid phase. Particle trajectories in this phase reveal the surprising square shell structure. Experimental results are compared with a molecular dynamics simulation based on Verlet algorithm.

1 Introduction

The study of self-organization of particles is important for both fundamental research and applications. For example in the fabrication of nano-structured particle systems and in soft-matter physics which include colloids, liquid crystals, foams, granular materials and even biological tissues.

We are used to speak about crystals for systems composed of atoms or molecules. However in 1934 Paul Wigner predicted theoretically that electrons at certain conditions crystallize and form a lattice. In 1979 Wigner crystallization of electrons on the surface of liquid helium was reported [1]. Since that other related systems which exhibit Wigner crystal-like ordering were studied. They are e.g. colloidal systems, dust particles in plasma, 2D superconducting vortex lattice.

The structural and dynamical properties of small classical 2D clusters confined in circular confinement have been a subject of recent experimental studies and computer simulations [2]. It was found that there is a competition between two types of ordering: ordering into triangular lattice structure and ordering into a shell structure, which leads to clusters with interesting self-organized patterns that show concentric shells at small N hexagonal cores surrounded by circular outer shells at large N.

In our work, we study new experimental system, where Wigner–like crystal can be observed. It is a system of finite number of small disc magnets moving on an air layer produced by an air table. Our work is related also to thermal-like behaviour of granular systems, studied e.g. in [3, 4].

2 Method

In our experiment we place 64 disc magnets on rectangular plexiglass pad with small holes. Magnets repel each other by dipolar magnetic interaction. Magnets are moving freely on an air layer. We can influence their velocities by changing the flow rate of air blown to the air table. We record the system with a webcam and we trace trajectory of each particle by analyzing the video. More details of the method are given in [5] of this proceedings. At constant intensity of air blowing into air table steady state is achieved and we define the effective temperature $\tau = \left(\sum v_i^2\right)/N$, where v_i is velocity of i-the particle, N is the number of particles.

Second part of this work is devoted to a molecular dynamics simulation of a similar system. We used the Verlett algorithm [6] to compute the positions of the magnetic dipoles in 2D system. Magnetic moments of the particles are perpendicular to the plane so they interact by repulsive dipolar magnetic interaction with each other and also with the square system border.

3 Results

In the plot of trajectories in Figure 1 we can notice that at low temperature 2D hexagonal lattice is formed, particles oscillate only around their equilibrium positions in both the experiment and the simulation. Increase of the temperature causes the movement of particles around the whole system area and despite of that trajectories create underlying square lattice with regions of larger particle presence probability.

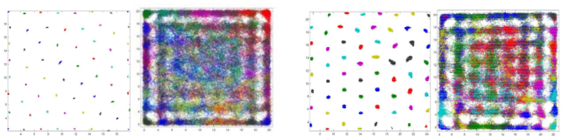

a) b)

Figure 1. a) Particle trajectories from the simulation. $\tau = 0.15\,\mathrm{cm^2s^{-2}}$ (left), $\tau = 12\,\mathrm{cm^2s^{-2}}$ (right). b) Particle trajectories from the experiment. $\tau = 0.6\,\mathrm{cm^2s^{-2}}$ (left), $\tau = 12.9\,\mathrm{cm^2s^{-2}}$ (right).

The topological defects play a role in melting process. In Voronoi diagrams shown in Figure 2 the defects (non six-sided cells) are marked by green colour for sevenfold and by blue colour for fivefold coordination number. Figure 3 plots the dependence of averaged number density of defects on effective temperature where suddden change of the slope indicates transition to the liquid phase.

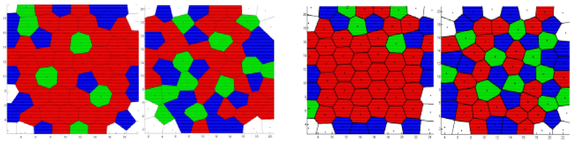

a) b)

Figure 2. a) Voronoi diagrams from the simulation. $\tau = 0.15\,\mathrm{cm}^2\mathrm{s}^{-2}$ (left), $\tau = 12\,\mathrm{cm}^2\mathrm{s}^{-2}$ (right). b) Voronoi diagrams from the experiment. $\tau = 0.6\,\mathrm{cm}^2\mathrm{s}^{-2}$ (left), $\tau = 12.9\,\mathrm{cm}^2\mathrm{s}^{-2}$ (right).

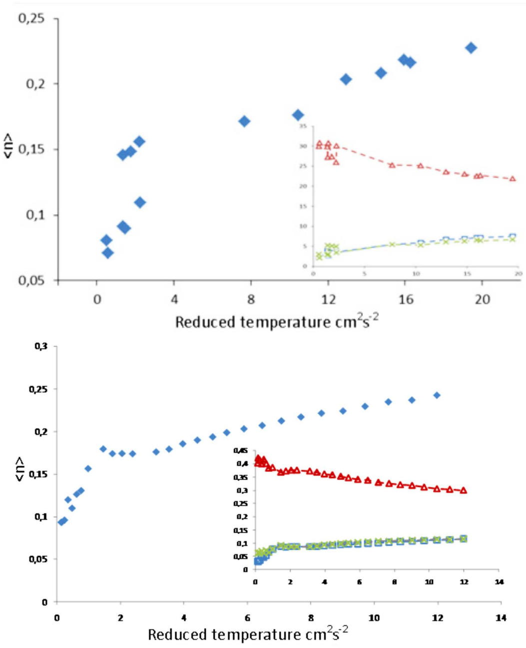

Figure 3. Averaged number density of defects vs reduced temperature. Insert: Plot of number of n-fold coordinated particles in dependence on temperature. With increasing temperature the amount of particles with 6 (red) neighbours decreases and amount of particles with 5 (blue) and 7 (green) neighbours; a) experiment b) simulation.

The increase of the temperature causes the movement of particles around the whole system area and despite of that trajectories create underlying square lattice with regions of larger particle presence probability. We suppose that it reveals a similar phenomenon as in circular shell structure described in [2]. For a better illustration of the underlying square lattice in the liquid phase, we made a program to draw the probability of particle presence in a 3D graph. Here we can clearly see the square symmetry of areas with higher probability of a particle presence. However it looks more like a square shell structure, rather than a regular square lattice. The particle diffusion arises first in the square shells while inter shell diffusion is less probable. This hopping process is more

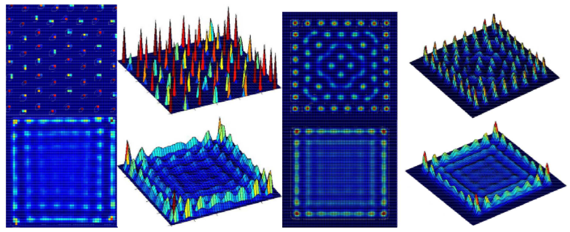

a) b)

Figure 4. a) Voronoi diagrams from the simulation. $\tau = 0.15\,\mathrm{cm}^2\mathrm{s}^{-2}$ (left), $\tau = 12\,\mathrm{cm}^2\mathrm{s}^{-2}$ (right). b) Voronoi diagrams from the experiment. $\tau = 0.6\,\mathrm{cm}^2\mathrm{s}^{-2}$ (left), $\tau = 12.9\,\mathrm{cm}^2\mathrm{s}^{-2}$ (right).

probable in the centre of the system area than near the border.

4 Conclusion

We have studied the melting behaviour in experimental two–dimensional square system of small disc magnets with repulsive dipolar interaction moving on an air layer. The results of experiment we compared with molecular dynamics simulation and similar features were found. 2D hexagonal lattice forms at low temperature. The dependence of averaged number density of defects on the temperature exhibits sudden increase indicating transition to the liquid phase. Particle trajectories in this phase reveal the surprising square shell structure. Our work belongs to a broad, intensively studied region of self organization phenomena in systems of particles interacting through various types of interactions.

References

[1] C. Grimes, G. Adams, Phys. Rev. Lett. **42**, 795 (1979).

[2] M. Kong, B. Partoens, F. M. Peeters, Phys. Rev. E, **67**, 021608, (2003).

[3] R. P. Ojha, P. A. Lemieux, P. K. Dixon, A. J. Liu, D. J. Durian, Nature **427**, 521 (2004).

[4] P. M. Reis, R. A. Ingale, M.D. Shattuck, Phys. Rev. Lett. **96**, 258001 (2006).

[5] M. Géci, M. Liščinský, M. Šviková, see contribution in this proceedings, p. 37.

[6] F. Ercolessi. *A molecular dynamics primer.* WWW: http://www.fisica.uniud.it/~ercolessi/md/md/node30.html.

Photoelectric transport properties of BiOX (X = Cl, Br, I) semiconductors

D. Lotnyk[1], V. Komanicky[1], V. Bunda[2], and A. Feher[1]

[1]*dmytro.lotnyk@student.upjs.sk, Centre of Low Temperature Physics, Faculty of Science, P. J. Šafarik University & IEP SAS, Park Angelinum 9, 041 54 Kosice, Slovakia*
[2]*Transcarpatian State University, Uzhorod, Ukraine*

Abstract. In this work transport properties of photosensitive semiconductors bismuth oxyhalides BiOX (X = Cl, Br, I) single crystals were investigated. We chose these compounds because they exhibit promising magnetooptical properties and are good substrates for both low temperature superconductor (Nb) and high temperature superconductor ($YBa_2Cu_3O_{7-\delta}$) thin films. We experimentally obtained temperature dependences of resistivity for BiOX single crystals without laser excitation and under laser excitation. We used lasers with wavelength 532 nm (or 2.33 eV) and 640 nm (1.93 eV); and measurements were performed in a in-plane and out-of-plane geometry; at a zero and 1T magnetic fields. The most promising results were obtained for BiOI sample under both 532 nm and 640 nm laser excitations. For this sample metal-insulator transition was observed. Such behavior could be explained by the lowest indirect energy band from all three studied semiconductors gap ($E_{g(\mathrm{BiOI})} = 1.85\,\mathrm{eV}$; $E_{g(\mathrm{BiOBr})} = 2.76\,\mathrm{eV}$; $E_{g(\mathrm{BiOCl})} = 3.44\,\mathrm{eV}$) and the lowest Debye temperature $\theta_D \approx 146\,\mathrm{K}$ ($\theta_D \approx 168\,\mathrm{K}$ for BiOBr and 205 K for BiOCl).

1 Motivation

In order to study electrical properties of photosensitive semiconductor/superconductor heterostructures it is necessary to obtain transport properties of photosensitive semiconductors. We chose bismuth oxyhalides BiOX (X = Cl, Br, and I) single crystals due to their promising magneto-optical properties [1]. We also chose these materials because of their following advantages:

1. surface smoothness makes them suitable deposition substrates for both low temperature superconductor (Nb) and high temperature superconductor ($YBa_2Cu_3O_{7-\delta}$);
2. they contain oxygen and do not further oxidize even on air at elevated temperature. For this reason they should not cause oxygen deficiency in oxygen containing superconductors;
3. crystalline structure is similar to YBaCuO (see Table 1), in particular, BiOX and YBCO are layered compounds with similar lattice parameters.

2 Crystalline structure

The crystallinity and morphology of the BiOX crystals was examined by X-ray diffraction (XRD), and field effect-scanning electron microscopy (FE-SEM). The lattice parameters were refined by X-ray powder diffraction data with a Si internal standard (high purity) and by using a least square method. All of the sharp diffraction peaks in the XRD patterns were perfectly indexed as pure phase of BiOCl, in good agreement with the standard JCPDS file (No. 06-0249) of BiOCl. A Laue photograph taken parallel to the large face of the platelets showed clearly a fourfold symmetry axis characterizing (001) planes of a matlockite tetragonal PbFCl-like structure (see Figure 1) $D^7_{4h} - P^4_n mm$ (No. 129) [2] with two formula units in the unit cell and the following atom position [3]:

- $2Bi$ *in position* $(2c)$ $(0, 1/2, z)(1/2, 0, \bar{z})$ *of* $4mm$ (C_{4v}) *symmetry*
- $2O$ *in position* $(2a)$ $(0, 0, 0)(1/2, 1/2, 0)$ *of* $\bar{4}2m$ (D_{2d}) *symmetry*
- $2X$ *in position* $(2c)$ $(0, 1/2, z')(1/2, 0, \bar{z}')$ *of* $4mm$ (C_{4v}) *symmetry*

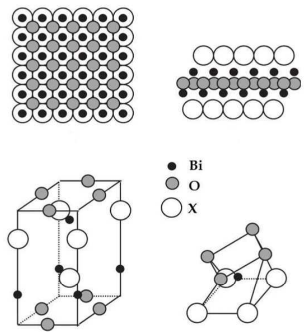

Figure 1. Structure unit cell for BiOX compound.

Compound	Structure	Lattice parameters, A
BiOCl	Tetragonal	$a = b = 3.883$, $c = 7.347$
BiOBr	Tetragonal	$a = b = 3.915$, $c = 8.076$
BiOI	Tetragonal	$a = b = 3.984$, $c = 9.128$
Nb	FCC	$a = b = c = 3.3004$
YBCO ($\delta < 0.4$)	Orthorhombic	$a = 3.82$, $b = 3.89$, $c = 11.68$
YBCO ($\delta > 0.4$)	Tetragonal	$a = b = 3.84$, $c = 11.68$

Table 1. Comparative table of lattice parameters of BiOX, Nb and $YBa_2Cu_3O_{7-\delta}$.

3 Experimental methods

Electric transport measurements were performed at the commercial Physical Property Measurement System (PPMS) using external electrometer Keithley 6517B. Schematic diagrams of experimental and measurement set-ups. Thermal contact was implemented by installing sample on a massive Cu plate. Sample was insulated from Cu plate using thin sapphire plate. Temperature and magnetic field were controlled by PPMS apparatus interfaced with PC through QD server program provided by Quantum Design. Resistivity was measured by electrometer Keithley 6517B. Laser excitations with 532 nm (2.33 eV) and 640 nm (1.94 eV) were obtained by two CNI laser devices with the power 300 mW and 200 mW, respectively.

4 Results and discussions

Figure 2 shows the temperature dependences of the photoconductivity (a) and conductivity for BiOI sample in out-of-plane and in-plane geometry, respectively. As one can see laser excitation (532 nm and 640 nm) significantly improves conductivity properties of the considered samples (green and red curves). We can see the colossal increase in photoconductivity (up to 1000 times) obtained in BiOI at temperatures near 10 K for both geometries. Such behavior could be explained by the lowest indirect energy band from all three studied semiconductors gap ($E_{g(\mathrm{BiOI})} = 1.85$ eV; $E_{g(\mathrm{BiOCl})} = 2.76$ eV; $E_{g(\mathrm{BiOBr})} = 3.44$ eV) and the lowest Debye temperature $\theta_D \approx 146$ K ($\theta_D \approx 168$ K for BiOBr and 205 K for BiOCl). High conductivity plateau observed at temperatures near 90 K at both excitations could be useful for investigating transport properties of photosensitive semiconductor/high temperature superconductor (e.g. $YBa_2Cu_3O_{7-\delta}$) heterostuctures under laser excitation while low resistivity behavior under green laser excitation was observed down to 4 K which allows to investigate transport properties of photosensitive semiconductor/low temperature superconductor (e.g. Nb) heterostuctures.

5 Conclusions

1. The most promising results were obtained for BiOI sample under both 532 nm and 640 nm laser excitations. For this sample metal-insulator transition was observed. Such behavior could be explained by the lowest indirect energy band from all three studied semiconductors gap $E_{g(\mathrm{BiOI})} = 1.85$ eV and the lowest Debye temperature $\theta_D = 146$ K.

2. Low resistivity behavior under green laser excitation in BiOI sample allows to investigate transport properties of photosensitive semiconductor/low temperature superconductor (e.g. Nb) heterostuctures while investigating of the transport properties of photosensitive semiconductor/high temperature superconductor (e.g. $YBa_2Cu_3O_{7-\delta}$) heterostuctures is possible under both laser excitations.

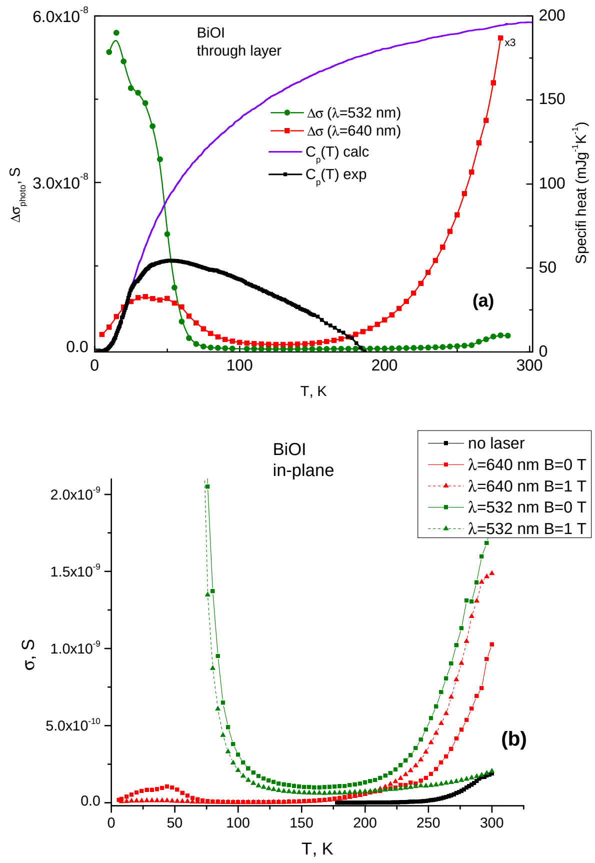

Figure 2. Temperature dependence of excess conductivity for BiOI in out-of-plane geometry (a) and temperature dependence of conductivity in in-plane geometry.

Acknowledgments

This work was supported by the ERDF EU (European Union European regional development fond) grant, under the contract No. ITMS26220220186 and ERDF EU project No. ITMS26220120005.

References

[1] V. V. Bunda, S. O. Bunda, Superconductors – Properties, Technology, and Applications, 323–341 (2012).

[2] H. P. Beck, T. Beyer, Zeitschrift für Kristallographie **221**, 565–571 (1997).

[3] D. M. Bercha, G. D. Puga and A. N. Borets, Physica Status Solidi (B) **55**, 69–78 (1973).

Alkali Intercalation of Highly Ordered Pyrolytic Graphite in Ammonia Solution

Bence G. Márkus[1] and Ferenc Simon[1†]

[1]Department of Physics, Budapest University of Technology and Economics, P.O. Box 91, H-1521 Budapest, Hungary
[†]f.simon@eik.bme.hu

Abstract. We report the intercalation of highly ordered pyrolytic graphite (HOPG) with alkali atoms (Li and K) using liquid ammonia. While the liquid ammonia alkali intercalation route of carbonaceous compounds is well known, to our knowledge it is the first report with the aim to intercalate HOPG. We characterize the successful intercalation by the apparent color change of the samples and the occurrence of the electron spin resonance signal due to the electron charge transfer. It is suggested that this synthesis route may facilitate the chemical exfoliation of graphite which could lead to high quality and defect free graphene.

1 Introduction

Alkali atom intercalation of carbonaceous phases has lead to the discovery of several compelling physical phenomena including e.g. superconductivity at relatively high temperatures (T_c = 11.5 K in CaC_6 [1] and T_c = 33 K in Cs_2RbC_{60} [2]), spin-density wave states [3], one-dimensional polymers [4]. Concerning applications, the use of Li intercalated graphite is widespread as anode in Li-ion batteries. More recently, the alkali atom intercalation found an important application as a first step toward chemically exfoliated graphene [5–7]. The latter material is prospective for a broad range of applications.

Conventional intercalation of graphite with alkali atoms include the vapor phase method, which is useful for the heavier alkali element (K, Rb, and Cs)[8]. Therein an excess amount of the alkali atoms are kept in a sealed quartz or glass ampoule at elevated temperatures together with the graphite flakes or powder. The alkali-graphite stages are controlled by the relative temperature between the graphite and the alkali atoms [8]. This method is however more difficult for Li and Ca as these have higher boiling temperatures where the alkali atoms react with the quartz ampoule. Li intercalation of graphite was successfully performed using stainless steel containers [9]. An alternative method is the so-called immersion one; therein graphite is immersed into molten Li [10–12] (or Ca:Li mixture for the synthesis of CaC_6 [1]). However, this method has several limitations: i) there is a relatively narrow temperature window for Li intercalation between around $350 - 400°$C as at higher temperature Li forms carbides [10], ii) even around 400°C, the intercalation requires several hours, iii) the method is only conceivable for HOPG disks as Li covers the sample surface, iv) control of the staging phenomenon is more difficult as depends sensitively on the temperature.

Herein, we report on a novel intercalation method of graphite with Li using liquid ammonia which has several advantages over the conventional methods (vapor or immersion). The method proceeds at sub-zero temperatures i.e. it is carbidization free, it takes only a few minutes, it works on powder samples, too, and in principle it can be performed with a stoichiometric amount of the alkali dopant. We describe the technical details of the method and the characterization of the samples using optical microscopy and electron spin resonance spectroscopy. We also present results with the same method for K intercalation.

2 Experimental

During sample preparation SPI Grade-1 HOPG discs with 3 mm of diameter and $50 - 70$ μm of thickness have been used. Alkali metals were from Sigma Aldrich with a purity of 99.9+%. The used amount of alkali was near stoichiometric (LiC_6 and KC_8). The HOPG and alkali was prepared under argon atmosphere in a dry-box. Special, flask-ended quartz tubes were used to maximize the efficiency of the reaction. The system used for the chemical synthesis is shown in Figure 1.

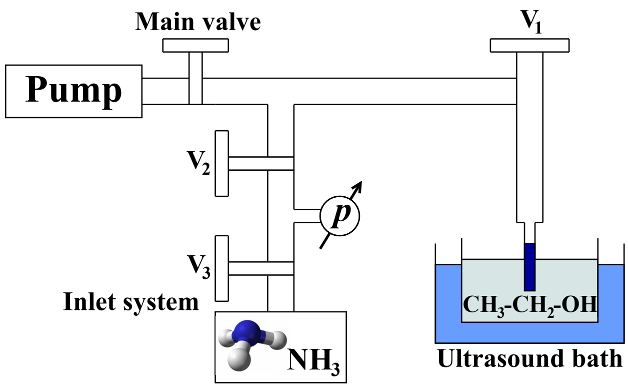

Figure 1. The setup used for the alkali intercalation of HOPG in liquid ammonia.

After the removal of argon on a vacuum stand, 900 mbar of ammonia was introduced to the sample. Liquid ammonia condenses on the sample as long as it is kept around −50°C using an ethanol bath (the latter is cooled with liquid nitrogen). Alkali atoms are known to dissolve very effectively in liquid ammonia [13, 14]. The dissolution is facilitated with an ultrasonic bath which surrounds the ethanol container. The reaction proceeds for about 15 minutes which is followed by pumping out the ammonia while the sample is heated to 200°C for 30 minutes. Finally, the samples are sealed under vacuum in quartz capillaries.

The samples were measured in a Bruker Elexsys E580 X-band ESR spectrometer and photographed in a Nikon Eclipse LV150N optical microscope.

3 Results and Discussion

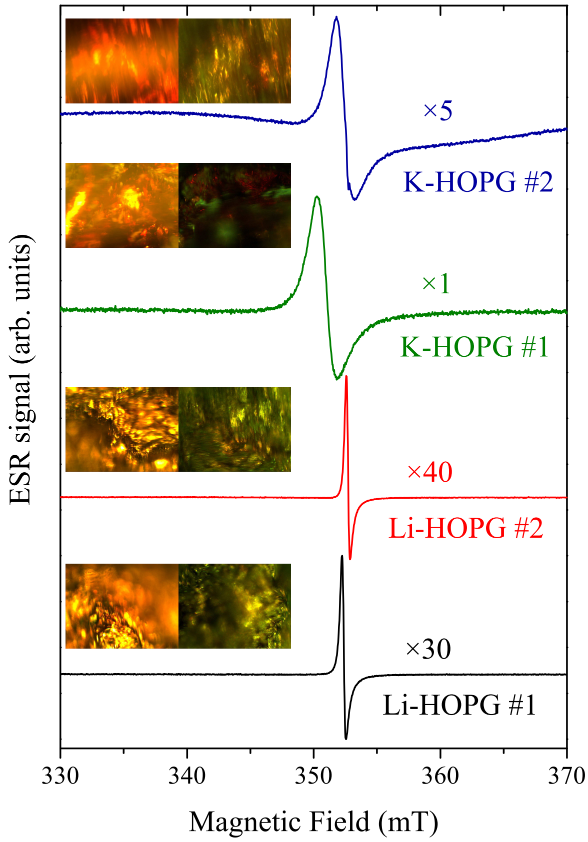

Figure 2. ESR spectra of the prepared samples with high-resolution bright field (on the left) and dark field (on the right) optical microscopy images. Both lithium and potassium intercalated HOPG discs have Dysonian ESR line-shape.

ESR spectra are presented on Figure 2. and the insets show bright field (BF) and dark field (DF) images. We find that lithium intercalated samples have a golden-yellow color thus identified as Stage-I LiC_6. The potassium doped ones are mostly red with some yellowish parts which can be interpreted as a mixture of Stage-I and Stage-II systems. It is known that there exists a metastable state of alkali intercalated graphite with the approximate stoichiometry of AC_{10} [15] which has mostly a red color.

Sample	w (mT)	Phase
Li #1	0.28	27.7
Li #2	0.25	32.5
K #1	1.33	26.4
K #2	1.24	24.7

Table 1. Spectrum parameters of the samples (w width, Phase when Dysonian is approximated with two derivative Lorentzians).

In ESR the characteristic line-shapes of conduction electrons are observed, the so-called Dysonian line-shapes [16]. This attests the successful bulk intercalation of the samples at least down to the skin-depth (about 10 microns [17]). The line is narrower for Li intercalation ($\sim$ 0.26 mT) than for K ($\sim$ 1.29 mT) which is understood in the framework of the Elliott–Yafet theory of spin-relaxation in metals [18, 19], i.e. for Li the spin-orbit coupling is much weaker than for K. We note that pristine HOPG has a linewidth of about 0.6 mT. The ESR parameters of the spectra were determined by fitting and the result is summarized in Table 1. The ESR data is in a good agreement with previous results on vapor and immersion prepared alkali intercalated HOPG measurements [8, 20]. This means that our method provides samples of comparable quality to the standard ones.

Acknowledgements

Work supported by the European Research Council Grant No. ERC-259374-Sylo.

References

[1] T. E. Weller, *et al.*, Nature Physics **1**, 39 (2005).
[2] K. Tanigaki, *et al.*, Nature **352**, 222 (1991).
[3] O. Chauvet, *et al.*, Phys. Rev. Lett. **72**, 2721 (1994).
[4] P. W. Stephens, *et al.*, Nature **370**, 636 (1994).
[5] Y. Hernandez, *et al.*, Nature Nanotechnology **3**, 563 (2008).
[6] J. M. Englert, *et al.*, Advanced Materials **21**, 4265 (2009).
[7] J. M. Englert, *et al.*, Nature Chemistry **3**, 279 (2011).
[8] M. Dresselhaus, G. Dresselhaus, Advances in Physics **30**, 139 (1981).
[9] P. Pfluger, *et al.*, Synthetic Metals **3**, 27 (1981), second Conference on Intercalation Compounds of Graphite.
[10] D. Guerard, A. Herold, Carbon **13**, 337 (1975).
[11] M. Zanini, S. Basu, J. Fischer, Carbon **16**, 211 (1978).
[12] S. Basu, *et al.*, Materials Science and Engineering **38**, 275 (1979).
[13] C. Chambers, A. K. Holliday, *Modern Inorganic Chemistry* (Butterworth, London, United Kingdom, 1975).
[14] N. N. Greenwood, A. Earnshaw, *Chemistry of the Elements* (Butterworth, London, United Kingdom, 1998).
[15] F. J. Salzano, S. Aronson, The Journal of Chemical Physics **47**, 2978. (1967).
[16] F. J. Dyson, Phys. Rev. **98**, 349 (1955).
[17] G. Fábián, *et al.*, Phys. Rev. B **85**, 235405 (2012).
[18] R. J. Elliott, Phys. Rev. **96**, 266 (1954).
[19] Y. Yafet, Physics Letters A **98**, 287 (1983).
[20] P. Lauginie, *et al.*, Physica B+C **99**, 514 (1980).

Transverse momentum spectra fits in Pb Pb collisions at $\sqrt{s_{NN}} = 2.76$ TeV

Ivan Melo[1,3] and Boris Tomášik[2,3]

[1]melo@fyzika.uniza.sk, Physics Department, Faculty of Electrical Engineering, University of Žilina, Univerzitná 1, 010 26 Žilina
[2]boris.tomasik@cern.ch, Faculty of Nuclear Science and Physics Engineering, Czech Technical University, Břehová 7, 11519 Prague, Czech Republic
[3]Fakulta prírodných vied, Univerzita Mateja Bela, Tajovského 40, 974 01 Banská Bystrica, Slovakia

Abstract. We analyse identified hadron spectra in transverse momentum with the help of blast-wave model. Our approach properly includes all resonance decays contributing to hadron production. The fit is performed for $p, \bar{p}, \pi^+, \pi^-, K^+, K^-, K^0, \Lambda$ and separately also for Ξ and Ω.

1 Introduction

Hot nuclear matter (fireball) created in ultrarelativistic heavy-ion collisions at LHC expands and cools down very fast. At $T_c \sim 175$ MeV the fireball undergoes a phase transition from the quark-gluon plasma phase into the hadron gas phase and the hadrons continue their collective expansion and cooling until (in the common interpretation) they first drop out of the chemical and then out of the local thermal equilibrium when their mutual interactions stop and their momenta are frozen-out.

Observed transverse momentum (p_t) spectra carry information about the state of the fireball at the freeze-out, in particular about the (kinetic) freeze-out temperature $T_{\rm kin}$ and the mean transverse expansion velocity $\langle v_t \rangle$. Knowledge of these two quantities for collisions of different centralities and for different hadron species can give us simple and important insights about the fireball evolution and make it easier to compare results of experiments at different energies.

This freeze-out state is described by hydrodynamically inspired parametrisations which differ in details of the assumptions for the density and velocity profiles or the exact shape of the freeze-out hypersurface. In our analysis we shall make use of the so-called blast wave model [1].

An important part of final state hadrons does not originate directly from the fireball but comes from decays of unstable resonances. In spite of this, this contribution is often omitted in calculations and analyses due to its computational complexity [2–4]. Here we compare Monte-Carlo-generated transverse momentum spectra with the data measured in Pb+Pb collisions at $\sqrt{s_{NN}} = 2.75$ TeV by ALICE collaboration [5–7] with resonance contribution included in the simulation. This allows us to deduce the values of kinetic freeze-out temperature and transverse expansion velocity much more reliably than in fits with only direct thermal production included, e.g. [5].

2 Model

For hadron generation we used the package DRAGON [8] with the built-in blast-wave model and the proper treatment of resonances. Chemical equilibrium is assumed to find relative numbers of different hadrons. The spectrum of directly produced hadrons of type i is obtained as

$$E\frac{\mathrm{d}^3N}{\mathrm{d}p^3} = \int g_i \frac{m_t \cosh(\eta - y)}{(2\pi)^3} \frac{1}{\left(\exp\left(\frac{p_\mu u^\mu}{T_{\rm kin}}\right) + s_i\right)} \times \theta\left(1 - \frac{r}{R}\right) r\,\mathrm{d}r\,\mathrm{d}\varphi\,\delta(\tau - \tau_0)\,\tau\,\mathrm{d}\tau\,\mathrm{d}\eta\,. \quad (1)$$

where $\tau = \sqrt{t^2 - z^2}$ is longitudinal proper time, $\eta = \frac{1}{2}\ln((t+z)/(t-z))$ space-time rapidity, r and φ are polar coordinates used in the transverse plane, p_μ, m_t, y are respectively 4-momentum, transverse mass and rapidity of the hadron. We use proper quantum statistical distributions with $s_i = 1$ (-1) for fermions (bosons) and g_i the spin degeneracy. This prescription assumes sharp freeze-out along the hypersurface $\tau = \tau_0$ and uniform density distribution within the radius R.

The expansion of the fireball is represented by the velocity field $u^\mu = (\cosh\eta_t \cosh\eta, \sinh\eta_t \cos\varphi, \sinh\eta_t \sin\varphi, \cosh\eta_t \sinh\eta)$ where the transverse velocity is $v_t = \tanh\eta_t = \eta_f \left(\frac{r}{R}\right)^n$. Here η_f parametrises transverse flow gradient and n the profile of transverse velocity. The mean transverse velocity is then $\langle v_t \rangle = \frac{2}{n+1}\eta_f$. The transverse size R and the freeze-out proper time τ_0 influence total normalisations of transverse momentum spectra which we neglect in this study.

Resonances are also generated as described by (1) and then decay exponentially in time according to their width.

3 Results

We generate Monte Carlo p_t spectra for several hadron species as a function of systematically varied $T_{\rm kin}$, η_f and n parameters. The calculated spectra are then compared to measured data by ALICE collaboration [5–7] and the value of χ^2 is obtained. The minimum χ^2 then yields the best fit parameters. We performed fits for $p, \bar{p}, \pi^+, \pi^-, K^+, K^-, K^0, \Lambda, \Xi$ and Ω hadrons for several centrality classes from the most central collisions (0-5%) to peripheral collisions (40-60%).

First we fitted only $\pi^\pm, K^\pm$, and $p, \bar{p}$ spectra in order to compare our method to the simple blast-wave fits by the ALICE collaboration [5] which do not include resonance decays. DRAGON/ALICE fits for the no resonance case are shown in Table 1 for 0-5% and 40-50% centrality classes. The agreement is good (small differences are induced by the finite steps in the T_{kin}, η_f and n simulation grid). When we switched on the resonance decays, the DRAGON results changed significantly as shown in the last two lines of Table 1. This is in spite of the fact that the p_t ranges used for the fits were chosen by ALICE collaboration to avoid the region where resonances are expected to be important.

centralities [%]	T_{kin} (MeV)	$\langle v_t \rangle$
0–5 (no res.)	98/95	0.645/0.651
40–50 (no res.)	110/112	0.572/0.574
0–5 (res.)	82/–	0.662/–
40–50 (res.)	118/–	0.581/–

Table 1. Best fits of T_{kin} and $\langle v_t \rangle$ illustrating resonance contributions and comparison with no resonance fits

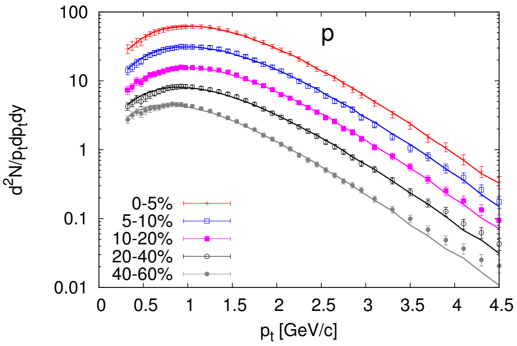

Figure 1. p spectra. Data as points, our fits as lines.

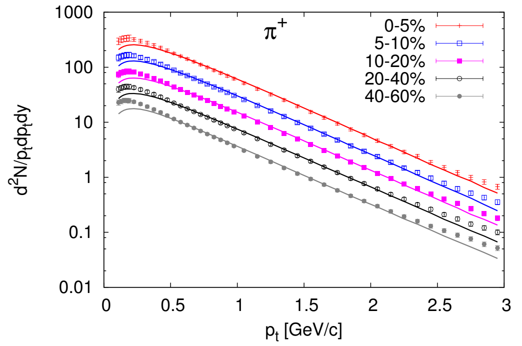

Figure 2. π^+ spectra. Data as points, our fits as lines.

In our subsequent fits we included also K^0 and Λ hadrons. We show results (resonances included) for p and π^+ spectra (normalization is arbitrary) for several centrality classes in Figures 1, 2. At the high p_t end the bins for which our prediction was more than 10 % away from the data were excluded from the fit in order to remove nonthermal effects. At the low p_t end the fits forced us to remove the first 9 bins from the pion spectra – the difference between Monte Carlo and the data here requires further study, probably an introduction of a pion chemical potential. Best fit parameters are summarized in Table 2 for several centrality classes. The temperature rises towards more peripheral events, which is consistent with a picture of a smaller size fireball which decouples earlier while the system is still hot. Also there is little time to build up a significant transverse velocity.

Ξ and Ω hadrons consistently spoil the joint fits with other hadrons and had to be fitted separately, yielding a higher freeze-out temperature $T_{\mathrm{kin}} = 126$ MeV (instead of 98 MeV for other species) for the most central collisions (and likewise for other centralities). This indicates an earlier freeze-out for multiple-strange hadrons.

centralities [%]	T_{kin} (MeV)	$\langle v_t \rangle$	χ^2/N_{dof}
0–5 (res.)	98	0.654	0.21
5–10 (res.)	98	0.649	0.27
10–20 (res.)	106	0.642	0.27
20–40 (res.)	114	0.612	0.29
40–60 (res.)	138	0.548	0.34

Table 2. Best fits of T_{kin} and $\langle v_t \rangle$ for 8 species $(p, \bar{p}, \pi^+, \pi^-, K^+, K^-, K^0, \Lambda)$

We acknowledge financial support by grants APVV-0050-11, VEGA 1/0457/12 (Slovakia) and MŠMT grant LG13031 (Czech Republic). Computing was performed in the High Performance Computing Center of the Matej Bel University in Banská Bystrica using the HPC infrastructure acquired in project ITMS 26230120002 and 26210120002 (Slovak infrastructure for high-performance computing) supported by the Research & Development Operational Programme funded by the ERDF.

References

[1] E. Schnedermann, J. Sollfrank and U. W. Heinz, Phys. Rev. C **48**, 2462 (1993) [nucl-th/9307020].

[2] J. Sollfrank, P. Koch and U. W. Heinz, Phys. Lett. B **252**, 256 (1990).

[3] J. Sollfrank, P. Koch and U. W. Heinz, Z. Phys. C **52**, 593 (1991).

[4] U. A. Wiedemann and U. W. Heinz, Phys. Rev. C **56**, 3265 (1997) [nucl-th/9611031].

[5] B. Abelev *et al.* (ALICE collaboration), Phys. Rev. C **88**, 044910 (2013).

[6] B. Abelev *et al.* (ALICE collaboration), Phys. Rev. Lett. **111**, 222301 (2014).

[7] B. Abelev *et al.* (ALICE collaboration), Phys. Lett. B **728**, 216 (2014).

[8] B. Tomasik, Comput. Phys. Commun. **180**, 1642 (2009) [arXiv:0806.4770 [nucl-th]].

Cascade projects competition for high school students

Ivan Melo[1]

[1]melo@fyzika.uniza.sk, Department of Physics, University of Žilina, Univerzitná 1, 010 26 Žilina, Slovakia

Abstract. Cascade projects is a competition for high school teams of 3–6 students. The teams with help from physicists work on projects from particle physics for several weeks and prepare 20 min presentations which they deliver in their schools. They send videos of their talks to the jury which selects the best teams. The competition is quite popular.

1 Introduction

Cascade projects spread in Slovakia through International Particle Physics Outreach Group (IPPOG), a network of physicists and science educators engaged in informal science education and outreach for particle physics [1]. IPPOG was formed in 1997. Its growing membership currently includes representatives from each member state of CERN, each major experiment at CERN's Large Hadron Collider (LHC) and several physics laboratories in the USA and Europe.

IPPOG's aim is to serve anyone who wants to know more about particle physics, especially educators and students (from school to university), raise standards of global outreach efforts and strengthen understanding and support of particle physics and related sciences across the globe. IPPOG can help students telling them about outreach programs in their area and how to get involved and point them to recommended learning resources on-line. Teachers can benefit from recommended tools and materials for their classroom audiences and scientists from recommended tools and materials to effectively engage young people during talks, presentations, and discussions.

The group meets twice each year: once at CERN and once elsewhere. First IPPOG meetings were almost exclusively used for exchanging education and outreach ideas and resources, where each country or experiment presented their core activities and gained some insight into outreach efforts elsewhere. Later IPPOG became more proactive organizing its own activities such as International Particle Physics Masterclasses and the database of outreach material. At one of the meetings I heard a talk about Cascade projects in Birmingham.

2 Cascade projects

International Particle Physics Masterclasses (MC) offer a chance to high school students to become particle physicists for one day. They come to a nearby university, listen to lectures about particles, do the measurements on real experimental data from LHC and during final video-conference talk to other students elsewhere in the world and physicists at CERN about their results. Masterclasses seem very successful in motivating high school students. However, it is only a one day event and some of students are ready for another adventure. Cascade projects offer a chance for those who would like to get deeper into the realm of particle physics. The format was developed at the University of Birmingham [2].

In the Cascade competition teams of 3–6 high school students work for several weeks on projects on topics from particle physics and cosmology and then make 20 minute presentations at their schools. The teams are helped by mentors (volunteers from the high energy physics community) and their teachers. Teams then send videos of their presentations plus .ppt files to organizers. Jury selects best teams and invites them to the Grand Final. The best team in the Final wins an interesting prize, such as the trip to CERN. The recommended topics typically include:

– What are we all made of? Atoms – Quarks – ?
– Particle Accelerators – How do they work?
– Medical Applications of Particle Accelerators
– Recreating the Early Universe at the LHC
– Antimatter
– Dark matter
– Quantum nature of elementary particles
– Neutrinos
– Are there more than 3 spatial dimensions?
– Search for new particles. Higgs boson
– History of the Universe

Students can also come up with their own topic which organizers have to approve.

In Slovakia [3] we started in 2009 with 4 teams and since then the number of participating teams quickly rose and stabilized at 15–20 teams/year. We use annual International Masterclasses to advertize Cascade projects. Teams are usually mixed (boys and girls). Students have typically 5–6 weeks to work on the projects. They can consult their mentor. Most teams exchanged a few emails with mentors, some did not contact the mentor at all.

Given the time they had, the quality of presentations was good and some of them were very good and funny. Nevertheless, many teams tried to cover too many things and inevitably they were superficial and made many errors. The lesson we try to teach them is that “less is often more“.We also hope to teach them in the future by publishing best presentations on Cascade pages and giving them more time for the projects (3–4 months rather than 6 weeks). The winning team in 2011, e.g., did not cover too much but they tried to be thorough and honest in each concept they introduced and at the same time they were original and

Figure 1. One of the teams at the Grand Final.

funny. As they put it, „we enjoyed it all the way“. And so did the audience.

Figure 2. Jury and audience at the Grand Final.

The format is very successful. Students enjoy working in teams and presenting things. Masterclasses is a good springboard for Cascade. Most of the teams are formed from Masterclass participants. The competition is relatively easy to organize. The first round (presentations at schools) does not require presence of the organizers nor judges. Grand Final is jointly organized by one of the high schools and a university. Teams present their projects in front of the jury and the high school audience.

Best Cascade projects have the qualities we had hoped for. Solid scientific content and fresh, entertaining presentations which are a fun to watch. Team members are often interested in pursuing scientific career.

3 Rules in Slovakia (short version)

1. Teams consist of 2 or 3 students. Each member has to contribute in a significant way.
2. The team registers by filling in the registration form. Chosen topic must be indicated.
3. Recommended topics can be found at `http://fyzika.uniza.sk/cascade/`.
4. You can choose your own topic but we have to approve it.
5. After receiving your registration, we will assign a mentor to your team. Mentor is not your supervisor but rather a good friend on e-mail. Do not be afraid to ask him/her questions.
6. Your presentation should be $20 \pm 2\,\mathrm{min}$ long.
7. Talk only about things which you understand (of course, many things you will understand only to a certain level – in that case do not go beyond that level in your presentation).
8. Presentation must include a `.ppt` (or `.pdf` or `.odp`) element.
9. We expect your audience to be at least 25 students 14–19 years old.
10. After the presentation at your school send us DVD with:
    - video of your presentation in mp4 format
    - `.ppt` (or `.pdf` or `.odp`) file
    - original registration form
    - file with details about audience
11. Send the DVD by . . . . . . date
12. Your presentations will be judged by the jury according to these criteria:
    - scientific content 50%
    - quality of presentation (correct explanation, audible/entertaining, capturing audience interest, good `.ppt` 50%
13. Best 4 teams will be invited to Grand Finals where they will repeat presentations in front of jury and invited high school audience.
14. Videos of your presentations can be published on Cascade web pages.

This work was supported by grant KEGA 022ŽU-4/2013.

References

[1] `http://ippog.web.cern.ch`
[2] `http://www.hep.ph.bham.ac.uk/cascade/`
[3] `http://fyzika.uniza.sk/cascade/`

Anisotropic flow and the reaction plane reconstruction with the CBM experiment

Vasily Mikhaylov[1,2], Andrej Kugler[1], Vasilij Kushpil[1], Selim Seddiki[3], Ilya Selyuzhenkov[3], and Pavel Tlusty[1]

[1]mikhaylov@ujf.cas.cz, Nuclear Physics Institute, Academy of Sciences of Czech Republic, 250 68 Řež, Czech Republic
[2]Czech Technical University in Prague, 166 36 Prague, Czech Republic
[3]GSI Helmholtzzentrum für Schwerionenforschung GmbH, 64291 Darmstadt, Germany

Abstract. The Compressed Baryonic Matter (CBM) experiment at the Facility for Antiproton and Ion Research (FAIR) will study heavy-ion collisions at beam energies 2-35 AGeV. The Projectile Spectator Detector (PSD) of the CBM is a compensating hadron calorimeter, which will measure projectile spectator nucleons and fragments with the aim to determine reaction centrality and reaction plane. Results of particles flow simulation and the reaction plane reconstruction performance with the PSD detector are presented. Directed flow and reaction plane resolution are simulated for Au+Au collisions using four heavy-ion collision event generators: UrQMD, DCM-QGSM, LA-QGSM and HSD. Simulations are performed for the range of beam energies between 2 and 30 AGeV, which covers the expected beam energies of SIS100 and SIS300 accelerator rings at FAIR. Results are compared with the experimental data from AGS E877, E895 and STAR.

1 Motivation

The Compressed Baryonic Matter (CBM) experiment will be a dedicated setup for the measurement of fixed target heavy ion collisions at the future FAIR facility [1]. It is being designed for the investigation of the properties of highly compressed baryonic matter. Projectile Spectator Detector (PSD) is a detector of non-interacting nucleons and fragments emitted at very low polar angles in forward direction in nucleus-nucleus collisions. It will be used to determine the collision centrality and the orientation of an event plane. A precise characterization of the event class is of crucial importance for the analysis of event-by-event observables. The study of collective flow requires the measurement of an event plane.

The PSD is a fully compensating modular lead-scintillator calorimeter which provides very good and uniform energy resolution (Figure 1). The calorimeter comprises 44 individual modules, each consisting of 60 lead/scintillator layers with a surface of $20 \times 20\,\mathrm{cm}^2$. The scintillation light is read out via wavelength shifting (WLS) fibers by Multi-Avalanche Photo-Diodes (APD) with an active area of $3 \times 3\,\mathrm{mm}^2$ and a pixel density of $10^4/\mathrm{mm}^2$.

Figure 1. Layout of the Projectile Spectator Detector for the CBM experiment.

2 Directed proton flow: Input vs. Data

The accuracy of the collision centrality and the reaction plane determination depends on the multiplicity, energy distribution of particles and on the amount of the directed flow v_1 that they carry. Directed flow and reaction plane resolution are simulated for Au+Au collisions using four heavy-ion collision event generators: UrQMD [2], DCM-QGSM, LA-QGSM [3] and HSD [4]. Simulations are performed for the range of beam energies between 2 and 30 AGeV, which covers the expected beam energies of SIS100 and SIS300 accelerator rings at FAIR. Example of directed flow as function of rapidity at 8 AGeV is shown in Figure2. Protons are chosen for the directed flow comparison as the most abundant particles in this region.

The slope of proton directed flow at midrapidity for different collision generators compared with E895 [5] and STAR [6] data is shown in Figur 3. As one can see, directed flow is very different for different collision generators and DCM-QGSM seems to be the most consistent with data all over the SIS100/SIS300 energy range.

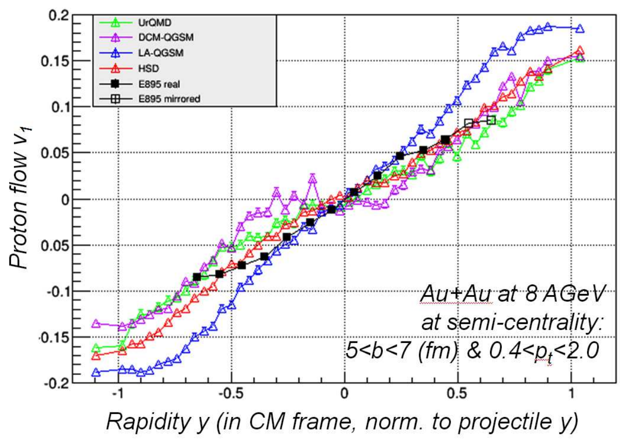

Figure 2. Proton directed flow at 8 AGeV at semi-centrality for different collision generators compared with E895 data.

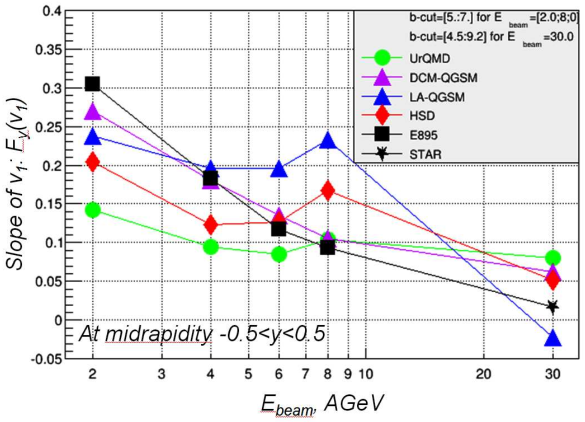

Figure 3. Slope of proton directed flow at midrapidity for different collision generators compared with AGS E895 and STAR data.

3 Reaction plane resolution with PSD

Reaction plane reconstruction performance is simulated in CBMROOT environment with GEANT4 Monte-Carlo simulation framework. PSD performance study is done for three physics cases. Case 1 – check the effect of detector's acceptance with pure Monte-Carlo tracks in the PSD geometrical acceptance ($0.215° < \theta < 5.0°$ for $E_{beam} = 2$–8 AGeV and $0.115° < \theta < 2.7°$ for $E_{beam} = 30$ AGeV). Case 2 and Case 3 – check the effect of detector's bias due to granularity and magnetic field with PSD-geometry applied and magnetic field B turned OFF/ON. Reaction plane resolution in terms of correction factors for the directed flow obtained with DCM-QGSM generator compared with E877 data point is shown in Figure 4. Even though magnetic field introduces more bias than PSD granularity, PSD reaction plane resolution is still good. Correction factors obtained are in good agreement with E877 data [7].

Reaction plane resolution reconstructed with PSD-geometry applied and magnetic field B turned ON for four different event generators is shown in Figure 5. Reaction plane resolution does not differ too much for different event generators.

4 Summary

Directed flow and reaction plane resolution are simulated for Au+Au collisions using four heavy-ion collision event generators: UrQMD, DCM-QGSM, LA-QGSM and HSD for beam energies 2–30 AGeV.

DCM-QGSM generator is the most consistent with data in terms of flow v1 and gives slightly better reaction plane resolution.

All the four event generators are in good agreement with E877 data in terms of reaction plane correction factors. Even though directed flow of protons differs significantly for different event generators and data from AGS E895 and STAR, reaction plane resolution achieved with PSD is very good for all of them.

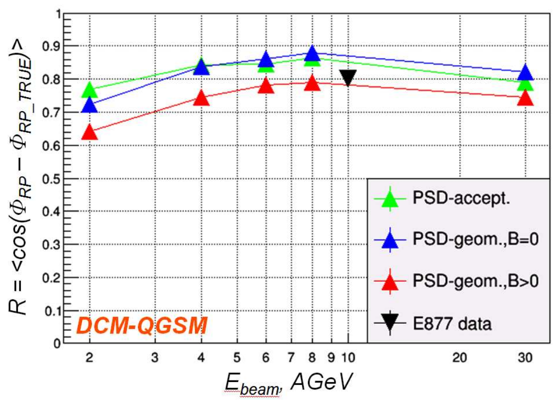

Figure 4. Reaction plane resolution correction factors for the directed flow for different simulation cases compared with E877 data.

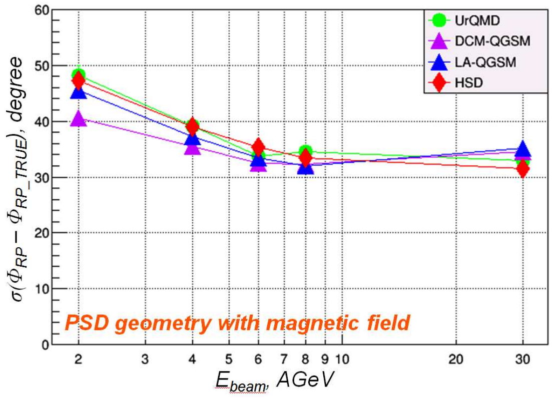

Figure 5. Reaction plane resolution for different collision generators.

Acknowledgments

This work has been supported by the European Community FP7 – Capacities, contract HadronPhysics3 n°283286 and grant MSMT LG12007 of the Ministry of Education of the Czech Republic. We would like to thank V. Friese, M. Golubeva, K. Gudima, E. Bratkovskaya. for their help with collision events generation.

References

[1] FAIR, FAIR Baseline Technical Report 2006, http://www.fair-center.eu/fileadmin/fair/publications_FAIR/FAIR_BTR_6.pdf (2006).

[2] The UrQMD model, http://urqmd.org.

[3] The SHIELD code, http://www.inr.ru/shield/index.html.

[4] The HSD model, http://fias.uni-frankfurt.de/~brat/HSD/index1.html.

[5] H. Liu *et al.* (E895 Collaboration), Sideward Flow in Au + Au Collisions Between 2A GeV and 8A GeV, Phys. Rev. Lett. **84**, 5488–5492 (2000).

[6] L. Adamczyk *et al.* (STAR Collaboration), Beam-Energy Dependence of Directed Flow of Protons, Antiprotons and Pions in Au+Au Collisions, Phys. Rev. Lett. **112** (2014).

[7] J. Barrette, *et al.* (E877 Collaboration), Energy and Charged Particle Flow in 10.8 A GeV/c Au+Au Collisions, Phys. Rev. C **55**, 1420–1430 (1997).

Investigation of the Higgs boson properties

Michaela Mlynáriková[1]

[1]michaela.mlynarikova@gmail.com, Institute of Particle and Nuclear Physics, Faculty of Mathematics and Physics, Charles University in Prague, V Holešovičkách 2, 180 00 Prague 8, Czech Republic

Abstract. We investigated a method for determination of the spin and parity of the Higgs boson in various $\mathrm{H} \to \tau^+\tau^-$ decays, both the hadronic and leptonic. The method is based on the angular and energy correlations of final products from the decays mentioned above. Additionally, we studied the possibility of signal (Higgs boson decay) and background ($\mathrm{Z} \to \tau^+\tau^-$ decay) discrimination in the case of a spin 1 decaying boson.

1 Introduction

The Higgs boson is the last discovered elementary particle predicted by the Standard Model of elementary particles (SM). Existence of the Higgs boson is necessary in the description of the so–called spontaneous electroweak symmetry breaking and in generation of particle masses through Brout-Englert-Higgs mechanism (BEH), see [1, 2].

In July 2012 the ATLAS and CMS experiments at CERN's LHC announced that they had observed a new boson consistent with the Higgs boson [3, 4]. The excess of signal over background was observed in the mass region around 125 GeV. In March 2013, after updating the ATLAS and CMS results, CERN announced that the observed particle was indeed a Higgs boson [5]. However, it remains an open question whether this is the Higgs boson predicted by the SM or possibly the lightest of several bosons predicted by some theories that go beyond the SM. More data are needed to find the answer to this question.

The most important channels for the detection of the Higgs boson at the LHC are: $\mathrm{H} \to \gamma\gamma$, $\mathrm{H} \to ZZ^{(*)}$, $\mathrm{H} \to WW^{(*)}$, $\mathrm{H} \to \tau^+\tau^-$ and $\mathrm{H} \to b\bar{b}$. The Higgs boson decaying to a fermion-antifermion pair is of special interest, since the coupling constant depends on the fermion mass. The decay channel $\mathrm{H}\to \tau^+\tau^-$ can also contribute to the determination of the spin and parity of the Higgs boson.

2 The Higgs boson decays to pair of tau leptons

We explored the energy correlations of the charged final products from the Higgs boson decay to tau lepton pair, and the possibilities of identifying spin and parity of the Higgs boson. We considered Higgs boson decays to pair of tau leptons with these subsequent decays:

$$\mathrm{H} \to \tau^+\tau^- \to (h^+\bar{\nu}_\tau)(h^-\nu_\tau) \tag{1}$$

$$\mathrm{H} \to \tau^+\tau^- \to (\ell^+\nu_\ell\bar{\nu}_\tau)(\pi^-\nu_\tau) \tag{2}$$

$$\mathrm{H} \to \tau^+\tau^- \to (\ell^+\nu_\ell\bar{\nu}_\tau)(\ell^-\bar{\nu}_\ell\nu_\tau) \tag{3}$$

where H is scalar, pseudoscalar, vector or axial vector decaying boson, $h^\pm$ is $\pi^\pm$ or $\rho^\pm$ meson and $\ell^\pm$ is $e^\pm$ or $\mu^\pm$. The flight directions of final state products are correlated due to the correlations between spins of tau leptons and due to the parity violation in weak interactions. SM predicts the existence of one scalar Higgs boson. There are also theories beyond the SM (such as the MSSM) in which a number of Higgs bosons are predicted. The presence of a pseudoscalar Higgs boson in particular represents one of the crucial differences between the SM and its extensions. The energy correlations of a spin 1 decaying particle can be used to distinguish between the $\mathrm{H}\to \tau^+\tau^-$ event and its main background process $\mathrm{Z}\to \tau^+\tau^-$ in the region of not very high Higgs boson masses. All calculations were realized in the first order of perturbation expansion.

3 Calculations and results

We calculated the differential decay width of the CP-even and CP-odd Higgs boson decay to a tau lepton pair, and the subsequent decay to hadrons or leptons. The differential decay width of the vector and axial vector particle decay to a tau lepton pair was also calculated. The differential decay width is given by formula

$$\mathrm{d}\Gamma = \frac{1}{2m_H}\overline{|\mathcal{M}|^2}\,\mathrm{dLIPS}_4,$$

where m_H is the mass of the decaying boson, $\overline{|\mathcal{M}|^2}$ is the spin-averaged matrix element squared and dLIPS_4 is element of the Lorentz invariant phase space of four particles. From this differential decay width, we derived the angular distributions and energy correlations of the charged final products (detailed calculations can be found in [6, 7]). The angular distribution of the charged final products can be written in the general form

$$\frac{\mathrm{d}\Gamma}{\mathrm{d}\cos\theta^+\mathrm{d}\cos\theta^-\mathrm{d}\varphi} \propto \left[K + A\times\left(\cos\theta^+\cos\theta^- + B\times\sin\theta^+\sin\theta^-\cos\varphi\right)\right] \tag{4}$$

where θ^+ (θ^-) is the polar angle of h^+/ℓ^+ (h^-/ℓ^-) in the τ^+ (τ^-) rest frame with respect to the direction of the τ^+ in the Higgs boson rest frame, $\phi = \phi^+ - \phi^-$, where ϕ^+ (ϕ^-) is the azimuthal angle of h^+/ℓ^+ (h^-/ℓ^-) in the τ^+ (τ^-) rest frame with respect to the direction of the τ^+ in the Higgs boson rest frame. The factors K, A and B are listed below.

3.1 Hadronic decays

Parameters of the angular distribution (Equation (4)) A and B for the decay (1) are listed in Table 1. The presence of ρ mesons in the final state results in suppression of the angular dependence of the distribution with respect to the two pion final state topology. For the decay $\mathrm{H} \to \tau^+\tau^- \to (\pi^+\bar{\nu}_\tau)(\rho^-\nu_\tau)$ the angular distribution is suppressed by the factor $\frac{m_\tau^2-2m_\rho^2}{m_\tau^2+2m_\rho^2}$

decaying boson	A	B
scalar	1	-1
pseudoscalar	1	1
vector	$-\frac{m_H^2-2m_\tau^2}{m_H^2+2m_\tau^2} \approx -1$	$\frac{2m_\tau^2}{m_H^2-2m_\tau^2} \approx 10^{-4}$
axial vector	-1	0

Table 1. Parameters of the angular distributions for the decay $\mathrm{H} \to \tau^+\tau^- \to (\pi^+\bar{\nu}_\tau)(\pi^-\nu_\tau)$ and constant factor $K = 1$.

and in the case of the $\mathrm{H} \to \tau^+\tau^- \to (\rho^+\bar{\nu}_\tau)(\rho^-\nu_\tau)$ decay the angular distribution is suppressed by the term $\left(\frac{m_\tau^2-2m_\rho^2}{m_\tau^2+2m_\rho^2}\right)^2$.

From Table 1 we can see that CP-even (scalar) and CP-odd (pseudoscalar) Higgs boson differ in the sign of B in the formula (4). The $(\sin\theta^+ \sin\theta^- \cos\varphi)$ term is strongly suppressed in the case of spin 1 particle decay in all of the considered processes with charged hadrons in the final state. In other words, same direction of the transverse momenta components of the final state hadrons are preferred in pseudoscalar Higgs boson decays ($\varphi = 0$), whilst the opposite is true in scalar Higgs boson decays ($\varphi = \phi$). The energy correlations are identical for both of the considered spin 0 particles - regardless of whether the Higgs boson is scalar or pseudoscalar particle. Likewise, the distributions are also identical for both of the considered spin 1 particles, the vector and axial vector Higgs boson.

In the case of the spin 0 decaying boson, the preferred energy distribution is for one of the charged hadrons to carry the maximum energy of $\frac{m_H}{2}$, whilst the other carries the minimum energy. In the case of the spin 1 decaying boson the preferred energy distribution is for both charged hadrons to carry either the maximum energy or the minimum energy.

3.2 Semileptonic decays

Parameters of the angular distribution (Equation (4)) A and B for the decay (2) are listed in Table 2.

decaying boson	A	B
scalar	-1	1
pseudoscalar	-1	-1
vector	$\frac{m_H^2-2m_\tau^2}{m_H^2+2m_\tau^2} \approx 1$	$\frac{2m_\tau^2}{m_H^2-2m_\tau^2} \approx 10^{-4}$
axial vector	1	0

Table 2. Parameters of the angular distribution for the decay $\mathrm{H} \to \tau^+\tau^- \to (\ell^+\bar{\nu}_\tau\nu_\ell)(\pi^-\nu_\tau)$ and constant factor $K = 3$.

The contribution of φ is strongly suppressed in this decay. In the case of the spin 0 decaying boson, the preferred energy distribution is for both charged decay products to carry the minimum energy. In the case of the spin 1 decaying particle the preferred energy distribution is for the charged lepton to carry the minimum energy, whilst the charged pion carries the maximum energy.

3.3 Leptonic decays

Parameters of the angular distribution (Equation (4)) A and B for the decay (3) are listed in Table 3.

decaying boson	A	B
scalar	1	-1
pseudoscalar	1	1
vector	$-\left(\frac{m_H^2-2m_\tau^2}{m_H^2+2m_\tau^2}\right)^2 \approx -1$	$\frac{2m_\tau^2}{m_H^2-2m_\tau^2} \approx 10^{-4}$
axial vector	-1	0

Table 3. Parameters of the angular distribution for the decay $\mathrm{H} \to \tau^+\tau^- \to (\ell^+\bar{\nu}_\tau\nu_\ell)(\ell^-\nu_\tau\bar{\nu}_\ell)$ and constant factor $K = 9$.

Contribution of angle φ is strongly suppressed in this decay. The highest probability scenario is for both charged leptons to carry from this decay the minimum energy in the case of a spin 0 as well as spin 1 decaying boson.

4 Conclusion

The energy distribution can be used to determine the spin and parity of the decaying particle in the $\mathrm{H} \to \tau^+\tau^-$ decay, in particular in discriminating between the spin 0 and spin 1 decaying boson. However, the volume of existing data is currently not large enough to ascertain a statistically significant result. We expect about ten times larger statistics to be obtained by the LHC which is scheduled to start up again in 2015, operating at its design energy of 7 TeV per beam.

Acknowledgments

I would like to thank to my supervisor Mr. Rupert Leitner for leading my master's thesis, for his suggestions, help and support. Financial support by the grant of Ministry of Education, Youth and Sport of the Czech Republic under the reference LG13009 is acknowledged.

References

[1] F. Englert, R. Brout, *Broken symmetry and the mass of gauge vector mesons*, Selected Papers on Gauge Theory of Weak and Electromagnetic Interactions, 127 (1981).

[2] P. W. Higgs, *Broken symmetries, massless particles and gauge fields*, Physics Letters **12**, 132–133 (1964).

[3] ATLAS Collaboration, *Observation of a new particle in the search for the Standard Model Higgs boson with the ATLAS detector at the LHC*, Physics Letters B **716** 1–29 (2012).

[4] CMS Collaboration, *Observation of a new boson at a mass of 125 GeV with the CMS experiment at the LHC*, Physics Letters B **716**, 30–61 (2012).

[5] ATLAS Collaboration, *Evidence for the spin-0 nature of the Higgs boson using ATLAS data*, arXiv:1307.1432 (2013).

[6] T. Davídek, R. Leitner, V. Shmakova, Úhlové korelace v rozpadu H→ $\tau^+\tau^-$, CZ-SK Top meeting Praha 2008 (2008).

[7] M. Mlynáriková, *Investigation of the Higgs boson properties with the ATLAS experiment* (Master's thesis, 2014).

Preliminary results of pion induced reaction with carbon and polyethylene targets obtained by HADES-GSI in 2014

Pablo Rodríguez-Ramos[1,2] for the HADES collaboration

[1]ramos@ujf.cas.cz, Nuclear Physics Institute, Academy of Sciences of the Czech Republic, Řež, Czech Republic
[2]Czech Technical University in Prague, Faculty of Nuclear Sciences and Physical Engineering, Prague, Czech Republic

Abstract. In the summer of 2014 HADES was measuring with secondary pion-beam with the aim to measure dielepton radiation from baryonic resonances. Most of the beam time was dedicated to measurement of e^+e^- production from PolyEthylene target at pion beam momentum of 0.69 GeV/c. In addition we run part of the time with pure carbon target to allow precise subtraction of carbon contribution to deduce the inclusive e^+e^- production on hydrogen.

1 Introduction

The HADES spectrometer is installed at SIS18 synchrotronin GSI Darmstadt, Germany. It is designed to measure systematically production of electron-positron pairs in elementary and heavy-ioncollisions at SIS18 energy range. It covers almost full azimuthal angle and polar angle $18° - 85°$.

2 Motivation

A modification of hadron masses and their lifetimes in nuclear matter at normal density and zero temperature with respect to the values measured in vacuum has been predicted by recent theoretical calculations to occur as a precursor phenomenon of the chiral symmetry restoration that should take place at high density and temperature.

3 Experimental Layout

We used PE as well as Carbon targets at pion beam momentum of 656 MeV/c, 690 MeV/c, 748 MeV/c, 800 MeV/c, see Table 1.

Target	p[MeV/c]	sum events	Data
PE	690	774.7	175.56
PE	748	76.5	11.61
PE	656	42.4	14,08
PE	800	52.4	7,48
C	690	115,7	13,06
C	800	41,2	6,27
C	748	42,2	6,8
C	656	41,9	14,75

Table 1. Collected statistics in beam time Aug14/Sep14.

3.1 Pion-Beam

The addition of a secondary pion beam to the already available proton and heavy ion beams will allow to study properties of hadrons with the same detector system at different nuclear matter densities produced by pion, proton and HI beams. In the first step, pions are produced by the interaction of an intense primary beam of N on a thick target of C. The outgoing spectrum of pions is widely open both in momentum and in angle [1]. The pion production target is located in the main beam-line coming from the synchrotron, see Figure 1. A primary N beam intensity of $6.0 \cdot 10^{10}$ $pions/spill$ with a 10 s total spill length, producing a pion beam intensity in a range of $1.2 \cdot 10^5 - 4.4 \cdot 10^5$ $pions/spill$.

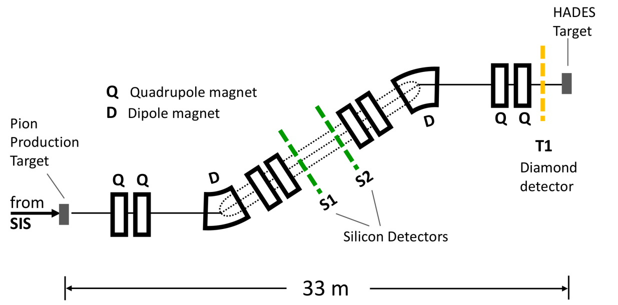

Figure 1. Schematic drawing of the pion beam-line.

3.2 Targets

Properties of the targets are given in Table 2. We used it to calculate the no. of carbon atoms in each target to further deduce a factor for subtraction the C contribution from the PE=C_2H_4 target, to obtain correct yield of reaction with hydrogen. Using the corresponding factor $f = (No.\ C\ atoms\ in\ PE/No.\ C\ atoms\ in\ C) = 0.78$ taken from Table 2, we can subtract finally the C contribution from PE using the formula: $H = PE - f \cdot C$.

Target	PE= C_2H_4	C
Diameter/cm	1.2	1.2
Length/cm	4.6	2.52
M/(g/mol)	28	12
Density/(g/cm^3)	0.93	1.85
No. of carbon atoms	$18.4 \cdot 10^{22}$	$23.4 \cdot 10^{22}$

Table 2. Properties of the targets.

3.3 Selection of elastic events

We want to normalized the yield using the πp elastic scattering. In the first plot we see a mixture of all the particles produced in the PE target, doing the properly cuts, we select these ones in which we are interested, in this case we want to study the pion-proton elastic collisions from PE target, making a cut in the angle $\Delta\phi = 180°$ between p and π^-. We isolated the pions and the protons from elastic scattering of PE target to further normalize the yield with the number of pions. Resulting plot is shown in the lower panel, see Figure 2.

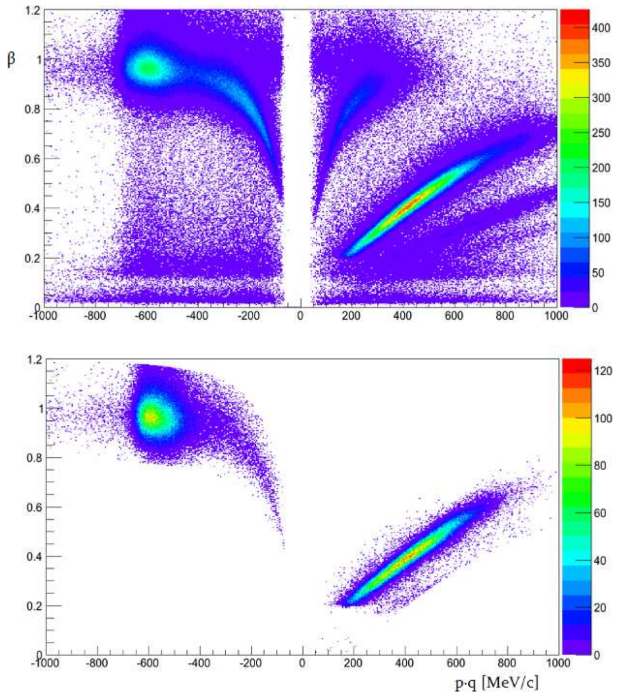

Figure 2. PE target plot of β vs. Momentum · Charge with cut in $\Delta\phi = 180° \pm 5°$.

3.4 Subtract Carbon from PE target

To subtract the C from the PE target the first of all we have to normalized the signal with the number of pions that go through START detector, Signal-scaled=Inv.Mass-CB/Livetime where Livetime=(M2&&START/M2&&START-rate), where M2&&START is the number of triggers, and M2&&START-rate with the correction of dead time. The yield it will be finaly normalized by Signal-scaled/START.

In this plot we can see the spectra of elastically scatter pions already normalized by the no. of pions START. It show us that for different pion beam momenta the normalization is different. Looking for a reason, we think that it can be because the target was smaller than the START detector, that means that there were pions hitting the START detector but not the target.

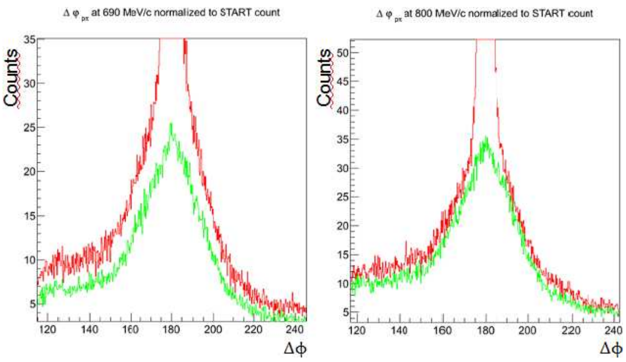

Figure 3. $\Delta\phi$ Spectra to compare the normalization.

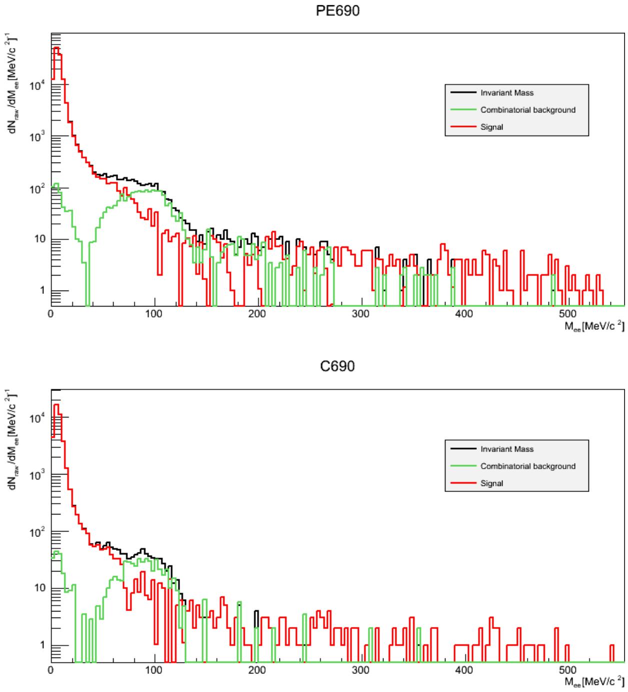

Figure 4. Comparison of spectra for PE and C targets for the same pion-beam momenta.

3.5 Dileptons spectra

The dileptons were selected by requiring hit in RICH combined with proper cut on velocity, see Figure 4. The combinatorial background was obtained as the arithmetic mean of like-sign e^+e^+ and e^-e^- pairs and was subtracted from the measured e^+e^- sample. Considering an unlike-sign two particle invariant mass spectrum, the uncorrelated background in the unlike-sign pair sample is estimated by the number of like-sign pairs within each event. The signal S of the number of unlike-sign pairs N_{+-} is then given by $S = N_{+-} - 2\sqrt{N_{++}N_{--}}$ [2].

4 Conclusions

Like-sign method provides already a fair description of combinatorial background. We need more investigation about the focusing of our beam corresponding the problem normalization of START, to proper subtract the contribution of C from PE.

Acknowledgements

This work has been supported by the European Community FP7–Capacities, contract HadronPhysics3 n° 283286,GSI, HIC for FAIR, EMMI and AS CR M100481202 grants.

References

[1] J. Biernat, E. Epple, L. Fabbietti, *et al.*,“A secondary pion beam for the HADES experiment”.

[2] B. Ramstein [HADES Collaboration], “Study of electromagnetic processes with the dielectron spectrometer HADES,” AIP Conf. Proc. **1257**, 695 (2010).

Charged jet reconstruction in Au+Au collisions at $\sqrt{s_{NN}} = 200$ GeV at RHIC

Jan Rusňák[1]

[1]rusn@email.cz, Nuclear Physics Institute ASCR, Na Truhlarce 39/64, 180 86 Praha 8, Czech Republic

Abstract. Jets represent an important tool to explore the properties of the hot and dense nuclear matter created in heavy-ion collisions. However, full jet reconstruction in such events is a challenging task due to extremely large and fluctuating background, which generates a large population of combinatorial jets that overwhelm the true hard jet population. In order to carry out accurate, data-driven jet measurements over a broad kinematic range in the conditions of small signal to background ratio, we use several novel approaches in order to measure inclusive charged jet distributions and semi-inclusive charged jet distributions recoiling from a high p_T hadron trigger in central Au+Au collisions at $\sqrt{s_{NN}} = 200$ GeV. A very low infrared cutoff on jet constituents of 200 MeV/c is applied in all measurements. These jet measurements allow a direct comparison of jet quenching at RHIC and the LHC.

1 Motivation

Jets - collimated sprays of hadrons - are well calibrated tools to study the properties of the matter created in heavy-ion collisions [1]. They are created by fragmentation and hadronization of scattered partons generated in hard momentum exchange in the initial stages of the collision. While traversing the medium, they interact with the surrounding hot and dense matter resulting in modification of their fragmentation with respect to the vacuum case (jet quenching)[2]. This modification of parton fragmentation provides sensitive observables to study properties of the created matter.

Jet reconstruction in the environment of a high energy nuclear collision is a challenging task, due to the large and complex underlying background and its fluctuations within an event which can easily disturb measured jet distributions. In order to overcome the obstacles of jet reconstruction in heavy-ion collisions, we utilize two different methods. The first method filters out the fake "combinatorial" jets by imposing a cut on the transverse momentum of the leading hadron of each jet. This procedure however imposes a bias on the jet fragmentation. The second method chooses the hard event by requiring a high momentum hadron trigger. A jet back-to-back to the trigger is then reconstructed. No cut is imposed on the jet constituents (except a low-p_{T} cut of 200MeV/c) and the jet fragmentation is therefore nearly unbiased.

2 Analysis

We have analyzed data from 0-10% central Au+Au collisons at $\sqrt{s_{NN}} = 200$ GeV measured by the STAR experiment at RHIC during the run 2011.

Jets are reconstructed using only charged tracks recorded by the STAR Time Projection Chamber (TPC). All tracks are required to have $p_{\mathrm{T}} \geq 200$ MeV/c. Implementation of the anti-k_{T} algorithm in the FASTJET software [3] is used for jet reconstruction.

The jet resolution parameter R is chosen to be $R = 0.3$. The fiducial jet acceptance is then $|\eta| < 1 - R$ in pseudorapidity and full azimuth.

In the next step, reconstructed jet transverse momentum p_{T}^{rec} is corrected for the average background energy density

$$p_{\mathrm{T}}^{corr} = p_{\mathrm{T}}^{rec} - \rho \cdot A \tag{1}$$

where $\rho = \mathrm{med}\{\frac{p_{\mathrm{T},i}^{rec}}{A_i}\}$ is the event-wise median background energy density and A is the jet area calculated with the k_{T} algorithm using the method [4].

2.1 Inclusive Jet Analysis

In order to determine the response of the jet to the presence of the highly fluctuating and complex background we embed a simulated jet with known transverse momentum (p_{T}^{emb}) into a real event and calculate δp_{T} as

$$\delta p_{\mathrm{T}} = p_{\mathrm{T}}^{rec} - \rho \cdot A - p_{\mathrm{T}}^{emb} = p_{\mathrm{T}}^{corr} - p_{\mathrm{T}}^{emb} \tag{2}$$

It was shown, that the δp_{T} distribution is not significantly dependent on the choice of the fragmentation model of the embedded jet [5]. With the knowledge of the δp_{T} and with use of a Monte Carlo (MC) generator, a response matrix of the system can be calculated which maps the true p_{T} distribution to the measured one.

A jet momentum distribution is smeared not only by background fluctuations, but also by detector effects. An MC simulation using a parametrization of the TPC tracking efficiency is used to calculate an approximate detector response matrix.

In order to reduce the combinatorial background, a cut on the transverse momentum of the leading hadron ($p_{\mathrm{T}}^{leading}$) of the jet is imposed. Also a cut on the jet area [4] $A > 0.2$ in case of $R = 0.3$ and $A > 0.09$ for $R = 0.2$ is applied.

In the final step, the measured p_{T}^{corr} distribution is corrected for the background and detector effects using an iterative unfolding technique based on Bayes' theorem [6].

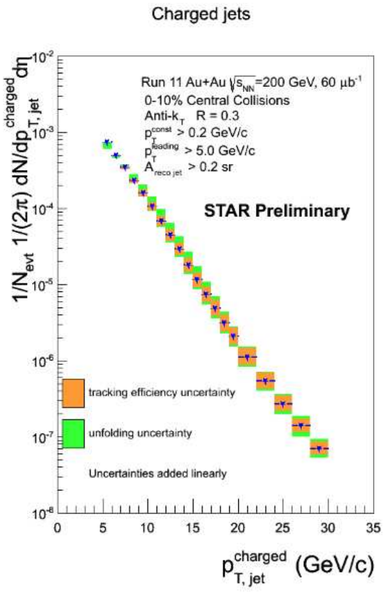

Figure 1. The corrected p_T spectrum of inclusive charged jets in central Au+Au collisions at $\sqrt{s_{NN}} = 200$ GeV for $R = 0.3$.

Results

Figure 1 shows the p_T spectrum of inclusive charged jets in central Au+Au collisions at $\sqrt{s_{NN}} = 200$ GeV for $R = 0.3$ corrected for background and detector effects.

2.2 Trigger Recoil Jet Analysis

A trigger hadron is required to have momentum $9 \leq p_\mathrm{T} \leq 19$ GeV/c. A jet is then reconstructed in azimuth ϕ satisfying

$$|\phi - \pi| < \frac{\pi}{4} \tag{3}$$

where the position $\phi = 0$ is defined by the trigger position.

In order to estimate the effect of the presence of the fluctuating background a set of Mixed Events (ME) is created. A mixed event is composed of N tracks randomly picked up from N different, randomly chosen events (however all the N events come from the same centrality bin, z-vertex bin and event plane direction Ψ_{EP} bin). All high-p_T tracks are discarded. Such a mixed event does not exhibit any physical correlations between the tracks; on the other hand it describes the key features of the background (detector acceptance inhomogenities, total track multiplicity, etc.). The mixed event distribution is then subtracted from the (unmixed) Same Event (SE) distribution.

Instead of correcting the results for background and detector effects by means of unfolding, a simulated PYTHIA p+p spectrum is smeared by these effects. This smeared p+p reference is then compared with the measured Au+Au data.

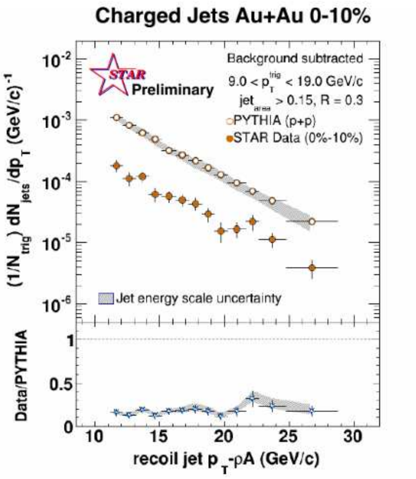

Figure 2. The recoil jet spectrum in central Au+Au collisions and smeared PYTHIA p+p spectrum at $\sqrt{s_{NN}}$ = 200 GeV for $R = 0.3$.

Results

Figure 2 shows a comparison of the measured recoil jet spectrum (SE-ME) in central Au+Au collisions and smeared PYTHIA p+p spectrum for $R = 0.3$. A suppression of the measured spectrum is apparent with respect to PYTHIA.

3 Conclusion

We have presented preliminary results of ongoing jet measurements at the STAR experiment. These measurements utilize low-bias methods of jet reconstruction allowing direct comparison with theory.

We have used a new technique of the mixed events for jet background estimation in heavy-ion collisions.

Further detector corrections and other effects are yet to be included.

4 Acknowledgment

The work has been supported by the MEYS grant CZ.1.07/2.3.00/20.0207 of the European Social Fund (ESF) in the Czech Republic: "Education for Competitiveness Operational Programme" (ECOP).

References

[1] B. I. Abelev *et al.*, Phys. Rev. Lett. **97**, 252001 (2006).
[2] Miklos Gyulassy and Michael Plumer, Phys. Lett. B **243**, 432-438 (1990).
[3] M. Cacciari, G. P. Salam, G. Soyez, FastJet user manual, arXiv:1111.6097 (2011).
[4] M. Cacciari, G. P. Salam and G. Soyez, JHEP **0804**, 005 (2008).
[5] P. Jacobs, Background Fluctuations in Heavy Ion Jet Reconstruction, arXiv:1012.2406 (2010).
[6] G. D'Agostini, Improved iterative Bayesian unfolding, arXiv:1010.0632 (2010).

Electromagnetic Calorimeter for the HADES Spectrometer

Ondřej Svoboda[1], Christoph Blume[2], Wojciech Czyżycki[3], Eliane Epple[4], Laura Fabbietti[4], Tetyana Galatyuk[5], Marina Golubeva[6], Fedor Guber[6], Stanislav Hlaváč[7], Alexander Ivashkin[6], Marcin Kajetanowic[8], Behruz Kardan[2], Wolfgang Koenig[9], Andrej Kugler[1], Kirill Lapidus[4], Sergey Linev[9], Edward Lisowski[3], Oleg Petukhov[6], Jerzy Pietraszko[9], Andrei Reshetin[6], Pablo Rodríguez-Ramos[1], Adrian Rost[5], Piotr Salabura[8], Yuri Gennadievich Sobolev[1], Pavel Tlustý[1], and Michael Traxler[9]

(on behalf of the HADES collaboration)

[1] *svoboda@ujf.cas.cz, Nuclear Physics Institute, Academy of Sciences of the Czech Republic, Řež, 250 68, Czech Republic*
[2] *Institut für Kernphysik, Goethe-Universität, 60438 Frankfurt, Germany*
[3] *Institute of Technology Cracow, 31-155 Cracow, Poland*
[4] *Excellence Cluster 'Origin and Structure of the Universe', Technische Universität München, 85748 Garching, Germany*
[5] *Technische Universität Darmstadt, 64289 Darmstadt, Germany*
[6] *Institute for Nuclear Research, Russian Academy of Sciences, 117312 Moscow, Russia*
[7] *Institute of Physics, Slovak Academy of Sciences, 845 11 Bratislava, Slovakia*
[8] *Smoluchowski Institute of Physics, Jagiellonian University of Kraków, 30-059 Cracow, Poland*
[9] *GSI Helmholtzzentrum für Schwerionenforschung GmbH, 64291 Darmstadt, Germany*

Abstract. The HADES spectrometer currently operating on the beam of SIS18 accelerator in GSI will be moved to a new position in the CBM/HADES cave of the future FAIR complex. Electromagnetic calorimeter (ECAL) will enable the HADES@FAIR experiment to measure data on neutral meson production in heavy ion collisions at the energy range of 2–10 AGeV on the beam of the new accelerator SIS100@FAIR. Calorimeter will be based on 978 massive lead glass modules read out by photomultipliers and a novel front-end electronics. Layout of the ECAL detector as well as beam test of single modules and electronics are shortly described.

1 Motivation

The High Acceptance DiElectron Spectrometer (HADES) focuses on dielectron measurements to study in-medium modifications. An extensive study of proton – proton, pion – proton, proton – nucleus, pion – nucleus, and nucleus – nucleus collisions up to Au-Au@1.23AGeV [1] have been done in the past decade.

HADES is currently operating on the beamline of SIS18 accelerator at GSI Darmstadt, Germany. The current setup consist of a diamond start detector (START), Ring Imaging Cherenkov detector (RICH), four layers of multiwire drift chambers (MDC), a superconducting toroidal magnet (ILSE), time of flight walls from resistive plate chambers (RPC) and plastic scintillators (TOF), pre-shower detector (SHOWER) and Forward Wall detector [2]. After build-up of FAIR the Hades spectrometer will be moved to a newly build cave shared with the CBM experiment and will continue with the studies at higher energies.

Electromagnetic calorimeter (ECAL) is developed to be included into HADES and measure the respective π^0 and η meson two gamma decay yields together with the dielectron data measured in HADES spectrometer for the knowledge of dielectron cocktail at incident heavy ion energies 2–10 AGeV. ECAL will also offer better electron/pion suppression for large momenta (p>400 MeV/c) as compared to the present situation (at lower momenta the electron/hadron identification is provided by the RICH and RPC detectors from HADES spectrometer). Furthermore the ω production via the $\pi^0\pi^+\pi^-$ and the $\pi^0 e^+ e^-$ decays can be investigated (the latter being of importance for the still unsettled question of the ω electromagnetic transition form factor). Last but not least the photon measurements are of large interest for the HADES strangeness program which addresses spectroscopy of neutral $\Lambda(1405)$ and $\Sigma(1385)$ resonances in elementary and HI reactions.

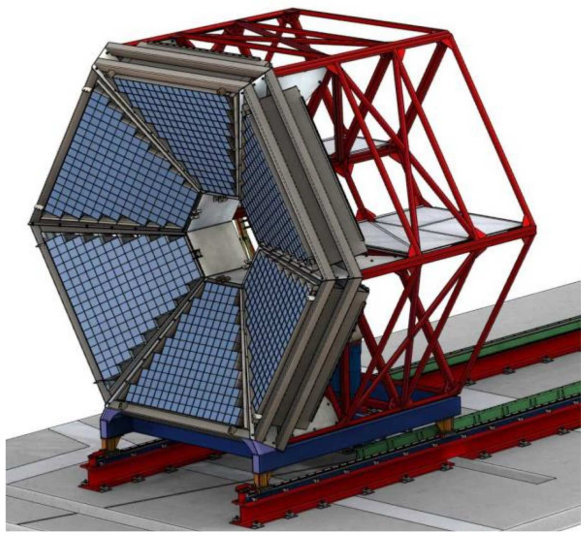

Figure 1. Layout of the electromagnetic calorimeter for the HADES spectrometer.

2 ECAL layout

The ECAL is following basic HADES geometry – six separate sectors covering almost full azimuthal angle and polar angle 18° to 45°, see Figure 1 or [3].

Calorimeter will consist of 978 modules of lead glass read out by a photomultiplier.

The lead glass crystal of CEREN 25 type has dimensions 92×92×420 mm^3. Two sizes of photomultipliers (PMT) will be used to read out the modules, 1.5” EMI 9903KB and 3” Hamamatsu R6091. Two independent read-out systems named “Cracow” and “PaDiWa Amps” are being developed for the calorimeter.

3 In-beam tests of single modules

Secondary gamma beam at MAMI Mainz facility was used to test relative energy resolution of the modules and electronics. Dedicated measurements were done with declined beams to test energy leakage between the modules.

Modules with 1”, 1.5” and 3” PMTs were tested at eight different energies and with MA8000 shaper and CAEN DT5742 ADC. Module with 1” PMT Hamamatsu R8619 was proved to be not suitable because of non-linear response and worse relative energy resolution, see Figure 2.

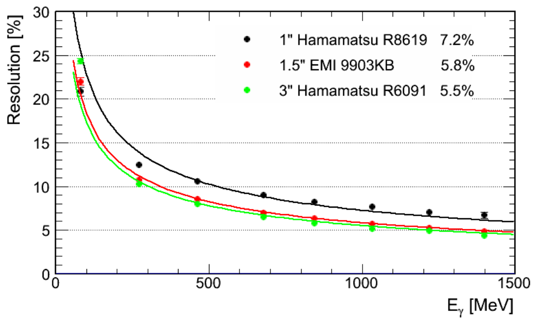

Figure 2. Relative energy resolution of calorimeter modules equipped with different photomultipliers (numbers behind the names stand for resolution at 1 GeV).

Tests of the two front-end boards showed that they are fully comparable in terms of energy resolution. Their results were even better than with the standard CAEN ADC.

Energy leakage between two modules was examined hitting one module with the gamma beam closer and closer to the common boarder. The 6° and 12° declined beams with respect to the module axis were also used. As shown in Figure 3, original energy of the photon can be reconstructed for all studied cases. Relative energy resolution does not significantly depend neither on the gamma position nor the incoming angle.

4 Summary

Electromagnetic calorimeter ECAL is being built to enhance experimental possibilities and physics program of the HADES spectrometer. The ECAL will enable to measure gamma photons coming from various decays as well as neutral pions.

Beam tests of ECAL modules were performed on secondary gamma beam from MAMI Mainz facility. Relative energy resolution was measured to be 5.5 % for modules with 3” photomultiplier and 1 GeV photons, respectively 5.8 % for 1.5” photomultiplier. Energy leakage between the neighbour modules was tested with parallel and declined beams and energy of original photon was successfully recovered.

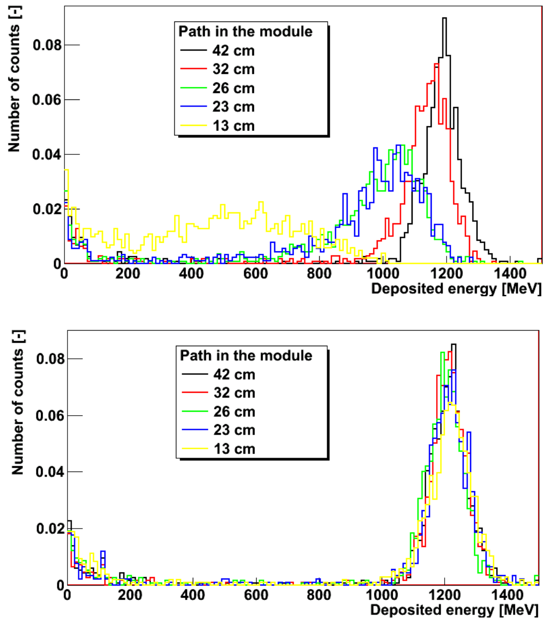

Figure 3. Energy deposited in one module hit by the gamma beam (upper) and sum of energies deposited in both neighboring modules (lower). Case of 1217.8 MeV and different “path-length” of the photon inside the module (measured with declined beam and different hit position).

Acknowledgments

This work has been supported by Czech MSMT LG 12007, GACR 13-067595, AS CR M100-481202 and by the European Community FP7 – Capacities, contract HadronPhysics3 n° 283286. We would like to thank to A. Neiser, P. Ott, P. Otte, A. Thomas, and P. Skott from IK-JGU, for their help with measurements.

References

[1] G. Agakishiev *et al.* (HADES collaboration), Hades experiments: investigation of hadron in-medium properties, J. Phys.: Conf. Ser. **420**, 012013 (2013).

[2] G. Agakishiev *et al.* (HADES collaboration), The high-acceptance dielectron spectrometer HADES, Eur. Phys. J. A **41**, 243 (2009).

[3] A. Kugler *et al.* (HADES collaboration), Electromagnetic Calorimeter for HADES Experiment, Proceedings of the 14th ICATPP Conference, **vol. 8** (2013).

Strangeness enhancements in heavy-ion collisions from SPS to LHC

Ladislav Šándor[1]

[1]*sandor@saske.sk, Institute of Experimental Physics, Slovak Academy of Sciences, Watsonova 47, 040 01 Košice, Slovakia*

Abstract. Studying strange and particularly multi-strange particle production in relativistic heavy-ion interactions is a unique tool to investigate the properties of the hot and dense matter created in the collision, because of no net strangeness content in the initially colliding nuclei. In particular, an enhanced production of strange particles in A-A with respect to p-p interactions was one of the earliest proposed signatures of the creation of a deconfined Quark-Gluon Plasma (QGP). The results of strangeness enhancement measurements from the WA97/NA57 (SPS), STAR (RHIC) and ALICE (LHC) experiments are briefly reviewed. The energy, centrality and strangeness content dependencies of enhancements are discussed.

1 Introduction: why strangeness?

The study of strange and multi-strange particle production in high-energy collisions of heavy nuclei is considered as a unique tool to investigate the properties of the hot and dense matter created in the course of collision. These processes are highly sensitive to the reaction dynamics, as there is no net strangeness content in the initial state of colliding nuclei. Strange quarks as the lightest and most abundantly produced among the heavier ones are well accessible for the study.

An enhanced production of strange, and particularly multi-strange particles in A-A with respect to p-p inter-actions was one of the earliest proposed signatures of a deconfined QGP creation [1, 2]. This proposal was based on two main arguments:

– in a QGP strangeness can be easily produced via creation of strange - anti-strange quark pairs (basic processes: fusion of two gluons or two light quarks),
– the equilibration times of partonic reactions, especially due to the gluon fusion process, are much shorter than the ones of hadronic reactions. The difference is particularly large for multi-strange (anti)baryons.

Strange and multi-strange hadrons are usually measured by their weak decays into charged particles. Main goal of experiments is the extraction of yields (average particle multiplicity per event) and spectra of particles under study.

2 Strangeness enhancements at the SPS

First hints for the enhanced strangeness production were obtained from the NA35 streamer chamber experiment [3, 4] and the WA85 experiment at the Omega facility [5] with the beams of sulphur ions with energy of 200 A GeV at the SPS. The approximately twofold increase of strange particle production with respect to negatively charged particles (mainly pions) has been observed.

Strangeness enhancements at central rapidity in Pb-Pb collisions at energy 158 A GeV were systematically studied in the WA97 [6, 7] and NA57 [8] experiments.

Enhancements E are defined as ratios of the strange particle yields measured in heavy-ion collisions normalized to the mean number of nucleons participating in the collision $<N_{\rm part}>$, to the corresponding quantities in nucleon-nucleon interaction at the same energy. In the mentioned experiments (no liquid hydrogen target available) instead of p-p the p-Be collisions were measured as a reference. The enhancements for Λ, Ξ and Ω hyperons, measured in the NA57 experiment, are plotted in Figure 1 as a function of collision centrality. The mean numbers of participant nucleons $<N_{\rm wound}>$ for each centrality class were calculated using the Glauber model.

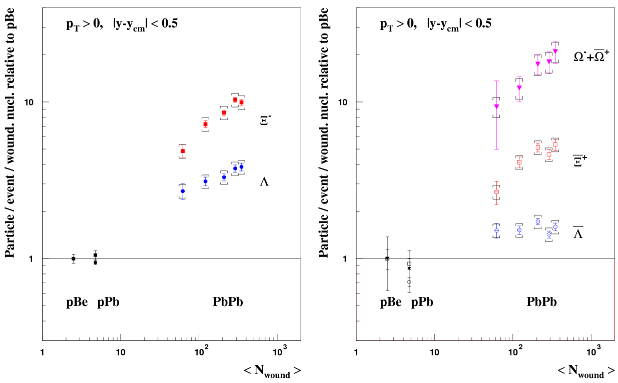

Figure 1. Strangeness enhancements E from the NA57 experiment as a function of collision centrality characterized by a mean number of participant nucleons (figure taken from citesandor:8).

The main NA57 results can be summarized as follows: the enhancement pattern of strange hyperon abundances in central Pb-Pb collisions at 158 A GeV, first observed by the WA97 experiment [7], has been confirmed. The enhancement grows with the strangeness content of particle and amounts to about a factor 20 for the Ω hyperons, containing three strange valence quarks. The enhancements increase with the centrality, i.e. with the number of nucleons participating in the collision. So far, it has not been possible to fully reproduce these results within conventional hadronic models of nucleus-nucleus collisions.

The NA57 experiment studied also Pb-Pb interactions at lower energy of 40 A GeV [9]. The centrality depen-dence of enhancements is steeper and for central collisions the enhancement is larger at 40 as at 158 A GeV. The strangeness production was investigated at SPS by the NA49 experiment, too. The measured amounts of enhancements are consistent with the NA57 data (see, e.g., [10]).

More details from the strangeness study in heavy-ion collisions at SPS could be found in [11]. It is worth to mention the analysis of the transverse mass distributions for the strange particles, indicating a collective expansion of hot and dense matter at a speed close to 50 % of the light velocity, superimposed on a thermal distribution. This suggests the generation of a very strong pressure, as would be expected in the case of deconfinement.

3 Enhancements at RHIC and LHC

In the last decade, strangeness production at mid-rapidity was studied at higher collision energies at the RHIC (Relativistic Heavy Ion Collider, BNL) in the STAR experiment [12] and at the LHC (Large Hadron Collider, CERN) in the ALICE experiment [13]. STAR data came from the Au-Au and p-p collisions at energy 200 GeV per nucleon pair, whereas the ALICE Pb-Pb data were taken at energy 2.76 TeV per nucleon pair and using the interpolated reference p-p data. In Figure 2 the ALICE data on the enhancements of Ξ and Ω hyperons are presented in comparison with the corresponding STAR and NA57 data.

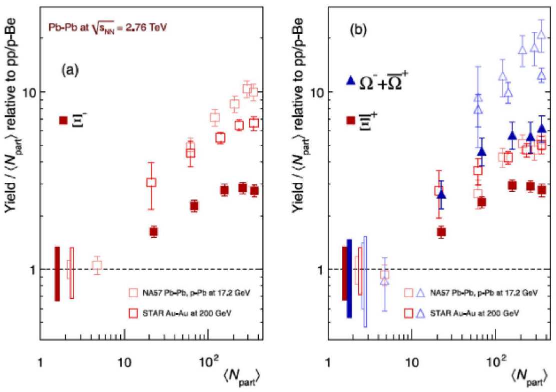

Figure 2. Enhancements in the rapidity range $|y| < 0.5$ as a function of the mean number of participants $<N_{\mathrm{part}}>$, showing LHC (ALICE, full symbols), RHIC and SPS (open symbols) data. The LHC data use interpolated p-p reference values (figure taken from [13]).

ALICE results demonstrate enhancements larger than unity for all the particles, increasing with the strangeness content of the particle, showing the hierarchy already observed at lower energies and consistent with the picture of enhanced strange quark pair production in a hot and dense partonic medium. The same shape and scale is observed for baryons and anti-baryons, as expected because of the vanishing net-baryon number at the LHC energy. Comparing the ALICE measurements (full symbols) with those from the experiments STAR at RHIC and NA57 at the CERN SPS (Pb-Pb collisions at energy 17.3 GeV per pair of nucleons), represented by the open symbols, the enhancements are found to decrease with increasing centre-of-mass energy, confirming the general picture first observed at the SPS.

ALICE and STAR experiments measured also Ξ/π and Ω/π hyperon-to-pion ratios as a function of centrality for both p-p and A-A collisions (see, e.g. [13]). They clearly indicate the enhanced strangeness production in A-A with respect to p-p interactions, rising with centrality up to $<N_{\mathrm{part}}>$ ˜150, and apparently saturating thereafter. However, they also demonstrate that different mechanisms contribute to the enhancements as defined above, requiring further quantification of the specific enhancements of strange particles out of the general relative increase of multiplicity at mid-rapidity.

4 Conclusions and outlook

Strangeness enhancements, measured in wide range of collision energy, are consistent with predictions of Rafelski and Müller [1, 2], demonstrating a significant dependence on the collision centrality and on the strangeness content of particle. So far, no conventional hadronic model of nucleus-nucleus collision reproduces fully these results. A two-component geometrical core-corona approach [14] seems to work successfully.

Enhancements decrease with increasing energy of colliding nuclei, indicating a gradual removal of canoni-cal suppression.

New precision ALICE results are eagerly awaited, particularly the p-p reference data and new data at higher LHC energy.

I am grateful to Karel Šafařík and Ivan Králik for enlightening discussions.

References

[1] J. Rafelski and B. Müller, Phys, Rev. Lett. **48**, 1066 (1982).
[2] P. Koch, B. Müller and J. Rafelski, Phys. Rep. **142**, 167 (1986).
[3] J. Bartke *et al.* Zeitschr. Phys. C **48**, 191 (1990).
[4] R. Stock *et al.* Nucl. Phys. A **525**, 221c (1991).
[5] S. Abatzis *et al.* Nucl. Phys. A **525**, 445c (1991).
[6] E. Andersen *et al.* Phys. Lett. B **449**, 401 (1999).
[7] F. Antinori *et al.* Nucl. Phys. A **661**, 130c (1999).
[8] F. Antinori *et al.* J. Phys. G **32**, 427 (2006).
[9] F. Antinori *et al.* J. Phys. G **37**, 045105 (2010).
[10] M. Mitrovski for the NA49 Collaboration, J. Phys. G **37**, 094003 (2010).
[11] L. Šándor, *Overview of strangeness production at the CERN SPS,invited talk at the International Conference on Strangeness in Quark Matter, Los Angeles, March 26-31, 2006*; J. Phys. G **32**, S127 (2006).
[12] B.I. Abelev *et al.* Phys. Rev. C **77**, 044908 (2008).
[13] B. Abelev *et al.* (ALICE Collaboration), Phys. Lett. B **728**, 216 (2014); Erratum – *ibid.* **734**, 409 (2014).
[14] J. Aichelin and K. Werner, Phys. Rev. C **79**, 064907 (2009). Erratum – *ibid.* 029902 (2010).

The NPI Center of Accelerators and Nuclear Analytical Methods (CANAM), Basic and Applied Research with Ion Beams

E. Šimečková, P. Bém, M. Majerle, J. Mrázek, J. Novák, and M. Štefánik[1]

[1]*simeckova@ujf.cas.cz, Nuclear Physics Institute, 250 68 Řež, Czech Republic*

Abstract. The Nuclear Reaction Department of NPI – the member of the European Consortium on Nuclear Data – provides experimental data required for the validation of computational tools and the nuclear data libraries that are being developed for fusion applications. A determination and validation of fusion related activation cross-sections of neutron and deuteron induced reactions are performed using CANAM infrastructure – fast neutron sources and ion-beam irradiation chamber. A methodical approach and some results will be presented.

1 Introduction

Today there is still a large demand of data in neutron-induced reactions above 14 MeV and of deuteron activation cross sections. For many cases reaction cross sections are unknown or known with poor precision. The neutron energy range between 1 and 40 MeV concerns several applications in particular, nuclear waste transmutation in ADS (Accelerator Driven System); innovative nuclear power reactors (fast reactors), so called Generation IV reactors; fusion applications like the IFMIF (International Fusion Material Irradiation Facility) and the ITER (International Thermonuclear Experimental Reactor). The knowledge of deuteron cross sections is of high importance for IFMIF accelerator hardware. The more precise measurement of the above reactions is important for knowledge of neutron spectra in reactors gas production in material for nuclear engineering, ADT (Accelerator Driven Transmutation) neutron multiplication calculation.

The Nuclear Physics department of NPI is a member of the European Consortium on Nuclear Data – a group of institutes that provides experimental data required for the validation of the nuclear data libraries (FENDL, EAF) that are being developed for fusion applications.

2 CANAM

Experimental facilities of CANAM (Center of Accelerators and Nuclear Analytical Methods) infrastructure are proffered to the users in Open Access mode [1]. CANAM infrastructure consists of three major research laboratories of the Nuclear Physics Institute of the ASCR:

- Laboratory of Tandetron – operating an accelerator Tandetron 4130 MC
- Neutron Physics Laboratory (NPL) – providing facilities at the reactor LVR-15
- Laboratory of Cyclotron and Fast Neutron Generators (LC&FNG) – operating the isochronous cyclotron U-120M.

2.1 LC&FNF

The energy-variable cyclotron U-120M deliveries p(6-25 MeV), d(2–20 MeV), ^{3}He (18–50 MeV) and ^{4}He (24–38 MeV) ions with intensities up to some few μA in positive mode of accelerating to the experimental hall (Figure 1). The Fast Neutron generators (FNG) are alternatively placed on the line of cyclotron working in negative mode of accelerating while the protons (6–37 MeV) or deuterons (11–20 MeV) with intensities up to 30 μA are provided.

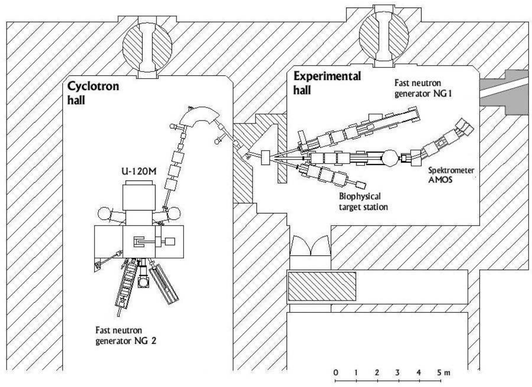

Figure 1. Design of variable energy cyclotron U-120M facilities.

2.2 White spectrum p-D_2O neutron source

The deuteron break-up process induced by 37 MeV protons on flowing heavy water target was found to produce neutrons with high intensity, mean energy of 14 MeV and spectrum extending to 32 MeV. Neutron flux up to 5×10^{10} n/cm^2/s provided suitable tool for IFMIF-relevant cross-section benchmarks [2] or various neutron detector testing.

2.3 Quasi-monoenergetic p-^{7}Li neutron source

The standard ^{7}Li(p,n) reaction on thin lithium target induced by 20–35 MeV proton beam from the cyclotron is used for the production of quasi-monoenergetic neutron field. A self-supporting Li target and the carbon beam stopper are utilized.

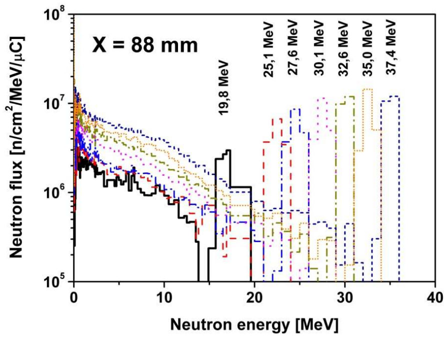

Figure 2. Spectral neutron flux of the p+^{7}Li reaction evaluated by MCNPX code. Proton incident energies are shown.

3 Cross section measurements

3.1 Neutron cross section evaluation

The reaction ^{7}Li(p,n) produces high-energy quasimonoenergetic neutrons with a tail at lower energies (Figure 2). The flux density and neutron spectra were evaluated [3] by MCNPX code using LA-150h cross section data library. Foils of material under interest (e.g. Co, Nb, Fe, Cr) were irradiated in several runs (duration 8–10 hours) at various neutron fields. The gamma-rays from activated foils were measured repeatedly by two calibrated HPGe detectors. The activation cross sections at certain neutron energies were determined by common analysis of a set of runs performed at various proton energies with step of about 2.5 MeV [4].

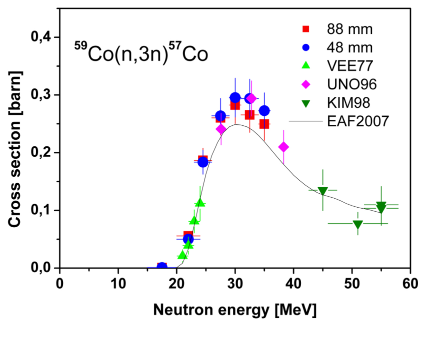

Figure 3. Cross section of the ^{59}Co(n,3n)^{57}Co reaction.

In the Figure 3 are shown resulting cross sections for the ^{59}Co(n,3n)^{57}Co reaction together with the data of other authors and with evaluation of the EAF library, as an example.

3.2 Deuteron cross section evaluation

The activation cross sections were measured by a stack-foil technique. The foils of examined elements (e.g. Al, Cu, Fe, Co) were inserted in the irradiation chamber by turn with the foils utilized for additional monitoring of beam current. The mean energy, energy thickness and energy spread in each foil was set out by SRIM 2003 code.

The cross sections were calculated from the specific activities, measured by two calibrated HPGe detectors, corrected to the decay using total charge and foil characteristic as well. The cross sections of deuteron induced reactions on $^{\mathrm{nat}}$Cu [5, 6]. are shown in the Figure 4.

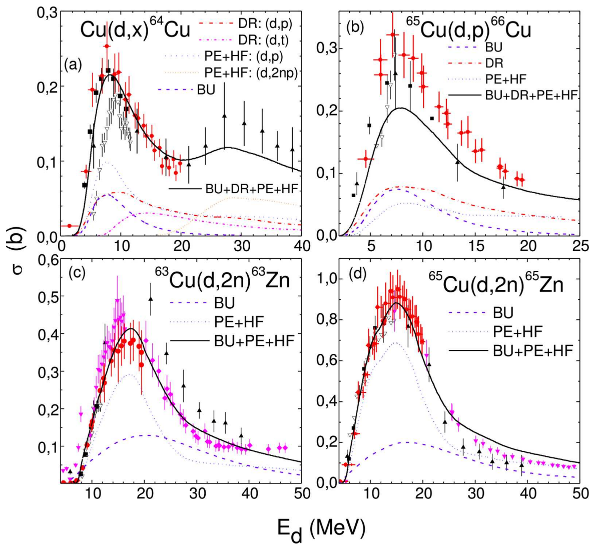

Figure 4. Comparison of measured data and analysis results.

Acknowledgement

This work was carried up at the CANAM infrastructure of NPI ASCR supported by Ministry of Education, Youth and Sports of the Czech Republic under project No. LM2011019.

References

[1] http://canam.ujf.cas.cz.

[2] P. Bém, V. Burjan, M. Götz *et al.*, Fusion Engineering and Design **75-79**, 829 (2005).

[3] S. P. Simakov, U. Fischer, P. Bém *et al.*, *Inter. Conf. on Nucl. Data for Sci., and Techn.*,– ND2010, 1856 (Jeju, Korea, 2010).

[4] E. Šimečková, P. Bém, V. Burjan et al., *Inter. Conf. on Nucl. Data for Sci., and Techn.*,– ND2010, 1801 (Jeju, Korea, 2010).

[5] E. Šimečková, P. Bém, M. Honusek, M. Štefánik, M. Avrigeanu *et al.*, Phys. Rev. C **84**, 014605 (2011).

[6] S. P. Simakov, P. Bém, V. Burjan, E. Šimečková et al, Fusion Engineering and Design **83**, 1547 (2008).

CERN Programmes for Teachers

Miriam Šimralová[1]

[1]*simmiriam@gmail.com, Gymnázium, Šrobárova 1, 04001 Košice, Slovakia*

Abstract. Among the major missions of CERN is education, and one of the efficient ways to achieve it is to “teach the teachers”, as they then will bring back to the schools their knowledge. Two types of programme are organized at CERN for high-school physics teachers: National teacher programmes are run in the participants’ mother tongue and the lectures are usually given by the physicist from the corresponding member state. All member states, and even some non-member ones, are using this possibility to send their teachers to CERN. The second option is a three-week comprehensive course held in English at the beginning of summer, called High-School Teachers (HST) programme. In addition to education in physics, the HST goals are: to promote the exchange of knowledge and experience among teachers of different nationalities, to expose teachers to the world of research, and to stimulate activities related to the popularization of physics within and beyond the classroom. All lectures are archived and openly accessible, providing an invaluable resource for teachers and students.

1 Introduction

Education is one of the CERN’s key missions. A very efficient way to achieve this goal is to “teach the teachers”, as they then will bring back to the schools their knowledge. Two types of programme are organized at CERN for physics teachers [1]:

- High-School Teacher (HST) programme;
- National teacher programmes.

The overview of CERN educational programmes is schematically shown in Figure 1.

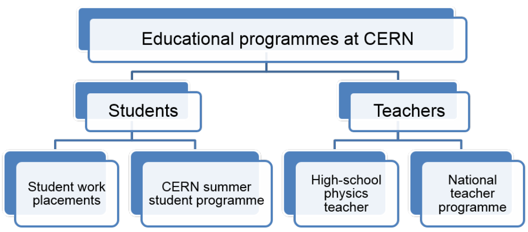

Figure 1. Overview of CERN educational programmes.

An essential prerequisite to technological progress is a functional educational system. This was one of the key factors for CERN that contributed to the creation of a system of active interaction with students and educators. Teachers are very important in this system because they are role models, multipliers, and they provide the crucial link for bringing modern science into school classes.

2 HST Programme

The HST is a three-week comprehensive course held in English at the beginning of the summer [2]. It is attended by about 50 selected teachers, from both member and non-member states. In addition to advanced physics education, the HST goals are: to promote the exchange of knowledge and experience among teachers of different nationalities, to expose teachers to the world of research, and to stimulate activities related to the popularization of physics within and beyond the classroom. HST is the longest programme for teachers, with several activities. The agenda usually includes:

- Lectures (introduction to CERN, particle physics and cosmology, LHC detectors, accelerators, medical applications, IT applications and GRID computing);
- Visits to experimental facilities;
- Teacher labs and workshops;
- Formal and informal discussions with physicists.

In the past similar, shorter programmes run over a weekend for 3–4 days, with more focus on visits to experimental installations, have also been organized.

The HST programme in 2013 was held from June 30 to July 20, 2013, at CERN. Main organizer was Mick Storr and CERN Education Group. Particularly useful were presentations of tools and subjects directly transferable to classrooms. Examples of these are:

- Workgroup HYPATIA — training program using real data from the ATLAS experiment in class [3], Figure 2;
- Lecture on antimatter by Rolf Landua, head of the CERN Education Group;
- One day workshop of Perimeter Institute (Waterloo, Ontario, Canada) [4].

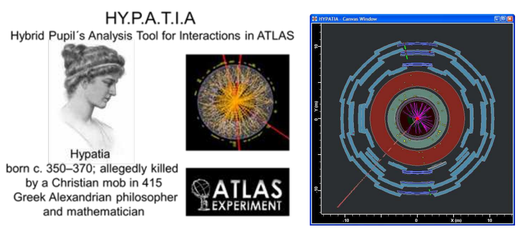

Figure 2. HYPATIA – educational program using real data from the ATLAS experiment.

3 National Teacher Programmes

As many as 25–30 national programmes are run yearly, with a duration of 3 to 5 days. All member states, and also some non-member states, are using this possibility to send their teachers to CERN. Lectures are given by scientists from the teachers' country in their mother tongue and all materials are archived and made openly accessible [5]. The first national teacher group was from Hungary in August 20–26, 2006. In 2008 a record was set – four Polish teacher programmes were run in that year. National programmes are usually coordinated by former HST participants. The coordinator for Slovakia is Zuzana Ješková from the Faculty of Sciences, UPJŠ Košice [6]. In April 2007 was the Slovak teacher programme for the first time, thanks to the institutions which financially supported this unique opportunity for Slovak teachers (Figure 3). The first common Czech-Slovak group of teachers visited CERN in 2013, with the enthusiastic participation of the CERN Director-General Rolf-Dieter Heuer.

Figure 3. Logos of institutions supporting Slovak teacher programmes.

4 Participation

The participation in the CERN teacher programmes from the four countries represented at this conference during the past 16 years is summarized in Table 1. For comparison, the normalization to the number of inhabitants was used in Figure 4. The involvement from these countries is higher than the CERN member-state average, except for the HST participation of Poland. Hungarians, and especially Slovaks, are among those nationalities using these educational programmes most efficiently. The amount of Slovak teachers who visited CERN (221 to date) corresponds to about 10% of all high-school science teachers in the country.

However, a closer look reveals that the participation from these four countries is significantly declining in the past three years, probably due to less support from funding agencies.

Country	HST	National
Czech Republic	16	146
Hungary	18	348
Poland	20	544
Slovakia	17	221

Table 1. Number of participants in two CERN teacher programmes in the years 1998–2013 from the four countries represented in this conference.

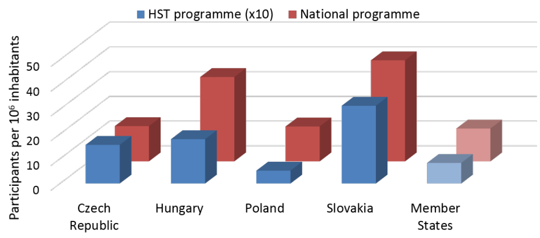

Figure 4. Number of participants from the four countries involved in this conference, normalized to 10^6 inhabitants, compared to the average values for CERN member states.

5 Conclusion

The CERN programme for teachers initiates them to particle physics and motivates them to introduce this subject to students. The training provides the teachers with new tools and methods for teaching modern physics. It also offers a precious opportunity to compare teaching of physics in different countries and to find that we share many similar challenges. Visits of the underground detectors demonstrate why a large international collaboration is necessary for preparing "big science" experiments. Meetings with scientists and engineers from all around the word evidence the advantages of international cooperation, independent of political views and religion.

Despite the not very favourable situation for scientific education at high schools in our region, there is evidence for an increase in the number of students choosing to study physics, engineering, and other scientific disciplines, among those who got acquainted with CERN [7]. The high Slovak participation in the CERN training is certainly favoured by the well-organized coordination network for teachers.

Acknowledgement

I would like to thanks to Zuzana Ješková, Rolf Landua, and Mick Storr for providing me with statistical data about the CERN teachers programmes and valuable comments on my poster.

References

[1] http://home.web.cern.ch/students-educators
[2] http://teachers.web.cern.ch/teachers/
[3] http://hypatia.phys.uoa.gr/ReadAbout/
[4] http://www.perimeterinstitute.ca/
[5] http://ufv.science.upjs.sk/_projekty/cern/program_2013_06.php
[6] http://ufv.science.upjs.sk/_projekty/cern/index.php
[7] Z. Ješková, M. Vargová, Československý časopis pro fyziku, **5–6**, 400–404, (2012)

Center of Accelerators and Nuclear Analytical Methods (CANAM): Fast Neutron Generators

Milan Štefánik[1,2], Pavel Bém[1], Milan Honusek[1], Mitja Majerle[1], Jaromír Mrázek[1], Jan Novák[1], and Eva Šimečková[1]

[1]stefanik@ujf.cas.cz, Nuclear Physics Institute of The Academy of Sciences of the Czech Republic, pri, Řež 130, Řež, Czech Republic, 250 68

[2]Czech Technical University in Prague, Faculty of Nuclear Sciences and Physical Engineering, Prague, Czech Republic, 115 19

Abstract. The cyclotron based neutron generators of the white- and quasi-monoenergetic spectra are operated under the CANAM infrastructure of the NPI ASCR Řež utilizing the variable-energy proton beam (up to 37 MeV) and the D_2O (flow), Be (thick), and Li(C) targets. The intensity and the energy range of the produced neutron fields are suitable for the validation of the neutron cross-sections for fusion applications. The accelerator driven fast neutron sources are characterized, and the neutron fields with a broad neutron spectrum determined by the multi-foil activation technique and validated against the Monte Carlo MCNPX calculations are presented. The research programs realized in this neutron fields are outlined.

1 Introduction

Nuclear Physics Institute of the ASCR in Řež has developed and is operating the accelerator-driven fast neutron generators of white and quasi-monoenergetic spectra. The source reactions of p + D_2O and p + Be employing the variable-energy proton beam of the U-120M isochronous cyclotron are used to produce the high intensity continuous spetra up to 34 MeV, and similarly the p + ^{7}Li(C) source reaction serves for the quasi-monoenergetic spectra production in the energy range of 18–35 MeV. They represent the useful tool for nuclear data mesurements and validation.

Now, these neutron sources are part of experimental facilities of the CANAM infrastructure at the NPI, and they are proffered to the users in Open Access mode. The proposals can be submitted via the CANAM User Portal (`http://canam.ujf.cas.cz`).

2 Materials and methods

2.1 Target stations of NG-2 neutron generator

Target stations with D_2O, Be, and Li targets were built-up on the beam line of the U-120M cyclotron operated in the negative-ion mode of acceleration, and they are marked as the NG-2 neutron generator. In this regime, the high proton beam power and good beam-current stability pose the suitable basis for irradiation experiments.

The heavy water target station (Figure 1) uses the target chamber with thickness of 16 mm. The flowing D_2O has the input and output temperatures of 20 °C and 22 °C, and in separated refrigerator it is cooled by the 5 °C ethanol. The standard operational parameters such as the input/output temperature and input/output pressure of water, temperature of cooling ethanol as well as the proton beam current at the target and both collimators are monitored and recorded by the PC during the experiment.

The beryllium target station (Figure 2) contains the beryllium cylinder with thickness of 8 mm and diameter of 50 mm, which is cooled by the ethanol to the temperature of 5 °C; the proton beam current, temperature and pressure of cooling alcohol are digitized and registered by the PC as well.

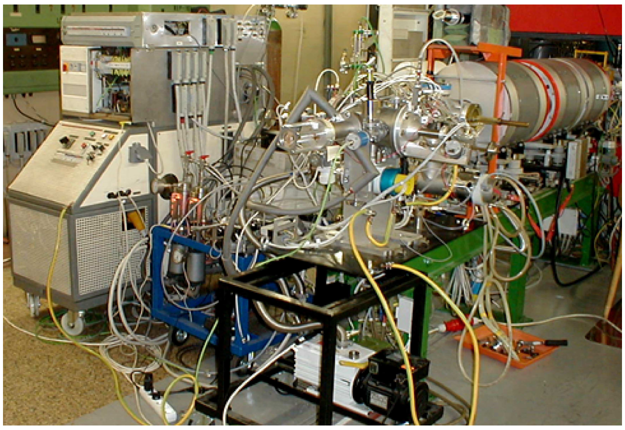

Figure 1. Heavy water target station of NG-2 neutron generator at NPI

2.2 The p(37)-D_2O and p(35)-Be neutron fields

The white neutron fields of source reactions p(37)-D_2O and p(35)-Be were determined by the multi-foil activation technique (as formerly applied in [1, 2]). In both cases, the large set of activation foils were irradiated for 12–18 hours in the close vicinity from the source target. After the irradiation, the activation foils were repeatedly measured by the HPGe detector, and the saturated activities and subsequently the reaction rates were obtained. The irradiation systems were also simulated in Monte Carlo transport code MCNPX [3] utilizing the Los Alamos LA-150h [4] and ENDF/B-VII.1 [5] nuclear data library to obtain the guess neutron spectra for both source reactions. For neutron spectra reconstruction from measured reaction rates and MCNPX guess spectra, the unfolding procedure of SAND-II code [4] together with cross-sections from EAF-2007 data library [6] were used.

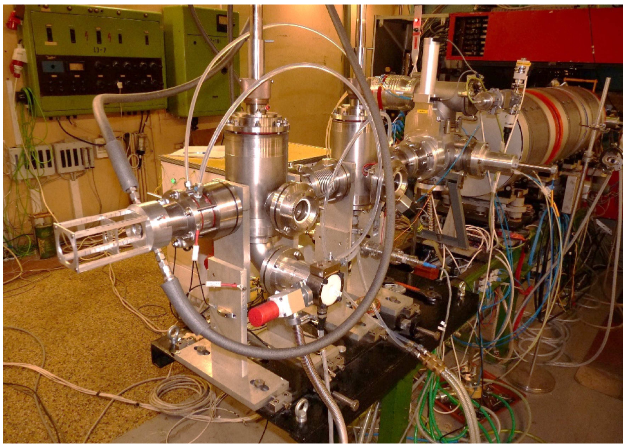

Figure 2. Beryllium target station of NG-2 neutron generator at NPI

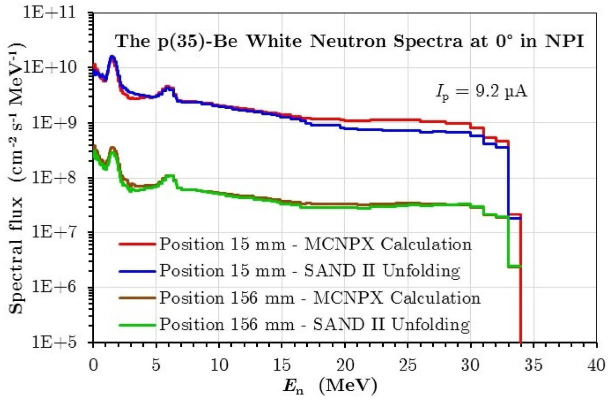

Figure 4. Neutron field of NG-2 generator with p(35)-Be source reaction at NPI [9].

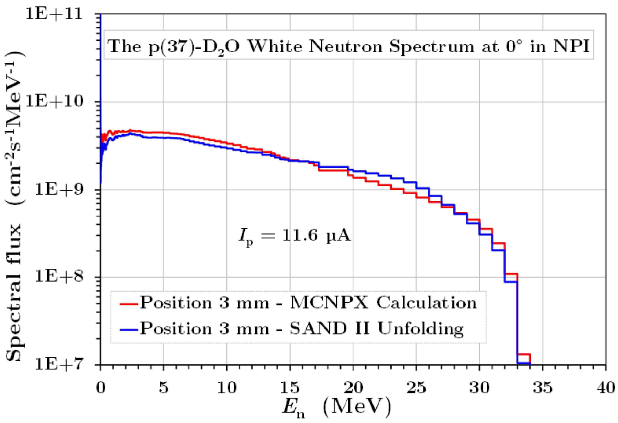

Figure 3. Neutron field of NG-2 generator with p(37)-D$_2$O source reaction at NPI [8].

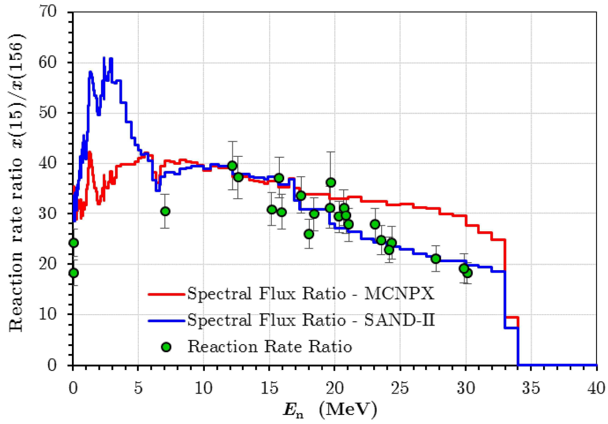

Figure 5. Reaction rates and spectral flux ratios for p(35)-Be fast neutron source at NPI [10].

The neutron room background out of the direct fast neutron beam was assessed as well, and based on measured reaction rates, the background spectrum was described by the special analytical function [7].

3 Conclusions

The determined neutron spectrum of the p(37)-D$_2$O source reaction at a distance of 3 mm from the target is displayed in Figure 3 and in more details discussed in [8]. Neutron field of p(35)-Be generator for two irradiation positions (15 and 156 mm) is depicted in Figure 4, and spectral flux ratio in Figure 5 confirms the correctness of the unfolded spectra [9, 10]. Both target stations provide the spectrum up to 34 MeV with the mean energy of 14 MeV and total flux up to 10^{11} neut. cm^{-2}s^{-1}. The neutron fields of the NG-2 generator are used for the integral benchmarks, cross-section data validation, testing the hardness of electronics against the fast neutrons, and other types of irradiation experiments.

Measurements were carried out at the CANAM infrastructure of the NPI ASCR Rez supported through MŠMT project No. LM2011019.

References

[1] S. P. Simakov *et al.*, Reactor Dosimetry State of the Art 2008, 532–540 (2009).

[2] M. Stefanik, P. Bem *et al.*, Trans. Am. Nucl. Soc. **106**, 894–896 (2012).

[3] D. B. Pelowitz *et al.*, MCNPX Users Manual v.2.6.0, Los Alamos National Laboratory (2008).

[4] SAND-II, PSR-345, UKAEA FUS (1996).

[5] M. B. Chadwick, M. Herman *et al.*, Nucl. Data Sheets **112**, 2887–2996 (2011).

[6] R. A. Forrest, EAF-2007 **48**, UKAEA FUS (2007).

[7] M. Stefanik, P. Bem *et al.*, Proceedings of the 13th International Scientific Conference Electric Power Engineering 2012 **2**, 1275–1279 (2012).

[8] M. Stefanik, P. Bem *et al.*, Proceedings of the 2014 15th International Scientific Conference on Electric Power Engineering, 743–748 (2014).

[9] M. Stefanik, P. Bem *et al.*, Nuc. Data Sheets **119**, 422–424 (2014).

[10] M. Stefanik, P. Bem *et al.*, Rad. Phys. Chem. **104**, 306–309 (2014).

Study of jet quenching in heavy ion collisions at LHC using ATLAS detector

Pavol Štefko[1]

[1]*pavol.stefko@gmail.com, Institute of Particle and Nuclear Physics, Faculty of Mathematics and Physics, Charles University, V Holešovičkách 2, 180 00 Prague 8, Czech Republic*

Abstract. Quark-Gluon Plasma (QGP) is one of the most extreme states of matter which exists only in extraordinary conditions of heavy-ion collisions that can be achieved at particle accelerators. Interactions between the partons and the hot, dense QGP are expected to cause the loss of the jet energy, which is phenomenon called jet quenching. In this talk we provide an introduction to the problematics of ultra-relativistic heavy ion collisions and we show how the jet quenching can be used to analyze the properties of QGP. We also present some "work in progress" results of the jet analysis done on the data taken by the ATLAS detector during the 2011 heavy-ion run at the LHC. Jets are studied as a function of collision centrality and dijet energy imbalance. Dijets are observed to be increasingly asymmetric with increasing centrality. The study of charged particles indicates an increase of yields of low-p_{T} tracks in events with strongly quenched jets.

1 Introduction

Collisions of the heavy ions at ultra-relativistic energies are expected to produce a dense medium of extremely high temperatures in order of trillion kelvins. This phase of matter consisting of deconfined quarks and gluons as degrees of freedom is called quark-gluon plasma (QGP). It is believed that the QGP existed at the very early stage of our universe. Therefore the study of the properties of this phase may provide a critical insight into the dynamics of this era.

2 Jets as the QGP probes

High transferred momentum interactions of quarks and gluons in colliding heavy ion beams are known to produce highly collimated clusters of hadrons and other particles produced by hadronization referred to as jets.

The products of the hard scattering processes interact heavily with the ambient plasma and, as first suggested by Bjorken [1], might experience collisional and radiative energy loss, via scattering and gluon bremsstrahlung ("gluonstrahlung"), respectively [2, 3]. The amount of energy loss is predicted to be proportional to the energy density of the medium. Hence jets, which have lost significant amount of energy while propagating through the medium, can be used as probes of the medium, providing information about its structure and properties [3]. This mechanism is referred to as jet quenching and is schematically depicted on Figure 1.

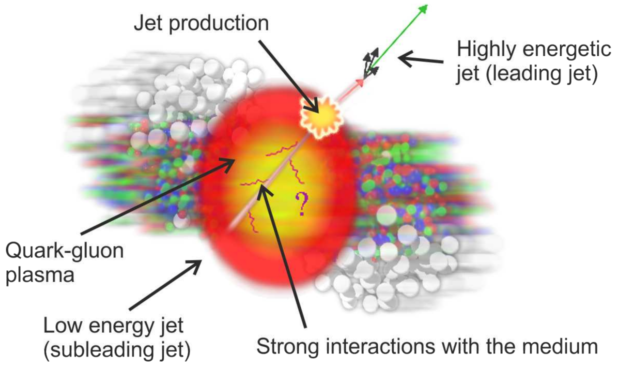

Figure 1. Sketch of the jet quenching mechanism during heavy ion collision.

3 Experimental Apparatus

The analysis in this work was made using the data from heavy-ion collisions at nucleon-nucleon center-of-mass energy $\sqrt{s_{NN}} = 2.76$ TeV, which were collected by the ATLAS detector at the LHC in 2011.

The Large Hadron Collider (LHC) is a particle accelerator and collider located at CERN outside Geneva, Switzerland. ATLAS (A Toroidal LHC ApparatuS) is one of seven particle detectors at the LHC and together with the CMS (Compact Muon Solenoid) one of two general purpose detectors.

4 Experimental Analysis

4.1 Missing transverse momentum

The law of conservation of momentum dictates that the total sum of vectors of transverse momentum, $\mathbf{p}_{\mathrm{T}}$, of all the particles created in the collision should be zero. This conservation law is, however, almost never observed in real experiments and we can talk about a missing transverse momentum vector, $\not{\mathbf{p}}_{\mathrm{T}}$, defined as:

$$\not{\mathbf{p}}_{\mathrm{T}} \equiv -\sum_{i=0}^{N} \mathbf{p}_{\mathrm{T},i} = -\mathbf{p}_{\mathrm{T}}. \tag{1}$$

where the sum denotes vector sum over all particles in the studied p_{T} range. It should be noted that the following analysis has been done for four individual p_{T} ranges: $(0.5-\infty)$ GeV/c, $(0.5-2)$ GeV/c, $(2-4)$ GeV/c, $(4-\infty)$ GeV/c. These ranges have been chosen in order to see the differences in effects of quenching on particles with various momenta.

4.2 Collision centrality

The collision centrality can be intuitively thought of as the degree of overlap of the two colliding nuclei. It is one of the most important factors in heavy-ion physics, because the system produced in the most overlapping heavy-ion collisions is expected to create the best conditions necessary for QGP production.

Centrality bins are expressed in terms of percentiles with 0% representing the most central (head-on) events.

4.3 Overall energy balance of dijet events

It is important to characterize the dijet energy balance (or imbalance) with a single quantity. To do so, the jet asymmetry ratio, A_J, was introduced [4]:

$$A_J = \frac{E_{\mathrm{T1}} - E_{\mathrm{T2}}}{E_{\mathrm{T1}} + E_{\mathrm{T2}}}, \tag{2}$$

where the first jet is required to have a transverse energy $E_{\mathrm{T1}} > 100$ GeV, and the second jet is the highest tranverse energy jet in the opposite hemisphere with $E_{\mathrm{T2}} > 25$ GeV. It has been observed [4] that in the case of peripheral collisions the dijet asymmetry distribution in both proton-proton and simulated events is similar to that in lead-lead events. However, as the events become more central, the lead-lead data distributions develop different characteristics, indicating an increased rate of highly asymmetric dijet events. This is a result of the jet quenching.

To learn more details about the energy loss mechanism, one can study the overall energy balance in events with asymmetric dijets. This overall energy balance can be quantified using the projections of $\not{\boldsymbol{p}}_{\mathrm{T}}$ vector of reconstructed tracks onto the axis of leading jet, $\langle \not{p}_{\mathrm{T}}^{||,\mathrm{LJ}} \rangle$. Probability distributions of this projection for individual p_{T} ranges and centrality bins are displayed in the upper panel of Figure 2. One can see that the distributions are rather broad, although a clear shift of the mean values can be seen. We can, therefore, average the results over events to obtain the mean values of the projections $\langle \not{p}_{\mathrm{T}}^{||,\mathrm{LJ}} \rangle$. This quantity was evaluated as a function of asymmetry A_J for two centrality ranges, as displayed in Figure 2 (bottom).

The physics picture concluded from these plots is following: with increasing asymmetry A_J the imbalance increases and the lack of the high-p_{T} particles in the subleading jet (negative values of projections) is compensated by the excess of soft particles (positive values of projections). The effect is stronger for central collisions, as shown in lower left panel of Figure 2, which can be explained by the fact that in central collisions the subleading jet is very often strongly quenched, which means that the yield of hard particles is suppressed.

5 Summary

In this work, the data collected by ATLAS detector have been used to investigate the behavior of missing transverse momentum in PbPb collisions at center-of-mass energy $\sqrt{s_{NN}} = 2.76$ TeV. First, “work in progress” results have been presented. A strong increase of yields of highly unbalanced dijets has been shown to be correlated with an increase of production of soft particles associated with the strongly quenched subleading jet.

These results will provide a critical qualitative and quantitative insight into the transport properties of the medium created in heavy-ion collisions. Furthermore, they are in a very good agreement with previously published results by CMS [5].

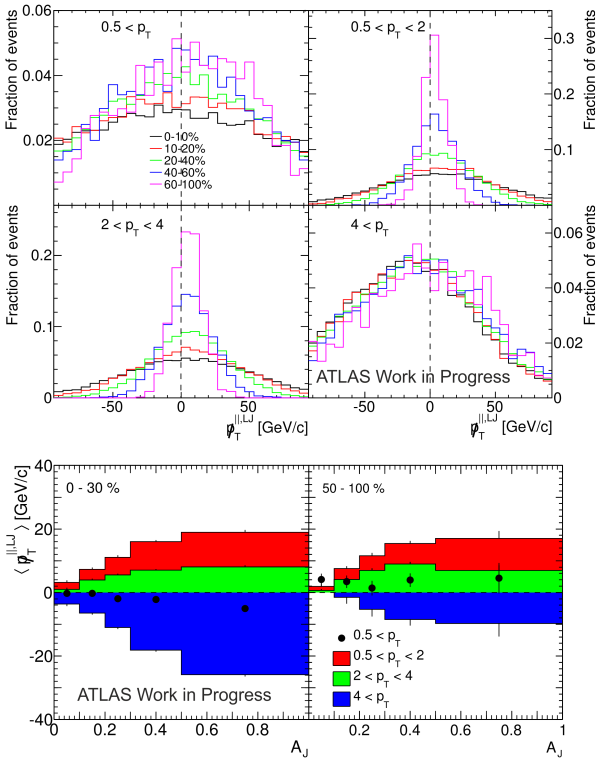

Figure 2. (top) Probability distributions of the scalar projection of the $\not{p}_{\mathrm{T}}$ vector onto the leading jet axis for four studied p_{T} ranges. (bottom) Average missing transverse momentum projected onto the leading jet axis. The $\langle \not{p}_{\mathrm{T}}^{||,\mathrm{LJ}} \rangle$ values are shown as a function of dijet asymmetry, A_J, for $(0-30)$% centrality (left) and $(50-100)$% centrality (right).

References

[1] J. D. Bjorken, FERMILAB-PUB-82-059-THY (1982).

[2] X. N. Wang, M. Gyulassy, Phys. Rev. Lett. **86**, 3496 (2001).

[3] X. N. Wang, Phys. Rep. **280**, 287 (1997).

[4] ATLAS Collaboration, Phys. Rev. Lett. **105**, 252303 (2010).

[5] CMS Collaboration, CMS-PAS-HIN-14-010 (2014).

Effect of magnetic fluid layer thickness on the spectral transmittance

Norbert Tarjányi[1] and Marek Mlynarčík[2]

[1]tarjanyi@fyzika.uniza.sk, Dept. of Physics, Faculty of Electrical Engineering, University of Žilina, Univerzitná 1, 01026 Žilina, Slovak Republic
[2]student at Dept. of Telecommunications and Multimedia, Faculty of Electrical Engineering, University of Žilina, Univerzitná 1, 01026 Žilina, Slovak Republic

Abstract. Magnetic fluid found its first major commercial application in the 60s of the 20th century as part of the rocket fuel. The idea was to control the transfer of the fuel in condition of a weightless environment by means of a magnetic field. Since then a lot of interesting applications in electronics, electrical engineering, material science, medicine or even optics has emerged utilizing these colloidal suspensions consisting of solid magnetic nanoparticles dispersed in a carrier fluid. This contribution presents the results of the investigation of spectral transmittance of the magnetic fluid layer depending on its thickness. The achieved results are interpreted in terms of the possibility of using magnetic fluid layers with different thicknesses as optical filters.

1 Introduction

Magnetic fluid represents a compromise between a liquid and a magnet. It is a stable colloidal system consisting of a monodomain ferro- or ferrimagnetic particles dispersed in a carrier liquid, such as water, oil, or saline.

Monodomain particles are most often made from iron oxides (Fe_3O_4, Fe_2O_3) or transition metals as Fe, Ni, Co and their nitrides and borides. The dimensions of the particles are in the range 1–20 nm, so they move in the carrier liquid due to Brownian motion.To prevent mutual aggregation of the particles due to the existence of attractive forces between them the surface-active agents – surfactants are added to the carrier liquid which provide coating of the particles and their repulsion [1].

Magnetic fluid as a set of m onodomain nanoparticles dispersed in a carrier liquid is a paramagnetic one and the magnetic moment is carried by the nanoparticles dispersed in the base liquid.

The connection of liquid and magnetic properties of a matter is very interesting in terms of basic research [2–5] as well as in terms of technical applications [6–9]. This contribution presents the first results of the investigation of spectral transmittance of the magnetic fluid layer depending on its thickness. The achieved results are interpreted in terms of the possibility of using magnetic fluid layers with different thicknesses as optical filters.

2 Experimental

For the investigation we used a magnetic fluid with Fe_3O_4 nanoparticles (5 % concentration, diameter of particles of about 10 nm) dispersed in transformer oil ITO 100 as a base liquid. The magnetic fluid was produced at Institute of Experimental Physics, SAS in Košice.

The experimental set-up used consisted of a halogen lamp, collimating lens, sample holder with a reference sample (oil ITO 100 only) and a sample under the test (oil ITO 100 based magnetic fluid), spectrometer for VIS spectral region and a computer which controlled the spectrometer and collected the measured data. The set-up is schematically shown in Figure 1.

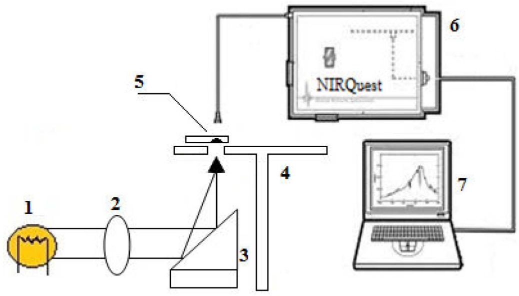

Figure 1. Set-up for investigation the optical transmittance of magnetic fluid layer: 1. Halogen lamp, 2. Collimating lens, 3. Mirror, 4. Holder for reference and investigated samples, 5. Sample, 6. Spectrometer for VIS, 7. Computer.

Layers of magnetic fluid were prepared in glass cells made of two microscopic slides put one over another. Various thicknesses of the layers we achieved by inserting the defined spacers bodies between microscopic slides. The thicknesses were measured by a micrometer screw gauge and the values were determined with an error of max. ±5 µm.

2.1 Transmittance measurement

Measurement of transmittance was performed by a spectrometer HR2000+ within the range of wavelengths 380–1000 nm. The operating software of the spectrometer defines the transmittance as the percentage of energy passing through a sample relative to the amount that passes through the reference. So, the transmittance is expressed and calculated according to equation

$$T(\lambda) = \{[S(\lambda) - D(\lambda)] / [R(\lambda) - D(\lambda)]\} \cdot 100\,\%, \quad (1)$$

where $S(\lambda)$ is the sample intensity, $D(\lambda)$ is the dark intensity and $R(\lambda)$ is the reference intensity.

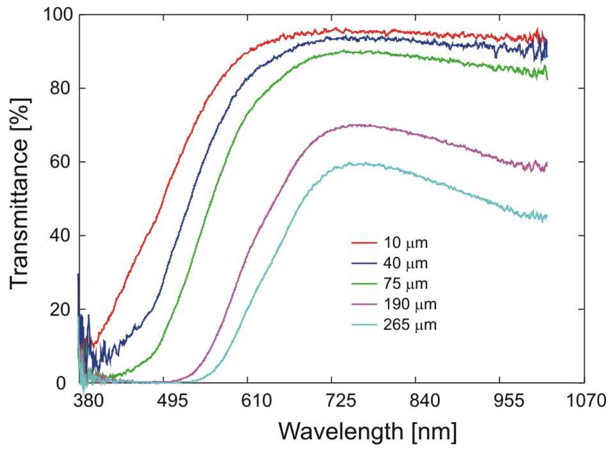

Figure 2. Spectral transmittances of magnetic fluid layer measured for different thicknesses of the layer.

The measured transmittances for VIS spectral region are, for various thicknesses of the magnetic fluid layers, depicted in Figure 2.

3 Results and discussion

Let $B \cdot [\exp(-\alpha_{\mathrm{B}}) \cdot t]$, $G \cdot [\exp(-\alpha_{\mathrm{G}}) \cdot t]$ and $R \cdot [\exp(-\alpha_{\mathrm{R}}) \cdot t]$ denote the blue, green and red transmittances, respectively, where α is coefficient of absorption and t is a sample thickness. The ratio of the transmitted intensities, e.g. for green and red lights is $(G/R) \cdot [\exp(\alpha_{\mathrm{R}} - \alpha_{\mathrm{G}}) \cdot t]$. If the red absorbance is less than the green, then as the thickness t increases, so does the ratio of red to green transmitted light (Figure 3a).

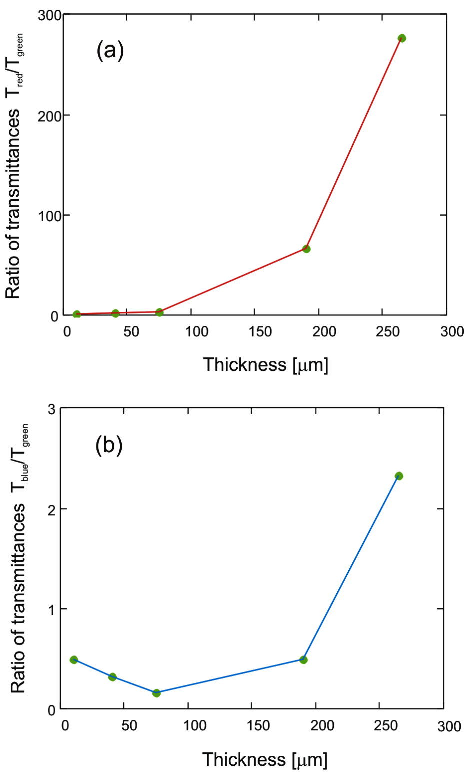

Figure 3. Ratios of transmittances for two wavelengths as function of sample's thickness: (a) 633 nm/514 nm, (b) 447 nm/514 nm.

4 Conclusion

The obtained partial results indicate that a thin layer of magnetic fluid can, in principle, be used to construct an optical attenuator. It is interesting that the absorbance is function of wavelength of light used and a layer thickness, too. This opens possibilities for tuning the values of attenuation in an optical system. Further research will be focused on increasing the accuracy of measurement of thickness and the effect of the external magnetic field on the transmittance of the magnetic fluid layers.

Acknowledgment

Authors akcnowledge the Institute of Experimental Physics SAS, Košice and the colleague Dr. Jozef Kúdelčík for providing the sample of magnetic fluid.

References

[1] M. P. Pileni, Adv. Funct. Mater. **11**, 323 (2011).

[2] S. Y. Yang, W. S. Tse, H. E. Horng, H. C. Yang, CH. Y. Hong, J. Magn. Magn. Mater. **226–230**, 1992 (2001).

[3] L. B. Popescu, V. Socoliuc, D. Bica, Rom. Journ. Phys. **51**, 791 (2005).

[4] F. Herchl, P. Kopčanský, M. Timko, M. Koneracká, K. Marton, I. Kolcunová, Acta Phys. Pol. **113**, 569 (2008).

[5] R. Q. Lv, Y. Zhao, N. Xu, H. Li, J. Magn. Magn. Mater. **337–338**, 23 (2013).

[6] Sh. Pu, X. Chen, L. Chen, W. Liao, Y. Chen, Y, Xia, Appl. Phys. Lett. **87**, 021901 (2005).

[7] Y. Zhao, Y. Zhang, R. –Q. Lv, Q. Wang, J. Magn. Magn. Mater. **323**, 2987 (2011).

[8] J. J. Chieh, C. Y. Hong, S. Y. Yang, H. E. Horng, H. C. Yang, J Nanopart Res **12**, 293 (2010).

[9] W. Yuan, Ch. Yin, P. Xiao, X. Wang, J. Sun, S. Huang, X. Chen, Zh. Cao, Microfluid Nanofluid **11**, 781 (2011).

J/ψ measurements in the STAR experiment

Barbara Trzeciak[1] (for the STAR Collaboration)

[1]Faculty of Nuclear Sciences and Physical Engineering, Czech Technical University in Prague, Brehova 7, 115 19 Praha 1, Czech Republic

Abstract. In this paper, we present recent STAR J/ψ results. J/ψ nuclear modification factors (R_{AA}) in Au+Au collisions at $\sqrt{s_{NN}}$ = 200, 62.4 and 39 GeV and in U+U collisions at $\sqrt{s_{NN}}$ = 193 GeV are measured and compared to different theoretical calculations. We also report J/ψ elliptic flow (v_2) results in Au+Au collisions at $\sqrt{s_{NN}}$ = 200 GeV and the first $\psi(2S)$ to J/ψ ratio measurement in $p+p$ collisions at $\sqrt{s}$ = 500 GeV.

1 Introduction

It was proposed that quarkonia are dissociated in the hot medium due to the Debye screening of the quark-antiquark potential and thus this "melting" can be a signature of Quark-Gluon Plasma (QGP) formation [1]. But there are other mechanisms that can alter quarkonium yields in heavy-ion collisions relative to $p+p$ collisions, for example statistical recombination of heavy quark-antiquark pairs in the QGP or cold nuclear matter (CNM) effects. Systematic measurements of the quarkonium production for different colliding systems, centralities and collision energies may help to understand the quarkonium production mechanisms in heavy-ion collisions as well as the medium properties.

2 J/ψ and $\psi(2S)$ measurements

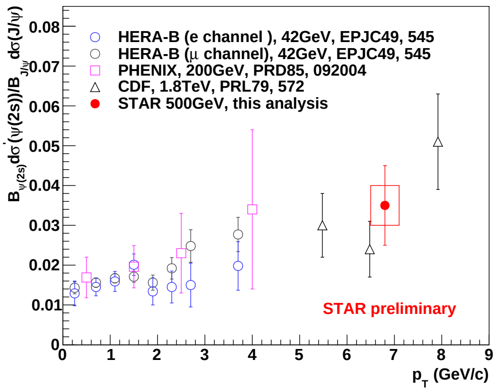

Figure 1. Ratio of $\psi(2S)$ to J/ψ in $p+p$ collisions at $\sqrt{s}$ = 500 GeV from STAR (red circle) compared to results from other experiments at different energies.

STAR has measured J/ψ p_T spectra [7, 11] and polarization [12] in $p+p$ collisions at $\sqrt{s}$ = 200 GeV via the dielectron decay channel (B_{ee} = 5.9%) at mid-rapidity ($|y|$ < 1). These results are compared to different model predictions to understand J/ψ production mechanism in elementary collisions. In order to further test the charmonium production mechanism and constrain the feed-down contribution from the excited states to the inclusive J/ψ production, the J/ψ and $\psi(2S)$ signals were extracted in $p+p$ collisions at $\sqrt{s}$ = 500 GeV. Figure 1 shows $\psi(2S)/J/\psi$ ratio from STAR (red full circle) compared to measurements of other experiments at different colliding energies, in $p+p$ and p+A collisions. The STAR data point is consistent with the observed trend, and no collision energy dependence of the $\psi(2S)$ to J/ψ ratio is seen with current precision.

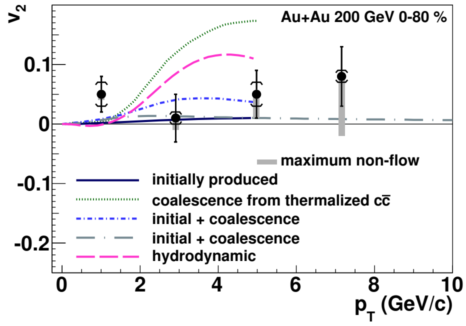

Figure 2. J/ψ v_2 in Au+Au collisions at $\sqrt{s_{NN}}$ = 200 GeV at mid-rapidity in 0-80% central events [2] with different model predictions ([3–6]). The gray boxes represent a non-flow estimation.

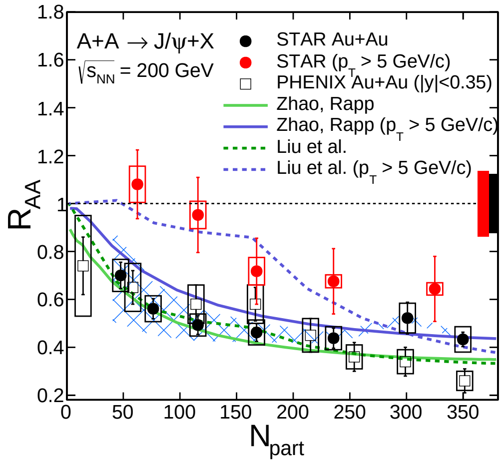

Figure 3. J/ψ R_{AA} as a function of N_{part} in Au+Au collisions at $\sqrt{s_{NN}}$ = 200 GeV at mid-rapidity ([7, 8]) with two model predictions ([9, 10]). The low-p_T (< 5 GeV/c) result is shown as black full circles and the high-p_T (> 5 GeV/c) measurement as red full circles.

In Au+Au collisions at $\sqrt{s_{NN}}$ = 200 GeV STAR has measured J/ψ p_T spectra for different centrality bins [7, 8]. It was found that at low p_T ($\lesssim$ 2 GeV/c) the J/ψ p_T spectra are softer than the Tsallis Blast-Wave prediction, assuming that J/ψ flows like lighter

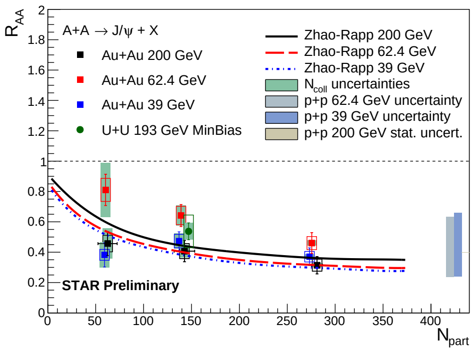

Figure 4. J/ψ R_{AA} as a function of N_{part} in Au+Au collisions at $\sqrt{s_{NN}} = 200$ (black), 62.4 (red) and 39 (blue) GeV at mid-rapidity with model predictions ([9]). As the green circle the minimum bias U+U measurement at $\sqrt{s_{NN}} = 193$ GeV is also presented.

hadrons [8]. This suggests that recombination may contribute to low-p_T J/ψ production. Measurement of J/ψ v_2 may provide additional information about the J/ψ production mechanisms. Figure 2 shows J/ψ v_2 measured in STAR in Au+Au collisions at $\sqrt{s_{NN}}$ = 200 GeV [2]. At $p_T > 2$ GeV/c v_2 is consistent with zero. Compared to different model predictions [3–6], data disfavor the scenario that J/ψ with $p_T > 2$ GeV/c are dominantly produced by recombination (coalescence) from thermalized $c\bar{c}$ pairs. Figure 3 shows J/ψ R_{AA} as a function of the number of participant nucleons (N_{part}) in Au+Au collisions at $\sqrt{s_{NN}} = 200$ GeV, separately for low- (< 5 GeV/c) [8] and high-p_T (> 5 GeV/c) [7] regions. Suppression increases with collision centrality and the R_{AA} at high p_T is systematic higher than the low-p_T one. The strong suppression of high-p_T J/ψ observed in central collisions (0-30%) indicates color screening or other QGP effects – at $p_T > 5$ GeV/c J/ψ are expected to be less affected by the recombination and CNM effects. The R_{AA} results are compared with two models, Zhao and Rapp [9] and Liu *et al.* [10]. Both models take into account direct J/ψ production with the color screening effect and J/ψ produced via the recombination of c and $\bar{c}$ quarks. The Zhao and Rapp model also includes the J/ψ formation time effect and the B-hadron feed-down contribution. At low p_T both predictions are in agreement with the data, while the high-p_T result is well described by the Liu *et al.* model and the model of Zhao and Rapp underpredicts the measured R_{AA}.

Low-p_T J/ψ R_{AA} measurements in Au+Au collisions at various colliding energies: $\sqrt{s_{NN}} = 200$ (black), 62.4 (red) and 39 (blue) GeV are shown in Figure 4. Within the uncertainties, a similar level of suppression is observed for all three energies, which can be described by the model predictions of Zhao and Rapp [9]. However, it should be noted that due to lack of precise $p+p$ measurements at 62.4 and 39 GeV Color Evaporation Model calculations [13] are used as baselines, which introduce large uncertainties. Figure 4 also shows the Minimum Bias R_{AA} measurement in U+U collisions at $\sqrt{s_{NN}} = 193$ GeV as a full circle. In U+U collisions one can reach up to 20% higher energy density compared to Au+Au collisions in the same centrality bin [14]. No difference in suppression compared to other measurements presented in Figure 4 is observed.

3 Summary

In summary, significant suppression of low p_T J/ψ is seen in Au+Au collisions at various colliding energies: $\sqrt{s_{NN}} = 200$, 62.4 and 39 GeV, and in U+U collisions at $\sqrt{s_{NN}} = 193$ GeV. No strong energy dependence of the J/ψ suppression in Au+Au is observed. Also, high-p_T J/ψ in Au+Au collisions at $\sqrt{s_{NN}} = 200$ GeV are strongly suppressed in central collisions, which suggests the QGP formation. $\psi(2S)$ to J/ψ ratio was measured for the first time in $p+p$ collisions at $\sqrt{s} = 500$ GeV. When compared to results from other experiments, no collision energy dependence of the ratio is seen.

Acknowledgements

This publication was supported by the European social fund within the framework of realizing the project „Support of inter-sectoral mobility and quality enhancement of research teams at Czech Technical University in Prague", CZ.1.07/2.3.00/30.0034.

References

[1] T. Matsui, H. Satz, Phys. Lett. B **178**, 416 (1986).

[2] L. Adamczyk *et al.* (STAR Collaboration), Phys. Rev. Lett. **111**, 052301 (2013), [arXiv:1212.3304].

[3] L. Yan, P. Zhuang, N. Xu, Phys. Rev. Lett. **97**, 232301 (2006), [arXiv:0608010 [nucl-th]].

[4] V. Greco, C. Ko, R. Rapp, Phys. Lett. B **595**, 202 (2004), [arXiv:0312100 [nucl-th]].

[5] X. Zhao, R. Rapp (2008), [arXiv:0806.1239].

[6] Y. Liu, N. Xu, P. Zhuang, Nucl. Phys. A **834**, 317C (2010), [arXiv:0910.0959].

[7] L. Adamczyk *et al.* (STAR Collaboration), Phys. Lett. B **722**, 55 (2013), [arXiv:1208.2736].

[8] L. Adamczyk *et al.* (STAR Collaboration), Phys. Rev. C **90**, 024906 (2014), [arXiv:1310.3563].

[9] X. Zhao, R. Rapp, Phys. Rev. C **82**, 064905 (2010), [arXiv:1008.5328].

[10] Y. Liu, Z. Qu, N. Xu, P. Zhuang, Phys. Lett. B **678**, 72 (2009), [arXiv:0901.2757].

[11] B. Abelev *et al.* (STAR Collaboration), Phys. Rev. C **80**, 041902 (2009), [arXiv:0904.0439].

[12] L. Adamczyk *et al.* (STAR Collaboration), accepted by Phys. Lett. B (2014), [arXiv:1311.1621].

[13] R. Nelson, R. Vogt, A. Frawley, Phys. Rev. C **87**, 014908 (2013), [arXiv:1210.4610].

[14] D. Kikola, G. Odyniec, R. Vogt, Phys. Rev. C **84**, 054907 (2011), [arXiv:1111.4693].

Development of high-repetition rate lasers in the HiLASE project

Hana Turčičová[1], Ondřej Novák[2], Martin Smrž[3], Taisuke Miura[4], Akira Endo[5], and Tomáš Mocek[6]

[1]turcic@fzu.cz, [2]novakon@fzu.cz, [3]smrz@fzu.cz, [4]miura@fzu.cz, [5]endo@fzu.cz, [6]mocek@fzu.cz
HiLASE Centre, Institute of Physics ASCR, Za Radnicí 828, 25241 Dolní Břežany, Czech Republic

Abstract. The HiLASE project aims the development of a new generation of diode pumped high-average-power lasers which will be used in industry and science for special applications. The main part of our in-house development is based on a new progressive technology where the lasing medium has a shape of a thin disk. The thin disk in our case is a single crystal of Yb:YAG (1 cm diameter, 0.2 mm thickness) inserted as an active mirror into a resonator of a regenerative amplifier. Opposite to the thin disk is a parabolic mirror assuring many passes of the pump light from laser diodes through the thin lasing medium so that practically all the pumping radiation is absorbed. The amplification of oscillator pulses proceeds in those thin disk regenerative amplifiers in dependence on the beam parameters required for our beamlines called A, B and C. All beamlines will offer kilowatt level beams but they will differ in pulse energy and repetition rate. The state-of-the-art of the HiLASE project is presented together with the intended applications.

1 Introduction

All over the world many high-power lasers are operated, some of them on very high output power, such as on petawatt (10^{15} W) level, however, usually at very low repetition rate, e.g. one shot per tens of minutes, so that the average output power is low. The aim of the HiLASE project is the development of a new generation of diode pumped lasers operating at high repetition rate and high output power. The diode pumping, due to the low quantum defect in the lasing process, leads not only to a high optical-to-optical efficiency but at the same minimizes the heat load to the medium. The state-of-the-art thin disk technology enables production of picosecond pulses which will be used for the high-tech industry purposes. The advantage of such very short pulses when interacting with the surface of a material consists in avoiding the melting of the material in the vicinage of the laser beam.

2 The HiLASE project basement

The HiLASE centre will offer three beamlines A, B, and C, based on the thin disk technology. Figure 1 presents a scheme of the thin disk assembly (for a detailed description see [1]). The thin disks are pumped by fibre

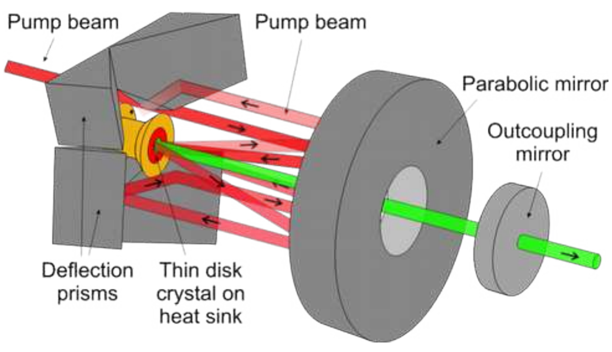

Figure 1. Thin disk (0.2 mm Yb:YAG) assembly with the pumping (red) and laser (green) beams (A. Giesen et al., Appl. Physics B **58**, 363, 1994).

coupled diode laser modules supplying 1 kW at a wavelength of 969 nm [2].

The Beamline A will be delivered as a complex by Dausinger&Giesen company, the output power of 1.3 kW at 0.75 J in < 3 ps pulsewidth are expected. One of its main applications will be laser induced damage testing (LIDT) in order to support development of high quality optical elements. The beamlines B and C will be fully developed by the HiLASE researchers.

The laser parameters of the B-beamline will be 500 W at 0.5 J pulse energy in 2–3 ps and a repetition rate of 1 kHz. It will be used besides others as a driving laser of EUV plasma sources for semiconductor lithography and for EUV micromachining. A part of the B-beam will be amplified in a one slab amplifier aiming 1 J pulses at 120 Hz, 1–2 ps. The technical structure of the B and C-lines is similar: the oscillator beam is stretched (up to 0.2 ns or 3 ns, accordingly) and amplified in a one/two regenerative amplifies, the output pulse is then optically compressed.

The beamline C will be a high repetition rate system also of 500 W, but at 100 kHz, and 5 mJ in 1–2 ps pulsewidth. Its application will be in laser micromachining, as a pre-pulse for EUV lithography, mid-IR pulse source for bio-medical application, and to extend its application the C-beam will also be converted into higher harmonics.

Besides the three beamlines the HiLASE centre will operate also a kilowatt-class multi-slab laser system [3, 4], 100 J in 2–10 ns pulsewidth at 10 Hz, which is constructed in the co-operation with the Central Laser Facility, RAL, Didcot, UK.

3 Present status and activities

Figure 2 presents the beam profile of the B-line. The energy output was 45 mJ at a repetition rate of 1 kHz. The result was obtained at experiments with pulse pumping at 969 nm wavelength [5, 6]. It was found that the pulse pumping improved the beam quality and the optical-to-optical efficiency, 19 % was achieved.

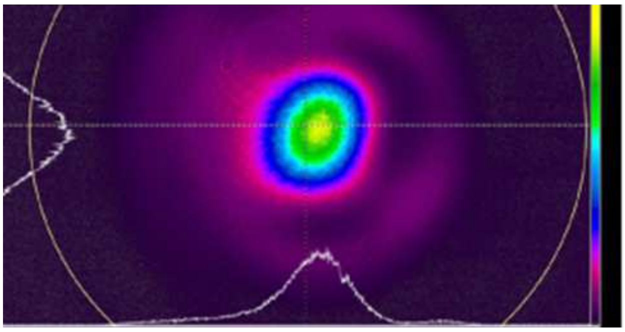

Figure 2. Profile of the B beamline at 45 mJ pulse energy at 1-kHz repetition rate with 500 µs pump pulse duration at 969 nm wavelength.

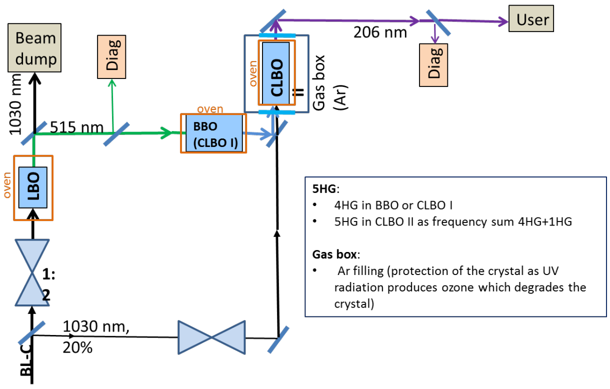

Figure 4. Generation of the fifth harmonic frequency of the primary beam in the C beamline.

The pulse energy in the beamline C has up to now achieved 0.85 mJ at 100 kHz, pulse duration of < 2 ps. We showed advantages of pumping at 969 nm over 939 nm pumping [7]. So as to manage 5 mJ in one pulse, more intense pumping, larger beam on the thin disk, and better cooling of the thin disk is planned. Regardless the lower pulse energy in the C-line beam, the schemes for the fundamental wavelength (1030 nm) up and down conversions have been under development.

Figure 3 presents the scheme of the frequency down conversion in optical parametric processes. A part of the primary beam pumps an optical parametric generator (OPG) and the output oscillator beam is amplified in an optical parametric amplifier (OPA) pumped by the rest of the primary beam [8]. The energy of 100 µJ is expected in the signal and idler beams of the OPA. The mid-IR beams will be used for spectroscopic purposes and laser-beam-material interactions.

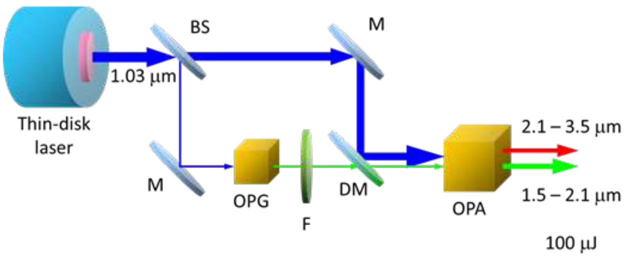

Figure 3. Generation of the mid-infrared radiation from the primary beam in the C beamline.

Figure 4 is a schematic of the up conversion scenario for the primary laser beam, namely for the generation of the fifth harmonic frequency. Three nonlinear crystals will be used, LBO for 2HG, CLBO/BBO for 4HG and another CLBO for 5HG. The latter crystal will be in a box filled with argon so as to protect the crystal surface against ozone, produced in air by VUV.

Acknowledgement

This work is co-financed by the European Regional Development Fund, the European Social Fund and the state budget of the Czech Republic (project HiLASE: CZ.1.05/2.1.00/01.0027, project DPSSLasers: CZ.1.07/2.3.00/20.0143, and project Postdok: CZ.1.07/2.3.00/30.0057). This research was partially supported by the grant RVO 68407700.

References

[1] M. Smrž, O. Novák, M. Chyla, T. Miura, A. Endo, T. Mocek, Czech. J. for Physics **63**(6), 331 (2013).

[2] M. Divoký, M. Smrž, M. Chyla, *et al.*, High Power Laser Science and Engineering **2**, e14 (2014).

[3] A. Lucianetti, M. Sawicka, O. Slezak, M. Divoký, J. Pilař, V. Jambunathan, S. Bonora, R. Antipenkov, T.Mocek, High Power Laser and Engineering **2**, e13 (2014).

[4] J. Pilař, S. Bonora, O. Slezák, M. Divoký, M. Sawicka-Chyla, A. Lucianetti, t. Mocek, Proc. of SPIE Vol. 8960, 89600W (2014).

[5] M. Chyla, T. Miura, M. Smrž, P. Severová, O. Novák, A. Endo, T. Mocek, Proc. SPIE 8959, Solid State Lasers XXIII: *Technology and Devices*, 89590S (2014).

[6] M. Chyla, T. Miura, M. Smrž, H. Jelínková, A. Endo, T. Mocek, Optics Letters **39** (6), 1441 (2014).

[7] M. Smrž, T. Miura, M. Chyla, S. Nagisetty, O. Novák, A. Endo, T. Mocek, Optics Letters 39 (16), 4919 (2014).

[8] O. Novák, T. Miura, M. Smrž, J. Huynh, P. Severová, A. Endo, and T. Mocek, Proc. SPIE 9135, Laser Sources and Applications II, 91350I (2014).

Study of jet properties in p+p collisions at $\sqrt{s}$ =7 TeV and p+Pb collisions at $\sqrt{s}$ =5.02 TeV using POWHEG-Box framework

Michal Vajzer[1,2]

[1] michal.vajzer@cern.ch, Nuclear Physics Institute ASCR, Na Truhlarce 39/64, 180 86 Praha 8, Czech Republic
[2] michal.vajzer@fjfi.cvut.cz, FNSPE CTU in Prague, Břehová 7, 115 19 Praha 1, Czech Republic

Abstract. In this contribution, next-to-leading order (NLO) simulations of jet production are presented. These simulations are carried out using POWHEG-Box framework [1], implementation of POWHEG next-to-leading-order generator, with parton showering provided by PYTHIA8 [2]. We focus on p+p collisions with centre of mass energy of 7 TeV and p+Pb collisions at 5.02 TeV, where we study jet production cross sections and ratio of jet spectra reconstructed in different collisions systems. Parton distributions considering effects of heavy ions are implemented using nuclear parton distribution functions (nPDFs) such as HKN07 [3] and using nuclear modification factors provided in EPS09 [4]. Jet reconstruction is done using anti-k_T algorithm included in FastJet package [5].

1 Introduction to jets

When a parton, a quark of gluon, is created with sufficient energy, it undergoes a complex evolution that produces a lot of final state particles. In theory jet is this final state of such parton, however, in experiment there is no information about the origin of particles, only spray of collinear particles are observed. The jet algorithm is then applied to reconstruct the jet and it has to produce consistent results.

The jet evolution can be theoretically described using to hadron production factorisation. Individual stages of evolution happen at different energy scales and therefore can be calculated separately and combined.

2 Analysis overview

In the analysis presented here, POWHEG-Box framework was used. It is based on a next-to-leading order momentum ordered processes. As an input, it uses PDF parametrisation described by CTEQ6.6 [6]. The output of POWHEG-Box are only particles involved in hard scatterings and these have to undergo further parton shower evolution. For this purpose PYTHIA8, monte-carlo event generator, has been used. It produces final state particles for given hard processes, which are subsequently analysed by anti-k_T jet algorithm, standard algorithm used by the LHC experiments, from FastJet package.

Main sources of systematic uncertainties in jet production in the described setup originate from variation of renormalisation and factorisation scales in the process generation itself, 13% uncertainty and from parametrisations of PDFs and nPDFs, approx. 6%.

3 Jet spectra in p+p at 7 TeV collisions

Figure 1 shows comparison between fully corrected jet cross section reconstructed from charged tracks only by the ALICE collaboration [7] and results of simulation with analysis setup described in Section 2 with cuts following those used in real data analysis for several values of resolution parameter, R, which describes area of the jet. Good agreement between data and simulation is observed. This serves as a baseline for further analyses.

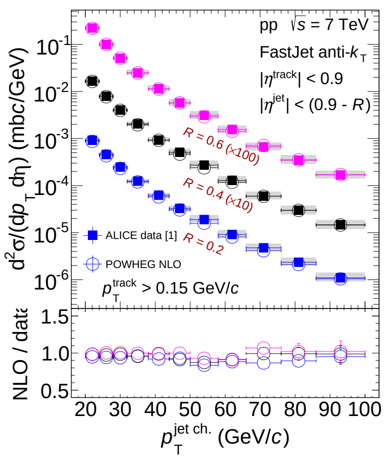

Figure 1. Jet spectra reconstructed using anti-k_T algorithm as obtained by ALICE (full squares) and by NLO simulations (open circles).

4 Jets in p+Pb at 5.02 TeV collisions

The study of p+Pb collisions provides information about cold nuclear effects or initial state effects that can be further used to improve understanding of medium before collisions and differentiate effects due to cold and hot media in heavy-ion collisions. To account for lead nuclei in the simulation framework, the PDF of second colliding proton has to be changed. This can be either directly to nuclear PDF, such as HKN07, or by using modification factors on already existing proton PDFs as in case of EPS09, both options are considered.

In order to observe changes in jet spectra with respect to the changed type of colliding particles, variable R_{p+Pb} is defined as a ratio of jet cross section in p+Pb collisions with respect to baseline of p+p collision at same centre of mass energies scaled by number of binary collisions. Figure 2 are $R_{\rm pPb}$ for different resolution parameters of reconstructed anti-$k_{\rm T}$ jets for both HKN07 and EPS09 nPDFs. The second one is systematically above 1, however, all results plotted are consistent with observation made by the ALICE collaboration [8].

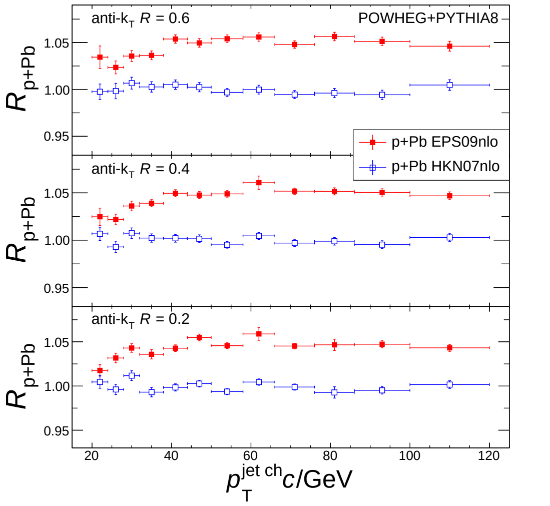

Figure 2. Ratio of jet spectra in p+Pb collisions with respect to p+p baseline for various resolution parameters.

5 Measrements using Bjorken's x

Variables x_1 and x_2 describe fraction of energy carried by partons in colliding nuclei with respect to the energy of these ions. They can be obtained directly from hard scattering simulation information. Additionally, they can be obtained from information of scattered hadronized partons in leading order processes. However, in the NLO processes the leading jets reconstructed in acceptance range of $-4.5 < y < 4.5$ are used with resolution parameter of 0.2. In order to calculate x_1 and x_2, formulae

$$x_1 = \frac{p_{\rm T}}{\sqrt{s}}\left(e^{y_3} + e^{y_4}\right), x_2 = \frac{p_{\rm T}}{\sqrt{s}}\left(e^{-y_3} + e^{-y_4}\right),$$

are used, where y_3 and y_4 represents rapidity of leading and subleading jet, respectively and $p_{\rm T}$ is transverse momentum of leading jet.

As seen in Figure 3, where ratio of extracted differential spectra as a function of x_1 or x_2 in p+Pb collisions with respect to p+p case, similarly to the Sec. 3, information obtained from jets is consistent with direct information from simulation in wide range of x and there is no apparent modification of PDF as function of x_1, which is trued as this represents unchanged distributions function of proton.

In case of ion modified to account for lead, enhanced probability is observed at values of $x_2 \approx 0.1$ and followed by suppression of probability for smaller values of x_2. This is consistent with overall picture presented in [9].

6 Summary

Presented results show very good agreement between data and simulation in p+p collisions at $\sqrt{s} = 7$ TeV. Modification of analysis to account for p+Pb collisions has shown that there is no apparent modification of jet cross section which is validated by results from the LHC experiments. Study of jets with respect to extracted values of x_1 and x_2 have shown that these jets can be used to observe changes in PDFs of heavy ions with respect to protons, however, these changes are integrated over all the parton types and over the whole range of Q^2 in hard scattering. Additionally, wide rapidity range had to be used to investigate big values of $x_{1,2}$ as possible.

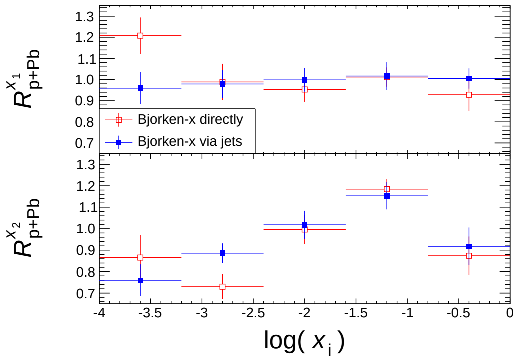

Figure 3. Modification of obtained PDFs in p+Pb collisions with respect to p+p case as a function of $x_{1,2}$.

7 Acknowledgement

This work was supported by the MEYS grant CZ.1.07/2.3.00/20.0207 of the European Social Fund in the Czech Republic: Education for Competitiveness Operational Programme, by the German Academic Exchange Service by the grant A/13/91563, by the grant LG 13031 of the Ministry of Education of the Czech Republic and by the Grant Agency of the CTU in Prague, grant SGS13/215/OHK4/3T/14.

References

[1] S. Alioli *et al.*, JHEP **1104**, 081 (2011).

[2] T. Sjostrand *et al.*, Comp. Phys. Com. **178**, 852 (2008).

[3] M. Hirai *et al.*, Phys. Rev. C **76**, 065207 (2007).

[4] K. J. Eskola *et al.*, JHEP **0904**, 065 (2009).

[5] M. Cacciari *et al.*, Eur. Phys. J. C **72**, 1896 (2012).

[6] P. M. Nadolsky *et al.*, Phys. Rev. D **78**, 013004 (2008).

[7] M. Vajzer (ALICE collab.), PoS EPS-HEP 2013, 464 (2013).

[8] J. F. Grosse-Oetringhaus (ALICE collab.), [arXiv:1408.0414].

[9] C. A. Salgado *et al.*, J. Phys. G **39** (2012) 015010.

List of participants

1. **Ing. Lucie Augustovičová**
Charles University, Praha, Czech Republic; augustovicova@karlov.mff.cuni.cz
2. **Mgr. Michal Belička**
Comenius University in Bratislava, Faculty of Pharmacy, Slovak Republic; belicka.michal@gmail.com
3. **Mgr. Jaroslav Bielcik, Ph.D.**
Czech Technical University in Prague, Czech Republic; jaroslav.bielcik@fjfi.cvut.cz
4. **prof. Ing. Július Cirák, CSc.**
Slovak Univ. of Technology in Bratislava, Fac. of El. Engineering and Inf. Technology, Slovak Republic; julius.cirak@stuba.sk
5. **Jana Crkovská**
Czech Technical University in Prague, Czech Republic; crkovjan@fjfi.cvut.cz
6. **Szabolcs Csonka, PhD.**
Budapest University of Technology and Economics, Budapest, Hungary; csonka@dept.phy.bme.hu
7. **prof. RNDr. Martin Černohorský, CSc.**
Masaryk University, Faculty of Science, Brno, Czech Republic; cernohorsky@physics.muni.cz
8. **Mgr. Daniel Červenkov**
Charles University, Faculty of Mathematics and Physics, Praha, Czech Republic; cervenkov@ipnp.troja.mff.cuni.cz
9. **RNDr. Jana Čisárová, PhD.**
Pavol Jozef Šafárik University in Košice, Institute of Physics, Slovak Republic; jana.cisarova@upjs.sk
10. **RNDr. Marcel Človečko, PhD.**
Institute of Experimental Physics, Slovak Academy of Sciences, Košice, Slovak Republic; clovecko@gmail.com
11. **RNDr. Jaroslav Dittrich, CSc.**
Nuclear Physics Institute AS CR, v.v.i., Řež, Czech Republic; dittrich@ujf.cas.cz
12. **Mgr. Pavla Doškářová, PhD.**
Czech Technical University in Prague, Fac. of Nucl. Sciences and Phys. Eng., Czech Republic; p.doskarova@gmail.com
13. **prof. John M. Dudley**
University of Franche-Comté, President of the European Physical Society, Besançon, France; john.dudley@univ-fcomte.fr
14. **Mr. Sami Dzsaber**
Budapest University of Technology and Economics, Budapest, Hungary; dzsaber.sami@gmail.com
15. **Dr. Zoltán Elekes**
MTA Atomki, Debrecen, Hungary; elekes@atomki.mta.hu
16. **prof. Mgr. Jiří Erhart, Ph.D.**
Technical University of Liberec, Department of Physics, Czech Republic; jiri.erhart@tul.cz
17. **Gyulnara Eyyubova**
Czech Technical University in Prague, Czech Republic; eyyubgyu@fjfi.cvut.cz
18. **Zuzana Fecková**
Matej Bel University, Banská Bystrica, Slovak Republic; zuzana.feckova@umb.sk
19. **Mgr. Pavol Federič, PhD.**
Nuclear Physics Institute AS CR, v.v.i., Řež, Czech Republic; pavol.federic@gmail.com
20. **Mgr. Juraj Feilhauer, PhD.**
Phys.-Techn. Bundesanstalt Braunschweig, Institute of Electrical Engineering, SAS, Bratislava, Slovak Republic; juraj.feilhauer@savba.sk
21. **Bc. Ondřej Ficker**
Czech Technical University in Prague, Institute of Plasma Physics AS CR, v.v.i., Czech Republic; oficker@gmail.com
22. **Jana Fodorová**
Czech Technical University in Prague, Fac. of Nucl. Sciences and Phys. Eng., Czech Republic; fodorova.jana@gmail.com

23. **Zsolt Fülöp, D.Sc.**
Inst. of Nuclear Research of HAS, Debrecen, Hungary; fulop@atomki.mta.hu
24. **Aurél Gábris**
Czech Technical University in Prague, University of Szeged, Czech Republic; gabris.aurel@fjfi.cvut.cz
25. **prof. dr hab. Adam Gadomski, ordin. prof. physics**
Group of Modeling of Physicochemical Processes, Physics Divsion, UTP Bydgoszcz, Poland; agad@utp.edu.pl
26. **RNDr. Lucia Gálisová, PhD.**
Technical University of Košice, Faculty of Mechanical Engineering, Slovak Republic; galisova.lucia@gmail.com
27. **Michal Géci**
Technical University of Košice, Slovak Republic; michal.geci.1995@gmail.com
28. **RNDr. Mikuláš Gintner, PhD.**
University of Žilina, Slovak Republic; gintner@fyzika.uniza.sk
29. **doc. PaedDr. Viera Haverlíková, PhD.**
Comenius University in Bratislava, Faculty of Medicine, Slovak Republic; viera.haverlikova@fmed.uniba.sk
30. **Mgr. Markéta Havrdová (Svatáková)**
Palacký University, Olomouc, Czech Republic; marketa.havrdova@upol.cz
31. **doc. RNDr. Richard Hlubina, DrSc.**
Comenius University in Bratislava, Fac. of Math., Physics and Informatics, Slovakia; richard.hlubina@fmph.uniba.sk
32. **prof. Karol Hricovini**
Université de Cergy-Pontoise, France; karol.hricovini@u-cergy.fr
33. **prof. Ing. Eduard Hulicius, CSc.**
Institute of Physics AS CR, v.v.i., Praha, Czech Republic; hulicius@fzu.cz
34. **Bc. Lukáš Chlad**
Charles University in Prague, Nuclear Physics Institute AS CR, v.v.i., Plzeň, Czech Republic; chlad@ujf.cas.cz
35. **Ing. Vítězslav Jarý**
Institute of Physics AS CR, v.v.i., Praha, Czech Republic; jary@fzu.cz
36. **RNDr. Jiří Kaštil**
Charles University, Praha, Czech Republic; jirka.kastil@gmail.com
37. **prof. Sándor Katz, PhD.**
Eötvös Loránd University, Budapest, Hungary; katz@bodri.elte.hu
38. **Mgr. Mária Klacsová, PhD.**
Comenius University in Bratislava, Faculty of Pharmacy, Slovak Republic; klacsova@fpharm.uniba.sk
39. **Mária Kladivová**
Technical University of Košice, Department of Physics, Slovak Republic; maria.kladivova2tuke.sk
40. **Mgr. Tomáš Kmječ**
Charles University in Prague, Faculty of Mathematics and Physics, Praha, Czech Republic; kmjec@mbox.troja.mff.cuni.cz
41. **Mgr. Mary Kolářová**
Palacký University, Olomouc, Czech Republic; maryko@seznam.cz
42. **doc. RNDr. Eva Komová, PhD.**
Technical University of Košice, Faculty of Aeronautics, Slovak Republic; eva.komova@tuke.sk
43. **doc. RNDr. Peter Kopčanský, CSc.**
Institute of Experimental Physics, Slovak Academy of Sciences, Košice; Slovakia
44. **Renata Kopečná**
Czech Technical University in Prague, Fac. of Nucl. Sciences and Phys. Eng., Czech Republic; rekopecna@seznam.cz
45. **RNDr. Martin Kozák, Ph.D.**
Charles University, Praha, Czech Republic; ma.kozak@seznam.cz

46. **Dr. Jozef Kravčák, PhD.**
Technical University of Košice, Fac. of El. Engineering and Informatics, Slovak Republic;
jozef.kravcak@tuke.sk
47. **Ing. Michal Křelina**
Czech Technical University in Prague, Fac. of Nucl. Sciences and Phys. Eng., Czech Republic;
michal.krelina@fjfi.cvut.cz
48. **RNDr. Dalibor Krupa, CSc., DPhil**
Institute of Physics, Slovak Academy of Sciences, Bratislava, Slovak Republic; krupa@savba.sk
49. **RNDr. Filip Křížek, Ph.D.**
Nuclear Physics Institute AS CR, v.v.i., Řež, Czech Republic; krizek@ujf.cas.cz
50. **doc. RNDr. Roman Kubínek, CSc.**
Palacký University, Olomouc, Czech Republic; roman.kubinek@upol.cz
51. **doc. RNDr. Jozef Kúdelčík, PhD.**
University of Žilina, Slovak Republic; kudelcik@fyzika.uniza.sk
52. **RNDr. Andrej Kugler, CSc.**
Nuclear Physics Institute AS CR, v.v.i., Řež, Czech Republic; kugler@ujf.cas.cz
53. **prof. Jenö Kürti**
Eötvös Loránd University, Department of Biological Physics, Budapest, Hungary; kurti@virag.elte.hu
54. **Mgr. Miroslava Lacková**
Pavol Jozef Šafárik University in Košice, Slovak Republic; miroslava.lacky@gmail.com
55. **Ing. Štefan Lányi, DrSc.**
Institute of Physics, Slovak Academy of Sciences, Bratislava, Slovak Republic; lanyi@savba.sk
56. **David Lee**
Secretary General, European Physical Society, Mulhouse, France; d.lee@eps.org
57. **doc. Rupert Leitner, DrSc.**
Charles University, Faculty of Mathematics and Physics, Praha, Czech Republic;
Rupert.Leitner@mff.cuni.cz
58. **RNDr. Jozef Leja**
Institute of Physics, Slovak Academy of Sciences, Bratislava, Slovak Republic; jozef.leja@stuba.sk
59. **RNDr. Tomáš Lešner**
Phywe, Praha, Czech Republic; lesner@phywe.cz
60. **Miss Chiara Liberatore, MsC**
Czech Technical University, HiLASE Centre, Institute of Physics AS CR, Dolní Břežany, Czech Republic;
liberatore@fzu.cz
61. **Jindřich Lidrych**
Czech Technical University in Prague, Czech Republic; lidryjin@fjfi.cvut.cz
62. **Martin Liščinský**
Technical University of Košice, Slovak Republic; martin.liscinsky@gmail.com
63. **Mgr. Dmytro Lotnyk**
Pavol Jozef Šafárik University in Košice, Slovak Republic; dmytro.lotnyk@gmail.com
64. **doc. RNDr. Libor Machala, Ph.D.**
Palacký University, Olomouc, Czech Republic; libor.machala@upol.cz
65. **RNDr. Jiří J. Mareš, CSc.**
Institute of Physics AS CR, v.v.i., Praha, Czech Republic; maresjj@fzu.cz
66. **Bence Gábor Márkus**
Budapest University of Technology, Budapest, Hungary; xymarkus@gmail.com
67. **doc. RNDr. Ivan Melo, PhD.**
University of Žilina, Faculty of Electrical Engineering, Slovak Republic; melo@fyzika.uniza.sk
68. **Ing. Vasily Mikhaylov**
Nuclear Physics Institute AS CR, v.v.i., Řež, Czech Republic; mikhaylov@ujf.cas.cz
69. **Mgr. Martina Miková**
Palacký University, Olomouc, Czech Republic; martik.mik@gmail.com
70. **Bc. Michaela Mlynáriková**
Charles University, Faculty of Mathematics and Physics, Praha, Czech Republic;
michaela.mlynarikova@gmail.com

71. **doc. RNDr. Jan Mlynář, Ph.D.**
Institute of Plasma Physics AS CR, v.v.i., Praha, Czech Republic; mlynar@ipp.cas.cz
72. **prof. RNDr. Jan Novotný, CSc.**
Masaryk University, Faculty of Education, Brno, Czech Republic; nnovotnyy@gmail.com
73. **prof. RNDr. Tomáš Opatrný, Dr.**
Palacký University, Olomouc, Czech Republic; opatrny@optics.upol.cz
74. **Vojtěch Pacík**
Czech Technical University in Prague, Fac. of Nucl. Sciences and Phys. Eng., Czech Republic; pacikvoj@fjfi.cvut.cz
75. **Radomír Pánek**
Institute of Plasma Physics AS CR, v.v.i., Praha, Czech Republic; panek@ipp.cas.cz
76. **RNDr. Radek Pleskač, PhD.**
GSI Darmstadt, Germany; r.pleskac@gsi.de
77. **Dr. Illa Ramakanth, PhD**
VŠB-Technical University of Ostrava, Nanotechnology Centre, Czech Republic; ramakanthilla@yahoo.com
78. **prof. RNDr. Marian Reiffers, DrSc.**
University of Prešov in Prešov, Fac. of Humanities and Natural Sciences, Slovak Republic; reiffers@unipo.sk
79. **Mgr. Lukáš Richterek, Ph.D.**
Palacký University, Olomouc, Czech Republic; lukas.richterek@upol.cz
80. **Mgr. Pablo Rodríguez Ramos**
Nuclear Physics Institute AS CR, v.v.i., Řež, Czech Republic; ramos@ujf.cas.cz
81. **Ing. Jan Rusňák**
Nuclear Physics Institute AS CR, v.v.i., Praha, Czech Republic; rusn@email.cz
82. **doc. Mgr. Jan Soubusta, Ph.D.**
Institute of Physics AS CR, v.v.i., Palacký University, Olomouc, Czech Republic; jan.soubusta@upol.cz
83. **prof. Józef Spałek, Ph.D.**
Jagiellonian University, Krakow, Poland; ufspalek@if.uj.edu.pl,jozef.spalek@uj.edu.pl
84. **Mgr. Bohumil Stoklasa**
Palacký University, Olomouc, Czech Republic; bohumil.stoklasa@upol.cz
85. **Ing. Ondřej Svoboda, PhD.**
Nuclear Physics Institute AS CR, v.v.i., Řež, Czech Republic; svoboda@ujf.cas.cz
86. **RNDr. Jindřiška Svobodová, Ph.D.**
Masaryk University, Faculty of Education, Brno, Czech Republic; svobodova@ped.muni.cz
87. **Lénárd Szolnoki**
Budapest University of Technology and Economics, Budapest, Hungary; leni536@gmail.com
88. **Karel Šafařík**
CERN, Meyrin, Geneva, Switzerland; Karel.Safarik@cern.ch
89. **RNDr. Ladislav Šándor, CSc.**
Institute of Experimental Physics, Slovak Academy of Science, Košice, Slovak Republic; sandor@saske.sk
90. **Bc. Filip Šidík**
Technical University of Košice, Faculty of Aeronautics, Slovak Republic; filip.sidik@gmail.com
91. **Mgr. Eva Šimečková, CSc.**
Nuclear Physics Institute AS CR, v.v.i., Řež, Czech Republic; simeckova@ujf.cas.cz
92. **Ing. Miroslav Šimko**
Czech Technical University in Prague, Czech Republic; simkomir@fjfi.cvut.cz
93. **RNDr. Miriam Šimralová**
Grammar school, Šrobárova 1, Košice, Slovak Republic; simmiriam@gmail.com
94. **Ing. Milan Štefánik**
Nuclear Physics Institute AS CR, v.v.i., Praha, Czech Republic; stefanik@ujf.cas.cz
95. **Bc. Pavol Štefko**
Charles University, Faculty of Mathematics and Physics, Praha, Czech Republic; pavol.stefko@gmail.com
96. **RNDr. Mária Šviková, CSc.**
Grammar school of St. Thomas Aquinas, Košice, Slovak Republic; svikova@gmail.com

97. **Ing. Norbert Tarjányi, PhD.**
University of Žilina, Slovak Republic; tarjanyi@fyzika.uniza.sk

98. **RNDr. Milan Timko, CSc.**
Institute of Experimental Physics, Slovak Academy of Sciences, Košice, Slovak Republic; timko@saske.sk

99. **Pavel Tlustý**
Nuclear Physics Institute AS CR, v.v.i., Řež, Czech Republic; tlusty@ujf.cas.cz

100. **dr. Barbara Trzeciak**
Czech Technical University in Prague, Czech Republic; barbara.trzeciak@gmail.com

101. **RNDr. Igor Túnyi, DrSc.**
Geophysical Institite, Slovak Academy of Sciences, Bratislava, Slovak Republic; igor.tunyi@savba.sk

102. **RNDr. Hana Turčičová, CSc.**
Institute of Physics AS CR, v.v.i, Praha, Czech Republic; turcic@fzu.cz

103. **Michal Vajzer**
Nuclear Physics Institute AS CR, v.v.i., Praha, Czech Republic; michal.vajzer@cern.ch

104. **RNDr. Alice Valkárová, DrSc.**
Charles University, Faculty of Mathematics and Physics, Praha, Czech Republic;
alice.valkarova@mff.cuni.cz

105. **Mgr. František Vavrek**
Institute of Experimental Physics, Slovak Academy of Sciences, Košice, Slovak Republic; vavrek@saske.sk

106. **Mgr. Karol Vegso, PhD.**
Institute of Physics, Slovak Academy of Sciences, Bratislava, Slovak Republic; karol.vegso@savba.sk

107. **Mgr. Ľubomír Vlček**
Independent researcher, Bardejov, Slovak Republic; lubomir.vlcek@gmail.com

108. **Bc. Vlastimil Vrba**
Palacký University, Olomouc, Czech Republic; willywillow@seznam.cz

109. **prof. RNDr. Radek Zbořil, Ph.D.**
Palacký University, Olomouc, Czech Republic; radek.zboril@upol.cz

110. **doc. RNDr. Ján Ziman, CSc.**
Technical University of Košice, Slovak Republic; jan.ziman@tuke.sk

Libor Machala, Lukáš Richterek (editors)

Proceedings of the 18th Conference of Czech and Slovak Physicists
Olomouc, Czech Republic, September 16–19, 2014

Executive Editor: Prof. RNDr. Zdeněk Dvořák, DrSc.
Responsible Editor: Mgr. Jana Kreiselová
Typeset by pdfCSLaTeX: Lukáš Richterek

1. edition

No English-language editing and proofreading was done either by the publisher or by the editors, so the quality of language of papers is under the authors' responsibility.

Palacký University Olomouc, Křížkovského 8, CZ-771 47 Olomouc, Czech Republic
WWW: www.upol.cz/vup
E-mail: vup@upol.cz

Olomouc 2015

Not for sale

Proceeding are available via the conference webpage
http://jcmf.upol.cz/kcsf18/

ISBN 978-80-244-4725-4 (CD)
ISBN 978-80-244-4726-1 (on-line)

9 788024 447254